Nanomechanical and Optomechanical Torque Magnetometry of Isolated Nanomagnetic Assemblies

by

Tayyaba Firdous

A thesis submitted in partial fulfillment of the requirements for the degree of

Doctor of Philosophy

Department of Physics
University of Alberta

Abstract

Nanomechanical torque magnetometry is emerging as a highly-sensitive method for gauging magneto-statics and magnetic dynamics in mesoscopic and nano-scale magnetic materials. Advances in torque magnetometry are presented here, which were unattainable using previous techniques. Silicon nitride membrane-based nanomechanical torque magnetometers were first fabricated and characterized using the resonance modes and magnetic hysteresis and integrated with ~ 350 bacterial magnetosome nanoparticles in a random assembly. Methods of assembling the magnetic materials (nanoparticles, mesoscopic magnetic disks) in geometrical shapes on the nanomechanical torque magnetometers were developed later on. Further, optomechanical torque magnetometers were developed to derive their highly sensitive transductions in ambient conditions. Optomechanical torque magnetometers were also used as RF susceptometers to acquire the vector-based susceptibility components. Finally, RF susceptometry was combined with the torque-mixing resonance spectroscopy for characterization of magnetic dynamics. The new nanophotonic optomechanical torque magnetometers developed in this Thesis can potentially be used for probing the magnetization, susceptibility, and spin resonances in a countable number of magnetic nanoparticles, leading to single spin detection in ambient conditions.

Preface

Some of the research work presented in this Thesis has been published in peer-reviewed journals. The conducted research here is part of an international research collaboration with groups of Profs. D. A. Bazylinski (University of Nevada), T. Prozorov (Ames Laboratory, US Department of Energy), P.E. Barclay (University of Calgary) and D. Vick at the National Institute for Nanotechnology (NINT). The fabrication of torque magnetometers was performed at the University of Alberta NanoFab and NINT. The details about the work contributions are listed below.

Chapter 3 presents the torque magnetometry of assembled nanoparticles on the nanomechanical devices. This work has been published as "Nanomechanical Torque Magnetometry of an Individual Aggregate of ∼350 Nanoparticles" by T. Firdous, D. Vick, M. Belov, F. Fani Sani, A. McDermott, J.E. Losby, D.A. Bazylinski, T. Prozorov, D.K. Potter and M.R. Freeman in the Canadian Journal of Physics 93: 1252-1256 (2015). I performed the experiments, collected data, and analyzed as well as wrote the manuscript. D. Vick performed the focused ion beam milling for device fabrication; F. Fani Sani helped in micromagnetic simulations; A. McDermott helped in the experiments; J.E. Losby contributed to manuscript editing; D.A. Bazylinski provided the magnetite nanoparticles; and T. Prozorov assembled the nanoparticles on the devices. D.K. Potter and M.R. Freeman were the supervisory authors and were involved with conceptual understanding and manuscript editing.

Chapter 4 presents the torque magnetometry of self-assembled nanoparticles

in geometrical shapes on the nanomechanical devices. I fabricated the devices, conducted the experiments and analyzed the data. D. Vick performed the focused ion beam milling for device cleaning. D.K. Potter and M.R. Freeman were the supervisors and helped in concept formation.

Chapter 5 shows the findings of magnetic susceptibility at Barkhausen steps in ambient conditions. This work has been published as, "Nanocavity Optomechanical Torque Magnetometry and Radiofrequency Susceptometry" by Marcelo Wu*, Nathanael L.-Y. Wu*, Tayyaba Firdous*, Fatemeh Fani Sani, Joseph E. Losby, Mark R. Freeman and Paul E. Barclay in Nature Nanotechnology 12:127 (2017). I am the equal first author of this paper (the three first authors are designated by *) and responsible for conducting the experiments, collecting data, analyzing data and for contribution to the manuscript. Marcelo Wu and Nathanael L.-Y. Wu designed and fabricated the devices. Marcelo Wu arranged the experimental setup. Marcelo Wu, Nathanael L.-Y. Wu, and Tayyaba Firdous performed the experiments and analyzed the data. Fatemeh Fani Sani helped in data analysis and simulations (I also performed simulations); Joseph E. Losby provided technical guidance; and Mark R. Freeman and Paul E. Barclay supervised this project. All authors contributed to the manuscript.

Chapter 6 presents the preliminary work for the miniature Einstein-de Haas experiment, and for the ultra-high sensitive field sensing magnetometers. I polished the YIG sample to make disks and M. Belov fabricated the devices. I performed the experiments, collected data and analyzed the scientific findings. Joseph E. Losby fabricated the double paddle resonator and M. Belov performed the YIG disk milling and transfer onto the paddles.

I conducted all the experiments, simulations and analyzed the data presented in the Appendices. I performed all the simulations detailed in Appendix B and fabricated the devices using the device fabrication processes listed in Appendix C, however, Joseph E. Losby trained me for nanofabrication processes.

I performed all the experiments for the nanoparticles in Appendix D. Jeremy Bau synthesized the nanoparticles described in Appendix D.2.1; Angela Brigley performed the bacteria lysing for nanoparticles in Appendix D.2.2; and Thomas Crawford provided the nanoparticle assemblies in Appendix D.2.3. I executed the mechanical grinding and polishing of the YIG in Appendix E. M. Belov fabricated the disk from the polished YIG lamella (see Appendix E.2.2) and D. Vick prepared the thin sections for TEM (see Appendix E.4). D. Vick performed the FIB on polished YIG samples and Jian Chen collected all TEM images in Appendix F. M. Belov prepared the YIG disks and Kai Cui obtained the Lorentz images in Appendix G. I performed the torque magnetometry measurements, Joseph E. Losby fabricated the devices, and Zhu Diao deposited the Co/CoO films on the devices in Appendix H.

For the glory of Allah

Acknowledgements

I would like to offer my profound acknowledgment to my supervisor, David Potter, for guidance and support. I would especially also like to thank all funding resources on the project. I would like to thank Mark Freeman for providing me the grounds to conduct my research.

I would like to thank all my lab fellows, peers, collaborators and supervisory committee for helping in understanding the knowledge, for sharing the idea and for their contribution: Joe Losby, Miro Belov, Doug Vick, Fatemeh Fani Sani, Dylan Grandmont, Petar Petrov, Marcelo Wu, Nathanael Wu, Dennis Bazylinski, Tanya Prozorov, Thomas Crawford, Wayne Hiebert, Al Meldrum, Frank Hegmann, and Paul Barclay. I would also like to thank Associate Chairs of Graduate Studies (Frank Marsiglio, Richard Marchand, and Sharon Morsink) for helping me out in special circumstances during my studies.

The University of Alberta Nanofab and NINT Nanofab deserves thanks for helping me to complete various processes for fabricating the devices. I would like to offer my sincere thanks to Joe Losby for training me on the Nanofab processes and for valuable discussions on the magnetometry measurements. I offer my thanks to Doug Vick for beneficial efforts on the focused ion beam. I would like to thank Fatemeh Fani Sani for helping me with the micromagnetic simulations. I am indebted to Marcelo Wu, and Nathanael Wu for teaching and training me on the optomechanical setup. I am thankful for the technical support, from Miro Belov for hardware and software issues in the experimental setup, and from David Fortin for excessively helping me in Labview programs.

In closing, I am grateful for my friends and family for providing me continuous support. I offer my gratitude and thank them all.

Contents

1 Introduction **1**

1.1 Objectives of the Thesis 1

1.2 Background and Integration of Ideas 3

1.2.1 Nanomechanics and Optomechanics 3

1.2.2 Self Assembly of Nanoparticles 7

1.2.3 Torque Magnetometry 11

1.3 Organization of the Thesis 14

2 Torque Magnetometry and Device Fabrication **17**

2.1 Introduction 17

2.2 Nanomechanical Torque Magnetometry 19

2.2.1 Fabry-Pérot Cavities 21

2.2.2 Nanomechanical Device Fabrication on Silicon Nitride Membranes 22

2.2.3 Nanomechanical Device Fabrication on Silicon-on-Insulator (SOI) 23

2.3 Cavity Optomechanical Torque Magnetometry 24

2.3.1 Nano-Beam Photonic Crystal Split-Beam Cavities 27

2.3.2 Nano-Cavity Split-Beam Optomechanical Device Fabrication 28

2.4 Torque-Mixing Resonance Spectroscopy (TMRS) 29

3 Nanomechanical Torque Magnetometry of an Individual Aggregate of ∼350 Nanoparticles **32**

3.1 Motivation . . . 32

3.2 Introduction . . . 33

3.3 Silicon Nitride Nanomechanical Torque Magnetometers . . . 34

3.4 Resonance Modes of Nanomechanical Devices . . . 37

3.5 Resonance Modes of Silicon Nitride Membrane . . . 39

3.6 Magnetic Hysteresis of ∼350 Magnetic Nanoparticles . . . 41

3.7 Conclusion . . . 43

4 Nanomechanical Torque Magnetometry of Self-Assembled Magnetic Nanoparticles in Geometrical Shapes **45**

4.1 Motivation . . . 45

4.2 Introduction . . . 46

4.3 Self-Assembly of Nanoparticles on Nanomechanical Devices . . . 50

4.3.1 Self-Assembly Approach . . . 51

4.3.2 Self-Assembling Nanoparticles on SOI Devices . . . 54

4.3.3 Cleaning the Anchored Nanoparticles at the Edges of the Devices . . . 55

4.3.4 Resonance Modes of the Devices . . . 59

4.3.5 Magnetic Hysteresis of Self-Assembled Nanoparticles at Room and Low Temperature . . . 60

4.4 Patterning Nanoparticles in Geometrical Shapes on the Devices 65

4.4.1 Patterning Nanoparticles in Geometrical Shapes on SOI devices . . . 66

4.4.2 Resonance Modes of Devices . . . 67

4.5 Conclusion . . . 68

5 Nanocavity Optomechanical Torque Magnetometry and Radiofrequency Susceptometry **70**

5.1 Motivation and Introduction 70
5.2 Nanomechanical Torque Magnetometry by a Laser Interferrometric Method 71
5.2.1 Device Designs 72
5.2.2 Raster Scans of the Device 74
5.2.3 Pressure Measurements and Hysteresis 75
5.3 Introduction to Optomechanical measurements 77
5.3.1 Optomechanical Torque Magnetometer Device and Split-Beam Nanocavity (SBC) 77
5.3.2 Optomechanical Measurement Setup and Applied Fields 79
5.4 Optomechanical and Spectral Transductions 83
5.4.1 Optomechanical Coupling and Transduction 83
5.4.2 Sensitivities 86
5.4.2.1 Thermomechanical Sensitivity 86
5.4.2.2 Displacement and Torque Sensitivities 88
5.4.2.3 Magnetic Sensitivities 89
5.4.2.4 Spectral Response and Magnetic Field Sensitivity 92
5.5 Magnetic Susceptibility and Suceptometery 94
5.5.1 Magnetic Hysteresis of the Permalloy Island 94
5.5.2 Magnetic Susceptibility Peaks at Barkhausen Steps . . . 96
5.5.3 Magnetic Susceptibility Peaks Analysis 98
5.5.3.1 Magnetic Susceptibility Peaks and Torque Terms 98
5.5.3.2 Magnetic Hysteresis Curve Variation with RF Field Amplitude 100
5.5.3.3 Magnetic Susceptibility Calculations for Peaks . 103
5.5.3.4 Effect of RF Field Direction on Peaks 106
5.5.3.5 Effect of DC Magnetic Field Direction on Peaks 107
5.6 Torque-Mixing Magnetic Resonance Spectroscopy (TMRS) . . . 109
5.6.1 Control Measurements 109

5.6.2 Torque-Mixing Resonance Measurements 111
5.7 Reproducibility and Throughput 117
5.8 Comparison with other technologies 118
5.9 Conclusion 119

6 Nanomechanical Torque Magnetometry of a Thick YIG 121
6.1 Motivation and Introduction 121
6.2 YIG Disk on the Silicon Membrane Nanomechanical Devices . . 124
6.2.1 Optical Fiber Setup and Resonance Modes Detection via Optical Fiber 129
6.3 YIG Disk on the SOI Nanomechanical Devices 131
6.4 Conclusion 140

7 Conclusions & Future Recommendations 142
7.1 Conclusions 142
7.2 Future Recommendations 143

Bibliography 145

Appendices 198

A Optical Cavities 199
A.1 Fabry-Pérot Cavity 199
A.2 Nanophotonic Cavity 201

B Micromagnetic Simulation Methods 202
B.1 Simulation Introduction 204
B.2 Nanoparticle Simulations 205
B.3 Magnetic Anisotropy of ∼350 Magnetic Nanoparticles 207
B.4 YIG Simulations 210
B.5 Permalloy Simulations 210

C Devices Fabrication **212**

C.1 Fabrication of Nanomechanical Devices in Silicon Nitride Membranes . . . 212

C.2 Fabrication of Nanomechanical Devices in SOI Chips . . . 213

C.3 Fabrication of Optomechanical Devices in SOI Chips . . . 219

D Magnetic Nanoparticles Self-Assembly Experiments **220**

D.1 Self-Assembly Preliminaries . . . 222

D.1.1 Patterning Nanoparticles using PMMA . . . 223

D.1.2 Patterning Nanoparticles using Pentane . . . 226

D.1.3 Patterning Nanoparticles using HSQ . . . 227

D.1.4 Patterning Nanoparticles using ZEP . . . 228

D.2 Other Methods for Nanoparticle Assembly . . . 229

D.2.1 Shape Anisotropic Nanoparticles . . . 230

D.2.2 Nanoparticles from Bacteria . . . 231

D.2.3 Nanoparticles Embedded in Polymer on Recording Media 232

E Thin Sectioning of YIG **235**

E.1 Introduction . . . 235

E.2 Thin sections of YIG by Mechanical Polishing . . . 237

E.2.1 Mechanical Grinding of YIG . . . 237

E.2.2 Mechanical Polishing of YIG . . . 240

E.3 Thin sections of YIG by Dicing Machine . . . 242

E.3.1 Dicing of Silicon . . . 243

E.3.2 Dicing of YIG . . . 245

E.4 Thin Slices of YIG for FIB and TEM . . . 246

F Ga+ Ion Damage on YIG and Silicon Nitride by Focused Ion Beam (FIB) **247**

F.1 Introduction . . . 247

F.2 Ga+ Ion Damage in YIG 249
F.2.1 Sample Preparation for TEM 251
F.2.2 Bright Field (BF) Images 252
F.2.3 STEM 253
F.2.4 High Resolution TEM (HRTEM) 254
F.2.5 Nanobeam Beam Diffraction (NBD) 255
F.2.6 Convergent Beam Electron Diffraction (CBED) 257
F.2.7 Elemental Mapping (EDS) and Energy-Filtered TEM (EFTEM) 258
F.2.8 HRTEM and Selected Area Electron Diffraction (SAED) 261
F.2.9 Damage Depth Calculations 262
F.3 Ga+ Ion Damage in Silicon Nitride 263
F.3.1 Bright Field (BF) Images 264
F.3.2 STEM 265
F.3.3 High Resolution TEM (HRTEM) 265
F.3.4 Convergent Beam Electron Diffraction (CBED) 266
F.3.5 Elemental Mapping (EDS) 267

G Preparation of YIG for Lorentz Microscopy 269

G.1 Introduction 269
G.2 Sample Preparation of YIG for Lorentz Microscopy 270
G.3 Lorentz Microscopy of Permalloy 272

H Exchange Coupling in Co-CoO layers 274

List of Tables

F.1 Dose and energy of each line 250

List of Figures

2.1 **Schematic of nanomechanical torque magnetometry setup (not to scale).** The white colour on the device paddle represents the deposited magnetic element. 20

2.2 **Schematic of the optomechanical torque magnetometry setup (not to scale).** The green colour represents the transmission line, the cyan colour shows the remaining components of the setup, the purple colour represents the chip, and the red colour represents the device layer. 26

2.3 **Top view of the split-beam nanocavity (SBC).** The colours represent the electric field of the optical wave confined in the central region. 28

2.4 **Applied field directions for TMRS (not to scale).** The magnetic disk is biased in an applied field $\boldsymbol{H}_0$ at mechanical resonance of the device f_{mech}. The RF fields $\boldsymbol{H}_1^{\mathrm{RF}}$ and $\boldsymbol{H}_2^{\mathrm{RF}}$ were applied for in-plane and out-of-plane drive. Reprinted with permission from [15]. 30

3.1 **False colour SEM of fabricated nanomechanical devices in silicon nitride membrane.(a)** A false colour SEM of (blue) the silicon nitride membrane incorporating triple-paddle resonators. The nanoparticles show up white; black is where the membrane has been cut away. **(b)** A selected triple paddle resonator. Most of the nanoparticles are on the central paddle. The small black rectangles at the corners of the device are reference marks used for focus ion beam alignment. The x, y, z coordinate system is indicated. The DC field is applied in the x direction, while the AC field is applied along the z-axis. The corresponding torque is produced in the y direction. 35

3.2 **Spectral response of resonance.** Vertical (z) displacement amplitude (proportional to y-mechanical torque and to x-net magnetization) showing resonance peaks for the triple-paddle resonator and the membrane. Magnetic torque actuation by the nanoparticle aggregates reveals many mechanical modes. Inset is the SEM of the corresponding positions at which the spectra were taken. 37

3.3 **Resonance mode of nanomechanical devices in silicon nitride membrane.** SEM and optical raster scanned images of the membrane: **(a)** SEM of the selected area; **(b)** DC reflected optical intensity of the membrane area; **(c)** interferometric AC signal amplitude at the torsional frequency mode (1.7447 MHz) of the selected resonator measured simultaneously; inset, the features in detail; **(d)** relative phase of the AC signal. The colour bars in (b) represent the reflected intensity in V_{DC}, and in (c) the interferometric AC magnitude signal from the lock-in amplifier rendered as $\log(V_{rms}/1V)$ units. 38

3.4 **Resonance modes of silicon nitride membrane.** Optical raster scanned images at various membrane resonance modes: **(a)** DC reflected intensity of the selected area; and **(b)-(d)** interferometric AC signal amplitude at different frequencies. The grey area in (d) indicates that no signal was recorded in that region. The background colour is represented by the zero reference from the colour bar in each panel. The red and blue colours show the displacements above and below the membrane, respectively. The colour bars in (a) represent the reflected intensity in V_{DC}, and in (b)-(d) the interferometric AC magnitude signal from the lock-in amplifier in V_{rms} units. 40

3.5 **Finite element simulations of the silicon nitride membrane with embedded nanomechanical resonators. (a)** torsional mode frequency of the device indicated; **(b)**, **(c)** frequencies showing the onset of membrane modes; **(d)** detail of a triple paddle torsional mode decoupled from the membrane highlighted in (a); and **(e)** detail of hybridized membrane-torsional modes highlighted in (b). The colour bars indicate the relative amplitude in the vertical (z) direction. 41

3.6 **Magnetic hysteresis of magnetic nanoparticles. (a)** Higher magnification SEM image of the central paddle, showing the deposit of ∼350 nanoparticles. Chains of particles are clearly visible within the aggregate. **(b)** Experimental data obtained for the magnetic hysteresis at room temperature. Vertical (z) displacement amplitude is proportional to y-mechanical torque and to x-net magnetization. The measurement, starting from the high positive end of the field, yields a minor hysteresis loop. 42

3.7 **Micromagnetic simulation of magnetic hysteresis,** for a two-dimensional cluster of particles mapped in a pattern created by the SEM image of Fig. 3.6a (inset). M_x is the normalized x-component of magnetization. 43

4.1 **Schematic of self-assembly of nanoparticles. (Not to scale.) a,** side view of schematic of nanoparticle deposition. Grey colour represents the base silicon ($700\mu m$ thick), brown colour is the silicon oxide layer ($1\mu m$ thick), and green colour is the top silicon layer used as the device layer (300nm thick). Water is displayed in blue while the nanoparticles are represented in red. **b,** top view of the schematic. The nanoparticle droplet covers the water droplet and the devices. **c,** side view of the device after the drying procedure. 52

4.2 **SEM images of self-assembly of nanoparticles on a silicon nitride surface. a,** green colour (false colour) represents the nanoparticle deposition on the silicon surface. **b,** nanoparticle self-assembly on a large scale, green colour (false colour) shows the silicon nitride window **c,** edge of the silicon nitride window with the nanoparticle assembly **d,** close packed nanoparticle distribution in the self-assembly. 53

4.3 **False colour SEM image of self-assembly of nanoparticles on SOI fabricated devices. a,** Three rows of devices are named as A, B and C series with numbers $1-9$. Green colour shows the suspended silicon devices with a silicon oxide layer on top of the silicon base (grey colour). The alignment marks are the edges of the devices and are also suspended and shown in green colour. A single pad beside the alignment mark is made . The scale bar is $10\mu m$ **b,** schematic of the anchoring of nanoparticles at the corners of the device. The green colour is the device and red colour indicates the anchored nanoparticles. 55

4.4 **Clamping at the corners of the device (B9). a,** false colour SEM image of the unclean devices **b,** false colour SEM image of the clean device (B9) with a 180° rotation of the scanning image. All scale bars are $3\mu m$. 56

4.5 **Cleaning steps of the device (B9) using a FIB. a,** Anchored unclean device **b,** side view of partially cleaned device. The torsional rod is cleaned in this step. **c,** cleaning one edge by cutting the paddle by 100 nm. **d,** cleaned device from both sides. All scale bars are $1.2\mu m$. 57

4.6 **Device (B5) cut to see the nanoparticles on the bottom side. a,** false colour SEM image of the cut device. The scale bar is $2.5\mu m$. **b,** false colour SEM image of the cut device on the bottom side. The white arrow indicates the oxide layer sandwich surface on the bottom side. The scale bar is $1.2\mu m$. 58

4.7 **Resonance peaks of the B9 device.** Grey colour shows the thermomechanical peak for the untrimmed device at room temperature. Blue colour is the thermomechanical peak for the trimmed device at room temperature. Orange colour represents the driven peak of the untrimmed device at 50 mV at 18.25K. . 58

4.8 **Resonance peaks of the B-series devices. a,** flexural mode of the devices **b,** torsional mode of the devices. 60

4.9 **Magnetic hysteresis of superparamagnetic nanoparticles.** The normalized torque is plotted versus H_x^{DC} field linear sweeps in all graphs. **a,** Hysteresis at room temperature **b,** zoomed-in area at low field of hysteresis at room temperature **c,** Hysteresis at low temperature (14 K) **d,** zoomed-in area at low field of hysteresis at low temperature (14 K). Blue colour represents the high to low field sweep, while red colour is the low to high field sweep. 61

4.10 **Magnetic hysteresis with magnetic field rotation at low temperature (14 K). a,** Normalized torque amplitude with rotating the DC magnet. The normalized torque is plotted versus H_x^{DC} field rotational sweeps in the graph. **b,** Phase shift in amplitude versus H_x^{DC} field rotational sweeps. 63

4.11 **Optical power at room temperature and at low temperature. a,** Torque amplitude at various optical powers and temperatures. **b,** torque amplitude for various RF outputs. . . . 64

4.12 **Torque amplitude and frequency shift at low temperature.** 65

4.13 **Nanoparticle circles by mask fabrication.** Scale bar for **a,** is $2\mu m$. Scale bar for **b, c,** and **d,** is 200 nm. 66

4.14 **Nanoparticle circles on SOI by nanofabrication. a,** and **b,** show the different device dimensions. The resonator paddle is 6 μm wide. 67

4.15 **Resonance spectra of nanoparticle circles on SOI devices. a,** torque amplitude of varous devices with nanoparticles. **b,** resonance spectrum of an individual device. Inset shows the Lorentzian shape of the resonance curve. 68

5.1 **Device designs.** False colour SEM images (a-d) and COMSOL simulation images (e-h) of modes of the optomechanical devices. 73

5.2 **The raster scan of an optomechanical device at the resonance frequency of 2.9939 MHz. a,** SEM image of the device **b,** DC raster scans of the device. **c,** AC torsional amplitude $\hat{x}$-component of the device. **d,** AC torsional amplitude $\hat{y}$-component of the device. The scanning window is $18 \times 18\ \mu m^2$, and colour bars has units of Volts, as shown in b, c, and d. . . . 74

5.3 **Resonance peak measured under various pressures. a,** resonance peak measurements of the optomechanical device by nanomechanical torque magnetometry at $\ll 5.0e^{-4}$mbar to 49.9 mbar. **b,** resonance peak measured from 49.9 mbar to 1013 mbar. The inset in Fig. 5.3b represents the resonance peak at 1013 mbar. The red colour in the inset represents the fitted Lorentzian curve. 75

5.4 **Magnetic hysteresis by interferometric detection. a,** Magnetic hysteresis of a device. Green and black colours show the hysteresis as-is having frequency shift with magnetic field. Blue and red colours show the corrected hysteresis after the frequency shift. **b,** linear frequency shift by DC magnetic field. The linear fit with equation $y = a + bx$ has parameters as $a = 2.99 \pm 2.43e^{-5}, b = 1.10e^{-5} \pm 2.58e^{-7}$. 76

5.5 **Split-beam cavity. a**, Tilted scanning electron micrograph (SEM) of a split-beam cavity device. Inset: top-view of the 40 nm thick permalloy film deposited onto the device. **b**, Top-view SEM of the nanocavity overlaid with a finite element simulation (COMSOL) of the normalized field distribution E_y of its optical mode. The colour bar shows the intensity of E_y. 78

5.6 **Schematic experimental set-up for nanocavity optomechanical torque magnetometry measurements (not to scale).** All the measurements are performed in an ambient nitrogen-purged environment (grey region). A dimpled fibre taper is used to probe the optomechanical nanocavity. A permanent magnet with an adjustable position provides varying static magnetic fields. The lock-in amplifier reference is power amplified and sent to coils below the device to create an RF magnetic field in the z direction. 79

5.7 **Actual experimental set-up for nanocavity optomechanical torque magnetometry measurements.** The two magnets and the microscope are perpendicular to each other at the device position. 81

5.8 **Device offset on top of coil and magnetic field of RF coil.** **a,** Schematic of the positioning Δx of the device relative to the center of the coil (red) and tilt θ relative to the plane of the permanent magnet. **b,** Hysteresis (high to low field) acquired when the device is at coil positions 1, 2, 3, and 4 labelled in a. **c,** Hysteresis (low to high field) acquired when the device is at coil positions 1, 2, 3, and 4 labelled in a. 83

5.9 **Optomechanical response.** **a**, $S_{VV}(\lambda, \omega)$ in ambient conditions as the fiber taper is touching the anchored nanocavity nanobeam. Scale bar on the right is in dBm. The white overlay with axis on the right is the optical transmission showing the optical resonance at 1528 nm. Sharp low amplitude features are laser mode-hops. **b**, Thermomechanical frequency response of the device at various wavelengths (left axis) and when hovering (right axis). Measurements were performed with no applied magnetic field ($H_z^{RF} = 0$). Two mechanical modes of interest, T_y and U_z, are indicated, with their displacement fields predicted by finite element simulations inset. Black arrows indicate prominent displacement directions. 84

5.10 **Displacement and torque sensitivities.** **a,** Displacement density (left axis) from the real-time spectrum analyser (RSA) that shows thermally driven mechanical modes T_y and U_z (blue) and the magnetically driven signal (narrow peak highlighted in red) generated by a magnetic driving field H^{RF} of 35 Am^{-1} applied with the permalloy island magnetization saturated by H_x^{DC}. Black lines are fits to the T_y and U_z Lorentzian-shaped peaks (solid line) and the measurement noise floor (dashed line). The green curve (right axis) indicates the predicted root mean squared displacement of the T_y resonance in the presence of a 35 Am^{-1} RF magnetic field as a function of frequency. Insets show simulated displacement profiles of T_y and U_z. **b,** Torque equivalent noise of the thermomechanical displacement signal in a. The red dotted line indicates the predicted torque in the presence of a 35 Am^{-1} H_z^{RF} field, and is labelled by the values on the left axis, assuming a 1s integration time. 89

5.11 **Magnetic moment sensitivity.** **a**, Device response as RF magnetic fields of various intensities are applied and swept from 2 to 4 MHz using the lock-in amplifier, for a constant field of $H_{\mathrm{x}}^{\mathrm{DC}} = 45$ kA/m. **b**, Maximum device response (located at 3 MHz) varies linearly with the applied RF field strength. When the applied field $H_{\mathrm{z}}^{\mathrm{RF}}$ is turned off, the minimum signal is limited by thermomechanical noise leading to an effective minimum detectable field H_{min} (0.61 A/m) indicated by the open circle. . 90

5.12 **Spectral response.** Wide bandwidth power spectral density of the nanocavity coupled optical signal. In blue, the RSA signal when $H_{\mathrm{z}}^{\mathrm{RF}} = 0$ shows the two main mechanical modes with secondary modes at 8 MHz and 21 MHz. In orange, the RF coil with $H_{\mathrm{z}}^{\mathrm{RF}} = 35$ A/m drives the device while the signal is recorded by the lock-in amplifier. An RF power amplifier was used (37 dB amplification, 150 kHz - 250 MHz range). Large noise at low frequency (< 1 MHz) is due to the fiber taper. At higher frequencies, the noise generated by the RF coil increases. Inset: Measured magnetic field sensitivity. 93

5.13 **Magnetic hysteresis of the permalloy island.** Magnetization response of the permalloy element with a varying applied DC field along x (five-run average). The RF drive field is $H_z^{RF} = 35\text{Am}^{-1}$. The solid blue trace is a decreasing field sweep and the solid red trace is an increasing field sweep. Results from micromagnetic simulations of the permalloy island (highlighted in red in the SEM inset in Fig. 5.5 and also used as the simulation mask) are plotted with black dashed lines. The bottom panel shows simulated magnetization textures at different points in the hysteresis loop. The colour wheel shows the in-plane direction of magnetization, with red parallel to the applied DC field. 95

5.14 **Enhanced room-temperature magnetic susceptibility at Barkhausen steps. a,b,** Hysteresis sweep with H^{RF} set to 45° (equal and same sign x and z components) **(a)** and 170° (opposite signed x and z components) **(b)**. A select number of upward and downward peaks are highlighted in blue to show the contribution to the torque from susceptibility. **c-e,** Low-field H_x^{DC} single forward and backward sweeps at three H^{RF} positions, 45° **(c)**, 90° **(d)** and 170° **(e)**. In all cases, the drive field $H^{RF} = 35\text{Am}^{-1}$. 97

5.15 **Peak labels.** The full magnetic hysteresis with peak numbers and lower branch zoom-in shown in **a** and **b** measured at non-zero out-of-plane drive amplitude. 99

5.16 **Hysteresis curve section with various applied RF drives (H^{RF}).** The legend shows the corresponding calculated H_z^{RF} for each curve. 101

5.17 **Peak 6 & 7 and minor hysteresis loop variation with RF drive ($H^{\mathbf{RF}}$).** The legend outside the figure shows the corresponding calculated H_z^{RF} for each curve. 102

5.18 **The experimental peak amplitude for different RF drives ($H^{\mathbf{RF}}$).** 103

5.19 **Estimated peak susceptibility** at select Barkhausen steps for $|H_x^{RF}| = |H_z^{RF}| = 15$A/m, for each peak identified in Fig. 5.15 as a function of RF drive. **a,** Susceptibility of each peak as a function of RF drive.The dashed lines shows the low-field quasi-static susceptibility that would be found in the lower branch in the absence of pinning (slope of linear fit to data in Fig. 5.15). **b,** Susceptibility calculation of peak 1 as sample calculations. . . 105

5.20 **Magnetic hysteresis and susceptibility measurement using a planar transmission line. a,**The hysteresis loop was acquired while sweeping H_x^{DC} and applying the RF drive along y using the central stripline (inset). The colours of the trace represent the direction of sweep. **b,**The hysteresis loop acquired at a slightly different position (500 μm away from center) on the stripline. 107

5.21 **Peak 4 amplitude variation with varying H^{DC}** by adding another DC magnet at various distances and polarities.**a,** H_x^{DC} when the second magnet is in the $-Z$ direction. The H_x^{DC} is shown in the inset when the second magnet is in the $+Z$ direction. **b,** the peak amplitude with varying H_x^{DC} **c,** the peak amplitude with varying H_z^{DC} **d,** the peak amplitude on the map of $H_{x,z}^{DC}$. The horizontal dashed lines shows the H_z^{DC} without second magnet. The difference of 0.023 kA/m on the horizontal axis is due to the different H_x^{DC} by inverting the magnet direction from $-Z$ to $+Z$. 108

5.22 **Characterization of low field sweeps. a**, Field sweeps with a drive field of $H_z^{RF} = 35$A/m (averaged for a $\sqrt{12}$ noise reduction factor) in the low field regions of the curve reveal features produced by the Barkhausen effect. The upper blue and red traces are the in-phase signals of the decreasing and increasing field sweeps. **b**, Same as **a** except a bias field $H_y^{DC} = 300$ A/m is applied. **c**, Device response at different input laser power as H_x^{DC} is swept at low fields. The responses at 175 μW and 35 μW power were normalized and slightly offset for ease of comparison. 110

5.23 **Transmission lines and stage. a,** the stage made from ABS plastic and its temperature map during the measurement. **b,** aluminum based stage to provide a better heat sink. 110

5.24 **Torque-mixing resonance amplitude in full field range. a,** sweeping the field from high to low. **b,** sweeping the field from low to high. The frequency axes correspond to f_1. 114

5.25 **Torque-Mixing resonance amplitude line scans in the low-field range. a,** high to low field sweep. **b,** low to high field sweep. 115

5.26 **High resolution torque-mixing resonance amplitude for high to low field sweep. a,** high to low field sweep in low field range with 0.0111 kA/m steps. **b,** zoom-in scan in the specified field range with 0.0112 kA/m steps. **c,** simultaneous acquisition of direct-torque actuated by H_y^{RF}. **d,** simultaneous acquisition of direct-torque actuated by H_z^{RF}. 116

5.27 **High resolution torque-mixing resonance amplitude for low to high field sweep. a,** low to high field sweep in the low field range with 0.0111 kA/m steps. **b,** simultaneous acquisition of direct-torque actuated by H_y^{RF}. 117

5.28 **Magnetic hysteresis of neighbouring devices.** Magnetic hysteresis measurements for devices fabricated immediately to the left **a** and right **b** on the same chip as the devices studied throughout this chapter. 118

6.1 **False colour SEM of the YIG disk on a fabricated nanomechanical device in the silicon membrane.** Green colour represents the nanomechanical device in the silicon membrane, and red colour shows the YIG disk. Scale bar is $10\mu m$. 125

6.2 **Spectral response of the device.** Grey colour represents the spectrum taken at the membrane near the device. Blue colour represents the spectral response of the device with the YIG disk. 126

6.3 **Raster scan of the YIG disk on a fabricated device in the silicon membrane at 0.982MHz. a,** Tilted false colour SEM of the YIG device. The scale bar is $10\mu m$. **b,** DC raster scan of the device. **c,** AC resonance scan of the device. **d,** phase of the resonance response. The x- and y-axis in **b, c,** and **d** are in microns. The colour bars show the amplitude in μV in **b** and **c**, and shows the phase in deg for **d**. 127

6.4 **Comsol simulations of the YIG disk on the device. a,** torsional mode **b,** flexural mode.The colour bars are in arbitrary units. 128

6.5 **Magnetic hysteresis of the YIG disk on a fabricated device in the silicon membrane.** Blue colour traces the high to low field sweep while red colour shows the low to high field sweep. 129

6.6 **Optical fiber laser setup.** 130

6.7 **Resonance spectrum in optical fiber laser setup.** 131

6.8 **False colour SEM of the YIG disk on nanomechanical devices fabricated on a SOI chip. a,** device with ear-shaped resonating paddle. **b,** device with square shape resonating paddle. Green colour shows the devices while red colour shows the YIG disks. The scale bars are $3\mu m$. 132

6.9 **Spectral response of the device in Fig. 6.8a fabricated on a SOI chip. a,** resonance peak of the device with ear-shaped resonating paddle. **b,** zoom-in spectrum of the device. Blue colour represents the resonance peak and red colour shows the corresponding phase shift on resonance. 133

6.10 **Raster scan of the YIG disk on the device in a SOI chip. a,** Tilted false colour SEM of the YIG device. **b,** DC raster scan of the device. **c,** x-component of the AC torque response of the device. **d,** y-component of the AC torque response of the device. The x- and y-axis in **b, d,** and **d** are in microns. The colour bars show the amplitude in μV. 134

6.11 **Magnetic hysteresis of the YIG disk.** Blue and red colours represent the high to low and low to high field sweeps of the experimental hysteresis curve respectively. Purple and green colours show the high to low and low to high field sweeps of the simulated hysteresis curve respectively. The inset is the colour scheme for magnetization orientation in simulations, for which the spin texture of the labeled points in experimental hysteresis curve are shown in the Fig. 6.12 135

6.12 **Spin texture of the magnetization from the micromagnetic simulations. A-F** are the images of spin texture at the points in experimental hysteresis curve labeled in the Fig. 6.11. 136

6.13 **Torque-mixing resonance mode.** Spin texture of the AC torque-mixing resonance mode in the YIG disk from the experiment. 139

6.14 **Ultra-high sensitive field sensing.** False colour SEM of two identical YIG disks on a fabricated nanomechanical Double paddle resonator in SOI. The YIG disks are 0.85μm in thickness and 2.6μm in diameter. Green colour represents the nanomechanical device, and red colour shows the YIG disks. (Image credit: J. Losby for device fabrication and M. Belov for YIG disk milling and transfer onto the device.) 140

B.1 **Micromagnetic simulations of magnetic nanoparticles in mumax.** The effect of temperature on the magnetic hysteresis in masked magnetite nanoparticles. The blue curve is at 0K and green curve is simulated at 300K. The anisotropy was neglected in these simulations. 206

B.2 **Tetrahedral mesh of magnetic nanoparticles in GMSH for nmag simulations.** The geometry file (*.geo) was created in python and then GMSH software was used for the FE mesh generation. This example is for 21×22 nanoparticles in a layer. 207

B.3 **Micromagnetic simulation of magnetic hysteresis by varying the applied DC bias magnetic field angles. (a)** M_x is the normalized x-component of magnetization, **(b)** M_y is the normalized y-component of magnetization 208

B.4 **The effect of anisotropy in the hysteresis loops of magnetite nanoparticles.** The legend shows the various uniaxial anisotropy constant values used for simulations. 209

B.5 **Micromagnetic simulation of permalloy in mumax.** Changing the parameters effects the hysteresis curve. 211

C.1 **Curling of device.** Triple paddle device fabricated in the silicon nitride membrane. The scale bar is 2 μm. 213

C.2 **Device fabrication step for SOI chips.** Reprinted with permission from [187] 214

D.1 **Nanoparticles self assembly using PMMA.** False colour SEM image of patterned circles and rectangles of magnetic nanoparticles. The scale bar is 50μm. 224

D.2 **Clearing the borderline of nanoparticles assembly. a-d,** False colour SEM images of patterned rectangles of magnetic nanoparticles. **c,** is the zoomed image of an area in **a**. **d,** is the zoomed image of an area in **b**. All scale bars are 500 nm. 225

D.3 **Nanoparticle circles. a-b,** False colour SEM images of patterned circles of magnetic nanoparticles. The scale bar in **a,** is 20μm and in **b,** is 200 nm. 226

D.4 **Nanoparticles assembly with pentane.** SEM image of patterned layer of magnetic nanoparticles. The scale bar is 200 nm. 227

D.5 **Nanoparticle assembly on devices with HSQ resist.** False colour SEM image of patterned devices with HSQ and magnetic nanoparticles. **a,** colour shows set of devices. The scale bar is 30 μm. **b,** colour shows a device covered with nanoparticles. The scale bar is 5 μm. **c,** colour shows a resonating paddle covered with nanoparticles. The scale bar is 500 nm. 228

D.6 **Nanoparticle assembly on devices with ZEP resist.** False colour SEM image of patterned devices with ZEP and magnetic nanoparticles. **a,** set of devices. The scale bar is 100 μm. **b,** colour shows a device covered with nanoparticles. The scale bar is 5 μm. **c,** colour shows a resonating torsional rod covered with nanoparticles. The scale bar is 1 μm. 229

D.7 **Anisotropic nanoparticles. a,** star and **b,** cube nanoparticle assemblies. Both scale bars are 100 nm. 231

D.8 **Bacterial Nanoparticles lysed in matrix.** The scale bar is 500 nm. 232

D.9 **Nanoparticle assembly in columns in polymer with magnetic tape.** Image credit: Thomas Crawford and Rahman. . . . 233

E.1 **YIG and GGG sandwich.** Optical image of the cross-section of $5mm \times 5mm$ chips. 237

E.2 **Mechanical grinding.** Grinding of the YIG sandwich until the bottom layer of the YIG is left. **a,** comparison of ground chip bonded on top of quartz crystal, with pristine chip. **b,** tilted optical image of the bottom YIG layer for transparency. The chip dimensions are $4.8mm \times 5.1mm$. 239

E.3 **Mechanical polishing. a,** onset of transparency of the YIG film with dark brown to green colour. **b,** Polishing of YIG film until yellow transparency to obtain required thickness. The chip dimensions are $4.8mm \times 5.1mm$. 241

E.4 **FIB fabricated YIG disks.** False colour SEM image of the fabrication of the YIG disks from the polished film in the FIB. The green colour shows the YIG disks and lamella and the blue colour is the handle of the metallic probe for plucking. The scale bar is 10 μm. (Image credit: M. Belov for YIG disks fabrication in FIB.) 242

E.5 **Idea to make the thin sections for TEM.** The red colour is the top view of the blue coloured thin slice of the diced sample. Ultra thin sections were prepared in the TEM as shown in the red colour. 243

E.6 **Dicing silicon with SD2000 blade.** False colour SEM images of the silicon chips. **a-b** stair-case silicon dicing. **c,** magnified image of one thin-section. The width of the thin-section is 30 μm. The scale bar in **a,** and **b,** is 1 mm, and 40 μm in **c**. 244

E.7 **Dicing silicon with a SD4000 blade.** False colour SEM image of the silicon chips. **a-c** stair-case and thin slices of silicon dicing. **d,** magnified image of one thin-section. The width of the thin-section is 9 μm. The scale bar is 1 mm in **a** and **c,** 500 μm in **b,** and is 5 μm in **d**. 245

E.8 **Dicing YIG with a SD4000 blade.** False colour SEM image of the silicon chips. **a,** thin slices of YIG slab. **b,** magnified image of one thin-section. The width of the thin-section is 5.5 μm. The scale bar is 1 mm in **a,** and 10 μm in **b**. 246

E.9 **Ultra-thin sections for TEM.** Sample prepared in the FIB by a high energy ion beam. The scale bar is 5 μm. 246

F.1 **Design for ion beam exposure. a,** SEM image of the ion beam exposed area in the YIG. **b,** Raith software design for the exposure. Red colour shows the reference line, and blue-to-green colour shows the lines with variable beam dose. 250

F.2 **Bright field cross sectional TEM micrographs of all damaged lines in the YIG. a,** Full view of the damaged lines with Ga ions. The lines are indicated with arrows and numbers. **b,** magnified image of lines 5, 6 and 7 in between the reference lines. Carbon and tungsten are deposited as sacrificial layers for specimen preparation. 251

F.3 **Magnified bright field cross sectional TEM micrographs of damaged lines in YIG. a-h,** BF images for lines 0-7 respectively, as labelled. 252

F.4 **STEM images of damaged lines 0 and 1 in the YIG. a,** BF TEM micrograph of lines 0 and 1. **b,** DF TEM micrograph of lines 0 and 1. 254

F.5 **HRTEM images of damaged areas in the YIG. a-h,** the HRTEM of each line labelled from 0 to 7 respectively. 255

F.6 **NBD patterns of defined areas in the YIG. a,** locations labelled for the NBD pattern for line 8. **b-e,** NBD pattern of locations 1-4 in order. **f,** BF image at location 5. 256

F.7 **NBD patterns of defined areas in the YIG. a-b,** locations labelled for the NBD pattern. **c-e,** NBD pattern of locations 5-7 in order. 257

F.8 **CBED patterns of defined areas in the YIG. a,** locations labelled for the CBED pattern. **b-h,** CBED pattern of locations 1-7 in order. 258

F.9 **EDS of line 0 in the YIG. a,** EDS X-ray spectrum. **b,** DF image of the area of interest of line 0. **c-g,** elemental maps for Ga, Fe, Y, O, and Bi respectively. All scale bars are 100 nm. . . 259

F.10 **EDS of line 0 and line 1 in the YIG. a,** EDS X-ray spectrum. **b,** DF image of the area of interest of line 0. **c-g,** elemental maps for Ga, Fe, Y, O, and Bi respectively. All scale bars are 100 nm. 260

F.11 **HRTEM and SAED images in the YIG. a,** HRTEM at the interface of line 0 **b,** magnified area of the interface. **c,** magnified area of the YIG matrix. **d,** SAED pattern for the YIG matrix, **e,** calculated miller indices for the SAED pattern. 262

F.12 **Damage depth variations with Ga dose in the YIG.** . . . 263

F.13 **Magnified bright field cross sectional TEM micrographs of damaged lines in Si_3N_4. a-h,** BF images for lines 0-7 respectively, as labelled. 264

F.14 **STEM images of damaged lines in Si_3N_4. a,** BF TEM micrograph of line 0 and 1. **b,** DF TEM micrograph of line 0. . 265

F.15 **HRTEM images of damaged areas in Si_3N_4. a-h,** the HRTEM of each line labelled from 0 to 7 respectively. 266

F.16 **CBED patterns of defined areas in Si_3N_4. a,** locations labelled for the CBED pattern. **b-f,** CBED pattern of locations 1-5 in order. 267

F.17 **EDS of line 0 in Si_3N_4. a,** EDS X-ray spectrum. **b,** DF image of the area of interest of line 0. **c-d,** elemental maps for Ga, and Si respectively. All scale bars are 100 nm. 268

F.18 **Damage depth variations with Ga dose in Si_3N_4.** 268

G.1 **TEM sample preparation of the YIG for Lorentz microscopy. a,** initial thinning at 30 keV. **b,** carbon and platinum deposition on top. **c,** further thinning at 5 keV. **d,** final polishing at 1 keV. All scale bars are 5μm. 271

G.2 **Family of YIG disks.** YIG disks fabricated in the thin sections. Scale bar is 3μm. 272

G.3 **YIG sample loading on carbon grid. a,** the YIG family is encircled. **b,** the YIG family is placed and welded onto the carbon grid. All scale bars are 5μm. 272

G.4 **Lorentz microscopy of permalloy. a,** under-focus condition **b,** in-focus condition **c,** over-focus condition. All scale bars are 2μm. 273

H.1 **SEM image of the Co/CoO layer devices.** 276

Nomenclature

τ	torque
$\mathbf{m}$	magnetic moment
μ_0	permeability of free space
m	mass
$\mathbf{H}$	applied magnetic field
Q	mechanical quality factor
V_{DC}	DC voltage
V_{rms}	AC voltage
A_{ex}	exchange constant
M_{s}	saturation magnetization
τ_{N}	Néel relaxation time
τ_0	attempt time
k_{B}	Boltzman constant
ΔE	Anisotropic energy barrier
τ_{m}	Measurement time
E_{ext}	magnetic energy due to external magnetic field
P	power loss
f	frequency of RF field
H	Applied field

ω	Angular frequency of RF field
χ_0	Low field susceptibility
ρ	Density of nanoparticles
ϕ	Volume fraction of nanoparticles
w	Mass of nanoparticles per unit volume
$\mathbf{m}_{\text{eff}}$	effective mass
Q_{m}	mechanical quality factor
Q_{o}	optical quality factor
ω_{m}	low mass resonance frequency
ω_{o}	nanocavity mode frequency
I	RMS current
N	number of turns in solenoid
L	length of solenoid
r_o	outer radius of solenoid
r_i	inner radius of solenoid
z_1	vertical distance from the device to the top of solenoid
$T(\lambda)$	wavelength (λ) dependent normalized transmission
P_{i}	fiber taper input power
P_{o}	transmitted power through fiber taper
$S_{\text{VV}}(\lambda, \omega_{\text{m}})$	electronic power spectrum
g_{om}	dispersive optomechanical coupling
g_{i}	dissipative optomechanical coupling
g_{e}	external optomechanical coupling
$G_{1,2}$	optomechanical gain
$S_{\text{zz}}^{\text{th}}(\omega)$	thermal displacement density
$\chi_{\text{x}}^{\text{peak}}$	peak susceptibility

Glossary of Terms

MRI	Magnetic Resonance Imaging
EPR	Electron Paramagnetic Resonance
NMR	Nuclear Magnetic Resonance
FMR	Ferromagnetic Resonance
TMRS	Torque-Mixing Magnetic Resonance spectroscopy
MEMS	Microelectromechancial Systems
NEMS	Nicroelectromechancial Systems
SQUID	Superconducting Quantum Interference Device
MOKE	Magneto-optic Kerr effect
AFM	Atomic Force Microscopy
MFM	Magnetic Force Microscopy
MRFM	Magnetic Resonance Force Microscopy
FMRFM	Ferromagnetic Resonance Force Microscopy
SOI	Silicon-on-Insulator
EBL	Electron beam lithography
ICPRIE	Inductively Coupled Plasma Reactive Ion Etch
SBC	Split-Beam Cavity
YIG	Yttruim Iron Garnet
FIB	Focused Ion Beam
AC	Alternating Current
SEM	Scanning Electron Microscope
SPM	Superparamagnetic

SSD	Stable Single Domain
RF	Radio Frequency
Py	Permalloy
SBC	Split Beam nanoCavity
RSA	Real-time Spectrum Analyzer
RBW	Resolution Bandwidth
LLG	Landau-Lifshitz-Gilbert
FDTD	Finite-Difference Time-Domain
GGG	Gallium Gadolinium Garnet

Chapter 1

Introduction

1.1 Objectives of the Thesis

The work presented in this Thesis is organized around advancements in nanomechanical and optomechanical torque magnetometry methods for magnetic assemblies. The study combines the advances in various fields as the core of the research presented here. These fields are nanomechanics, optomechanics, nanofabrication techniques, torque magnetometry, and magnetic material assemblies. The thesis details the nanofabrication of highly sensitive nanomechanical and nanophotonic optomechanical magnetometers (resonators or devices) for small-scale magnetic nanoparticle self-assemblies for torque magnetometry. The advancements in the above mentioned fields has resulted in the exceptional capability to fabricate devices with incredible sensitivities in ambient conditions. These highly-sensitive devices are useful for sensitive characterization of a countable number of nanoparticles in ambient conditions.

In torque magnetometry, the magnetic material produces a torque in the presence of an external magnetic field. This torque produces a measurable mechanical deflection when the material of interest is integrated with a compliant mechanical armature (nanomechanical resonator). The sensitive devices enable the study of magnetic interactions in magnetic assemblies containing a count-

able number of magnetic nanoparticles that are not possible to measure with traditional techniques. The study of these magnetic assemblies is advantageous for their optimized implementation in potential applications (e.g., spintronics, biomedical, nano-photonics, and many others).

In this Thesis, nanomechanical torque magnetometers were fabricated for the examination of various magnetic processes, such as magnetic hyperthermia and energy absorption in magnetic nanoparticle assemblies. As an extension of the work, nanophotonic optomechanical magnetometers were fabricated with high magnetic moment sensitivity to enable the investigation of magnetization, susceptibility and spin resonances in ambient conditions. The nanophotonic optomechanical magnetometers were optimized for magnetic signal transduction with high sensitivity using permalloy as a dry-run magnetic material, and are ready to be integrated with magnetic nanoparticle assemblies. The project was further extended to fabricate an ultra-high sensitive magnetic field sensing magnetometer. Major advances in the new experimental techniques were also made by developing and extending the functionality of nanomechanical and optomechanical magnetometers and susceptometers.

The main objectives of the study were as follows:

1. Integration of magnetic nanoparticle self-assemblies (countable number of nanoparticles) on nanomechanical torque magnetometers.

2. Optimization of nanophotonic optomechanical magnetometers/susceptometers with high sensitivity for ambient conditions, to enable the measurement of few magnetic nanoparticle assemblies in ambient conditions.

3. To build ultra-high sensitive field sensing magnetometers.

4. To demonstrate the new developed techniques.

1.2 Background and Integration of Ideas

Advances in various fields are integrated in the current research, presented in this Thesis. It combines the nanomechanics and optomechanics (for essential mechanical armature), magnetic material assemblies (nanoparticles, permalloy and yttrium iron garnet (YIG)), and torque magnetometry (technique). The developments in these fields are explained in the following subsections. The work has been laid out progressively from commercially available silicon nitride membranes to the current state-of-art research work (devices for ambient conditions) for versatility and evolution. The other essential components in the endeavor are nanofabrication techniques and signal transduction methods (by optical interferometry and optical taper fiber), which are listed in Chapter 2.

1.2.1 Nanomechanics and Optomechanics

One of the basics of nanomechanics arose from the torsional spring or torsional balance, which was invented by Charles-Augustin de Coulomb in 1785 [1] and by John Michell in 1783 independently. Coulomb used the torsional balance to measure the electric forces between two charges, and Michell's torsional balance was used by Henry Cavendish [2] in 1798 to measure the gravitational force between two masses. In both experiments, the torsional balance consists of a rod suspended with a fiber, with the charges or masses attached at the ends of the rod. The resulting forces generate torque, which is proportional to the rotating angle of the rod.

The same torsional balance was also used in the basic experiments of magnetization study. One of which is the Barnett effect [3, 4], discovered by Samuel Barnett in 1909, which explains the magnetization change in a rotating uncharged body. The opposite effect was predicted by Owen W. Richardson in 1908 [5], that the magnetization change can rotate the body. This prediction was experimentally confirmed by Albert Einstein and Wander Johannes de

Haas in 1915, known as the Einstein-de Haas effect [6]. The rotation of a body by magnetization occurs due to angular momentum conservation; the angular momentum of electrons aligns along the magnetization axis. They found the magnetomechanical ratio was the relation between angular momentum and the magnetic moment of electrons.

The Einstein-de Haas experimental apparatus is one of earliest experiments in magnetometry and became the basis of torque magnetometry. In Eintstein-de Haas experiment, the sample is attached to one end of a torsional rod in an external applied magnetic field. A mirror is attached to the torsional rod, which detects the rotation in the rod, produced by the twisting of sample, in the presence of magnetic field. In all aforementioned experiments, the torque generates the mechanical rotation. With the advent of modern technology, the miniaturization process also influenced the torsional balance, and led to nanoscale torque magnetometry, along with other microscopy (atomic force microscopy [7], magnetic force microscopy [8], and magnetic resonance force microscopy [9]) and spectroscopic methods (EPR spectroscopy [10], NMR spectroscopy [11], Mössbauer spectroscopy [12], Raman spectroscopy [13], ferromagnetic resonance spectroscopy [14], and torque-mixing resonance spectroscopy (TMRS) [15]).

The onset of miniaturization started with silicon integrated circuits in the 1950s, and then later on, microelectromechanical systems (MEMS), nanoelectromechanical systems (NEMS) in the submicron dimensions and lastly optomechanical systems using photonic cavities. These systems contain the mechanical element in the micron, submicron, and nanometer ranges including optical cavities. MEMS were used in the development phase in the 1970s, and in consumer applications since the 1990s. NEMS and MEMS have been employed in forms of microaccelerometers [16], gyrometers [17], magnetometers, microactuators [18], RF switches [19] and transistors [20], micro-mirrors [21], pressure sensors [22, 23], and biological sensors [24]. These forms are used in, for

example, automobiles and mobile phones, games, projectors, ink-jet printers, microelectronics [25], optics and biomedical devices [17]. The significant forms of miniaturization of NEMS assures low power consumption, high detection sensitivity, and on-chip device fabrication for research and applied purposes. The scaling-down of dimensions or miniaturization generate high responsivities and higher resonance frequencies for better signal, and higher sensitivities.

The device sensitivity has been used for displacement sensing, mass sensing, force sensing, torque sensing, energy sensing, and magnetic moment and field sensing. The shift in resonance frequency due to the mass load has been detected in the yoctogram range for mass sensing in recent years, using a vibrating carbon nanotube [26]. This shift has recently been extended to single-electron spin paramagnetic resonance [27], nuclear spin relaxation [28], zeptogram-scale mass sensing in a vacuum [29] and attogram-scale mass sensing in liquids [30], sub-femtometer displacement sensing [31], zepto-newton scale force sensing [32], high-sensitivity torque sensing [33], very high frequency [34] and high-sensitivity energy sensing [35]. Ultimately, NEMS will be concentrated towards the quantum mechanical limits of force [36, 37], mass [38] and displacement detection [39], and torque sensing [40], as well as using optical cooling to put down quantum back-action [31, 41]. The force detection has produced the magnetic resonance signal of a single electron, which can be used for single spin detection. Single spin detection is achieved by using the nitrogen vacancy centres in diamond [42], and using magnetic force microscopy [43].

Sensitive detection includes optomechanical transduction where an evanescently coupled optical gradient force in the proximity of the device transduces the signal or produces the deflection. Light interacts with mechanical systems with radiation pressure in optomechanics, while it involves the confinement of light in an optical cavity in cavity optomechanics. The radiation pressure originates from the momentum that light carries with it. The radiation pressure based cooling and the miniaturization of the mechanical element were utilized

together for high sensitivities and for eliminating thermal motion. The introductory efforts in cavity optomechanics started theoretically in the early 1990s [44] and validated experimentally in the late 1990s [45, 46].

Initially, radiation pressure cooling [47] and the optoemechanical effect was observed for mesoscopic and microscopic mirrors at cryogenic temperatures [21] in optical cavities. The high quality optical Fabry-Pérot cavities in the nanometer range made it possible to observe the optomechanical effects of the radiation forces at high sensitive scales. The limitations include damping [48], self induced oscillations [49] and dynamical back-action of the photothermal light forces [50], such that the exploration of non-dispersive radiation pressure [51] was discernible. With the advent of NEMS, optomechanical coupling was reported in cold atom clouds [37], nanorods [52], nanobeams [53], membranes [54, 48], microspheres [55], whispering gallery microdisks [56], Fabry-Pérot cavities [57, 58], photonic crystals [59], and photonic cavities [51].

NEMS have extreme flexibility and control over the dimensions of objects and the assembly, and on chip integration, in contrast to quantum coherent control in atomic systems where quantum states are used for atomic spin interactions. Cavity optomechanics mediates both aspects in the current state of the art technology. On one hand, cavity optomechanics is used for ultra-high sensitive detection of small-scale masses, displacement, energy and forces. On the other hand, it offers control over the mechanical motion in quantum states and systems. The combination of both routes gives devices with quantum information processing [60] and other hybrid devices [61]. Quantum measurement problem has been approached in various experiment, for microscopic and nanoscale objects, using the cavity optomechanics and its entangled quantum states [62]. Efforts are being put into utilize these superpositioned states in gravitational wave interferometers [63], studying light-matter interactions (photon-phonon entanglement) [64] and in quantum-gravity experiments [65, 66]. The prospects of integrating large masses in conjunction with quantum optical states and its

sensitive detection are being explored. One possible approach is to combine and assemble the optomechanical devices in large-scale arrays, for quantum entanglement problem.

Besides quantum measurements, cavity optomechanics have been employed in several other applications, such as in lasers [67], tunable optical filters [68], optical and quantum information processing [60], and single photon detection [69]. On-chip integration of optomechanical devices with photonics has brought new features and adaptability. The ability of cavity optomechanics in terms of damping and readout, both at higher mechanical frequencies, executes faster sampling and scanning rates, useful for many applications.

With comprehensive background of the nanomechanics and optomechanics, various mechanical structures were selected for further improvement (e.g., silicon nitride membranes and nanomechanical armatures). Finally, bringing cavity optomechanics and nanomechanical devices together will grant more functionality of devices. This would help in accomplishing the one of the aims of this Thesis, which was to use the optomechanical split-beam cavities and make useful optical and mechanical transductions at optical and mechanical resonance frequencies. The devices were progressively integrated from lower sensitivity silicon nitride membrane nanomechanical devices to highly sensitive optomechanical devices in this Thesis. The idea of progressive integration is dependent on the magnetic moment volume, which essentially depends on the number of the magnetic nanoparticles assembled on the devices.

1.2.2 Self Assembly of Nanoparticles

The magnetic [70, 71], optical [72, 73, 74], chemical [75], and electronic properties [75, 74] of nanoparticles are dependent on their size, shape, structure and composition. The adjustable size and high surface area to volume ratio allow one to alter of these properties in a highly fashioned order for tuning to a desired application. This flexibility of nanoparticles has potential applications in

fields like biomedical [76, 77, 78], nano-photonic [74, 79, 80, 81], nano-plasmonic [82, 83], nano-electronic [84, 85], nano-magnetic [71], spintronics [84] and enhanced oil recovery [86].

Magnetic nanoparticles are good candidates for the study of magnetic properties for various applications. Magnetic nanoparticles show remarkable magnetic properties such as superparamagnetism, magnetic hyperthermia [87] and tunable relaxation time. Magnetic nanoparticles are used in data storage devices [88, 89] and spin transport devices [85, 90] for their small size and single domain magnetic properties. They are also used in drug delivery [91, 92], and magnetic resonance imaging (MRI) [78, 89, 91] for their low toxicity and high contrast. These excellent properties make them ideal for fundamental studies on single particle or small arrays when compared with their bulk counterparts. One of the key considerations is conversion of magnetic energy to thermal energy [93]. This heat transfer of magnetic nanoparticles is being used as a capable mechanism for many applications.

The physical properties are dependent on the size of the nanoparticles. In the case of magnetism, it depends on the exchange length or the size of the magnetic domains. Such characteristics makes the magnetic nanoparticles unique from their bulk counterparts and their physical properties build a whole new field of magnetism. Reducing the size of magnetic nanoparticles, domains stabilize their energy from multidomain to single domain and further size reduction changes the nanoparticles from stable single domain to superparamagnetic. The critical multidomain to single domain size for magnetite Fe_3O_4 occurs at around 50-60 nm, the critical stable single domain to superparamagnetic size is around 25-30 nm [71, 94]. The spin in the single domain nanoparticles is often called super-spin or super-moment or giant-moment.

Such single domain nanoparticles are present in living organisms like bacteria, and ferritin which produce nanoparticles of distinct size, high crystallinity, highly ordered, exceptional morphology, and large monodispersity through

biomineralization processes. These processes involve the chemistry of inorganic matter with the organic substances for various purposes including iron storage, structural support, and magnetic interactions (magnetoreception). The resulting products are highly stable in harsh environments like high and low temperature, pressure and pH conditions [95, 96]. The best known magnetic biominerals are the magnetite iron oxide nanoparticles (Fe_3O_4) in magnetotactic bacteria [97]. Efforts are being made in biomimicry and bio-inspired synthesis of nanoparticles and their assembly in nanostructures and superlattices.

The membranes enclosing magnetic nanoparticles inside a magnetotactic bacteria are known as magnetosomes, mostly aligned in a chain form. These effectively provide a magnetic compass (a bar magnet) for the orientation of the bacteria along the external magnetic field (the earth's magnetic field). This alignment of microaerobic bacteria along the earth's magnetic field is called magnetotaxis, discovered by R. Blakemore in 1975 [98]. The magnetosomes crystallize themselves in the $< 111 >$ direction for an enhanced magnetic moment per particle, and these magnetic moments of individual particles align along the chain direction and build a giant magnetic moment [96]. The resulting torque on the chain, due to the giant magnetic moment and external magnetic field, redirects the bacterium to change its direction of motion [95]. The chain like structure of magnetosomes inspired many researchers to artificially assemble the nanoparticles in 1D, 2D and 3D arrays [99, 100, 101]. The magnetosomes by themselves have also been assembled in 2D and 3D arrays on millimeter and micrometer scales, using external electromagnets [96].

Nevertheless, there are challenges still to be explored for well-defined positioning, orientation and assembly on nanoscale dimensions. It requires modern nanofabrication techniques for controlled experiments and for governing the geometrical shape and interparticle distance. The magnetism of a random assembly of magnetic nanoparticles depends on the type and strength of dipolar

coupling and interactions. The organized assembly would involve the geometrical anisotropy parameters along with the dipolar strength. The magnetism of supersymmetrical shapes of magnetic nanoparticle assemblies is also called supermagnetism [102]. The correct positioning of nanoparticles at defined locations on the substrate is essential for further development. Various methods has been adopted in this regard during the past few years, including top down and bottom up approaches [103].

The self-assembly methods has been well studied [104]. The self-assembly could be directed [105, 106], force mediated [101, 107, 108], meniscus-mediated [109], lithographically controlled [110, 111, 112], templated-assisted [113], biotemplated [114], or by selective surface wetting [115]. For uncharged, and non-magnetic (strictly weak magnetic) nanoparticles, the intermolecular interactions and van der Waals forces drive the self assembly. For charged and (strongly) magnetic nanoparticles, the electrostatic and magnetic forces also take part in the self assembly along with the fluid dynamical forces. The directed self assemblies include micro-contact printing [116, 117] and scanning probe-based lithographies [118]. The assisted self assemblies demonstrate the patterning on templated surfaces using capillary forces [119, 113, 110, 120], and convective flows [121, 122, 123]. The templates could be made using optical lithography, electron beam lithography or ion beam lithography. The template assisted self assembly could be wet or dry; the wet method involves the capillary forces of the nanoparticle suspension [124]; the dry method uses van der Waals forces into the grooves of the template. The template assisted assembly is most commonly used because of its low cost and high throughput.

Using these approaches, many forms of assemblies have been achieved on the nanometer scale. The 3D assembly of nanoparticles has been achieved [125, 126]. The 2D sublattices [123, 127] and assemblies can be developed by the drop-cast on the substrate surface, where the evaporation rate of the fluid controls the long-range order [128, 129, 130, 131]. Aqueous interfaces are re-

ported for long range self assembly of nanoparticles that can be conveyed to the substrate surface [132, 133, 134, 135]. The resulting arrays are of exceptional quality with unique electronic and magnetic properties. The collective magnetic properties of 2D arrays of magnetic nanoparticles are different from their bulk counterparts or the individual nanoparticles. One dimensional (1D) assemblies have also been reported in literature [136].

The assembly of magnetic nanoparticles on nanomechanical devices have not been reported previously. Patterning 2D arrays of nanoparticles in geometrical shapes on top of the nanomechanical and optomechanical devices is one of the major aims in this Thesis. The number of nanoparticles and the geometrical arrangement of the array can be controlled, stabilized and the process is reproducible and could be extended to the wafer-scale mass production of devices, as presented in this Thesis.

1.2.3 Torque Magnetometry

A magnetometer can measure the magnitude, direction or the relative change of magnetization, or the magnetic field of a material. Besides the magnetic compass, the earliest magnetometer was invented in 1832 by Carl Friedrich Gauss for the measurement of the earth's magnetic field [137]. Magnetometer can provide information about magnetic ordering and other characteristics of the magnetic material. The efficiencies and capabilities of magnetometers are dependent on the sensitivities, noise detection, drift, stability, resolution, sampling rate and bandwidth. The pertinent magnetometers are SQUIDs (superconducting quantum interference devices), vibrating sample magnetometers (VSM), inductive coil magnetometers, Faraday force magnetometers, optical magnetometers (magneto-optic Kerr effect, MOKE), Hall effect magnetometers, magnetoresistive magnetometers, fluxgate magnetometers and torque magnetometers [138].

SQUIDs are vector magnetometers, sensitive up to 5 aT with $\sim$

0.4 $\mathrm{fTHz}^{-1/2}$ noise level sensitivity, but require low temperature for the measurements for cooling the superconductors [139]. Inductive coil magnetometers work on the induction principle and are only limited to ac magnetization detection. In vibrating sample magnetometer (VSM), the sample vibrates inside an inductive coil and a change in flux is measured. It is limited by sample vibration and heat, not useful for delicate samples, and has an order of magnitude reduced sensitivity than the SQUIDs [140]. Faraday force magnetometry requires the magnetic field gradients in the measurements and it is less sensitive than the SQUIDs. Magneto-optic Kerr effect (MOKE) magnetometry and the Faraday rotation magnetometry use optical polarization for magnetization measurements. Magnetometers can also be used for field sensing, for example most common field sensors are Hall effect sensors, magnetoresistive sensors, and fluxgate sensors. Magnetometers are being employed in various fields, for example, in archaeology, auroras, geology and geophysics, the military, mobile phones and electronics, spacecraft and many other fields.

Micro-SQUID has also recently achieved single spin sensitivity [141], though its limited operating temperature does not allow for room-temperature measurement. Planar micro-Hall measurements that are sensitive to the perpendicular component of a stray field offer room temperature sensitivities near that of nanoscale torque magnetometers, and have measured Barkhausen signatures associated with vortex core pinning in fabricated defect sites [142]. However, Johnson noise dominates and limits their detection sensitivity at high frequencies, and there have been no reports, to my knowledge, of RF susceptibility measurements associated with Barkhausen signatures in single nanoscale elements using the micro-Hall method. Recently, inductive methods for the sensitive measurement of magnetic resonance in single nanoscale elements have been developed [143, 144]. For inductive measurement of the irreversible magnetization changes at the static limit (DC), superconducting electronics would be required [145].

Besides these methods, there are microscopic methods for measuring magnetization. Inspired from atomic force microscopy (AFM) [7], there is magnetic force microscopy (MFM) where magnetic cantilevers sense the magnetic fields [8]. The MFM technique was extended to high resolution magnetic resonance force microscopy (MRFM) [9] along with electron and nuclear magnetic resonance imaging and detection, capable of single electron spin detection [43] and extra-ordinary spatial resolution (4nm) [146]. Another extension of these methods is ferromagnetic resonance force microscopy (FMRFM) [147] used for spin wave modes and magnetization dynamics studies.

Magnetic torque magnetometry has outstanding sensitivity, for measuring torque that is proportional to the magnetization of the magnetic material. The magnetic torque (τ) is produced by the equation, $\tau = \mu \times H$, where H is the external magnetic field, and μ is the magnetic moment. The resulting torque is a measure of net magnetization of the sample, however, torque magnetometry is capable of resolving and measuring the magnetization components in vector form, so that the orientational properties of the material can be obtained. The actuation of magnetic processes could be on the nanomechanical or optomechanical device, and read-out could be performed by electrical capacitance, optical interferometry, or laser taper fiber methods in the cavity optomechanical systems.

Torque magnetometry is not in direct competition with existing methods, but offers a complementary magnetometry tool at the nanoscale. In comparison to most other magnetometry methods involving nanodevices our torque magnetometry method provides direct, linear, non-invasive, broadband (DC magnetization to high frequency AC susceptibility) and fast acquisition of the magnetostatic hysteresis loop while also being able to capture the associated RF susceptibility. It has ability to measure complex 3D volumetric magnetization in vector form. Magnetic force [148] and diamond NV centre [149, 150, 151, 152, 153, 154, 155, 156, 157, 158, 159, 160] magnetometry offer

extremely high magnetic moment sensitivity for electron and nuclear spin resonance detection, and they are practically ideal for localized probing. However, experimental acquisition of the volumetric static moment of a micromagnetic element (and acquiring its hysteresis loop) would require lengthy imaging and reconstruction. This is further complicated if complex three-dimensional microstructures are to be measured (of which torque magnetometry is capable [15]).

Torque magnetometers are employed in this Thesis, using the nanomehcanical and nanophotonic optomechanical platforms. The torque magnetometry measurement capabilities were improved by further miniaturizing and optimizing the device dimensions for higher sensitivities. The setup involves the selection of the right detection scheme for enhanced signal: optical interferometry for nanomechanical devices; and optical fiber taper transduction for optomechanical devices. Furthermore, it can be combined with AC lock-in technique to get a clean signal at natural resonance frequency of the device.

1.3 Organization of the Thesis

The main divisions of this Thesis consist of Chapters that are arranged progressively, as the goals are accomplished. In the first Chapter, an introduction to basics of nanomechanics, optomechanics, self assembly of nanoparticles and torque magnetometry is presented. The objectives of the thesis are also established in this Chapter, along with explanations of the ideas behind the goals. The experimental techniques and brief nanofabrication methods are explained in Chapter 2.

Described in Chapter 3 are the results of fabrication of nanomechanical devices in silicon nitride membranes. A countable number of nanoparticles (~ 350) were assembled on a membrane and devices were fabricated using focused ion beam (FIB) milling. Single domain magnetite nanoparticles were

characterized by nanomechanical torque magnetometry. The magnetic torque driven AC resonant modes of the device and the membrane were studied, including the magnetic hysteresis of the nanoparticles. These devices were good enough to measure the 55 nm size stable single domain nanoparticles, but had not enough sensitivity to measure small size nanoparticles (9 nm). Better devices were made in Chapter 4.

A method to self-assemble nanoparticles in 2D geometrical shapes, integrated with the nanofabrication methods, is described in Chapter 4. The resulting square and circular geometries of magnetic nanoparticles were studied using nanomechanical torque magnetometry. The superparamagnetic nanoparticles were characterized at room and low temperature. The total power loss and energy absorption of the 2D magnetic nanoparticle assembly is discussed. These devices were good enough to measure a large number of 20 nm size nanoparticles, but had not enough sensitivity to measure only a few nanoparticles in ambient conditions. This then led to developing suitable devices for ambient conditions as presented in Chapter 5.

New optomechanical torque magnetometers were fabricated and studied using optomechanical torque magnetometry in Chapter 5. Nanocavity optomechanical detection for torque magnetometry and RF susceptometry were established. These highly sensitive devices operate under ambient conditions. This platform was built to further utilize the magnetic nanoparticles self assembly on the resonating paddle of the optomechanical torque magnetometers. These devices have good magnetic moment and torque sensitivity in ambient conditions, but relatively low magnetic field sensitivity, that led our group putting an effort into fabricating devices for ultra-high sensitive field sensing (presented in Chapter 6).

In Chapter 6, the fabrication of YIG of mesoscopic dimensions and its magnetic characterization by nanomechanical torque magnetometry is presented. These devices were developed for simultaneously probing the (i) spin resonance

for potential applications, (ii) a miniature Einstein-de Haas experiment, and (iii) ultra-high sensitive field sensing magnetometers. These experiments are still being conducted in the laboratory.

Future directions for prospective research and concluding remarks of the current research are presented in Chapter 7. The Appendices give details of the supplementary parts of the work in the main body of the Thesis. This includes the optical cavities, micromagnetic simulations, details of nanofabrication, magnetic nanoparticle self assembly attempts, YIG sample preparation, the ion damage study, and others.

Chapter 2

Techniques and Fabrication

2.1 Introduction

Developments in nano-fabrication has allowed us to obtain the feature sizes in the tens of nanometer range, which has contributed to the advancement of nanomechanics and optomechanics in combination with micromagnetic studies. The top-down approaches include soft lithography, photolithography, nanoimprint lithography, block copolymer lithography, scanning probe lithography, electron beam lithography (EBL), and focus ion beam (FIB) milling [103]. Soft lithography makes patterns using a polymer and transfers the pattern from the polymer mold to the substrate with a resolution of hundreds of nanometers. Photolithography is the most common approach because of its low cost and its wide nanometer range resolution. However, fine features in the 5 nm range are achievable with EBL, which transfers the design pattern from software to the resist on top of the substrate. The limits of EBL patterning depend on the electron beam diameter and the backscattering of electrons in the resist material. The 3D manipulation of the substrate can also be performed in FIB, allowing milling, etching and sputtering. Along with the freedom of manipulation of the substrate, FIB has a limitation due to the high energy ion damage to the substrate, which becomes more critical for magnetic samples.

The bottom-up approach includes atomic layer deposition, sol-gel nanofabrication, self-assembly, vapour phase deposition, and scaffolding [103]. The miniaturization comes down to the atomic level, where devices are created by the manipulation of atoms, which is observable in a scanning tunnelling microscope. The selection of these methods is dependent on the device size, sensitivity, and suitability.

This thesis combines the top-down (EBL and FIB) and the bottom-up (self-assembly) approaches, for fabricating the devices for self-assembled magnetic elements (magnetic nanoparticles, yttrium iron garnet (YIG) and permalloy (Py)). Complications in the self-assembly of magnetic elements come from several issues. For example, the combination of top-down and bottom up approaches brings problems of chemical compatibility. Secondly, the resist lift-off takes away part of self-assembled nanoparticles. Thirdly, the fast evaporation rate of the magnetic nanoparticle solution makes a "coffee-stain" structure instead of a uniform distribution. Fourthly, control over the self-assembly is critical to govern its shape. Lastly, low device sensitivity can cause noise in the measurements. Various methods were formulated to solve these issues and limitations.

Torque magnetometry is the main technique employed in this thesis. In the nanometer range, the mechanical torque magnetometer can be a nanomechanical torque magnetometer or an optomechanical torque magnetometer depending upon the device under study. In the following sections the nanomechanical torque magnetometery and optomechanical torque magnetometery will be discussed in detail from the technique/method perspective. From the fabrication point of view, three main methods were used, namely EBL, FIB and self assembly. EBL and FIB provide high spatial resolution to the device but with their own limitations.

For the small-scale studies, nanomechanical torque magnetometers were fabricated using FIB in the silicon nitride membranes, and presented in Chap-

ter 3. For better control of the shape of the nanoparticle assemblies and better device sensitivity, new nanomechanical torque magnetometers were fabricated in silicon-on-insulator (SOI), presented in Chapter 4 and Chapter 6. To further enhance the sensitivity at another scale, optomechanical devcies were designed and fabricated and presented in Chapter 5, which shows the magnetic measurements of permalloy.

2.2 Nanomechanical Torque Magnetometry

Nanomechanical motion detection consists of mechanical motion actuation and detection at a later stage. This involves pumping a magnetic system and obtaining an amplified signal from that system using the mechanical mode. The actuation in the nanomechanical device can produce displacement changes in the picometer range, so one needs the detection setup sensitive enough to measure that shift and its ability to filter noise [161]. An optical interferometry detection method was employed in Chapters 3, 4 and 6. The optical interferometry technique is based on the basic interference method and interactions. The interference pattern is defined by the moving device and the stationary substrate, detailed in the next subsection.

A schematic of the nanomechanical torque magnetometry setup is shown in Fig. 2.1. It consists of nanomechanical resonator with a Fabry-Pérot cavity, a DC magnetic field from a permanent magnet, and an AC magnetic field from a dither AC coil (solenoid). The axes are selected such that the DC magnetic field is in the x-direction, the AC magnetic field is in the z-direction and the mechanical torsional motion by the acting torque would be along the y-axis according to Eq. 2.3.

$$\tau_y = m_x \times \mu_0 H_z \tag{2.1}$$

where μ_0 is the permeability of free space, τ is the torque, m is the magnetic

moment, and H is the magnetic field.

The detection mechanism consists of the laser (HeNe 632 nm, Melles Griot), photodetector (New Focus 1801) and beam splitters. The incoming beam is splitted by the beam splitter. One part is focused onto the chip by an objective lens, and then the reflected signal beam and reference beam interact with each other. The reference beam is used for laser background and for interference. The sample was placed (in the vacuum chamber) inside the Oxford Instruments cryostat (Microstat Hires Mk2 30D x 86LG Pillar) which has a continuous He flow cryostat with a range of 4K to room temp (Cryomech LHep18 liquefaction system equipped with a turbo station (HiPace80) and temperature controller (ITC503)).

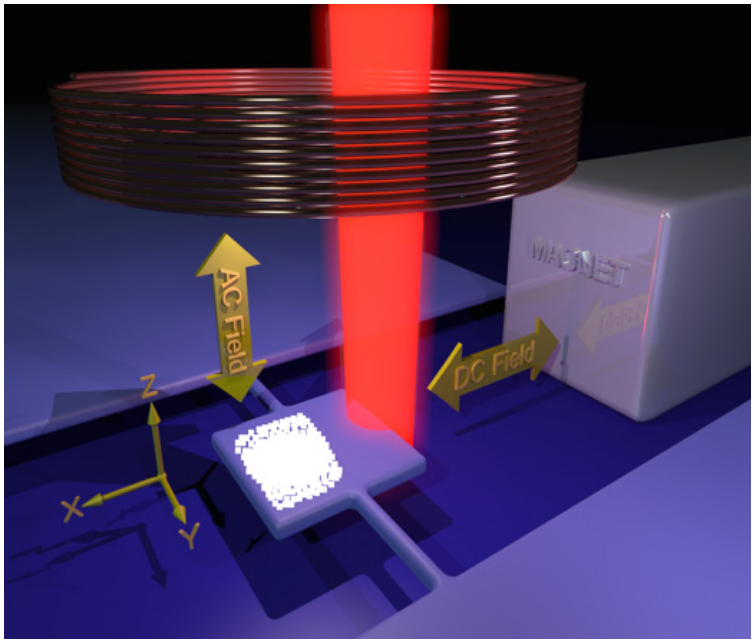

Figure 2.1: ***Schematic of nanomechanical torque magnetometry setup (not to scale).*** *The white colour on the device paddle represents the deposited magnetic element.*

The DC and AC signals are collected by the AC-coupled photodetector. The AC signal of the photodetector is then passed to the lock-in amplifier (Zurich Instruments: HF2LI or UHFLI, or Stanford Research Systems SRS844). The

lock-in output is connected to the power amplifier (ENI 300L, 40dB, 250kHz - 110MHz) to provide a reference current signal to the AC coil. The current in the AC coil is changed by the drive output through the lock-in amplifier. The DC magnet (N50 neodymium iron boron, 2.0 in^3, NB029-50NM, CMS Magnetics) is placed in a holder on top of the stepper motor rail and its motion is controlled by the Labview program. The program can move the magnet linearly on the rail (Velmex Unislide MB2527CJ-S2.5 equipped with a stepper motor Vexta PK264-02A), rotate the magnet by 180 degrees to reverse the sign of magnetic field along the selected axis, and is able to save a full magnetic hysteresis in one run. The program also records the signal data from the lock-in amplifier and DC magnetic field values from the 3-axis Hall probe sensor (HP, Senis C-H3A-2m E3D-2.5kHz-1%-0.2T). The Hall probe was placed close to the resonator outside the vacuum chamber. The devices and the AC coil are inside the vacuum chamber (10^{-8} Torr) and the laser spot is positioned with an objective housed in the 3-axis piezo stage, which allows fine positioning of the laser beam. The same piezo stage was used for raster scans on the device area. The AC magnetic field can be calculated using the on-axis solenoid equation by the known parameters (current, number of turns, length of solenoid), where current is selected in the sinosoidal mode. The Labview program recorded the lock-in signal (auxiliary components: X, Y, R, Phase) and the magnetic field at each step of the field sweep.

2.2.1 Fabry-Pérot Cavities

A Fabry-Pérot cavity consists of two parallel mirror planes. The device layer was used as one mirror and the substrate (base) was used as the second mirror. The gap between the two planes is determined by the fabrication method. The Fabry-Pérot interferometer or etalon is created for the nanomechanical devices by the sandwich method in the silicon nitride membranes, or by etching a buried oxide layer in the SOI (silicon on insulator) chips. The sacrificial layer (buried

oxide layer) thickness is chosen before the fabrication process to be compatible with the constructive interference pattern at the desired laser wavelength. The device layer (paddle, 145-300 nm thick) is transparent to the laser beam when the edge of the device is focused by the laser. The laser beam reflects from the device and part of it passes through the paddle, and reflects from the base substrate. The reflected beam from the device and from the base creates the interference which is then detected by the photodetector and passed to the lock-in amplifier. The device paddle resonates at the mechanical frequency and the substrate stays stationary. Further reading about Fabry-Pérot cavities is detailed in Appendix A.

2.2.2 Nanomechanical Device Fabrication on Silicon Nitride Membranes

The nanomechanical devices were fabricated in the silicon nitride membrane (100 nm thick) using 2D milling in the FIB, and are presented in Chapter 3. The silicon nitride is suspended on top of the silicon substrate. The ion beam was accelerated at 30 kV and 80 pA probe current was used for milling the devices in the Ziess NVision 40 FIB machine. The devices were only imaged with SEM and imaging with ion beam (low current) was avoided in order to prevent ion damage to the silicon nitride membrane and devices. The milling process ejects material (electron, ions, atoms). The ejected material can be absent completely or can redeposit in the proximity of the exposed area. The redeposition is dependent on the material and ion beam settings. After the fabrication of devices in the silicon nitride membrane, the Fabry-Pérot cavity was created by mounting the inverted silicon nitride chip on top of a clean silicon chip with a 25 μm spacing between them. The 25 μm spacing was created by using the transparent 3M tape in between the chips at the edges. The sandwich was then used in the interferrometric setup for nanomechanical

torque magnetometry.

2.2.3 Nanomechanical Device Fabrication on Silicon-on-Insulator (SOI)

Electron beam lithography (EBL) is the fundamental tool for device fabrication in SOI chips. The resolution of lithography is based on the wavelength of the electrons. The electrons interact with the polymeric resist material and change the cross-linking. The transformed polymer resist thus changes its properties, and hence it is possible to etch the exposed resist. Resist polymers could be chosen positive (ZEP, PMMA) or negative (HSQ, SU-8) depending upon the beam exposure and device layer. In a negative resist, the inverted device area is exposed in an opposite sense to the positive tone resists. In EBL the electron beam at the desired accelerating voltage and area dose can be selected along with many other elective parameters.

The SOI consists of a thin top layer of silicon (145-300 nm thick), a buffer layer (buried oxide layer) and a base silicon handle layer (substrate). The thickness of the buried oxide layer is an important parameter to select before starting the fabrication because the Fabry-Pérot cavity will be created in this layer. The thickness of the buried oxide layer will be the spacing for the Fabry-Pérot cavity that will create the interferrometer, and its spacing is very important to create the constructive interference. The oxide layer varied between 1-3 μm, for different devices in our case, and the silicon handle layer was 700 μm - 1 mm thick.

The fabrication process starts with the piranha cleaning of chips followed by the resist spinning at 4000 rpm for 40 s (with a pre-ramp of 100 rpm for 4 s). The resist was baked at 180°C for 10 minutes with a covered lid. The chips were transferred to the EBL (Raith 150-two system) load lock immediately after cooling in order to avoid any other exposure to the resist or to sidestep

the sensitivity of resist overtime. The corner of the chip was marked with a diamond scribe for beam focusing and alignment purposes. A small spread of gold nanoparticles can also be used for that purpose. After loading the samples, the focusing and alignment was performed similar to that of an SEM operation. The software design of the devices was then transferred to the resist by the electron beam. The resist was then developed in the respective solutions for positive or negative resists used (the details are given in Appendix C). After the resist development, an inductively coupled plasma reactive ion etch (ICPRIE) was used to transfer the design to the silicon layer. The plasma ions interact with the resist layer and etch out the developed regions, which is a standard procedure for silicon dry etching. The buried oxide layer was then etched out by the wet etching (BOE) process, which uses concentrated hydrogen fluoride acid at an etch rate of 55 nm/s. As a marker, plain paddles without the torsional rods and handle paddles were also included in the design to observe the releasing of the paddles. For the completely etched and released devices, the marker paddle should be vanished (washed away) completely. The released devices were transferred to isopropanol alcohol (IPA) and then dried out in a critical point dryer in a CO_2 environment at 0°C to hinder the stiction of the devices to the base silicon layer. Another fabrication cycle was repeated for the magnetic layer deposition as described in Appendix C.

2.3 Cavity Optomechanical Torque Magnetometry

The nanomechanical motion of the optomechanical devices was detected by the laser fiber taper optomechanical method. This method was much more sensitive than the previously described nanomechanical method. The displacement sensitivity and torque sensitivity is $1 \times 10^{-11}\mathrm{m}(\mathrm{Hz}^{1/2})^{-1}$ and $1.3 \times 10^{-20}\mathrm{Nm}(\mathrm{Hz}^{1/2})^{-1}$, respectively for this method. The nanomechani-

cal devices described in previous section has the torque sensitivity $\sim 70 \times 10^{-21}\mathrm{Nm(Hz^{1/2})^{-1}}$ [162]. The optical transduction method is based on the interaction of the laser field inside the fiber evanescently in the proximity of the device. The optomechanical torque magnetometery method was used in Chapter 5.

The schematic of the optomechanical torque magnetometry is shown in Fig. 2.2. It consists of a mechanical resonator fabricated in the optomechanical devices, an optical cavity (to be described in Section 2.3.1), a laser fiber, an RF coil, a DC magnet, and a rotating stage. The DC magnet (N50 neodymium iron boron, 1 in^3) was used to provide a stable H^{DC}, and was mounted on the motorized stepper rail. The RF coil was placed under the sample chip to generate the $H_{\mathrm{x}}^{\mathrm{RF}}$ and $H_{\mathrm{z}}^{\mathrm{RF}}$. The RF coil was replaced with the transmission line later on, for the better control over the direction and amplitude of RF fields. The field magnitudes were recorded with a three-axis Hall probe (Sentron 3M12-2) placed below the sample chip. The magnetic fields act similar to the nanomechanical setup in the above section and according to Eq. 2.3. The torque is actuated by the magnetic fields in the torsional paddle, transferred to the optomechanical beam and detected by the tapered fiber. The evanescently coupled laser fiber detects the optomechanical signal and then transfers it to the photoreceiver (New Focus 1811, IR DC-125 MHz), which is connected to the lock-in amplifier. The DC component is used to view the optical transmission of the laser, and the RF component is used for the real spectrum analyzer (Tektronix RSA 306, 9 kHz - 6.2 GHz, and Tektronix RSA 5103B) and lock-in amplifier (Zurich Instruments, HF2LI/UHFLI, 200-600 MHz). The RF coil was driven by a reference signal through the RF power amplifier (ENI 403L, 37 dB gain) connected to the lock-in amplifier. The incoming wave to the tapered fiber was controlled by the polarizer and the power strength controller. The laser (Santec TSL-510, wavelength range 1500-1630 nm) was used at 1520-1550 nm wavelength with the device resonance at 1526 nm.

The schematic of the setup is presented in Fig. 2.2 to demonstrate the steps mentioned above. The tapered fiber dimple is aligned (50 nm position resolution) on the fixed portion of the device near the nanocavity gap. The fiber can transduce the signal by evanescently coupling laser light in and out of the nanocavity in two modes: hovering mode and touching mode. All measurements were performed in the nitrogen purged environment at room temperature and pressure.

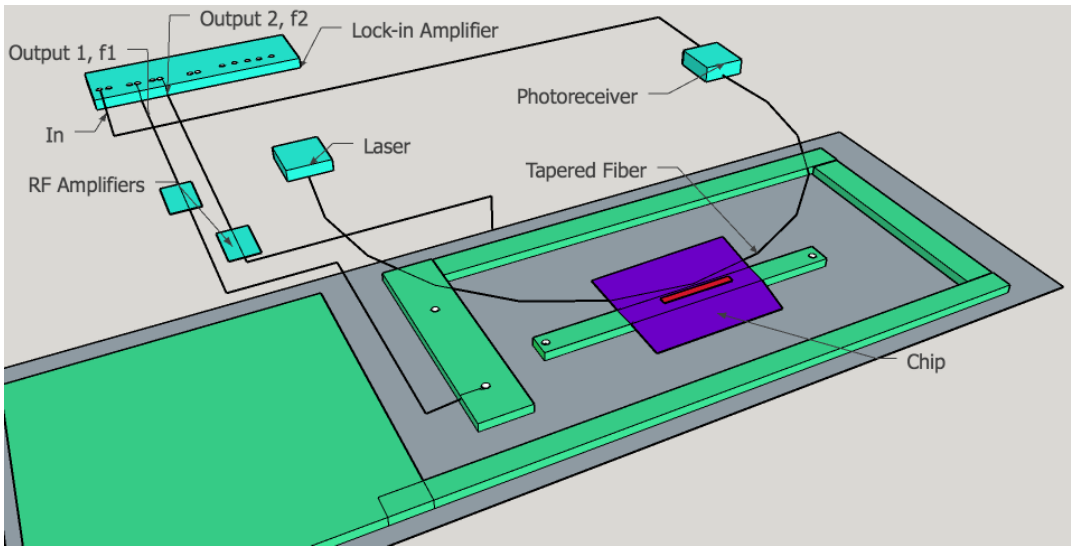

Figure 2.2: ***Schematic of the optomechanical torque magnetometry setup (not to scale).*** *The green colour represents the transmission line, the cyan colour shows the remaining components of the setup, the purple colour represents the chip, and the red colour represents the device layer.*

The current input to the transmission line is controlled by the drive output of power amplifiers through the lock-in amplifier. The labview program controls the DC magnet on the stepper rail (Suruga Seiki, stepping motor contoller, DS102) and records the data from the lock-in amplifier for magnetic hysteresis and for the torque-mixing spectroscopic scans. The DC field calibration is also recorded in a separate labview program by the 3-axis Hall probe, and is then fitted with a 9th order polynomial (for best fitting). The fit parameters for calibrations are then used to record the data at equally distant points in terms

of the magnetic field. The lock-in signal is recorded at each given field step for the magnetic field sweeps.

2.3.1 Nano-Beam Photonic Crystal Split-Beam Cavities

A photonic crystal is a periodic structure with lattice constants and symmetry. The periodicity in the material creates a band gap similar to the electronic bandgap in semiconductors. A defect in the periodic structure of the photonic crystal can create an optical cavity. A photonic crystal cavity can transduce the mechanical and optical modes and it confines the light in the material geometries. When the photonic crystal geometries transduce the optical field in the mechanical modes at mechanical resonances, this allows optomechanical devices to be formed. Optomechanical devices come in a variety of geometries including nanobeams, which consist of an array of holes in the beam acting as a Bragg's grating. The optomechanical nanobeams are a combination of waveguides (the material) and gratings (holes). The light is confined to the geometry in two ways: the total internal reflection inside the waveguide, and the grating filters the wavelengths in the band gap of the grating. A defect in the grating can create a localized state where the optical mode can be constrained.

The nanobeam photonic crystal cavity can be split in the middle to form two separate elements by the gap determined by the grating. This cavity is called a split-beam cavity (SBC), which consists of two independent nanomechanical resonators accompanying each other by the grating [163]. The associated mechanical resonances can be altered by changing the geometry of the mechanical elements. The outer holes of the gratings are called mirrors of the grating or the optical mirrors.

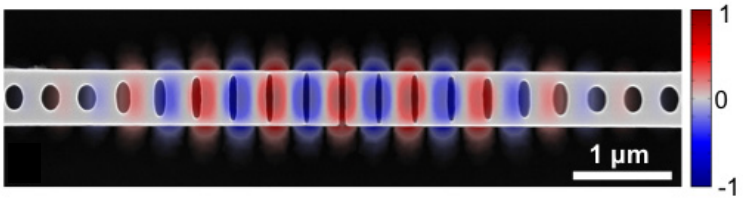

Figure 2.3: ***Top view of the split-beam nanocavity (SBC).*** *The colours represent the electric field of the optical wave confined in the central region.*

Figure 2.3 shows the top view of the SBC in silicon material in the SOI chip. In this SBC the cavity is formed by changing the hole shapes (gratings) and dimensions in the middle of the beam. The optical mode is localized between the cavity mirrors (inner holes), which are created by the array of holes which trend from circles to ellipses until the gap dimension is reached. The radiation losses are minimized by phase matching the band-edges of the holes and the gap. The optical mode modulation is carried out by the laser fiber in the proximity of the near field of the cavity. Hence, the SBC has both mechanical and optical resonances that can be tuned and detected separately. The optomechanical coupling and quality factor of the design can be simulated in the COMSOL software according to the requirements. The resonating paddle with magnetic material is on one side of the mechanical beam. This SBC favours the mechanical resonances with effective masses less than 1 pg.

2.3.2 Nano-Cavity Split-Beam Optomechanical Device Fabrication

The frequency of operation was chosen near the 1550 nm wavelength, with an effective wavelength ($1550\text{nm}/n_{Si}$) close to the device's features size and to the lattice constant of the holes. The refractive index in silicon, n_{Si}, is 3.5 such that the feature size is comparable to the device layer thickness $\sim$ 220 nm, as in our case for the optomechanical SBC. The width of the SBC was set to 600 nm such that it was not too large to favour multi-modes, and not too small to degrade

optical quality factor or create fabrication difficulties. The gap of the SBC was selected to be 50 nm commensurate with the elliptical shape in the center. There were 6 tapering cavity holes in between the central elliptical gap and the circular holes at the edges of the beam, to optimize optomechanical coupling. The number of circular holes (optical mirror holes) was selected by the mirror strength and optical field leakage. We chose 9 mirror holes for better mirror strength. This design was optimized in finite-difference time-domain (FDTD) software and gave an optical quality factor in the range of 10^6 at 1526 nm laser wavelength. A graphic database system information interchange (GDSII) file was created in the Matlab script for the device designs in raith software. The nanofabrication of the actual device was carried out in the same way as described in the section above and detailed in Appendix C.

2.4 Torque-Mixing Resonance Spectroscopy (TMRS)

TMRS is a sensitive technique and can simultaneously measure the net magnetic moment and spin resonances. It has ability to measure the transverse components of precessing magnetization. The torque amplitude is generated by the frequency mixing of RF fields in nanomechanical torque magnetometers. The transverse components of the dipole moment (in precession) produces torque, similar to the magnetic resonance phenomena in electromagnetic induction. But TMRS is broadband in comparison to the induction method, and is capable of simultaneously acquiring static and dynamic magnetization responses. For RF transverse component excitation, the magnetic element is biased by dc magnetic field $\boldsymbol{H}_0 = \boldsymbol{H}^{\mathrm{DC}}$, and RF fields $\boldsymbol{H}_1^{\mathrm{RF}}$ and $\boldsymbol{H}_2^{\mathrm{RF}}$ were applied for torque-mixing according to the scheme in Fig. 2.4.

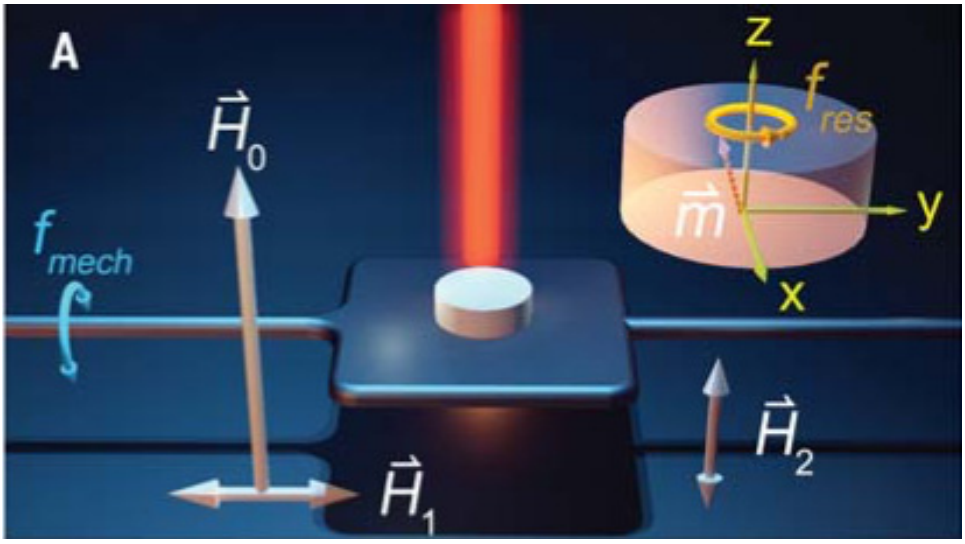

Figure 2.4: ***Applied field directions for TMRS (not to scale).*** *The magnetic disk is biased in an applied field $\boldsymbol{H}_0$ at mechanical resonance of the device f_{mech}. The RF fields $\boldsymbol{H}_1^{RF}$ and $\boldsymbol{H}_2^{RF}$ were applied for in-plane and out-of-plane drive. Reprinted with permission from [15].*

The applied RF fields were $\boldsymbol{H}_1^{\mathrm{RF}} = \boldsymbol{H}_{1\mathrm{y}}^{\mathrm{RF}} = H_{1\mathrm{y}}^{\mathrm{RF}}\hat{y}$, where $|\boldsymbol{H}_1^{\mathrm{RF}}| = H_1 cos(2\pi f_1 t)$, and $\boldsymbol{H}_2^{\mathrm{RF}} = \boldsymbol{H}_{\mathrm{z}}^{\mathrm{RF}} = H_2 cos(2\pi f_2 t)\hat{z}$. The H^{DC} is in $\hat{z}$ direction for this configuration, but the thin disks in-plane magnetization would also be present, which would be related to transverse susceptibility components ($\chi_{\mathrm{xy}} = -\chi_{\mathrm{yx}} = -\iota\chi_t(f_1)$) by the Polder tensor:

$$\begin{aligned} \mathbf{m} &= V\chi_t(f_1)\cdot\boldsymbol{H}_1^{\mathrm{RF}}, \\ \begin{pmatrix} m_x \\ m_y \end{pmatrix} &= V \begin{pmatrix} \chi_{\mathrm{xx}} & \chi_{\mathrm{xy}} \\ \chi_{\mathrm{yx}} & \chi_{\mathrm{yy}} \end{pmatrix} \begin{pmatrix} 0 \\ H_1 cos(2\pi f_1 t) \end{pmatrix} \end{aligned} \tag{2.2}$$

The direct torque term corresponding to x-component of magnetic moment would be:

$$\tau_y\hat{y} = m_x\hat{x} \times \mu_0 H_2\hat{z}. \tag{2.3}$$

Substituting Eq. 2.2 in Eq. 2.3 would result in:

$$\begin{aligned}\tau_{\mathrm{y}} &= -(-\iota\chi_t(f_1)H_1^{\mathrm{RF}}cos(2\pi f_1 t))(H_2^{\mathrm{RF}}cos(2\pi f_2 t)) \\ &= \iota\frac{\mu_0 V H_1 H_2}{2}\chi_t(f_1)\Bigg(cos(2\pi(f_1-f_2)t) + cos(2\pi(f_1+f_2)t)\Bigg)\end{aligned} \tag{2.4}$$

When the device is driven at $f_{\mathrm{mech}} = f_1 - f_2$, the mixing torque amplitude is proportional to the transverse susceptibility components such that:

$$\tau_{\mathrm{y}}|_{(f_{\mathrm{mech}})} = \frac{\mu_0 V H_1 H_2}{2}\chi_t(f_1) \tag{2.5}$$

For thin films, χ_{z} and other transverse components in the susceptibility tensor are ignored due to the shape anisotropy inherent in the thin films (i.e., permalloy thin film in Chapter 5). For a 3D mesoscopic magnetic disk, many susceptibility components contribute to generate torque in y-direction (see Chapter 6).

Chapter 3

Nanomechanical Torque Magnetometry of an Individual Aggregate of ∼350 Nanoparticles

The material presented in this chapter was published in the Canadian Journal of Physics 93: 1252-1256 (2015) by T. Firdous, D. Vick, M. Belov, F. Fani Sani, A. McDermott, J.E. Losby, D.A. Bazylinski, T. Prozorov, D.K. Potter, and M.R. Freeman.

3.1 Motivation

The magnetic and flow measurements of magnetic nanoparticles in bulk form, useful for many applications [164] has been well studied. However, with the advent of nanotechnology, the use of small scale systems is being used and studied immensely. In many studies the magnetic properties of isolated and small- scale assemblies of nanoparticles are derived from measurements of bulk nanoparticle systems. Our motivation here is to demonstrate how the properties of selected

small assemblies of single-domain magnetic nanoparticles can be determined from mechanical signals actuated by external field- induced torque, when the material of interest is integrated with a compliant mechanical armature. The measurements of magnetic hysteresis for aggregates of nanoparticles deposited on a surface are presented in this chapter.

3.2 Introduction

Nanoparticles synthesized in solution or harvested from aqueous natural environments are often droplet-dispensed and dried on surfaces, for subsequent characterization via microscopy, spectroscopy or magnetometry [165, 166, 167, 168]. Nanoparticle aggregation during such preparations is common, and combining microscopy with other measurements allows the correlation of physical properties with the structure of the aggregates. We report an application of this approach to selective hysteresis measurements among magnetic nanoparticle clusters. Aggregates of particles deposited on silicon nitride membranes are chosen by electron microscopy and isolated for magnetic study through focused ion-beam milling of nanotorsional resonators [161].

Micro- and nanomechanical systems are powerful tools in current research and technology [26, 169, 170, 171, 172, 173, 174]. Stoichiometric high-stress silicon nitride is used extensively as the starting point for micro- and nanomechanical sensors utilizing the mechanical resonance modes of plate [175], bridge [176], cantilever [177], membrane [178, 179, 180], and string [181] geometries to enhance sensitivity. The non-invasive nature and high sensitivity of membrane-based nanomechanical torque magnetometry enables studies of nanostructured magnetic materials.

Naturally occurring magnetite nanoparticles are interesting candidates for nanomechanical torque magnetometry. Magnetite nanoparticles are abundant in terrestrial rocks, and in a variety of organisms as biogenic products. One

major source of magnetite nanoparticles is from magnetotactic bacteria, which produce magnetosomes of high purity and crystallinity, often in the form of linear chains. These chains produce adequate net magnetic moment that is thought to aid navigation. The efficiency of magnetic alignment depends on the magnetic domain state of the magnetite nanoparticles. The domain state is strongly dependent on the size, shape, chain arrangement, and crystallographic features of the nanoparticles [167, 182]. The self-assembly of these magnetic nanoparticles is described in a recent study [70]. The magnetic properties of such assemblies are of particular interest, and better characterization and control of the magnetic properties has potential to enhance promising applications, including drug delivery, magnetic hyperthermia, MRI contrast agents, catalysts, as well as magnetic information storage and sensing technologies [76, 183, 91, 184, 185].

This chapter includes the study of magnetite nanoparticles derived from magnetotactic bacteria using nanomechanical torque magnetometry. The nanoparticles are deposited on high-stress Si_3N_4 membranes, to allow inspection by electron microscopy, followed by focused ion-beam milling of torsional resonators precisely located to capture selected aggregates within the membrane area. Torque magnetometry is performed using the resonators. I investigate also the magnetic torque-driven AC resonant modes of the modified supporting membrane. The observations are compared to numerical simulations of the mechanical modes, and to micromagnetic modeling of the hysteresis of a specific measured cluster of ∼350 nanoparticles.

3.3 Silicon Nitride Nanomechanical Torque Magnetometers

Cells of magnetotactic bacteria (Magnetovibrio blakemori, strain MV-1) were cultivated micro-aerobically and then suspended in the growth medium, fol-

lowed by collection using the protocol in ref. [186]. The ∼50 nm size magnetite nanoparticles were then deposited by a Nano eNabler (TM, BioForce Nanosciences) onto a 100 nm thick, high-stress, silicon nitride (Si_3N_4) window 40 μm × 200 μm in size (Norcada, Inc.). The nanoparticles formed diverse patterns on the membrane, which included aggregates across length scales from one to tens of micrometres, as seen in the scanning electron micrograph (SEM) of Fig. 3.1a.

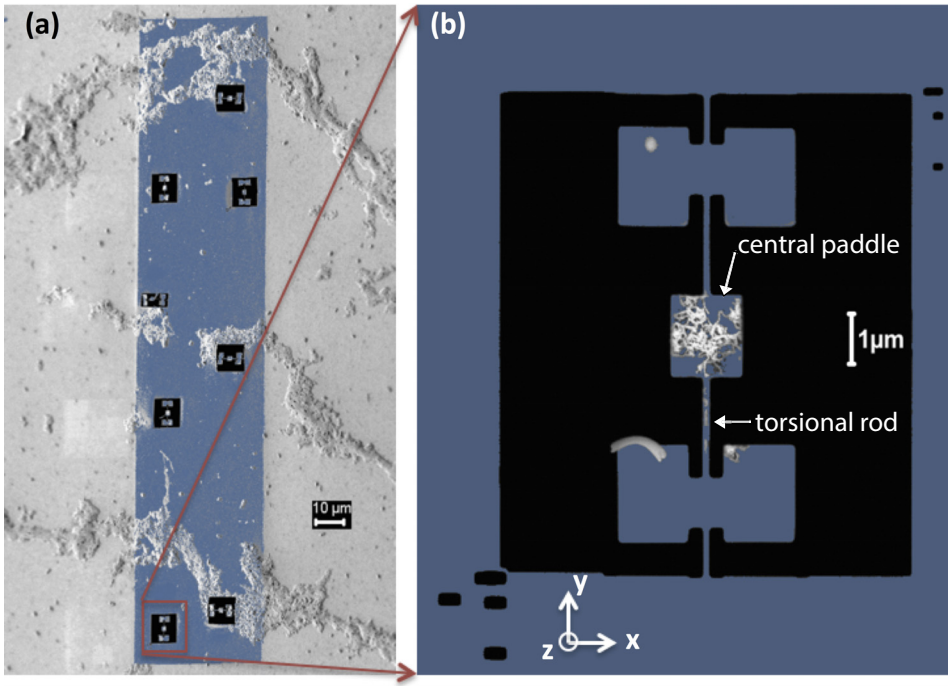

Figure 3.1: ***False colour SEM of fabricated nanomechanical devices in silicon nitride membrane.(a)*** *A false colour SEM of (blue) the silicon nitride membrane incorporating triple-paddle resonators. The nanoparticles show up white; black is where the membrane has been cut away.* ***(b)*** *A selected triple paddle resonator. Most of the nanoparticles are on the central paddle. The small black rectangles at the corners of the device are reference marks used for focus ion beam alignment. The x, y, z coordinate system is indicated. The DC field is applied in the x direction, while the AC field is applied along the z-axis. The corresponding torque is produced in the y direction.*

Selective areas of deposited nanoparticles can be isolated for magnetic measurements by fabricating torsional resonators within the membrane using a dual-beam focused ion milling machine (Zeiss NVision). This enables one to

obtain a documented geometry of nanoparticles on the device, as shown in Fig. 3.1b. The width of the torsion rod is ∼180 nm. Nanomechanical resonators, as torque magnetometer devices, were fabricated at various locations to encounter diverse distributions of nanoparticles on the device paddles. The nanoparticle deposits also lead to deformation of the torsion rods and paddles of the resonators, visible when tilting the sample in the SEM. The silicon frame supporting the membrane is affixed to a diced piece of silicon wafer, which serves as the back reflector of a low-finesse Fabry-Pérot etalon for interferometric displacement detection (gap 25 μm). The arrangement is placed inside a vacuum chamber ($10^6 Pa$) with optical access and an adjacent three-axis Hall probe. An in-plane applied DC bias magnetic field induces a net moment m in the specimen, and a perpendicular (out-of-plane) RF magnetic field H_z generates the magnetic torque, according to

$$\tau = m \times \mu_0 H_z \tag{3.1}$$

where μ_0 is the permeability of free space.

A 632 nm wavelength probe light is focused through a long working distance objective. The optical interference-modulated reflected intensity is detected by an amplified photodiode and demodulated via lock-in amplification. Maximum torque is detected when the bias field is perpendicular to the torsional rod, to maximize the magnetic moment in the x-direction. Small number of magnetic nanoparticles on the device paddle drive its mechanical vibrational modes. However, the larger aggregates of nanoparticles also drive whole-membrane vibrational modes. So, one should differentiate the vibrational modes of devices and those of the membrane. For that purpose, spatial imaging of mechanical resonance modes is performed by raster scanning the sample under the objective, which is described in 3.4 and 3.5.

3.4 Resonance Modes of Nanomechanical Devices

The mechanical resonance modes are first identified by swept-frequency spectroscopy at specific spatial positions, as shown in Fig. 3.2. The general resonance spectrum is complicated and contains peaks corresponding to independent torsion resonator and membrane modes, as well as coupled modes. The fundamental mode of the torsional device appears at 1.7447 MHz, and the strongest membrane mode in this instance is at 2.773 MHz. The mechanical quality factors (Q) of these two modes as determined by peak fitting are 179 and 78, respectively. This device has the magnetic moment sensitivity of $7 \times 10^8 \mu_B$ under vacuum condition.

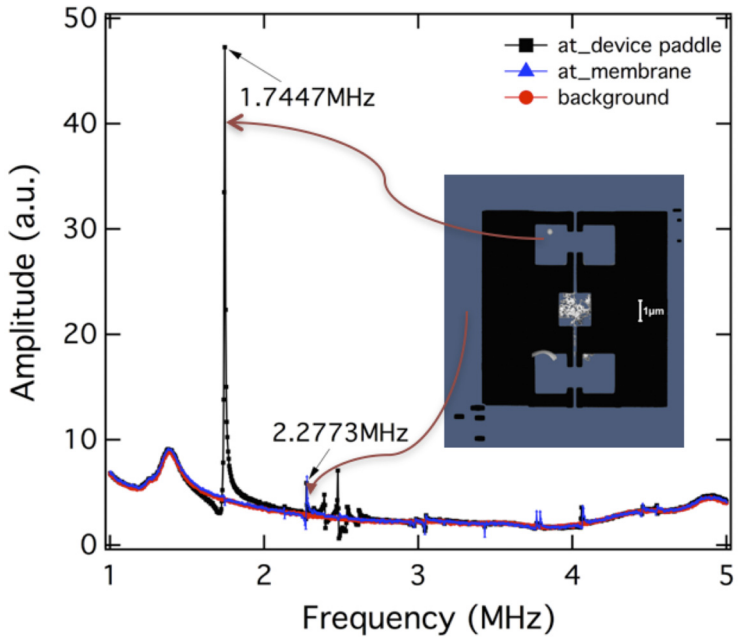

Figure 3.2: ***Spectral response of resonance.*** *Vertical (z) displacement amplitude (proportional to y-mechanical torque and to x-net magnetization) showing resonance peaks for the triple-paddle resonator and the membrane. Magnetic torque actuation by the nanoparticle aggregates reveals many mechanical modes. Inset is the SEM of the corresponding positions at which the spectra were taken.*

To complement the spectroscopy at fixed optical probe positions, the two-

dimensional spatial response at fixed drive frequency can also be mapped. Figure 3.3 shows raster-scanned imaging of the entire device when driven at the 1.7447 MHz torsional resonance of the structure in the lower left corner of the membrane. Figure 3.3a shows the SEM image of the device and membrane. The DC reflected optical intensity is monitored in parallel with the AC component demodulated by the lock-in. The reflected intensity map in Fig. 3.3b shows a pattern of reduced reflectance in the regions of larger nano- particle aggregates, in very good correspondence with the corresponding SEM image of Fig. 3.3a. The amplitude of mechanical response, rendered on a logarithmic scale in Fig. 3.3c, is strongly peaked at the locations of two of the detection paddles.

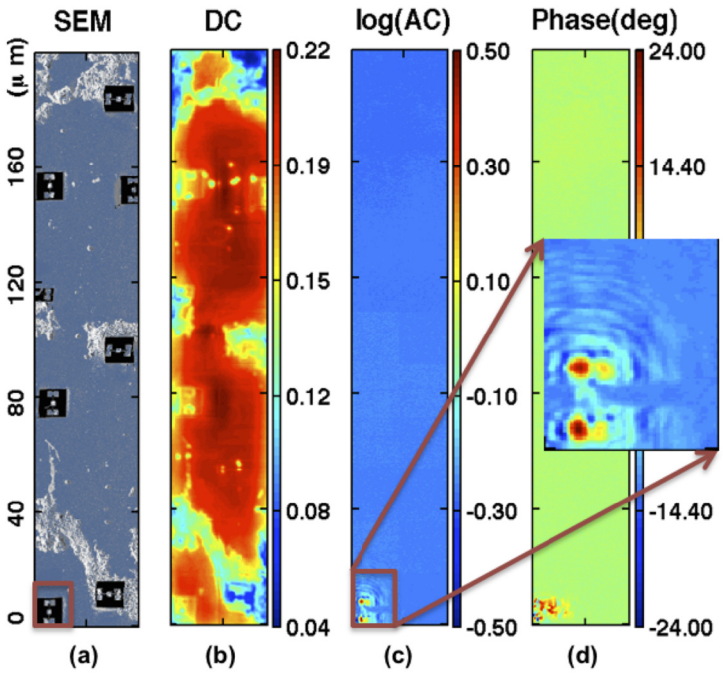

Figure 3.3: ***Resonance mode of nanomechanical devices in silicon nitride membrane.*** *SEM and optical raster scanned images of the membrane:* ***(a)*** *SEM of the selected area;* ***(b)*** *DC reflected optical intensity of the membrane area;* ***(c)*** *interferometric AC signal amplitude at the torsional frequency mode (1.7447 MHz) of the selected resonator measured simultaneously; inset, the features in detail;* ***(d)*** *relative phase of the AC signal. The colour bars in (b) represent the reflected intensity in V_{DC}, and in (c) the interferometric AC magnitude signal from the lock-in amplifier rendered as $log(V_{rms}/1V)$ units.*

Mechanical energy can be seen radiating away into the membrane, consistent with the relatively low mechanical Q. The left-right asymmetry of the AC optical signal is most likely due to non-parallelism of the resonator and back-reflector, which can also be contributed to by deformation of the paddles. This non-parallelism, together with the nonzero signal background from electrical crosstalk (red curve in Fig. 3.2) yields the intricate phase portrait seen in Fig. 3.3d.

3.5 Resonance Modes of Silicon Nitride Membrane

Spatial mapping of whole-membrane modes is also of significant interest. Several examples are shown in Fig. 3.4. The mechanical modes of the pristine membrane are strongly modified twice: first, by the addition of nanoparticle deposit; and second, by the subtraction of selected membrane areas in the FIB-milling procedure. The main take-away from Fig. 3.4 is that even these uncontrolled and accidental modifications can yield quite localized and high amplitude membrane resonances very effective for magnetometry, for example, near the left edge and 75 μm up from the bottom, at 3.156 MHz (Fig. 3.4c). This may be a useful complementary alternative to patterning resonators within, and intended to be largely decoupled from, the membrane.

Finite element simulations were performed to lend insight to the potential designs both of localized membrane modes and of strongly coupled membrane-torsional resonator hybrid modes. The layout of the patterned membrane as imaged by SEM was recreated in a finite element model (COMSOL), neglecting the effects of modification by the nanoparticle deposits. These results are presented in Fig. 3.5. The first torsional mode of the resonator in the lower left corner is fairly independent of the membrane, consistent with Fig. 3.3c, as seen in Fig. 3.5a (with an enlarged view in Fig. 3.5d). The simulated frequency

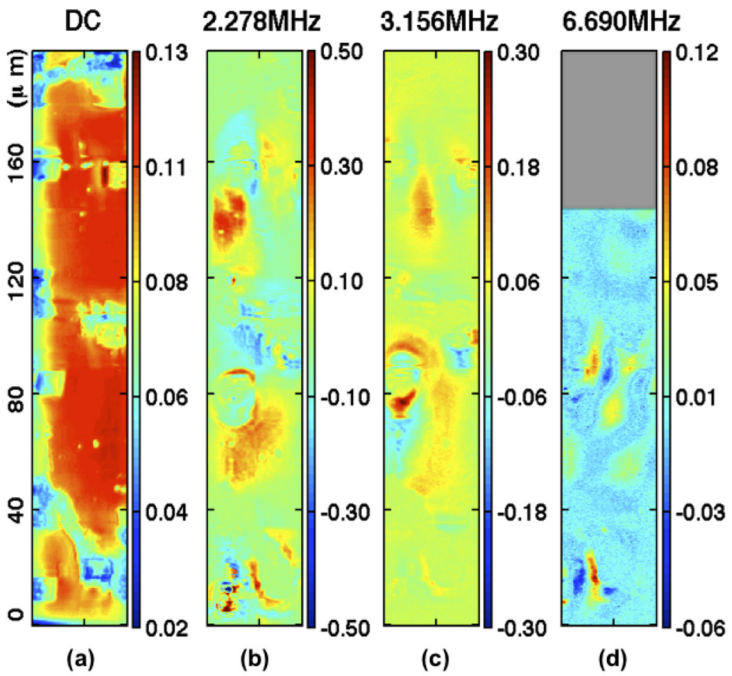

Figure 3.4: ***Resonance modes of silicon nitride membrane.*** *Optical raster scanned images at various membrane resonance modes:* ***(a)*** *DC reflected intensity of the selected area; and* ***(b)-(d)*** *interferometric AC signal amplitude at different frequencies. The grey area in (d) indicates that no signal was recorded in that region. The background colour is represented by the zero reference from the colour bar in each panel. The red and blue colours show the displacements above and below the membrane, respectively. The colour bars in (a) represent the reflected intensity in V_{DC}, and in (b)-(d) the interferometric AC magnitude signal from the lock-in amplifier in V_{rms} units.*

of the mode, 5.7159 MHz, is very different from our observed value of 1.7447 MHz. Such discrepancies arise not only from the nanoparticle loading. They are still fairly routine when modelling thin membrane devices, from a combination of uncertainties in the stress and the elastic properties (including modifications from the deposits and the ion milling). In Figs. 3.5b and 3.5c, relatively more- and relatively less-localized membrane modes are shown, with some features reminiscent of the experimental observations in Figs. 3.4c and 3.4d. The detail of a strongly hybridized membrane-torsional mode is illustrated in Fig. 3.5e. In contrast to experiment, the simulations show an opposite trend of frequency change through the evolution from isolated torsional modes to the coupled

and localized membrane modes. The contrary trend in experiment could be due to the additional mode-localization effects from the very non-uniform mass loading of the membrane.

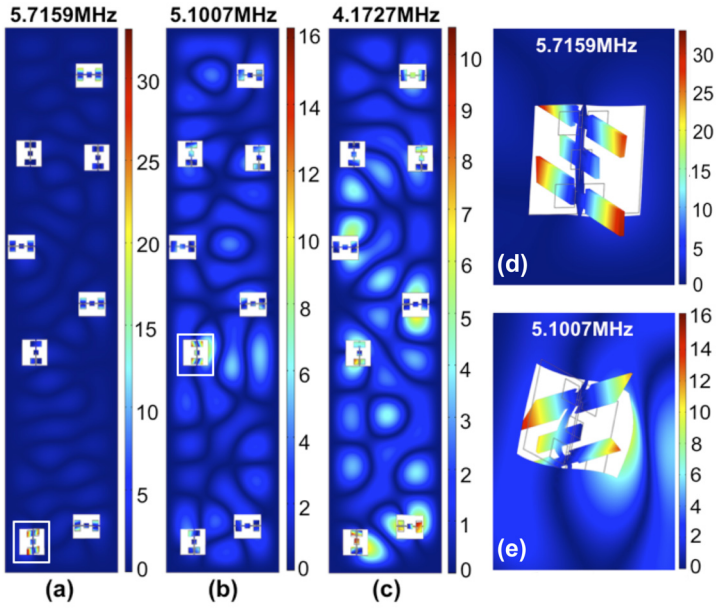

Figure 3.5: ***Finite element simulations of the silicon nitride membrane with embedded nanomechanical resonators.*** ***(a)*** *torsional mode frequency of the device indicated;* ***(b)***, ***(c)*** *frequencies showing the onset of membrane modes;* ***(d)*** *detail of a triple paddle torsional mode decoupled from the membrane highlighted in (a); and* ***(e)*** *detail of hybridized membrane-torsional modes highlighted in (b). The colour bars indicate the relative amplitude in the vertical (z) direction.*

3.6 Magnetic Hysteresis of ∼350 Magnetic Nanoparticles

The magnetic torque driving the torsional modes originates from the comparatively well-defined nanoparticle clusters that were chosen to occupy the central paddles. A field-swept hysteresis measurement performed using one of these modes will correspond to the magnetic hysteresis of the cluster in question. A demonstration is shown in Fig. 3.6. Figure 3.6a shows a higher magnification SEM image of the central paddle from the lower left corner of the membrane.

Figure 3.6b is the corresponding hysteresis measurement. The hysteresis data are obtained from the interferometric AC signal amplitude at the torsional frequency (1.7447 MHz) of the selected resonator.

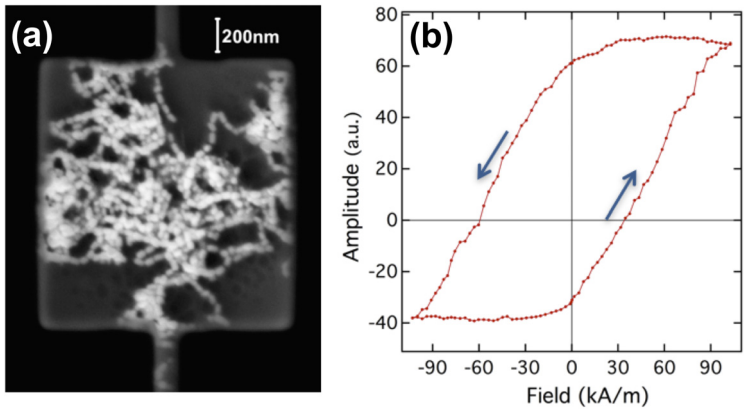

Figure 3.6: ***Magnetic hysteresis of magnetic nanoparticles.*** ***(a)*** *Higher magnification SEM image of the central paddle, showing the deposit of ∼350 nanoparticles. Chains of particles are clearly visible within the aggregate.* ***(b)*** *Experimental data obtained for the magnetic hysteresis at room temperature. Vertical (z) displacement amplitude is proportional to y-mechanical torque and to x-net magnetization. The measurement, starting from the high positive end of the field, yields a minor hysteresis loop.*

The hysteresis in this case is clearly a minor loop, and the aggregate is not being driven to saturation within the available applied DC field range. The loop has been corrected for the electrical crosstalk contribution seen in Fig. 3.2. The vertical and horizontal offsets are on account of this being a minor hysteresis loop. The SEM image can be used to make a mask for entering the same pattern of nanoparticles into a micromagnetic simulation. The resultant simulated hysteresis obtained with $\mathrm{MuMAX_3}$ GPU (graphical processing unit) code is shown in Fig. 3.7. An exchange constant $A_{\mathrm{ex}} = 1.3310^{-11} J/m$, saturation magnetization $M_{\mathrm{s}} = 480$ kA/m, and cell size of 6 nm were chosen for the micromagnetic simulations. Irregular steps appear in the simulated loop (at similar places in both field-sweep directions), from collective reorientation of sub-clusters of particles. The largest jump the experimental magnetic hysteresis in Fig. 3.6b has an amplitude of 8.25 mV while the largest jump in simulations

in Fig. 3.7 corresponds to 0.204 change in M_x. The nanoparticle sub-clusters reorientation for 8.25 mV amplitude signal corresponds to 55.68kA/m by normalizing the amplitude signal with the saturation magnetization (480kA/m) of magnetite. While (0.204×480kA/m $= 97.92$kA/m) is the change in magnetization from simulations. This difference in magnetization values of the jumps and the inability to differentiate from the experimental noise is the limitation of this method of measurement.

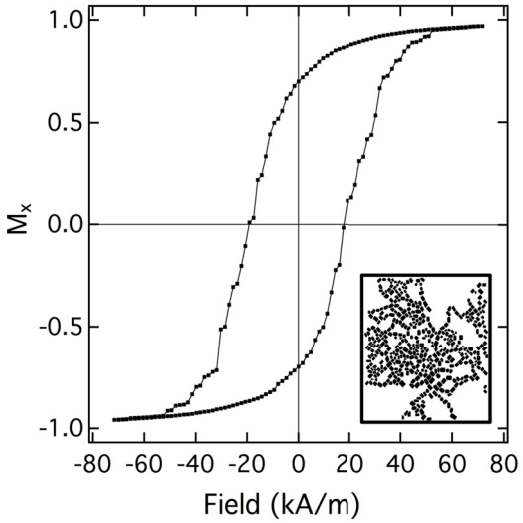

Figure 3.7: ***Micromagnetic simulation of magnetic hysteresis,*** *for a two-dimensional cluster of particles mapped in a pattern created by the SEM image of Fig. 3.6a (inset). M_x is the normalized x-component of magnetization.*

3.7 Conclusion

In summary, silicon nitride membrane-based magnetometry of selected aggregates of nanoparticles is demonstrated using magnetite harvested from bacteria. In-membrane patterned torsional resonators and localized membrane modes each show promise for magnetometry of aggregates on different length scales. The approach presented here scales naturally to both smaller and larger aggregates. The torsional resonator within-a-membrane could be extended, in principle, to magnetic studies of individual nanoparticles through the deposition

of more dilute, non-aggregating suspensions and the milling of more compliant torsional resonators. The study of smaller numbers of nanoparticles will benefit from torque sensors with greater sensitivity than the silicon nitride membrane resonators used here. Good candidates include those fabricated from silicon-on-insulator using electron beam lithography and etching, which are also suitable for patterned deposition of nanoparticles [187]. Studying the control of dipolar interactions through self-assembled aggregation will be of great interest. The dipolar interactions increase the blocking temperature of nanoparticle assemblies over those of isolated particles. The study of individual, small aggregates of particles can lend insight on dipolar ferromagnetism [188] and its potential applications in biomedical, information storage, and environmental monitoring applications [189, 190].

Irregularities in the experimental minor hysteresis curve could also be due to random clusters reorientation, but it is not definitive because it cannot be distinguished from experimental uncertainty at the present time. The device and technique presented in this Chapter does not have enough resolution to explain the irregularities in the experimental minor hysteresis curve (in order to distinguish random clusters reorientation from noise in the data). This technique was also unable to measure the magnetic signal of [Ni,Fe]O star shaped nanoparticles (6 nm in size) and cube shaped nanoparticles (9 nm in size) listed in Appendix D.2.1, because of the low magnetic moment sensitivity ($7 \times 10^8 \mu_B$) of the device under vacuum conditions. This leads one to develop more sensitive techniques in order to measure the magnetic properties of sub-clusters of nanoparticles with high certainty or to measure nanoparticles with small size. Chapter 4 describes the efforts to improve the device sensitivity, to reduce experimental noise in the data, and to integrate small sized nanoparticles onto the devices.

Chapter 4

Nanomechanical Torque Magnetometry of Self-Assembled Magnetic Nanoparticles in Geometrical Shapes

4.1 Motivation

The measurement of the magnetic properties of a small-scale assembly of nanoparticles has been a challenge. The magnetic properties of $\sim$ 350 magnetite nanoparticles by nanomechanical torque magnetometry, assembled by a Nano eNabler, was presented in Chapter 3. However, information was lost due to the random assembly of the nanoparticles on the device, and the magnetic properties average out along any given axis. A geometrical order to the magnetic nanoparticle patterning is desirable to rule out the random averaging, and to get a better insight into the magnetic properties. The nanopar-

ticles used in Chapter 3 were stable single domain nanoparticles (55 nm in size) having a larger magnetic moment. It would be interesting to fabricate devices with higher sensitivity that can also measure magnetic nanoparticles with lower magnetic moment and smaller size. For that purpose, superparamagnetic magnetic nanoparticles (magnetite, 20 nm in size) were selected for device characterization. This Chapter will discuss the procedures for assembling these superparamagnetic magnetic nanoparticles into geometrical shapes, and the properties of the assemblies.

4.2 Introduction

Magnetic nanoparticles are used in biomedicine both as contrast agents and to help cure diseases (e.g., cancer using magnetic hyperthermia) [76], and in the oil and gas industry both as contrast agents and for enhanced oil recovery [86]. Nanoparticles have to be compatible with the environment in which they are used, for example they should be biocompatible, nontoxic, have low protein absorption and have integrative capability for therapeutic and diagnostic techniques for nanomedicine applications to reduce any side effects. Superparamagnetic (SPM) iron oxide nanoparticles are one of the best candidates for their functionalization capability, biocompatibility and theragnostic potential.

Superparamagnetism appears in small ferromagnetic (e.g., iron) and ferrimagnetic (e.g., magnetite) nanoparticles when the magnetization flips randomly under the influence of temperature. In the superparamagnetic state, coericivity and remanence approaches zero (hysteresis loop closed) and the susceptibility is much larger than for a paramagnet. In the stable single domain (SSD) state, nanoparticles retain high coericivity and remanence (hysteresis loop open) over geological timescales and have enormous magnetic memory capability. There is a competition between the magnetic energy and the thermal energy of the particle. When the particle size is very small (SPM) the thermal

energy overcomes the magnetic energy. This theory was proposed by Louis Néel in 1949, and explains the time dependent magnetic viscosity [191, 192]. He considered the relaxation time of magnetization reversal dependent on the attempt time ($\sim 10^{-10}$ s) and the Boltzman probability such that:

$$\tau_{\mathrm{N}} = \tau_0 \exp\left(\frac{\Delta E}{k_{\mathrm{B}} T}\right) \tag{4.1}$$

where ΔE is the anisotropic energy barrier of the small nanoparticle, k_B is the Boltzmann constant, T the temperature, and τ_0 is attempt time dependent on the material. Due to the easy axis and magnetic shape anisotropy, an elliptical particle will have two energy minmia for which there is a good probability for magnetization stability and reversal. The mean time between two spin flips in the energy minimum area of the probability density is known as the Néel relaxation time expressed by τ_{N}. Depending on the size and shape of nanoparticle, the Néel relaxation time can vary between nanoseconds for superparamagnetic (SPM) nanoparticles and millions of years for stable single domain (SSD) nanoparticles.

However, the observation of Néel relaxation time is dependent on the blocking temperature which, in fact, is reliant on the measurement time, τ_{m}. The number of spin flips is dependent on the measurement time. For $\tau_{\mathrm{m}} > \tau_{\mathrm{N}}$, there will be magnetization reversal or spin flips several times, and the particles are identified in the superparamagnetic state. For $\tau_{\mathrm{m}} < \tau_{\mathrm{N}}$, magnetization does not flip, and the particles are considered in the blocked state. Thus, the state of being blocked or superparamagnetic is dependent on the measurement time. The transition between blocked and superparamagnetic state is observed, at $\tau_{\mathrm{m}} = \tau_{\mathrm{N}}$, or, by changing the thermal energy of the particles. The temperature at which the condition $\tau_{\mathrm{m}} = \tau_{\mathrm{N}}$ becomes true is known as the blocking temperature τ_{B} [102, 193, 194], however, blocking is not considered a phase transition rather it is a continuous transformation of τ_{N}. The superparamagnetic state is the frequent spin-flip state that occurs in small ferromagnetic or ferrimagnetic

single domain nanoparticles. This is also seen as the macro spins in collective approximation of nanoparticle assemblies [195].

Magnetic fields generate heat in magnetic materials (known as magnetic hyperthermia) by these independent mechanisms: Néel relaxation, Brownian relaxation, hysteresis loss and eddy currents. Eddy currents are only considerable for materials at a centimeter scale or larger, so are irrelevant for magnetic nanoparticles. Hysteresis loss would be significant when the nanoparticles are in the stable single domain (SSD) state. For small nanoparticles in the superparamagnetic (SPM) state, the heat is generated by a delay in the Néel relaxation (rotation of moments within the nanoparticles) or Brownian relaxation (rotation of the nanoparticles themselves). The magnetic field reversal time needs to be shorter than the magnetic relaxation (Néel and/or Brownian) for the heat dissipation mechanism to occur [76, 93, 196].

Hyperthermia can be achieved by radio frequency (RF), microwaves, and laser wavelengths. Magnetic hyperthermia in nanoparticles is exceptional because of its non-invasive way of heating, producing high contrast in MRI (i.e., combined diagnostic and therapeutic approaches), flexible functionalization capability, and high biocompatibility [197]. The generated heat by energy dissipation can elevate the body temperature to above $40-50°\mathrm{C}$, enough to destroy cancer cells (or tumours)[87, 197].

Since heat generating mechanisms in SSD and SPM are different, each have particular advantages and disadvantages. The ferromagnetic (FM) nanoparticles having hysteresis properties produce heat when a time varying magnetic field is applied. The power loss, in this case, is given by the hysteresis loop area and frequency (f) of the applied field (H):

$$P^{\mathrm{FM}} = \mu_0 . f \oint H \, dM \tag{4.2}$$

This equation ignores eddy current heating (since the nanoparticles are small), and ferromagnetic resonance (because frequencies are usually far below those

for ferromagnetic resonance to occur). When the FM nanoparticles are in the SSD state or blocked state, the power loss becomes independent of frequency, and can be obtained directly from the quasi-static hysteresis loop area [76].

However, when the nanoparticles are in the SPM state, heat is generated by Néel relaxation. For immobilized nanoparticles (as in the case of my devices), the Brownian motion does not take part and heat dissipation comes only from Néel relaxation. The power loss in this case, for non-interacting nanoparticles, is given by [93, 198]:

$$P = \frac{1}{2}\omega\mu_0\chi_0 H^2 \frac{\omega\tau}{1+\omega^2\tau^2} \tag{4.3}$$

where $\omega = 2\pi f$, and $\tau = \tau_{\mathrm{N}}$. When $\omega\tau \ll 1$, relaxation is fast and can occur within magnetic field oscillation. The above equation reduces, in this case, to:

$$P_{\omega\tau\ll 1} = \frac{1}{2}\omega^2\tau\mu_0\chi_0 H^2 \tag{4.4}$$

For $\omega\tau \gg 1$, the relaxation timescales are longer than the magnetic field oscillation, i.e., the magnetic field oscillates too fast than the relaxation can occur. The magnetic material is in blocked state under the blocking temperature in this case. Eq. 4.3 becomes independent of frequency in this case:

$$P_{\omega\tau\gg 1} = \frac{1}{2\tau}\mu_0\chi_0 H^2 \tag{4.5}$$

At critical frequency $\omega\tau = 1$ the power loss is maximum, when the relaxation time is equal to the magnetic field oscillation period. Eq. 4.3 becomes:

$$P_{\omega\tau=1} = \frac{1}{4}\omega\mu_0\chi_0 H^2 \tag{4.6}$$

The specific absorption rate (SAR) is related to power loss by the following

equation [87]:

$$P = (SAR) \cdot \rho \cdot \phi = (SAR) \cdot w \tag{4.7}$$

where ρ is the density, ϕ is the volume fraction, and w is the mass of nanoparticles per unit volume. The power loss can be maximized for more heat generation, by using higher frequency and field combinations, and by tuning the magnetic susceptibility of SPM nanoparticles. The non-interacting small size SPM nanoparticles, which were used in this Chapter, have higher susceptibilities. The nanoparticle surface coating weakens the dipole coupling and controls the interparticle distance. The above equations will be used to calculate power loss for nanoparticles deposited on nanomechanical devices.

4.3 Self-Assembly of Nanoparticles on Nanomechanical Devices

There are top-down and bottom-up approaches for building nanostructures in an orderly manner. Usually, the top-down and bottom-up designs are used separately to accomplish certain processes. There have been great efforts toward organizing nanostructures on silicon surface [199] but I demonstrate the patterning of nanoparticles on magnetometer devices for the first time. Here I use both processes, top-down and bottom-up, to achieve the required patterning of nanoparticles on the silicon-on-insulator (SOI) devices. The top-down processing used in this chapter includes making the devices and controlling the shape of the nanostructures, while the bottom-up process includes the self-assembly of nanoparticles.

Self-assembly, being the root of the bottom-up nanofabrication approach, allows the nanoparticles to pattern themselves in a geometrical order. It allows the spontaneous organization of the nanoparticles. The self-assembly can be

direct or indirect, free or assisted, depending upon the process involved. It includes template-assisted direct self-assembly, template-free direct self-assembly (molecular interactions), externally directed self-assembly (electric and magnetic field, flow fields), self-assembly at liquid interfaces, self-assembly by dewetting, and nano-imprinting.

The SOI devices have advantages of high sensitivity and good resonance modes, along with the elimination of membrane modes as in the case of devices made in a silicon nitride membrane. A standard procedure has been used to make these devices as described in [187]. Two kinds of nanoparticle assembly, detailed in sections below, are achieved by using the positive and negative resists, hydrogen silsesquioxane (HSQ) and $\alpha-$methylstyrene (ZEP) respectively, in device making (see details in Appendices C and D).

4.3.1 Self-Assembly Approach

Self-assembly at a liquid interface was chosen in order to get a single layer of nanoparticles on the device surface. Multiple self-assembled layers of nanoparticles can also be achieved by increasing the concentration of the prepared nanoparticle solution. A general procedure used here involved a deionized water droplet first on top of the devices on the chip, and then magnetic nanoparticles were dropped on top of the water droplet. A schematic diagram of the process is displayed in Fig. 4.1.

Nanomechanical torsional resonators were first fabricated, following the recipe in [187] on the SOI chip by using the negative resist hydrogen silsesquioxane (HSQ) in the NanoFab. The negative resist helps etching away all the top silicon layer (300nm thick) except the devices shown in Fig. 4.1.

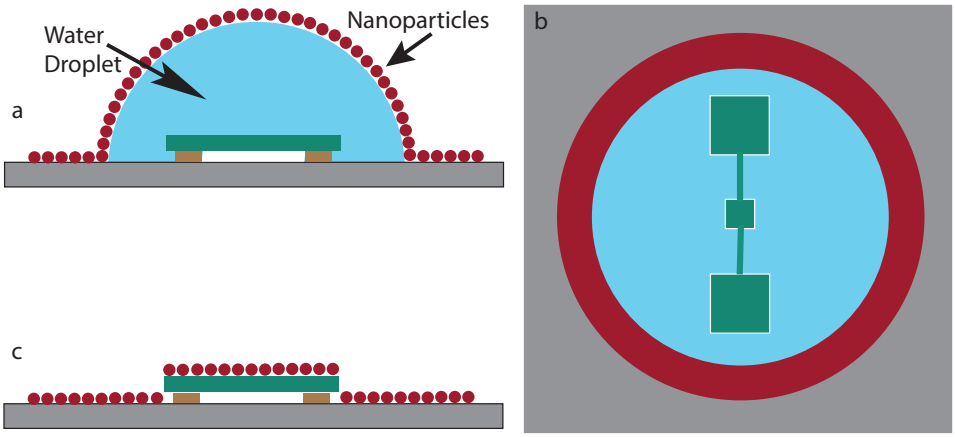

Figure 4.1: ***Schematic of self-assembly of nanoparticles. (Not to scale.)*** ***a,*** *side view of schematic of nanoparticle deposition. Grey colour represents the base silicon (700μm thick), brown colour is the silicon oxide layer (1μm thick), and green colour is the top silicon layer used as the device layer (300nm thick). Water is displayed in blue while the nanoparticles are represented in red.* ***b,*** *top view of the schematic. The nanoparticle droplet covers the water droplet and the devices.* ***c,*** *side view of the device after the drying procedure.*

The magnetic nanoparticles and water droplet were deposited on the ready made devices. A side view of the schematic is shown in Fig. 4.1a. The details of the nanofabrication of these devices is detailed in the Appendix C. The top view of schematic, shown in Fig. 4.1b, displays the nanoparticle layer on top of the water droplet on top of the devices. As the water evaporates slowly, the nanoparticles settle down on the device surface, shown in Fig. 4.1c.

Iron oxide magnetic nanoparticles are used for the experiments presented in this Chapter. The magnetic nanoparticle solution (Fe_3O_4 suspension from Sigma-Aldrich, 20 nm in size, 5mg/ml concentration, and 0.865 g/mL density) was diluted to a 1:50 ratio in toluene solvent and mixed using a vortex mixer (VWR VM-3000 mini vortexer) for 1 minute to produce a homogenous solution. The nanoparticles droplet volume of 0.05 μL was used on top of water. The nanoparticles were coated with oleic acid for a number of reasons including: biomedical compatibility, reduced agglomeration, surface charge control, and controlled dipole coupling.

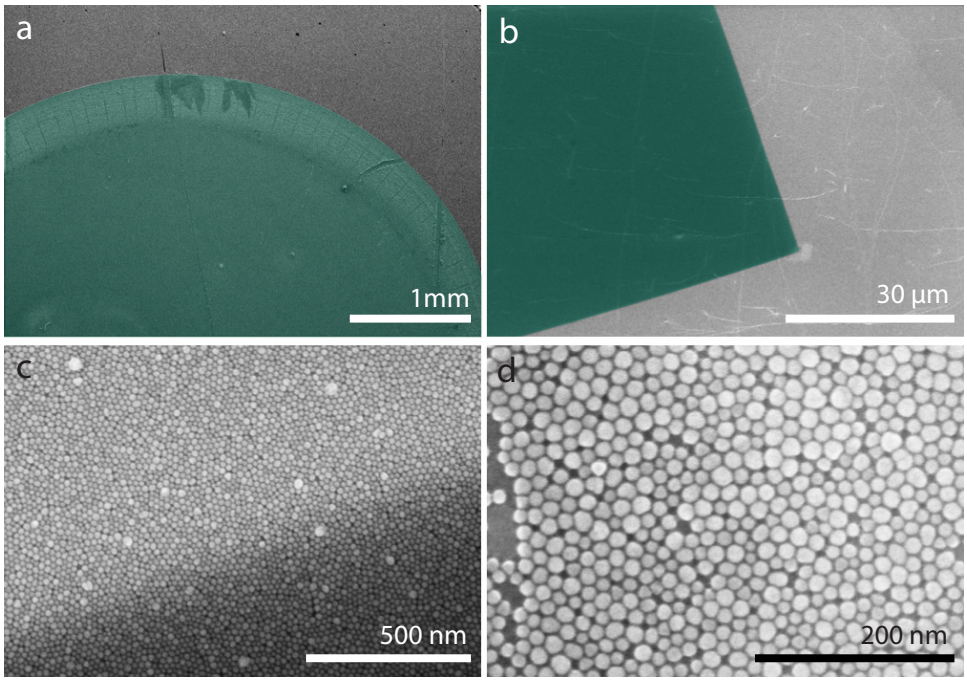

Figure 4.2: ***SEM images of self-assembly of nanoparticles on a silicon nitride surface. a,*** *green colour (false colour) represents the nanoparticle deposition on the silicon surface.* ***b,*** *nanoparticle self-assembly on a large scale, green colour (false colour) shows the silicon nitride window* ***c,*** *edge of the silicon nitride window with the nanoparticle assembly* ***d,*** *close packed nanoparticle distribution in the self-assembly.*

The nanoparticle deposition technique was tested on the silicon surface (see Fig. 4.2a) and the silicon nitride surface (see Fig. 4.2b) before deposition on actual SOI magnetometer devices. The green colour specifies the nanoparticle deposition area in Fig. 4.2a and silicon nitride membrane area in Fig. 4.2b while nanoparticle assembly covers the whole area in Fig. 4.2b. The silicon nitride membrane edge is clear in the contrast in Fig. 4.2c, while one can also see the nanoparticles in a close packed distribution. A zoomed-in image of the close packed distribution is shown in Fig. 4.2d.

4.3.2 Self-Assembling Nanoparticles on SOI Devices

The magnetic nanoparticles were deposited on the SOI fabricated devices by using the scheme shown in Fig. 4.1. A set of the devices with nanoparticles deposited is shown in Fig. 4.3. A set of pads of different sizes (larger than the paddles of the devices) were made beside the alignment marks for confirmation of the released devices. A couple of pads were etched away, while one of those was still there beside the alignment mark giving the real time etching rate of the silicon oxide layer.

The evaporation of water during the drying procedure in the nanoparticle deposition causes the nanoparticle film to bend and fold locally as seen in Fig. 4.2b and Fig. 4.3a. The devices A1−A4, in Fig. 4.3a, were underlying the bending fold of nanoparticles. The devices clear from the bending region were used in the magnetometry measurements. A leftover resist is seen on top of the C1 device that got stuck during the critical point drying procedure, in Fig. 4.3a.

Another phenomenon observed, besides the bending of nanoparticle film, was the anchoring of nanoparticles across the corners of the device. A schematic is shown in Fig. 4.3b. A more prominent anchoring of nanoparticles at the corner is shown in Fig. 4.5a from the experimental results. The nanoparticle film breaks at the edges of the device and torsional rod, and falls down on the base silicon, leaving behind the curvature around the corner resulting in anchoring. The formation of this anchoring gives information about the tensile strength and crystallinity of the nanoparticle film. The hexagonal close packed structure helps the formation of anchoring regions. The devices in the A, B and C series were compared for the respective measurements in the sections below.

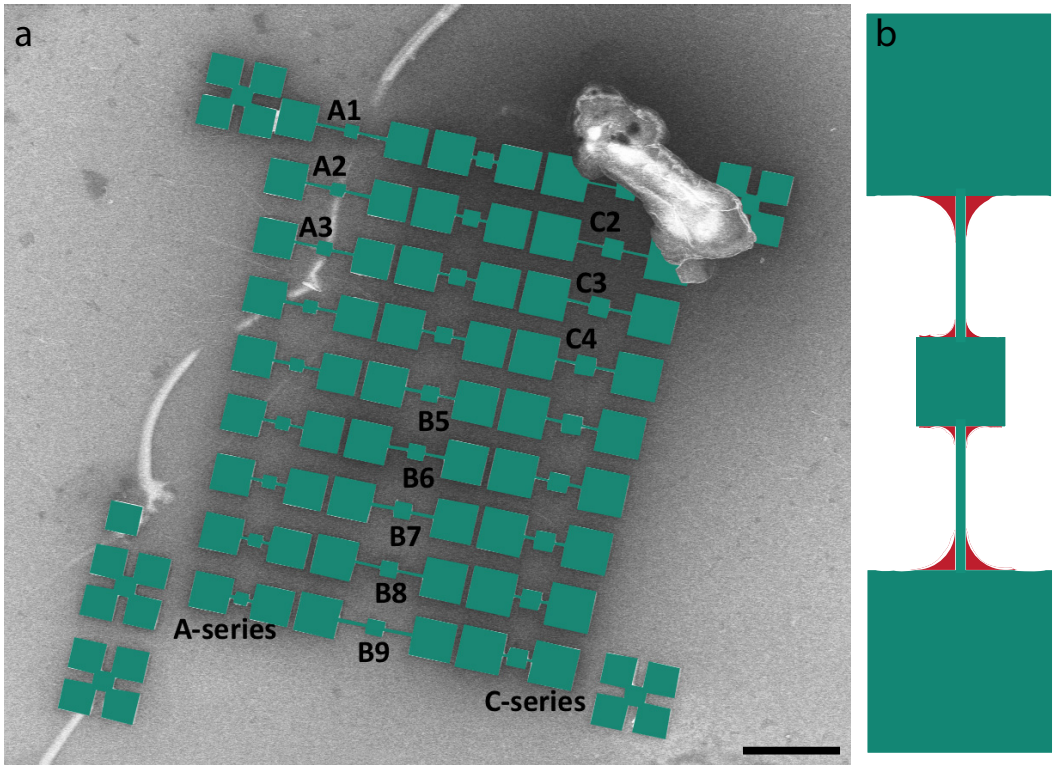

Figure 4.3: ***False colour SEM image of self-assembly of nanoparticles on SOI fabricated devices. a,*** *Three rows of devices are named as A, B and C series with numbers* $1-9$*. Green colour shows the suspended silicon devices with a silicon oxide layer on top of the silicon base (grey colour). The alignment marks are the edges of the devices and are also suspended and shown in green colour. A single pad beside the alignment mark is made . The scale bar is* $10\mu m$ ***b,*** *schematic of the anchoring of nanoparticles at the corners of the device. The green colour is the device and red colour indicates the anchored nanoparticles.*

4.3.3 Cleaning the Anchored Nanoparticles at the Edges of the Devices

The anchored regions affect the clamping points of the torsional rod, and hence the dissipation mechanism, affecting the nanomechanical torque amplitude and the quality factor of the device. It was then necessary to remove the extra clamping provided by the anchoring of the nanoparticles to reduce the damping. It was achieved by cleaning with a focused ion beam (FIB). A high energy gallium ion (Ga+) beam was used to clear the extra nanoparticles attached at

the corners of the device.

The clamped and anchored devices are shown in Fig. 4.4a. The first device in this series (named B9) was cleaned using FIB as shown in Fig. 4.4b. The torsional rods were rastered with a low dose beam while the edges of device paddle and support paddles were cleaned with a high dose to clear up the deposition.

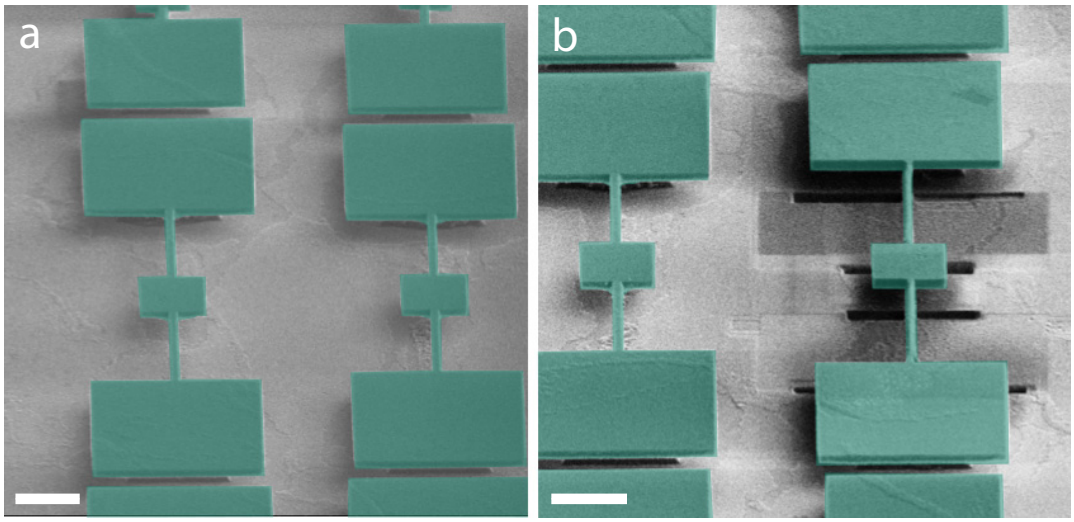

Figure 4.4: ***Clamping at the corners of the device (B9). a,*** *false colour SEM image of the unclean devices* ***b,*** *false colour SEM image of the clean device (B9) with a* 180° *rotation of the scanning image. All scale bars are* $3\mu m$*.*

The details of the cleaning procedure are shown in Fig. 4.5. In the first step, shown in Fig. 4.5b, the torsional rod is cleaned with a beam dose that just rasters the surface and cleans the rods. In the next step, the torsional paddle and the support paddle edges facing the anchoring were cleaned with a high dose to cut through the paddles, as shown in Fig. 4.5c. Figure 4.5d displays the section of the whole cleaned device. The focused ion beam (Ziess Nvision 40) was used in the milling mode (current = 13nA) for cutting the paddle and in the rastering mode (current = 1 pA) for cleaning the torsional rods.

Redeposition of melted material by the FIB underneath the paddle and melting of material on the torsional rod was observed as clearly seen in Fig.

4.5d. This removed the anchoring sections but changed the resonator shape a bit. Both of these contributed to the frequency shift of the device as seen in Fig. 4.7.

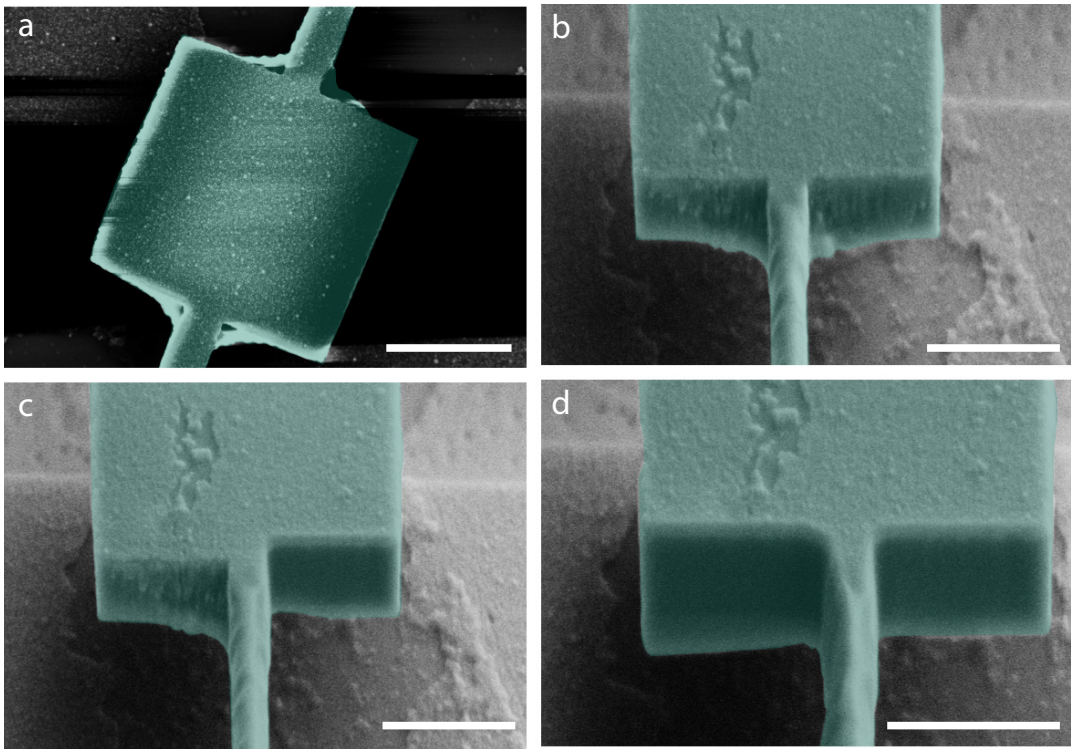

Figure 4.5: ***Cleaning steps of the device (B9) using a FIB. a,*** *Anchored unclean device* ***b,*** *side view of partially cleaned device. The torsional rod is cleaned in this step.* ***c,*** *cleaning one edge by cutting the paddle by 100 nm.* ***d,*** *cleaned device from both sides. All scale bars are* $1.2\mu m$.

It was then necessary to find out the nanoparticle deposition on the backside of the device. For this purpose, one of the devices (B5) was sacrificed to cut from one side of the torsional rod and flip over to see the bottom side of the device, as shown in Fig. 4.6. Figure 4.6a shows the B5 device cut and flipped over. A zoomed-in image of the cut device is shown in Fig. 4.6b. One can see small portions (encircled with white colour) of the nanoparticle deposition that came on the bottom side when the nanoparticle film broke and rested itself on the paddle. The rest of the contrast is the oxide layer remnants on the bottom side of the paddle.

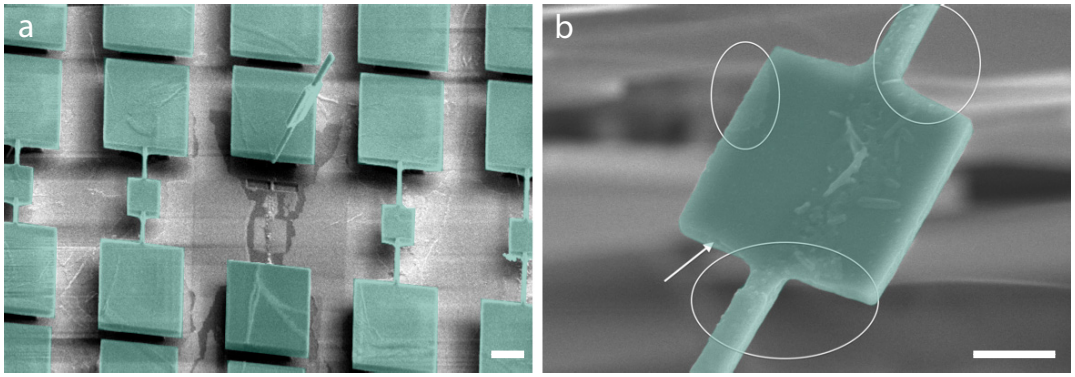

Figure 4.6: ***Device (B5) cut to see the nanoparticles on the bottom side.*** ***a,*** *false colour SEM image of the cut device. The scale bar is* $2.5\mu m$. ***b,*** *false colour SEM image of the cut device on the bottom side. The white arrow indicates the oxide layer sandwich surface on the bottom side. The scale bar is* $1.2\mu m$.

It is clear from Fig. 4.6 that nanoparticles were deposited on the top side of the resonator, so that the magnetic properties were coming only from the single layer square shape self-assembly of nanoparticles. There were 14400 nanoparticles counted on the top of paddle, on average. The resultant magnetic properties were the sum of all nanoparticles on the paddle.

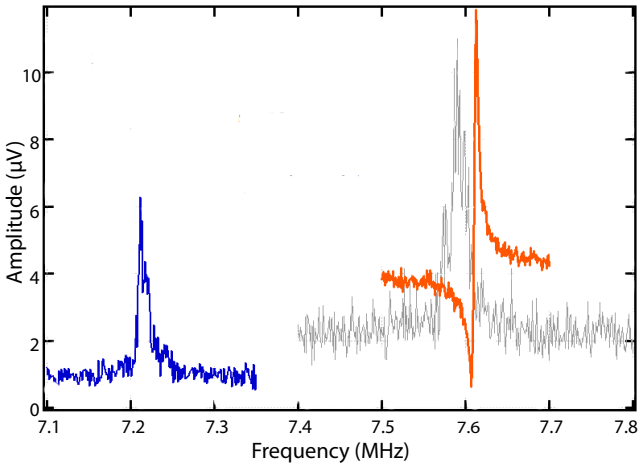

Figure 4.7: ***Resonance peaks of the B9 device.*** *Grey colour shows the thermomechanical peak for the untrimmed device at room temperature. Blue colour is the thermomechanical peak for the trimmed device at room temperature. Orange colour represents the driven peak of the untrimmed device at 50 mV at 18.25K.*

The cleaning and cutting of the resonator affects the mechanical properties

of the device. The mechanical properties of the device, in fact, translates the magnetic properties since later on the magnetic signal was converted into the mechanical signal. Figure 4.6 shows the shift in frequency of the trimmed and untrimmed device.

The quality factor of the flexural mode for the device (B9) changes from 18 to 36 of thermomechanical peak at room temperature, with a shift of resonance frequency from 7.59 MHz to 7.22MHz as shown in Fig. 4.7. It can be seen from Fig. 4.7 that it is difficult to drive the untrimmed device to higher amplitude because of the anchoring at corners.

4.3.4 Resonance Modes of the Devices

The magnetic torque acted upon the magnetic nanoparticles by the external magnetic fields and the magnetic moment was converted to the mechanical torque, such that the magnetic torque was read at the mechanical resonance of the device. The transduced mechanical torque was then optically detected by the interferrometric method as described in Chapter 2. The resonance modes of the devices in B-series are shown in Fig. 4.8. These resonance modes were measured before cleaning with the FIB. The devices were comparatively in the high frequency range as compared to the nanomechanical devices in Chapter 3. The length of the torsional rod increased from device B5 to device B9 changing the flexural and torsional resonance modes to the lower frequency. The device B9 was then selected for further magnetic measurements.

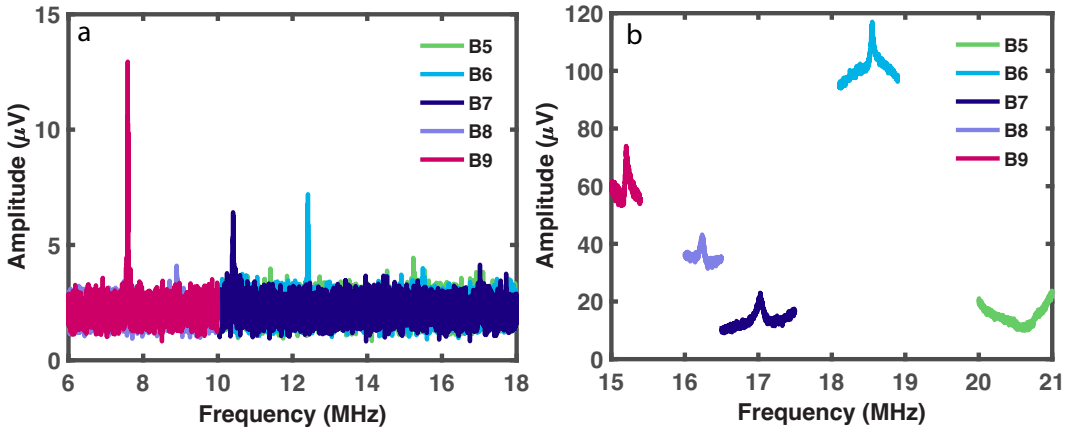

Figure 4.8: ***Resonance peaks of the B-series devices. a,*** *flexural mode of the devices* ***b,*** *torsional mode of the devices.*

4.3.5 Magnetic Hysteresis of Self-Assembled Nanoparticles at Room and Low Temperature

Magnetic torque and hence magnetic susceptibilities are a good measure to characterize the magnetic nanoparticles. By using the magnetic susceptibilities and magnetic hysteresis area, the power loss and hyperthermia output of magnetic nanoparticles can be calculated. Magnetic hysteresis of magnetite nanoparticles were obtained at room temperature and at low temperature. Figure 4.9a shows the hysteresis curve of superparamagnetic nanoparticles at room temperature. It can be clearly seen that nanoparticles are superparamagnetic since the hysteresis loop is closed. The low field zoomed-in area is shown in Fig. 4.9b. A change in the slope of the hysteresis curve at 1 kA/m and at -1 kA/m is observed that is due to a different nanoparticle size distribution. The nanoparticles 20 nm in size exhibit lower susceptibility compared to the smaller nanoparticles, such that higher susceptibility is observed between 1 kA/m and -1 kA/m. The particle size variation can be seen in Fig. 4.2d.

The low field susceptibilities were calculated for superparamagnetic nanoparticles measured at room temperature. The susceptibility was found

to be 203.956 in the $0-1$ kA/m applied field range (see Fig. 4.9b), and 30.440 in the $1-5$ kA/m field range, and 9.694 in the $7-20$ kA/m field range. These different susceptibilities at low field is the confirmation of polydispersity in nanoparticles sizes. The normalized magnetization contribution of various sized nanoparticles can be calculated from Fig. 4.9a and b. The intersection of slopes occurs at 0.56 and 0.222, which shows that 44% are of large size ($20nm, \chi_0 = 9.694$), 33.8% of intermediate size (less than 20 nm, $\chi_0 = 30.440$), and 22.2% of small size (much less than 20 nm, $\chi_0 = 203.956$).

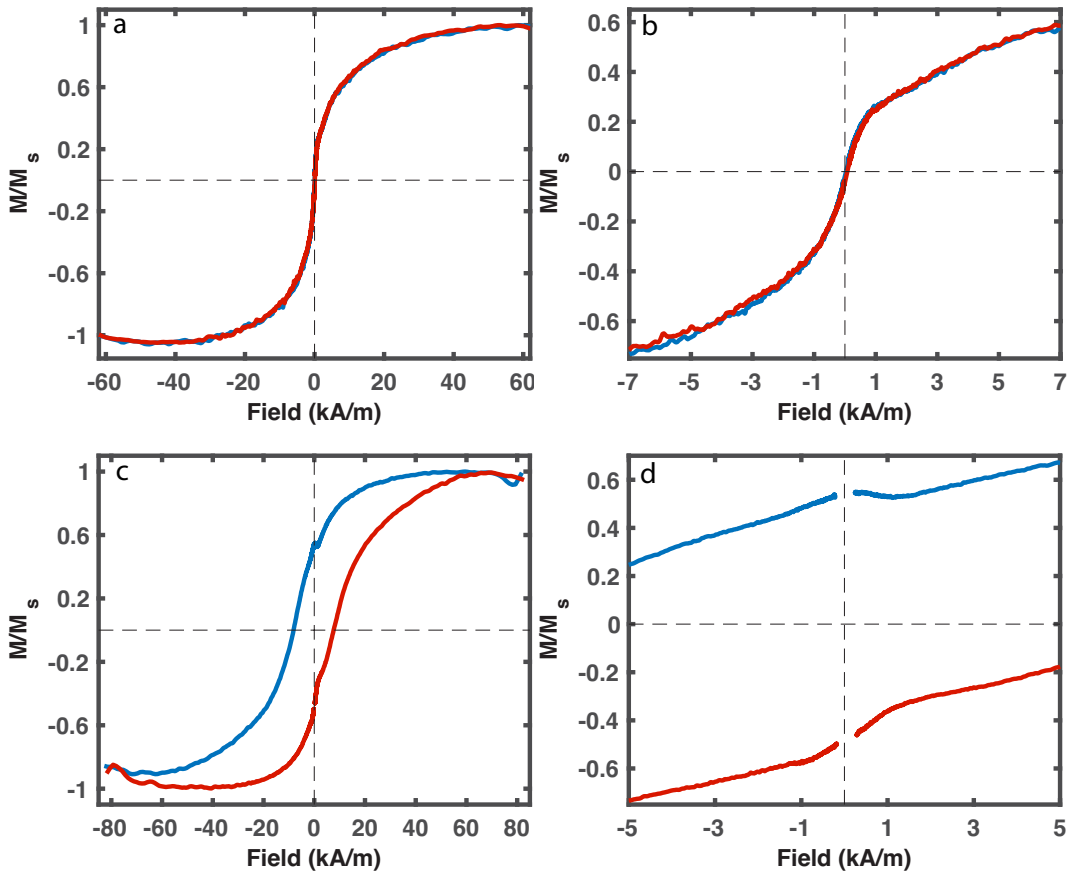

Figure 4.9: ***Magnetic hysteresis of superparamagnetic nanoparticles.*** *The normalized torque is plotted versus H_x^{DC} field linear sweeps in all graphs.* ***a,*** *Hysteresis at room temperature* ***b,*** *zoomed-in area at low field of hysteresis at room temperature* ***c,*** *Hysteresis at low temperature (14 K)* ***d,*** *zoomed-in area at low field of hysteresis at low temperature (14 K). Blue colour represents the high to low field sweep, while red colour is the low to high field sweep.*

For $\tau_0 = 10^{-10}$s, and particles in the 20 nm size range, τ was found to be 10^{-7}s, which gives $\omega\tau \approx 1$. For $\omega = 2\pi f = 2\pi \times 15.2MHz = 9.596 \times 10^7$ rad/s, $\chi_0 = 203.956$, and $H = 35A/m$, the calculated power loss using Eq. 4.6 was 1.178×10^{-5}W. The corresponding SAR was 5.015×10^7W/g for the 22.2% volumetric contribution (by using Eq. 4.7). The SAR was 1.145×10^7W/g and 4.748×10^6W/g for χ values of 30.440 and 9.694 with the volumetric contributions of 33.8% and 44% respectively. We can clearly see the higher SAR for nanoparticles with higher susceptibility. The total volumetric contribution to SAR would be 6.635×10^7W/g, which is pretty high (due to frequencies in the MHz range) as compared to a generally lower value to SAR ($\sim 10^3$)W/g for frequencies in the kHz range. Torque magnetometry is good for resolving the relative size distribution of nanoparticles.

The magnetic nanoparticles undergo a transition from the superparamagnetic state to the stable single domain state and the hysteresis loop opens up at low temperature (see Fig. 4.9c). The zoomed-in area of the hysteresis loop in the low field range at low temperature is shown in Fig. 4.9d. The hysteresis loop changes slope between 1 kA/m and -1 kA/m confirming the presence of a range of nanoparticle sizes. The ferrimagnetic transition of smaller nanoparticles is different from the larger size nanoparticles. The remanence value is nearly 0.5 of the saturation magnetization, which can be seen in Fig. 4.9c and d. This shows that the nanoparticles are in a stable single domain (SSD) state at low temperature, and are randomly oriented. The magnetic behaviour of magnetic nanoparticles (given by remanence, coercivity, and susceptibility) is dependent of the dipole interactions between particles. In the low temperature regime, the thermal energy barrier changes and an additional energy barrier is introduced by the dipolar interaction for the reversal of the particle moments. This gives rise to nonzero values of the remanence and coercivity at low temperature. The power loss and SAR in the SSD state in Fig. 4.9c were 2.198 W and 4.406×10^{13}W/g calculated by using Eq. 4.2 and Eq. 4.7. This means

that the hysteresis loss in the blocked state at low temperature is much larger than the Néel relaxation in the SPM state at room temperature. By selecting the appropriate nanoparticle size, the magnetic susceptibility and SAR can be tuned for the desired application. The magnetic susceptibility can be tuned by the particle shape and by the geometrical shape of the nanoparticle assembly, which is described in section 4.4.

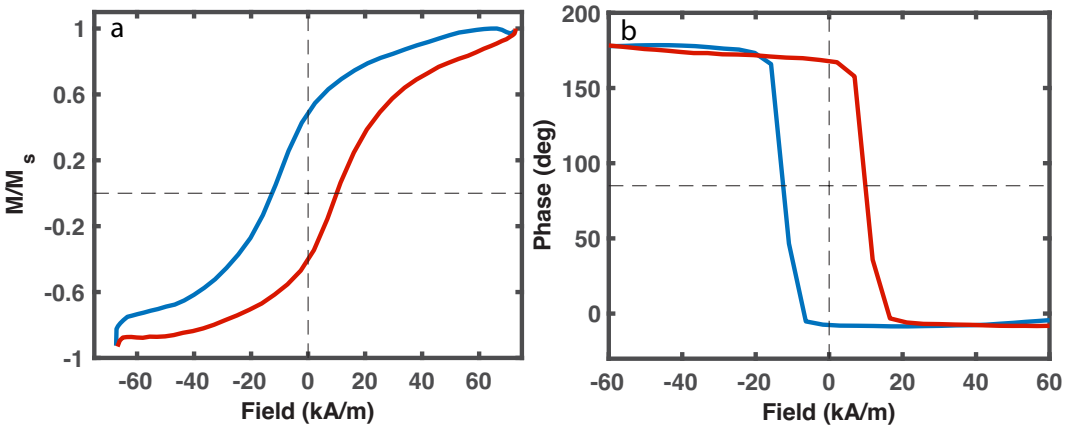

Figure 4.10: ***Magnetic hysteresis with magnetic field rotation at low temperature (14 K). a,*** *Normalized torque amplitude with rotating the DC magnet. The normalized torque is plotted versus H_x^{DC} field rotational sweeps in the graph.* ***b,*** *Phase shift in amplitude versus H_x^{DC} field rotational sweeps.*

The normalized torque for the field rotation at low temperature is shown in Fig. 4.10a. The shape of hysteresis shows that the magnetization is lagging behind the sweeping field because of the apparent shape anisotropy with rotating magnetic field. Figure 4.10b represents the phase behaviour of the measured torque. The sharp transition in phase occurs at the magnetization sign reversals and gives information about coercivity.

The increase in torque amplitude from room temperature to low temperature is seen in Fig. 4.11a. The optical laser power was then adjusted to lower values in order to avoid additional heating from the laser along with the selection of RF output as shown in Fig. 4.11b. The RF amplitude provides a bias field to the system as well as a measure of the RF heating in the system.

The capability of the system to integrate nanoparticles on the device makes it suitable for the "on-chip thermometry" once the magnetic properties of magnetic nanoparticles are calibrated. The ultrasensitive nanoscale calorimeter has been developed to be achievable at low temperature [200], similar possibility of implementation of magnetic nanomechanical devices studied here may be offered for a wide range of temperature using the magnetic hyperthermia.

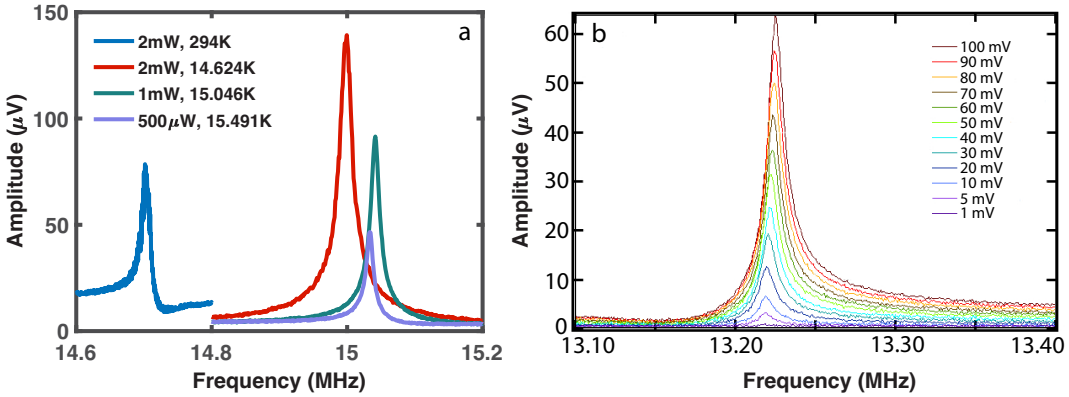

Figure 4.11: ***Optical power at room temperature and at low temperature. a,*** *Torque amplitude at various optical powers and temperatures.* ***b,*** *torque amplitude for various RF outputs.*

The shift in torque amplitude and corresponding frequency with increasing temperature is shown in Fig. 4.12. The possible reason for the frequency shift could be the frosting on the device at low temperature or it may come from the temperature dependence of SOI device strain.

The next step would be to measure the hysteresis at various temperatures during cooling and heating the magnetic nanoparticles. In zero field cooling (ZFC), the saturation field becomes large due to strong anisotropy at low temperatures (SSD), and hysteresis can only be obtained during the heating. However, if the system is cooled in the presence of field (field cooling (FC)), the magnetic moment aligns with the field and saturation is attained at low fields. The hysteresis can be collected during both the cooling and heating in the FC situation.

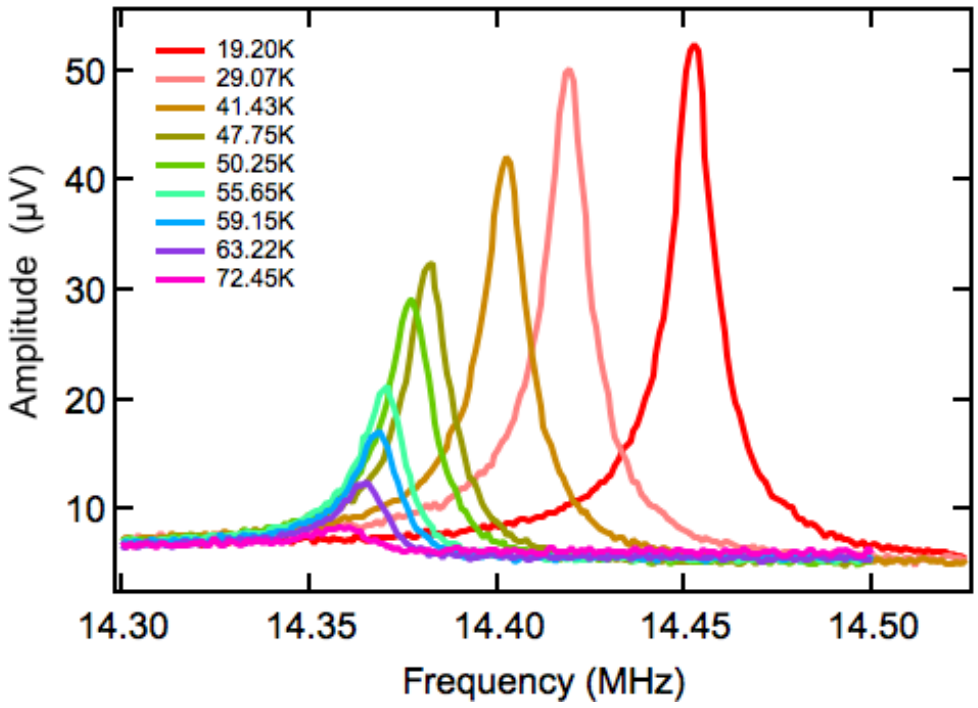

Figure 4.12: ***Torque amplitude and frequency shift at low temperature.***

4.4 Patterning Nanoparticles in Geometrical Shapes on the Devices

For the self-assembled nanoparticles on the device, two types of shape anisotropies can be introduced into the system, first by changing the shape of the individual nanoparticles and secondly by depositing the nanoparticles in a specified shape. In order to control the magnetic susceptibilities, the nanoparticles were deposited in geometrical shapes as shown in Fig. 4.13. It shows the nanoparticle deposition on a silicon surface in a circular shape of different sizes. It can be seen that nanoparticles, in a circular shape, can be deposited up to 200 nm diameter in size with ease.

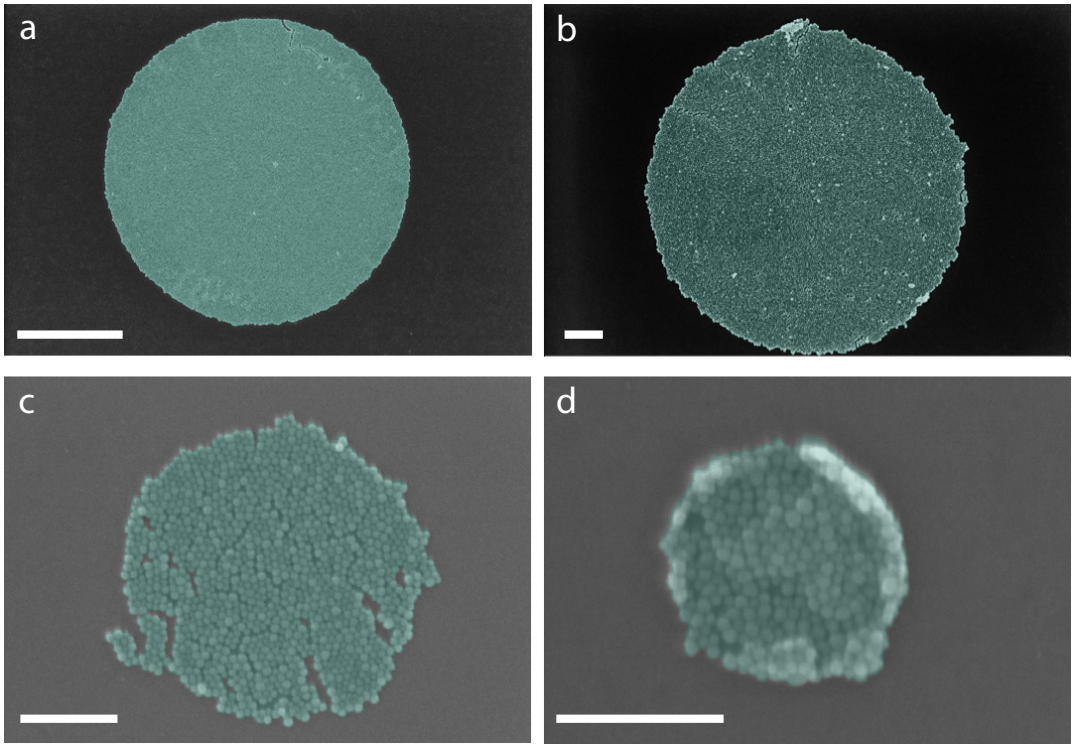

Figure 4.13: ***Nanoparticle circles by mask fabrication.*** *Scale bar for* ***a,*** *is* $2\mu m$*. Scale bar for* ***b, c,*** *and* ***d,*** *is 200 nm.*

4.4.1 Patterning Nanoparticles in Geometrical Shapes on SOI devices

After the successful geometrical deposition on the silicon surface, the magnetic nanoparticles were then deposited on the devices (made with $\alpha-$methylstyrene (ZEP) resist, see Appendix C) in circular shapes shown in Fig. 4.14. The dark circle around the nanoparticles on the devices is due to the backscattering of electrons in the poly methyl methacrylate (PMMA) resist layer during the electron beam lithography (EBL).

The full procedure of nanoparticle deposition was followed in the same way as described in paper the [187] except magnetic nanoparticles were deposited by the method described in the first section of this chapter, in place of the permalloy. The other notable change was that the removal of PMMA was

carried out in acetone instead of heated NMP (N-Methyl-2-Pyrrolidone) in order to avoid the reaction of magnetic nanoparticles with NMP and to avoid the destruction of magnetic properties at high temperature.

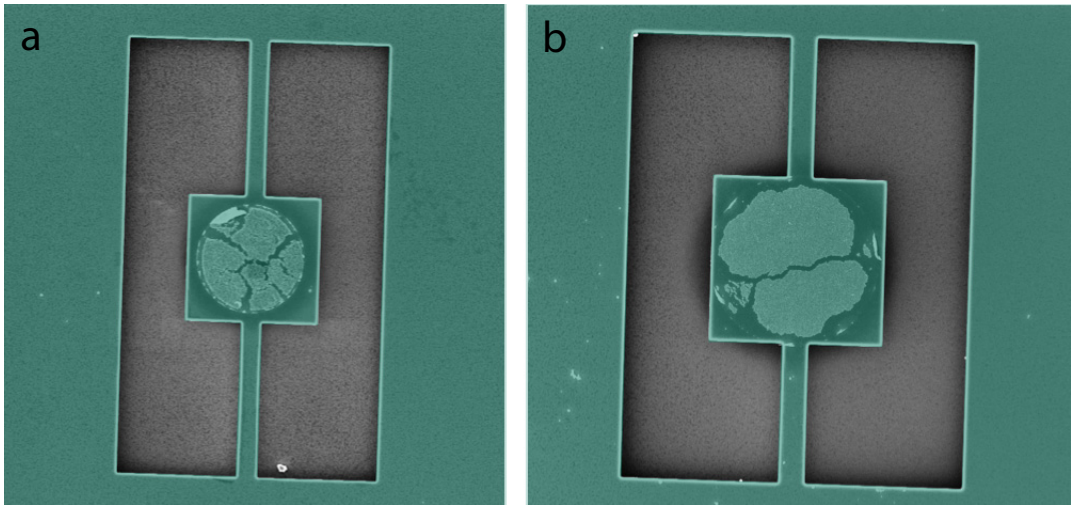

Figure 4.14: ***Nanoparticle circles on SOI by nanofabrication. a,*** *and* ***b,*** *show the different device dimensions. The resonator paddle is 6 μm wide.*

4.4.2 Resonance Modes of Devices

The devices were then measured for the mechanical signal in frequency sweeps of the lock-in amplifier. Fig. 4.15 shows the measured torque amplitude of various devices (named in legends). The flexural modes of the devices were around 2 MHz while the torsional modes were at higher frequency from 4 to 6 MHz. The amplitude in Fig. 4.15a shows that these devices had a much better signal than the device cleaned in the previous section. The resonance modes of an individual device is shown in Fig. 4.15b. The displacement, torque, and magnetic moment sensitivities were $7.5 \times 10^{-14}\mathrm{m}(\mathrm{Hz}^{1/2})^{-1}$, $7.0 \times 10^{-20}\mathrm{Nm}(\mathrm{Hz}^{1/2})^{-1}$, and $5 \times 10^{7}\mu_{\mathrm{B}}$ respectively, for the device shown in Fig. 4.15b.

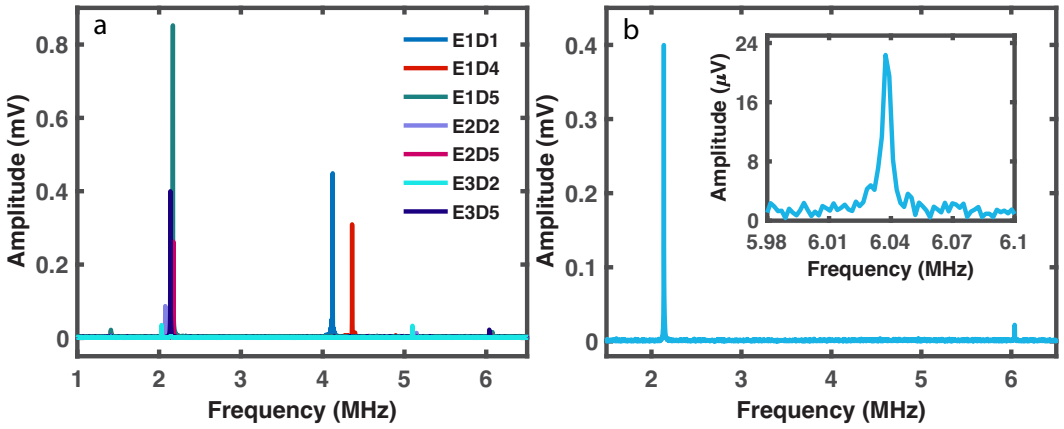

Figure 4.15: ***Resonance spectra of nanoparticle circles on SOI devices. a,*** *torque amplitude of varous devices with nanoparticles.* ***b,*** *resonance spectrum of an individual device. Inset shows the Lorentzian shape of the resonance curve.*

4.5 Conclusion

In summary, the nanoparticle deposition in geometrical shapes on top of nanomechanical devices has been presented. The processes involved standard Si-based nanofabrication and liquid interface nanoparticle deposition. Various geometrical shapes of small-size nanoparticle deposition have been demonstrated, i.e., square, rectangular, and circular (see also a linear shape in Appendix D). The magnetic hysteresis of deposited nanoparticles has also been demonstrated. The higher power loss and specific absorption rate (SAR) for superparamagnetic and stable single domain states were due to the higher resonance frequency of the device. The device sensitivities were good enough to measure the magnetic moment of $5 \times 10^7 \mu_B$ under vacuum conditions. In order to measure the small-scale self assemblies of magnetic nanoparticles in ambient conditions, one needs to fabricate highly sensitive devices which have better magnetic moment sensitivity in ambient conditions than the current magnetic moment sensitivity under vacuum conditions. The simple geometry of nanoparticles and better sensitivity of devices may lead to understanding the magnetic

interactions of the small-scale magnetic assemblies under ambient conditions. This motivation led to fabricate and optimize nanophotonic optomechanical split-beam nanocavity resonators, useful for ambient condition magnetic characterizations (magnetization, susceptibility, and spin resonances). These lab-on-chip devices, made for ambient conditions, are presented in Chapter 5.

Chapter 5

Nanocavity Optomechanical Torque Magnetometry and Radiofrequency Susceptometry

Sections of this chapter were published in Nature Nanotechnology 12:127 (2017), published online: 31 October 2016, by Marcelo Wu*, Nathanael L.-Y. Wu*, Tayyaba Firdous*, Fatemeh Fani Sani, Joseph E. Losby, Mark R. Freeman and Paul E. Barclay. *Tayyaba Firdous contributed equally to this work as first author.

5.1 Motivation and Introduction

Readout of magnetically driven motion has involved detection through free-space optical interferometric methods with very low optical-quality factor ($Q_o \approx 1$) Fabry-Pérot cavities formed between the nanomechanical resonator and its supporting substrate [161]. However, as device-dimensions scale down and the number of magnetic spins become too small or the dynamics too fast, the mechanical deflections become more difficult to detect. Migration to a more-sensitive readout scheme is essential. The integration of a nanoscale op-

tical cavity offers a natural path for improvement.

Nanophotonic optomechanical devices allow the observation of nanoscale vibrations with a sensitivity that has dramatically advanced the metrology of nanomechanical structures [201, 202, 203, 204, 205, 51, 206, 207, 208] and has the potential to impact studies of nanoscale physical systems in a similar manner [43, 209].

This potential is demonstrated in this chapter with a nanophotonic optomechanical torque magnetometer and radiofrequency (RF) magnetic susceptometer. Exquisite readout sensitivity provided by a nanocavity integrated within a torsional nanomechanical resonator enables observations of the unique net magnetization and RF-driven responses of single mesoscopic magnetic structures in ambient conditions. The magnetic moment resolution is sufficient for the observation of Barkhausen steps in the magnetic hysteresis of a lithographically patterned permalloy island [210]. In addition, significantly enhanced RF susceptibility is found over narrow field ranges and attributed to thermally assisted driven hopping of a magnetic vortex core between neighbouring pinning sites [211]. The on-chip magnetosusceptometer scheme offers a promising path to powerful integrated cavity optomechanical devices for the quantitative characterization of magnetic micro- and nanosystems in science and technology.

5.2 Nanomechanical Torque Magnetometry by a Laser Interferrometric Method

Torque magnetometry has seen a recent resurgence because of the miniaturization of mechanical devices [212]. The high detection sensitivity of resonant nanomechanical torque sensors has allowed for minimally invasive observations of magnetostatic interactions and hysteresis in a variety of magnetic materials, which include thin films [210], mesoscale confined geometries that are deposited [161] or epitaxially grown [213], and small aggregates of nanoparticles [214]. Be-

yond the static limit, nanomechanical torque magnetometry has been extended to timescales that allow for the detection of slow thermally activated dynamics [210], a.c. susceptibility [213] and magnetic resonance [215, 15].

This powerful technique relies on the detection of the deflection of a mechanical element by angular momentum transfer that originates from magnetic torques $\boldsymbol{\tau} = \mathbf{m} \times \mu_0 \boldsymbol{H}$, generated as the magnetic moments in the system $\mathbf{m}$ experience an orthogonally directed component of the applied magnetic field $\boldsymbol{H}$. So far, improvements to torque magnetometers have been driven primarily by enhancements to the response of nanomechanical resonators that result from their low mass and high mechanical quality factor (Q_{m}). Readout of magnetically driven motion has involved detection through free-space optical interferometric methods with very low optical-quality factor ($Q_{\mathrm{o}} \approx 1$) and low-finesse Fabry-Pérot cavities formed between the nanomechanical resonator and its supporting substrate [161]. Fabry-Pérot cavities used in this Thesis are used for excellent interferometric method (low-finesse) for signal transduction, while optical cavities are used for optical resonance transduction method (high-finesse).

5.2.1 Device Designs

Torque magnetometers were designed and fabricated to be used as torsional resonators. Various modules were tried in order to maximize the torsional amplitude. Figure 5.1 shows some of the designs made for torsional magnetometry measurements. In all designs, one side (left side) of the split beam nanocavity (SBC) is fixed with clamps/anchors in three sections, while the moving side (right side) is clamped at different points for different devices. The flexible moving side is also doubly clamped in Figs. 5.1 a, b, d; the position of clamps and the rectangular pad is varied. The right side of Fig. 5.1c is singly clamped giving it an in-plane flexural mode. The corresponding COMSOL images of dominant resonating modes of the devices in Figs. 5.1 a, b, c, and d are shown

in Figs. 5.1 e, f, g, and h respectively. All devices were measured and characterized for the torsional magnetometry measurements. The design of Fig. 5.1a gave the highest magnetic torsional amplitude and similar design (with tuned elliptical optical cavity) was thus used for all devices in the entire measurements in this chapter.

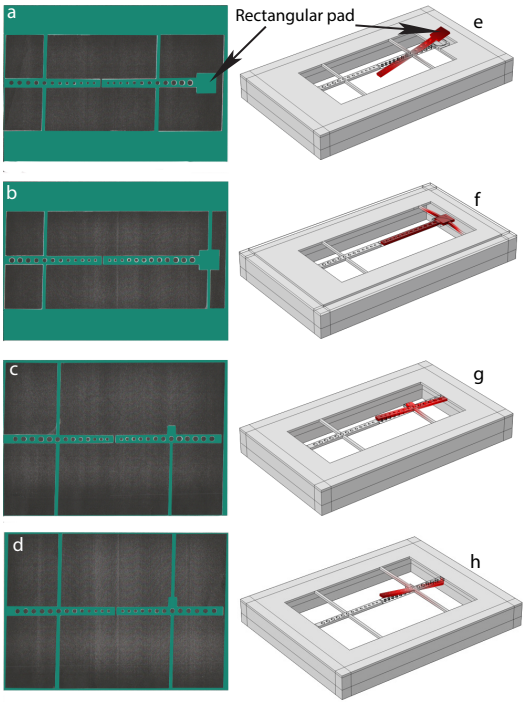

Figure 5.1: ***Device designs.*** *False colour SEM images (a-d) and COMSOL simulation images (e-h) of modes of the optomechanical devices.*

Permalloy structures with a thickness of 40 nm were patterned onto devices using ultrahigh vacuum collimated deposition and a lift-off process [187]. The pad of area 1.4×1.3 μm is partially covered with permalloy because of the imperfect lithographic alignment during the lift-off process, which results in the 'mushroom' shape of the island. As the polycrystalline permalloy is optically absorbing, the permalloy island is positioned far from the nanocavity centre, where it does not degrade Q_o by interacting directly with the nanocavity optical mode.

5.2.2 Raster Scans of the Device

The device in Fig. 5.1a was raster scanned using the nanomechanical torque magnetometry setup by the laser interferometric technique described in Chapter 2. The tilted image of Fig. 5.1a is shown in Fig. 5.2a. The DC raster scan in Fig. 5.2b defines the device position at the time of measurement. The device is straight in vertical orientation in Fig. 5.2b where the rectangular pad is on the bottom side of the device. The AC magnetometry signal has two components according to the reference axis shown in Fig. 5.5a. Figure 5.2c shows the in-phase component of the AC magnetometry signal where the torsional mode was maximized at the resonance frequency of 2.9939 MHz, while the quadrature component is shown in Fig. 5.2d where the light scattering at the device edges slightly changes the phase of the signal.

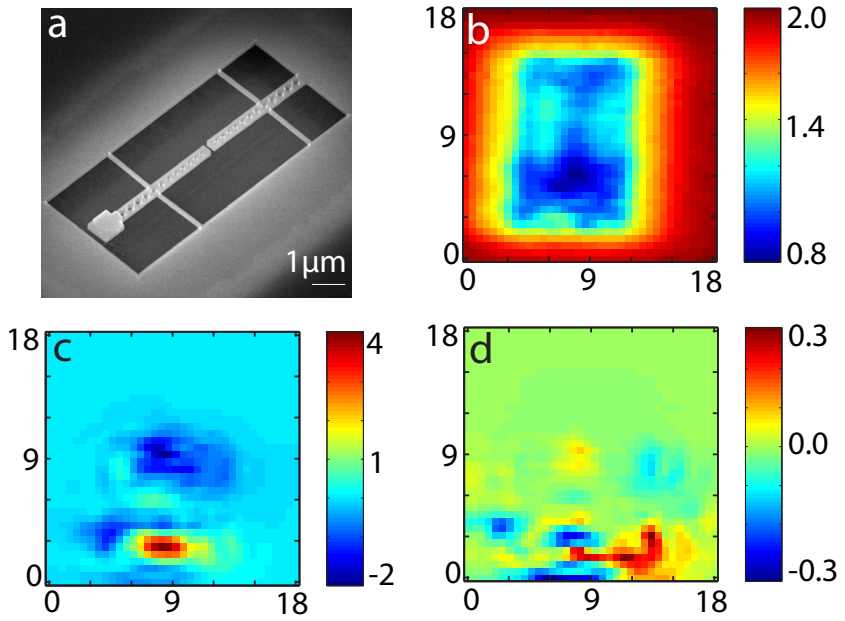

Figure 5.2: ***The raster scan of an optomechanical device at the resonance frequency of 2.9939 MHz.*** ***a,*** *SEM image of the device* ***b,*** *DC raster scans of the device.* ***c,*** *AC torsional amplitude $\hat{x}$-component of the device.* ***d,*** *AC torsional amplitude $\hat{y}$-component of the device. The scanning window is* 18×18 μm^2*, and colour bars has units of Volts, as shown in b, c, and d.*

5.2.3 Pressure Measurements and Hysteresis

To further demonstrate the capability of the device to transduce a signal under various pressure conditions, the device was first measured under base-pressure conditions ($\ll 5.0e^{-4}$mbar), and then measured under increasing pressure. Figure 5.3a shows the first few measurements under pressure while the continued measurements are shown in Fig. 5.3b. It is clear from Fig. 5.3 that the device is capable of measuring the torque magnetometry signal under various pressure conditions. The important thing to notice here is that the device has a good measurable signal under ambient conditions, although the quality factor has been compromised at the expense of air pressure. All pressure measurements were performed in the nanomechanical torque magnetometry setup described in Chapter 2. The mechanical quality factor, Q_{m}, changes from 1530 to 19 under base pressure to ambient pressure conditions.

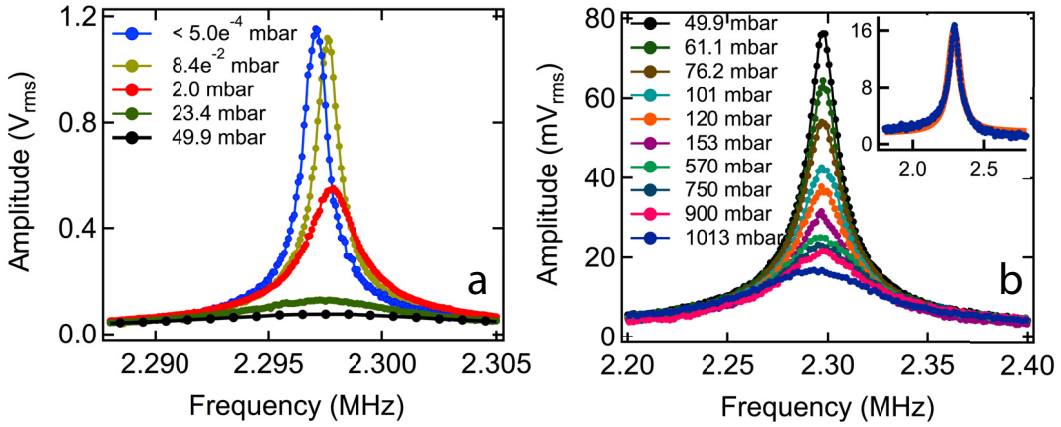

Figure 5.3: ***Resonance peak measured under various pressures. a,*** *resonance peak measurements of the optomechanical device by nanomechanical torque magnetometry at $\ll 5.0e^{-4}$mbar to 49.9 mbar.* ***b,*** *resonance peak measured from 49.9 mbar to 1013 mbar. The inset in Fig. 5.3b represents the resonance peak at 1013 mbar. The red colour in the inset represents the fitted Lorentzian curve.*

The magnetic hysteresis of the permalloy (Py) element deposited on the resonating pad of a device, measured by the interferometric technique under base pressure ($\ll 5.0e^{-4}$mbar), is shown in Fig. 5.4a. The initial hysteresis

encountered a frequency shift during the field sweep by magnet movement. The applied field cause additional spring constant to the resonator resulting in frequency shift, which is more prominent under vacuum conditions.

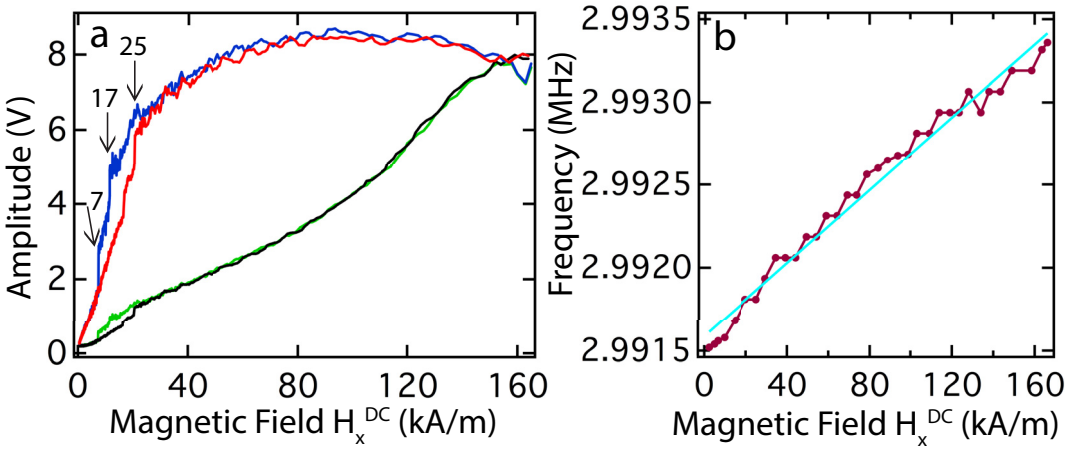

Figure 5.4: ***Magnetic hysteresis by interferometric detection.*** ***a,*** *Magnetic hysteresis of a device. Green and black colours show the hysteresis as-is having frequency shift with magnetic field. Blue and red colours show the corrected hysteresis after the frequency shift.* ***b,*** *linear frequency shift by DC magnetic field. The linear fit with equation* $y = a + bx$ *has parameters as* $a = 2.99 \pm 2.43e^{-5}, b = 1.10e^{-5} \pm 2.58e^{-7}$.

The measured frequency shift with field was plotted and linearly fitted to get various parameters (see Fig. 5.4b). The hysteresis curve was then corrected with the linear fit parameters. The corrected hysteresis curve shows that the saturation field $\sim$ 90 kA/m for this Py element is quite high because of the geometry of the magnetic element. The high magnetic field was obtained with a 2-inch cube magnet producing a magnetic field of 165 kA/m at a distance of 5 cm from the chip position. The vortex creation at 25 kA/m and vortex pinning at 17 kA/m and 7 kA/m, can be seen in Fig. 5.4a indicated by arrows, by sweeping the field from high to low. While sweeping the low to high field, the vortex is annihilated at 25 kA/m. The devices were then moved to the optomechanical setup described in Chapter 2 after this primary characterization. Note that one can see similar hysteresis measured with optomechanical fibre setup (see Fig. 5.6) in ambient conditions. One can take advantage of by-passing

the frequency shift problem (because of low Q_{m} in ambient conditions), having better signal transduction, and using the ambient conditions. The signal transduction using taper fiber and split-beam nanocavity (SBC) details are detailed in the sections below and in Chapter 2.

5.3 Introduction to Optomechanical measurements

Nanocavity-optomechanical devices enhance mechanical detection sensitivity by confining light to high-Q_{o} modes localized within the nanomechanical resonator. They have been exploited for metrology applications such as force and displacement detection [202, 203], inertial sensing [204], torque sensing [205, 51, 206] and the observation of mechanical quantum fluctuations [207]. Recently, microscale ($\sim 10-100\mu$m) cavity optomechanical devices were combined with magnetostrictive materials to create external magnetic field sensors [216]. Nanophotonic optomechanical devices with subwavelength dimensions have tremendous potential to impact mechanical sensing of the microscopic electronic and magnetic dynamics of meso- and nanoscale systems typically using conventional readout optical methods [43, 209].

5.3.1 Optomechanical Torque Magnetometer Device and Split-Beam Nanocavity (SBC)

The nanocavity optomechanical sensor is applied to a nanoscale condensed-matter system, and torque magnetometry is performed with sufficient sensitivity for the detection of Barkhausen features that were previously undetected in ambient conditions. This device is used to demonstrate a new form of nanomechanical RF susceptometry, and observe an enhanced magnetic susceptibility associated with single pinning and depinning events that can increase the torque

magnetometer sensitivity by over an order of magnitude.

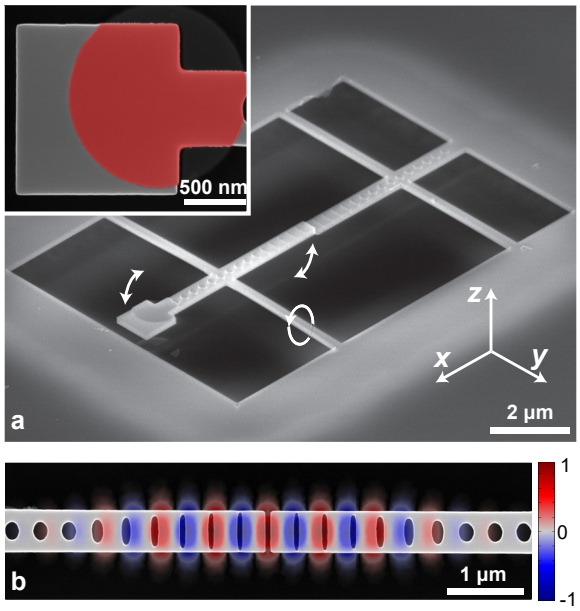

Figure 5.5: ***Split-beam cavity.*** ***a****, Tilted scanning electron micrograph (SEM) of a split-beam cavity device. Inset: top-view of the 40 nm thick permalloy film deposited onto the device.* ***b****, Top-view SEM of the nanocavity overlaid with a finite element simulation (COMSOL) of the normalized field distribution E_y of its optical mode. The colour bar shows the intensity of E_y.*

The high sensitivity of nanocavity optomechanical devices arises from a combination of large optomechanical coupling, large mechanical resonator susceptibility (low mass $\mathbf{m}_{\rm eff}$ and large $Q_{\rm m}$) and sharp optical-cavity response (large $Q_{\rm o}$). The device employed here, an example of which is shown in Figure 5.5a, is designed with these properties in mind. Referred to as a split-beam nanocavity (SBC) [51], it consists of two suspended silicon photonic crystal nano-beams– one anchored in three sections, and the other 'moving nanobeam' anchored by two supports. This supports an optical mode whose field, shown in Fig. 5.5b, is confined to the central gap region and has a high $Q_{\rm o}$ (∼5,000 for the device studied here) owing to careful mode matching between the local field supported by the gap with the field in the elliptical holes of the nanobeams [163].

5.3.2 Optomechanical Measurement Setup and Applied Fields

Vibrations of nanobeam mechanical resonances modulate both the gap width and the distance between the SBC and the fibre taper waveguide used to couple light evanescently into and out of the nanocavity, as illustrated in the experimental setup in Fig. 5.6. Of particular interest for torque magnetometry is the torsional resonance T_y of the moving nanobeam, where the nanobeam ends move anti-symmetrically out-of-plane, as shown schematically in Fig. 5.5a. This low mass ($m_{\rm eff}$ = 1 pg) resonance (frequency $\omega_m/2\pi$ = 3 MHz) can be excited efficiently by nanoscale sources of torque coupled to the SBC.

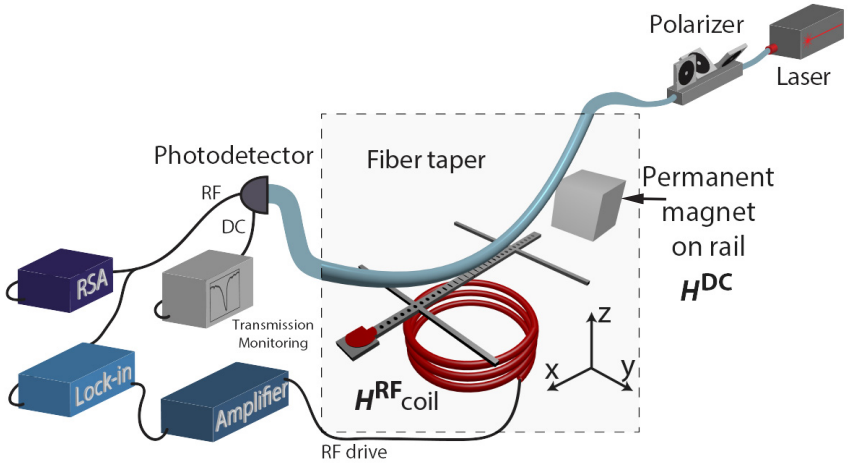

Figure 5.6: ***Schematic experimental set-up for nanocavity optomechanical torque magnetometry measurements (not to scale).*** *All the measurements are performed in an ambient nitrogen-purged environment (grey region). A dimpled fibre taper is used to probe the optomechanical nanocavity. A permanent magnet with an adjustable position provides varying static magnetic fields. The lock-in amplifier reference is power amplified and sent to coils below the device to create an RF magnetic field in the z direction.*

To perform nanocavity-optomechanical torque magnetometry, a permanent magnet (N50 neodymium iron boron, 2.5cm^3) was mounted on a motorized stepper rail and used to apply a stable and finely adjustable H_x^{DC} aligned along the device $\hat{x}$ axis. The 1-inch cubic magnet has a field magnitude of 760 G

at a distance of about 2.5 cm from the torque sensors. This is sufficient for near complete saturation of the moments in the soft magnetic system studied in this Chapter. The field magnitudes were recorded with a three-axis Hall probe placed below the sample chip (Sentron 3M12-2). The RF coil positioned beneath the sample chip was used to generate H_x^{RF} and H_z^{RF}. This coil was integrated into an optical fibre-taper probing set-up identical to that used in previous nanophotonic cavity optomechanics experiments [51]. The schematic of the set-up presented in Fig. 5.6 illustrates the detection of the nanobeam motion through a dimpled optical fibre taper.

The dimple was positioned in contact with the top surface of the fixed nanobeam such that, in the vicinity of the nanocavity gap region, the fibre taper was aligned $\ll 200$ nm from the device, where it induces significant dispersive optomechanical coupling [217] and evanescently couples light into and out of the nanocavity. The optical transmission of a tunable laser source (Santec TSL-510, wavelength range 1,500-1,630 nm) through the fibre taper was detected using a low-noise photodetector (New Focus 1811) and analysed using a real-time spectrum analyser (Tektronix RSA 5103B) and lock-in amplifier (Zurich Instruments HF2LI). The attachment of the fiber taper coming from above the sample is currently limiting the proximity of the magnet. For driving the RF coil, a reference tone was passed from the lock-in amplifier through an RF power amplifier (ENI 403 L, 37 dB gain). All the measurements were conducted at ambient temperature and pressure within a nitrogen-purged environment.

The implementation of permanent magnets is less common for variable magnetic field generation in magnetometry compared to the use of electromagnets, though the former offer advantages. Permanent magnets provide high and homogeneous fields over small regions, where the field stability is limited mainly by the resolution of the stepper motor used to vary the applied field. The very fine field resolution allows for direct correlation of events from multiple measurements (and are not prone to thermal drift as in electromagnets). The

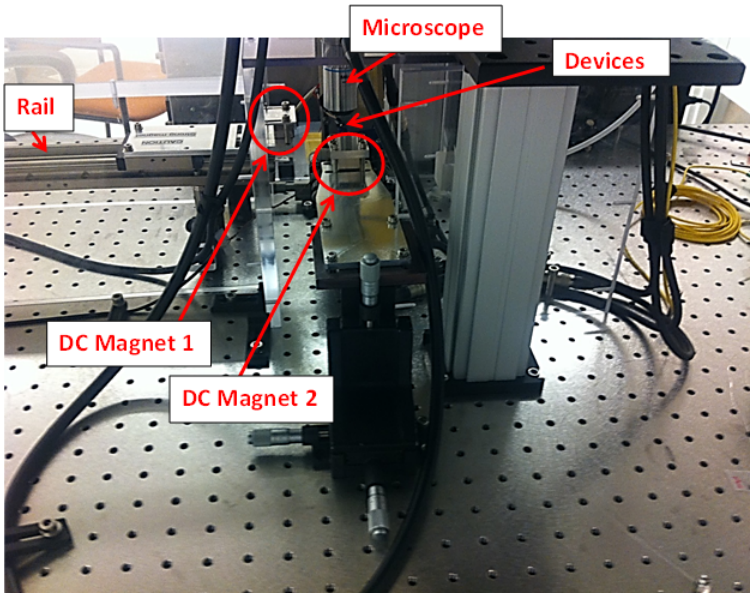

Figure 5.7: ***Actual experimental set-up for nanocavity optomechanical torque magnetometry measurements.*** *The two magnets and the microscope are perpendicular to each other at the device position.*

measurement setup is also greatly simplified, as using permanent magnets does not require a high power supply and cooling system as needed with electromagnets.

In addition to H_x^{DC}, the DC field H_z^{DC} aligned along $\hat{z}$ is created by introducing a small tilt ($\theta = 8°$) of the sample with respect to horizontal. This allows generation of a torque proportional to the magnetic susceptibility χ_x (discussed in the next section). The vector DC magnetic field in the frame of reference of the sample was calibrated with a 3-axis Hall probe placed at the sample location when the sample was removed. The magnetic field values were then measured as a function of magnet position on the stepper rail, and fit to a polynomial function. The fields were monitored during the measurements with the Hall probe sitting just below the sample, but the stepper position and a calibration procedure were used for more accurate values of the applied field strength.

The RF magnetic fields generated by the coil were measured indirectly

through the use of a current probe inserted between the output of the RF power amplifier (ENI Model 403L) and the coil. The maximum RF drive amplitude was $H_{\mathrm{z}}^{\mathrm{RF}} = 35$ A/m at 3 MHz, limited by harmonic distortion of the power amplifier. In laying out the cabling for the z measurement, it is necessary to adjust the arrangement to minimize RF crosstalk from the drive to the photoreceiver.

The coil used in the measurements had 3 turns of 0.49 mm diameter wire wound to an inner diameter of 3.4 mm. Using the measured RF current, the corresponding RMS magnetic field values were determined using Eq. (5.1) describing the on-axis field of a finite solenoid [218],

$$H^{\mathrm{RF}} = \frac{IN}{2\mu_r L(r_o - r_i)} \left[z_2 \ln\left(\frac{\sqrt{{r_o}^2 + {z_2}^2} + r_o}{\sqrt{{r_i}^2 + {z_2}^2} + r_i} \right) - z_1 \ln\left(\frac{\sqrt{{r_o}^2 + {z_1}^2} + r_o}{\sqrt{{r_i}^2 + {z_1}^2} + r_i} \right) \right] \tag{5.1}$$

with I being the RMS current, N the number of turns, and L, r_o, r_i the length, outer radius, and inner radius of the solenoid, respectively. z_1 is the vertical distance from the device to the top of the solenoid, and $z_2 = z_1 + L$.

In contrast to the on-axis case, there is no analytical formula for off-axis field values. The Biot-Savart law was used to calculate the magnetic field of a finite solenoid at an offset position near the coil by integrating over the current source.

When the chip is centered ($\Delta x = 0$ mm, about 2 mm above coils), $H_{\mathrm{z}}^{\mathrm{RF}}$ is at its strongest point while $H_{\mathrm{x}}^{\mathrm{RF}}$ is approximately zero due to symmetry. For the observations of RF susceptibility requiring a non-zero in-plane component of $\boldsymbol{H}^{\mathrm{RF}}$ the chip was positioned with offsets of $\Delta x = 1.9$ and -3.6 mm relative to the center of the coil as depicted in Fig. 5.8 a. When the chip is offset to the right ($\Delta x = 1.9$ mm), both x and z-components have comparable amplitudes such that $H_{\mathrm{x}}^{\mathrm{RF}} = H_{\mathrm{z}}^{\mathrm{RF}} = H^{\mathrm{RF}}$. When offset to the left at $\Delta x = -3.6$ mm, then $H_{\mathrm{x}}^{\mathrm{RF}} \approx -6 H_{\mathrm{z}}^{\mathrm{RF}}$.

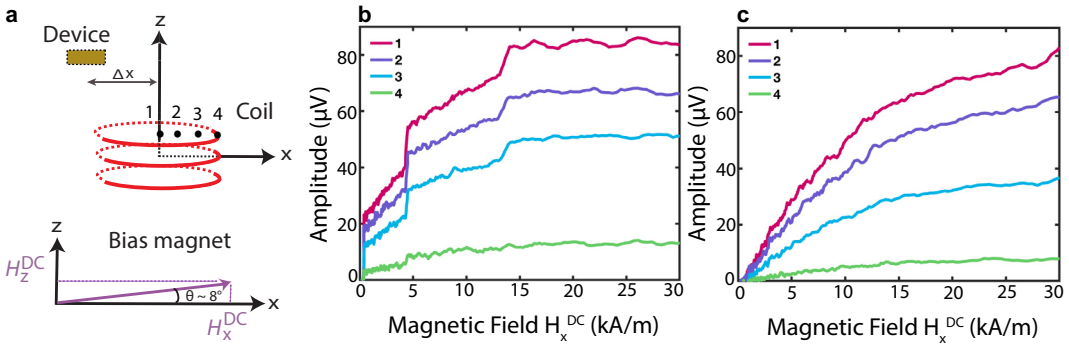

Figure 5.8: ***Device offset on top of coil and magnetic field of RF coil. a,*** *Schematic of the positioning Δx of the device relative to the center of the coil (red) and tilt θ relative to the plane of the permanent magnet.* ***b,*** *Hysteresis (high to low field) acquired when the device is at coil positions 1, 2, 3, and 4 labelled in a.* ***c,*** *Hysteresis (low to high field) acquired when the device is at coil positions 1, 2, 3, and 4 labelled in a.*

Time domain measurements, including resonant coupling between mechanical resonances and magnetic dynamics should be possible in future studies. The MHz operating frequency chosen here reduces technical noise related to the operating environment such that the measurement sensitivity is limited by photodetection shot noise. By adjusting the geometry of the supporting structure, higher or lower frequency operation is possible.

5.4 Optomechanical and Spectral Transductions

5.4.1 Optomechanical Coupling and Transduction

The cavity-optomechanical readout converts fluctuations in the nanobeam position to modifications of the optical nanocavity response measured through an external optical input and output coupling channel. In the experiments presented here, the nanocavity optical mode is probed by monitoring the wavelength (λ) dependent normalized transmission, $T(\lambda)$, of a dimpled optical

fiber taper [219, 220] positioned in the near-field of the split-beam nanocavity (SBC). Figure 5.9 shows typical $T(\lambda)$ when probing an SBC optical mode at $\lambda_o = 1528$nm with optical quality factor $Q_o \sim 5000$. Note that the fiber taper input power, $P_i \sim 175\mu$W, in this experiment is sufficiently large to introduce a slight thermal nonlinearity and associated non-Lorentzian optical response [221]. In this measurement the fiber taper dimple is positioned in contact with the anchored nanobeam, such that it interacts with the near-field of the moving nanobeam without touching it. This provides stable fiber-nanocavity coupling without affecting the motion of the moving nanobeam, while also enhancing optomechanical coupling to the mechanical resonance of interest, as described below.

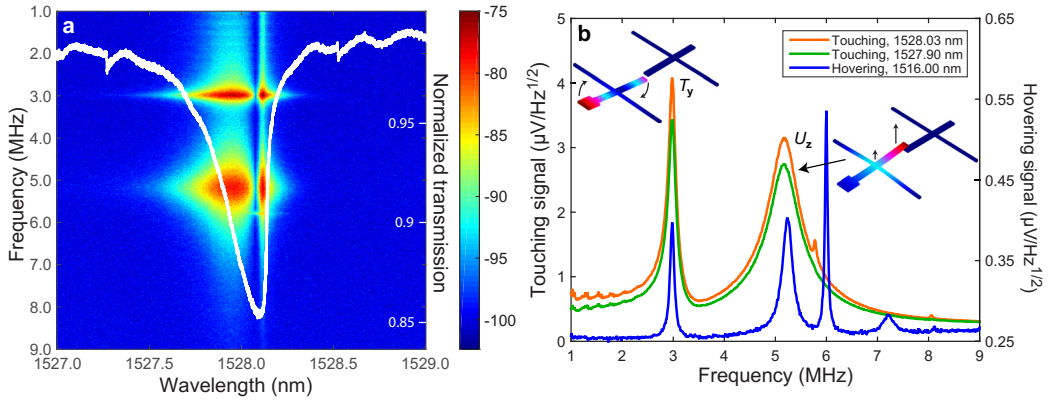

Figure 5.9: ***Optomechanical response.*** ***a****, $S_{VV}(\lambda, \omega)$ in ambient conditions as the fiber taper is touching the anchored nanocavity nanobeam. Scale bar on the right is in dBm. The white overlay with axis on the right is the optical transmission showing the optical resonance at 1528 nm. Sharp low amplitude features are laser mode-hops.* ***b****, Thermomechanical frequency response of the device at various wavelengths (left axis) and when hovering (right axis). Measurements were performed with no applied magnetic field ($H_z^{RF} = 0$). Two mechanical modes of interest, T_y and U_z, are indicated, with their displacement fields predicted by finite element simulations inset. Black arrows indicate prominent displacement directions.*

Optomechanically transduced motion of the moving nanobeam is probed by monitoring the fluctuations in $T(\lambda)$ detected by a photoreceiver and a real-time spectrum analyzer (RSA). The RSA outputs an electronic power spectrum

$S_{VV}(\lambda, \omega_m)$, as shown in Fig. 5.9a for λ swept from 1527-1529 nm across the optical mode of the device at $\lambda_o = 1528$nm. Peaks resulting from thermomechanical motion of the T_y and U_z nanomechanical resonances (Fig. 5.9b) are observed at $\omega_m/2\pi = 3$ MHz and 5.3 MHz, respectively. Their frequencies closely match with predictions from finite element simulations (COMSOL), as shown in Fig. 5.9b.

Peaks in the observed bimodal λ dependence of $S_{VV}(\lambda, \omega_m)$ are approximately aligned with maxima in $|dT/d\lambda|$ near detunings $|\lambda - \lambda_o|$ equal to half an optical mode linewidth. This is a signature of predominantly dispersive optomechanical coupling present in the device for sideband unresolved operation ($\omega_m \ll \omega_o/Q_o$, where $\omega_o = 2\pi c/\lambda_o$ is the nanocavity mode frequency). In SBC devices, dispersive (g_{om}), internal dissipative (g_i), and external dissipative (g_e) optomechanical coupling can all play a role in generating the transduced signal [51]. For the measurements shown in Fig. 5.9a, contributions from (g_{om}) dominate. Nominally, (g_{om}) vanishes for a vertically symmetric SBC optical mode interacting with the "odd" T_y and U_z resonances, however significant dispersive optomechanical coupling arises from the close proximity of the fiber taper dimple to the moving nanobeam and central nanocavity region. The presence of the fiber taper in the nanocavity near field breaks the vertical symmetry and renormalizes the nanocavity mode [217]. The resulting optomechanical coupling between the renormalized non-vertically symmetric mode and the T_y resonance is characterized by a measured dispersive optomechanical coupling coefficient $(g_{om})/2\pi \sim 1.4$GHz/nm.

The high sensitivity of SBC devices arises from a combination of mechanical, optical, and optomechanical properties that provide an enhancement compared to a stand-alone nanomechanical resonator [45]. As described in detail in Ref.[51], this can be quantified by the transduction gain of the device,

$$G|_{\omega=\omega_m} \propto P_i g_{om} Q_o Q_m / m_{eff.} \tag{5.2}$$

Here G converts a source of torque at frequency ω into a modulation in optical power P_o transmitted through the fiber taper. Equation (5.2) assumes that the torque is driving the nanocavity on-resonance ($\omega = \omega_m$) and that dispersive optomechanical coupling described by (g_{om}) is the dominant transduction mechanism. This equation (Eq. 5.2) has additional constants to compensate the units in Eq. 5.3.

In the measurements, λ is adjusted to maximize the optomechanical signal. As shown in Fig. 5.9b, by fixing λ on the red detuned shoulder of the optical resonance, a slightly stronger signal is obtained (orange trace). Although measurements are all performed with the fiber taper in contact with the anchored nanobeam, as described above, it is also possible to transduce nanomechanical motion when the fiber is "hovering" above the device. Such a measurement is shown in Fig. 5.9b. In these measurements the mechanical signal was found to be weaker and relatively unstable, as small fluctuations in fiber positioning would affect the coupling of light into the device [217]. Moreover, additional mechanical modes are present in the signal, as shown in Fig. 5.9b, since the hovering fiber does not damp out resonances of the fixed nanobeam. Such hovering measurements are made at a shorter operating wavelength as the position of the fiber away from the cavity decreases the local effective index and λ_o.

5.4.2 Sensitivities

5.4.2.1 Thermomechanical Sensitivity

The thermally-driven random motion of the SBC was used to characterize the SBC displacement sensitivity and to optimize, in real-time, the operating conditions (λ and fiber taper position) for maximum signal over noise. The optical signal collected by the photoreceiver carries the imprint of the mechanical spectral response of the device. This spectra can be analyzed either in real-time by the spectrum analyzer (RSA) or through post-processing of time series IQ

data collected by the RSA to calculate $S_{\mathrm{VV}}(\omega) = |V(\omega)|^2/\mathrm{RBW}$, where RBW is the resolution bandwidth set by the RSA measurement time and $V(\omega)$ is the Fourier transform of the photoreceiver output voltage. The spectral response can then be converted from V^2/Hz to m^2/Hz with a thermomechanical calibration of the peaks in $S_{\mathrm{VV}}(\omega)$ identified with a given mechanical resonance [222].

For the device studied here, Fig. 5.10a shows two overlapping peaks and thus the power spectral density can be fitted to an uncorrelated double Lorentzian curve with total noise floor $S_{\mathrm{VV}}^{\mathrm{noise}}(\omega)$:

$$S_{\mathrm{VV}}(\omega) = S_{\mathrm{VV}}^{\mathrm{noise}}(\omega) + G_1^2 S_{\mathrm{zz},1}^{\mathrm{th}}(\omega) + G_2^2 S_{\mathrm{zz},2}^{\mathrm{th}}(\omega) \tag{5.3}$$

Here, $G_{1,2}$ corresponds to the optomechanical gain described in Eq. (5.2). The thermal displacement density $S_{\mathrm{zz}}^{\mathrm{th}}(\omega)$ of a particular resonance is given by the fluctuation-dissipation theorem as [223]:

$$S_{\mathrm{zz}}^{\mathrm{th}} = \frac{4k_B T_{\mathrm{b}} \omega_{\mathrm{m}}}{Q_{\mathrm{m}}} \frac{1}{m[(\omega^2 - \omega_{\mathrm{m}}^2)^2 + (\frac{\omega\omega_{\mathrm{m}}}{Q_{\mathrm{m}}})^2]} \tag{5.4}$$

where k_B is Boltzmann's constant, T_{b} is the temperature of operation, Q_{m} is the mechanical quality factor, ω_{m} is the mechanical resonance frequency, and m is the effective mass calculated for each mode from finite element simulations. Resonances are identified by comparing their frequency with finite element simulations and m_{eff} for each resonance is calculated from the simulated displacement profile [224]. After fitting Eq.(5.3) to the data with Q_m for each mode and $G_{1,2}$ as fitting parameters, the spectral response can be calibrated (i.e. converted from V^2/Hz to m^2/Hz) to a particular peak. In Fig. 5.10a, the y-axis is calibrated such that the total displacement resolution of the torsional mode T_{y} is:

$$S_{\mathrm{zz},1}(\omega) = \frac{S_{\mathrm{VV}}(\omega)}{G_1^2} = S_{\mathrm{zz},1}^{\mathrm{th}}(\omega) + S_{\mathrm{zz}}^{\mathrm{noise}}(\omega) + \frac{G_2^2}{G_1^2} S_{\mathrm{zz},2}^{\mathrm{th}}(\omega) \tag{5.5}$$

where $S_{zz}^{noise}(\omega) = S_{VV}^{noise}(\omega)/G_1^2$ gives the displacement sensitivity for T_y in this case. Its effective mass and torsional spring constant (relating displacement to force) is calculated to be m_{eff} = 1pg and $k_{eff} = 4.6 \times 10^{-12}$N m with an extracted $Q_m = 25$, limited by damping from the N_2 operating environment.

5.4.2.2 Displacement and Torque Sensitivities

The interaction between nanobeam motion and nanocavity optical dynamics is characterized by the optomechanical coupling coefficient g_{om}. Detection of the vertical motion of the T_y resonance relies on the dispersive optomechanical interaction between the SBC and the fibre taper. The fibre taper renormalizes the nominally symmetric nanocavity field and induces $g_{om}/2\pi$ in the gigahertz per nanometre range [217]. The displacement sensitivity of the fibre-coupled SBC device can be calibrated by measuring the optomechanically transduced thermal motion, as shown in Figs. 5.10a,b. For typical operating conditions, it is in the tens of femtometres per $H_z^{1/2}$ range with an equivalent torque of 1.3×10^{-20}Nm$(\text{Hz}^{1/2})^{-1}$. All the measurements are performed in ambient conditions, resulting in Q_m<100 because of viscous air damping.

Nanocavity torque magnetometry can be performed by actuating the T_y mode with a magnetic field H that interacts with a magnetic moment m on the nanobeam [225, 226]. The magnetic properties of a ferromagnetic thin-film permalloy island integrated onto the rectangular pad at the end of the moving nanobeam, shown in the inset in Fig. 5.5a, were studied. When an in-plane static field H_x^{DC} was applied, the permalloy became magnetized with a net moment $m_x(H_x^{DC})$ along the field x direction. By applying an additional RF field H_z^{RF} directed in the out-of-plane z direction, a magnetic torque τ_y was generated proportional to m_x and directed along the torsion rod that supports the moving nanobeam. When the RF field was applied at the T_y resonance angular frequency ω_m, the resulting driven beam displacement could be detected optomechanically from the nanocavity optical response. A typical signal is

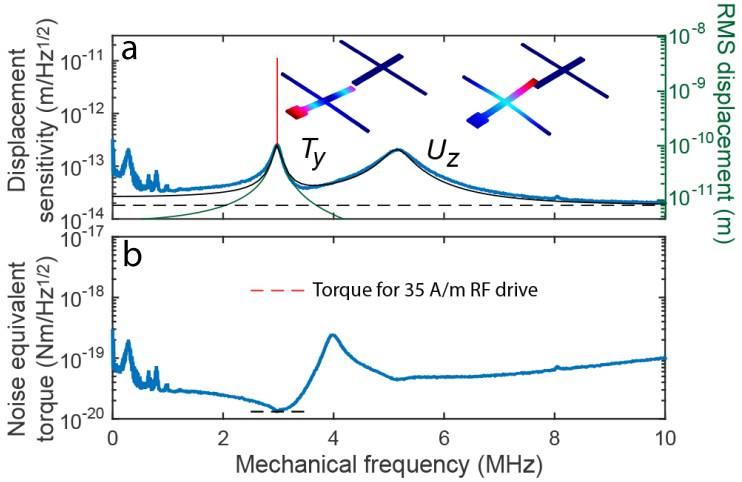

Figure 5.10: ***Displacement and torque sensitivities.*** ***a,*** *Displacement density (left axis) from the real-time spectrum analyser (RSA) that shows thermally driven mechanical modes T_y and U_z (blue) and the magnetically driven signal (narrow peak highlighted in red) generated by a magnetic driving field H^{RF} of 35 Am^{-1} applied with the permalloy island magnetization saturated by H_x^{DC}. Black lines are fits to the T_y and U_z Lorentzian-shaped peaks (solid line) and the measurement noise floor (dashed line). The green curve (right axis) indicates the predicted root mean squared displacement of the T_y resonance in the presence of a 35 Am^{-1} RF magnetic field as a function of frequency. Insets show simulated displacement profiles of T_y and U_z.* ***b,*** *Torque equivalent noise of the thermomechanical displacement signal in a. The red dotted line indicates the predicted torque in the presence of a 35 Am^{-1} H_z^{RF} field, and is labelled by the values on the left axis, assuming a 1s integration time.*

shown in the spectral domain in Fig. 5.10a, where it clearly emerges as a sharp peak at ω_{m} far above the thermomechanical noise. Although this device has the largest optomechanical magnetic transduction of those fabricated for this study, other devices were observed to display similar behaviour.

5.4.2.3 Magnetic Sensitivities

The ability of the optomechanical nanocavity to detect nanoscale magnetic phenomena arises from its torque sensitivity of $1.3 \times 10^{-20}\mathrm{Nm}(\mathrm{Hz}^{1/2})^{-1}$, which at field strengths on the order of the Earth's field $(44 - 60\mu\mathrm{T})$, corresponds to a magnetic moment sensitivity of $(2.4 \pm 0.4) \times 10^7 \mu_{\mathrm{B}}$. A minimum detectable volume of magnetic material of $0.015 \pm 0.005 \mu m^3$ is calculated for the largest

magnetic susceptibility enhancement; increasing the RF drive would allow for the measurement of even smaller volume samples. Despite operating in ambient conditions, this device is of comparable or better sensitivity than previous nanoscale torque magnetometry devices [210, 161, 15] reliant on free-space reflectometry and vacuum or cryogenic operation. Furthermore, its relatively low Q_{m} and megahertz operating frequency, in principle, allows megahertz bandwidth excitation and detection. Among nanoscale optomechanical torque metrology devices, the demonstrated sensitivity is only surpassed by systems that operate in vacuum [206] or cryogenic conditions [227], none of which have yet been used for magnetometry or to probe nanoscale condensed matter systems.

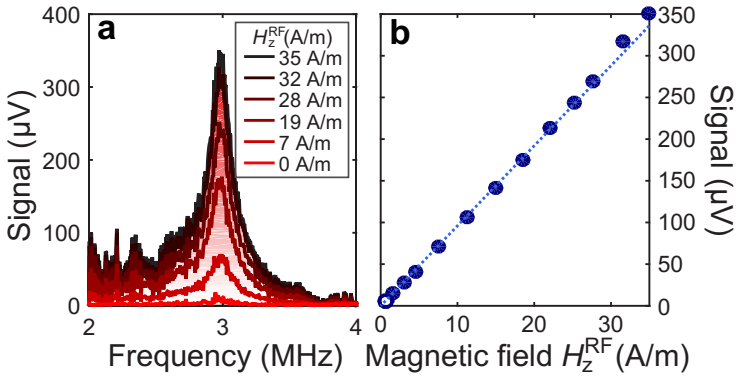

Figure 5.11: ***Magnetic moment sensitivity.*** ***a****, Device response as RF magnetic fields of various intensities are applied and swept from 2 to 4 MHz using the lock-in amplifier, for a constant field of* $H_x^{DC} = 45$ *kA/m.* ***b****, Maximum device response (located at 3 MHz) varies linearly with the applied RF field strength. When the applied field* H_z^{RF} *is turned off, the minimum signal is limited by thermomechanical noise leading to an effective minimum detectable field* H_{min} *(0.61 A/m) indicated by the open circle.*

Notwithstanding the practical advantages enabled by operation in ambient conditions, vacuum and low temperature T_{b} will reduce the thermal force fluctuations that scale with $\sqrt{T_{\mathrm{b}}/Q_{\mathrm{m}}}$ and limit the sensitivity [51]. For example, $Q_{\mathrm{m}} = 10^3 - 10^4$ for similar SBC devices has been observed in vacuum [51], and $Q_{\mathrm{m}} = 10^5$ has been observed at liquid helium temperatures for silicon

zipper nanocavity devices [228]. This indicates that a 10^4 improvement in the thermally limited sensitivity may be within reach. Even a modest improvement in sensitivity by an order of magnitude, in combination with a maximum driving field of $1kAm^{-1}$, could produce magnetic moment sensitivities below $2 \times 10^5 \mu_B$ [205], which enables nanomagnetism lab-on-chip studies of a wide range of systems [43, 209].

From the displacement sensitivity, the equivalent torque sensitivity (plotted in Fig. 5.10b) can be found using $\mathbf{S}_\tau(\omega) = \mathbf{r}^2 \times \mathbf{S}_{zz}(\omega)/|\chi_m(\omega)|^2$ [51, 222]. Here, $\mathbf{r}$ corresponds to the distance between the axis of rotation formed by the supports on the moving beam and the tip of the pad (approximately $3.5\mu m$). The mechanical susceptibility $\chi_m(\omega) = [m(\omega^2 - \omega_m^2 + i\omega\omega_m/Q_m)]^{-1}$ relates the displacement density to the applied force, and the torque is calculated from $\boldsymbol{\tau} = \mathbf{r} \times \mathbf{F}$.

The high torque sensitivity of the T_y resonance enables detection of magnetic torque signatures from the permalloy island. The measured frequency response for varying amplitude of H_z^{RF} is shown in Fig. 5.11a, with an applied bias field $H_x^{RF} = 45$kA/m saturating the permalloy moment. When the drive angular frequency ω_{RF} is tuned onto resonance with ω_m of the T_y resonance, a sharp signal superimposed upon the broad thermomechanical peaks in the RSA spectrum is observed (see Fig. 5.5b), indicating that H_z^{RF} is actuating the nanobeam. This was confirmed by sweeping $\omega_{RF}/2\pi$ from 0 - 22 MHz and monitoring the corresponding frequency component of the photoreceiver output demodulated at the lock-in amplifier.

The device's magnetic moment sensitivity may be calculated from the observed linear relationship of the response of the device with RF drive shown in Fig. 5.11b. At $H_z^{RF} = 0$A/m, the thermomechanical contribution limits the measurement sensitivity. For this particular device, this corresponds to an effective RF drive of $H_{min} = 0.61$A/m, as indicated by the open circle. With the assumption that all magnetic moments contribute to driving the signal, the

sensitivity is calculated to be $2.7 \times 10^9 \mu_B$(A/m). This sensitivity under ambient conditions is on a par with nanotorsional resonators using interferometric detection in vacuum [161, 229]. The corresponding torque sensitivity was calculated to be around 3.2×10^{-20}Nm , which was close to the thermally limited minimum torque sensitivity measured using the RSA. The slightly poorer sensitivity here is believed to be caused by additional technical noise due to RF pickup in the electronics, which can be alleviated with shielding.

Among torque magnetometers, the reported device has state-of-the-art sensitivity of 1.3×10^{-20}Nm, despite operating in ambient conditions where its mechanical resonances are significantly damped. Among optomechanical torque sensor devices not yet used for magnetometry, devices with better sensitivity have been demonstrated operating in vacuum and/or cryogenic conditions. For example, a see-saw double-photonic-crystal nanobeam [206] reaches a torque sensitivity of 9.6×10^{-21}N m/Hz$^{0.5}$ in 10^{-4} Torr vacuum, and optomechanical devices in mK conditions have been measured with record 10^{-24}N m/Hz$^{0.5}$ sensitivity [227]. However, none of these devices have yet been used for magnetometry or to probe other systems. This devices can reach, if not surpass, those sensitivities in similar conditions, where Q_{m} is expected to increase by orders of magnitude owing to elimination of air damping in vacuum and reduction of internal damping in silicon at low temperature [228].

5.4.2.4 Spectral Response and Magnetic Field Sensitivity

The broader bandwidth response of the nanocavity with and without driving field is depicted in Fig. 5.12. At $H_{\mathrm{z}}^{RF} = 0$, the signal $S(\omega)$ is broadband with low noise. The mechanical mode at 21 MHz is a second-order torsional mode. With H_{z}^{RF} on, shown in red and denoted as $N(\omega)$, the lock-in amplifier is able to detect the two main driven mechanical resonances T_{y} and U_{z}. The torsional mode T_{y} produced the strongest response due to the favourable geometry for the orthogonality of magnetic torque terms; thus all torque measurements were

performed at the frequency of T_y. The second mode responds weakly since its motional shape is less efficiently (about 50 times) actuated by torque. The overall noise floor is also much higher due to technical noise coming from the current in the RF coil and cables. This accounts for the slightly worse torque sensitivity of 3.2×10^{-20}Nm measured with the lock-in amplifier.

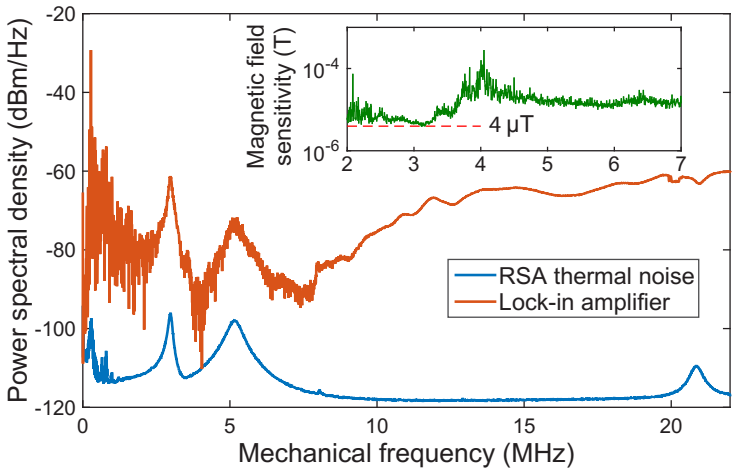

Figure 5.12: ***Spectral response.*** *Wide bandwidth power spectral density of the nanocavity coupled optical signal. In blue, the RSA signal when $H_z^{RF} = 0$ shows the two main mechanical modes with secondary modes at 8 MHz and 21 MHz. In orange, the RF coil with $H_z^{RF} = 35$ A/m drives the device while the signal is recorded by the lock-in amplifier. An RF power amplifier was used (37 dB amplification, 150 kHz - 250 MHz range). Large noise at low frequency (< 1 MHz) is due to the fiber taper. At higher frequencies, the noise generated by the RF coil increases. Inset: Measured magnetic field sensitivity.*

Although the primary function of the device is not field sensing, its magnetic field sensitivity can be estimated from the spectral analysis following the procedure laid out in Ref. [230]. First, a reference signal is calibrated at a particular frequency shown as the peak in Fig. 5.10a where a field $H^{RF} = 35$A/m or equivalently $B_{\text{ref}} = \mu_0 H^{RF} = 44\mu$T was applied. The minimum detectable magnetic field can then be expressed as $B_{\text{min}}(\omega_{\text{ref}}) = B_{\text{ref}}/\sqrt{SNR \cdot RBW}$ where SNR is the signal to noise ratio of the reference peak. To map this to an overall spectral sensitivity, the spectral responses with and without applied field, $N(\omega)$ and $S(\omega)$ respectively, can be combined to obtain the graph in the inset

of Fig. 5.12 using the following equation [216]:

$$B_{\min}(\omega) = \sqrt{\frac{S(\omega)N(\omega_{\text{ref}})}{S(\omega_{\text{ref}})N(\omega)}} B_{\min}(\omega_{\text{ref}}). \tag{5.6}$$

The highest sensitivity of 4μT occurs near the mechanical resonance at 3 MHz. This relatively low field sensitivity is typical for a permalloy pad with small volume $V_{\text{Py}} \sim 1\mu m^2 \times 40$nm compared to the orders of magnitude larger volumes of magnetic material used in other optomechanical or torsional systems [231, 216, 232].

5.5 Magnetic Susceptibility and Suceptometery

5.5.1 Magnetic Hysteresis of the Permalloy Island

To perform magnetometry on the permalloy island, hysteresis loops were measured by varying H_{x}^{DC} via translation of the permanent magnet while recording the optomechanically transduced RF signal for a fixed H_{z}^{RF} using the lock-in amplifier. Figure 5.13 shows the torque signal normalized to the value at saturation, with the corresponding scale for the net magnetization on the right axis. Beginning at high field (blue curve in Fig. 5.13), the magnetization was nearly saturated (section of the curve labelled A; the corresponding lettered frames in the bottom section of Fig. 5.13 are representations of the spin textures from micromagnetic simulation).

As the field decreases, three large discontinuities in the net moment inferred from the optomechanical signal are observed and correspond to irreversible changes in the spin texture, beginning with nucleation of a magnetic vortex with an out-of-plane core surrounded by an in-plane curling magnetization (section B of the curve in Fig. 5.13). As the DC field is further decreased, the

vortex core translates towards the centre of the element until an intermediate texture arises; it features pronounced closure domains along the short edges perpendicular to the applied field (section C). The transition near zero field forms a two-vortex state, shown in frame D of Fig. 5.13, where the permalloy island's mushroom-like shape supports a Landau state in the stem (right side) and a distorted circular vortex in the cap (left side) [233], in keeping with the demagnetizing energetic preference for the moments near edges to be nearly tangential to the boundaries.

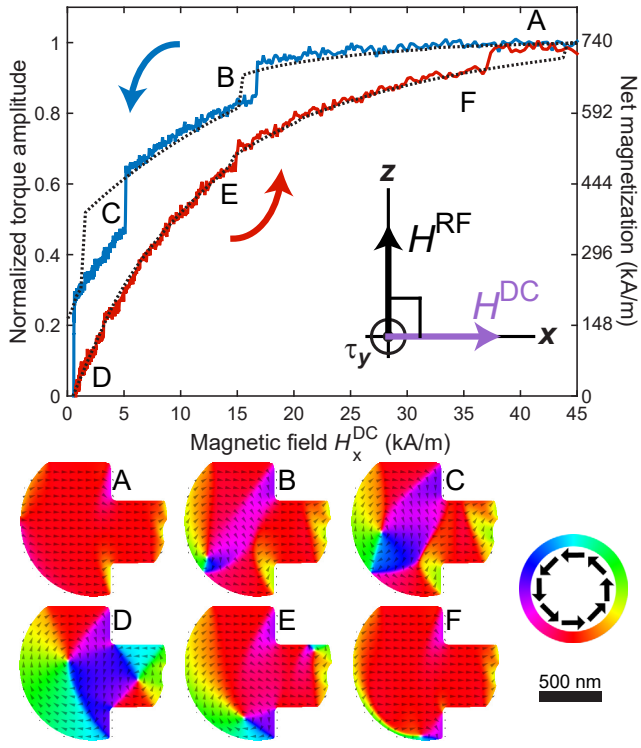

Figure 5.13: ***Magnetic hysteresis of the permalloy island.*** *Magnetization response of the permalloy element with a varying applied DC field along x (five-run average). The RF drive field is $H_z^{RF} = 35 Am^{-1}$. The solid blue trace is a decreasing field sweep and the solid red trace is an increasing field sweep. Results from micromagnetic simulations of the permalloy island (highlighted in red in the SEM inset in Fig. 5.5 and also used as the simulation mask) are plotted with black dashed lines. The bottom panel shows simulated magnetization textures at different points in the hysteresis loop. The colour wheel shows the in-plane direction of magnetization, with red parallel to the applied DC field.*

When $H_{\mathrm{x}}^{\mathrm{DC}}$ is subsequently increased (red curve in Fig. 5.13), the net moment increases monotonically with the applied field. In frame D of the simulation the two vortex cores move in opposite directions perpendicular to the field because the two circulations have opposite chiralities in this instance. The simulation frames E and F (Fig. 5.13) show the spin configurations just before each individual vortex core annihilates after the field-increasing sweep has pushed them too close to the edge to remain stable. The simulated hysteresis loop (black dashed line in Fig. 5.13) shows good qualitative agreement with observation, with the difference in the transition-field values in part because the simulations were performed without including thermal energy.

5.5.2 Magnetic Susceptibility Peaks at Barkhausen Steps

For non-normal H^{RF}, the nanocavity torque sensor can function as a susceptometer that probes RF magnetic susceptibility and provides new insights into the properties of the pinning processes. For these measurements, an in-plane x component of the RF field (parallel to the nominal H^{DC} field direction) is introduced by tuning the relative RF coil position off-centre to the device. Adjusting the relative chip-coil position is simplified experimentally by the ambient operating conditions and fibre-based readout. A small out-of-plane DC field H_{z}^{DC} combines with the oscillating field H_{x}^{RF} to generate torque in the y direction proportional to the in-plane magnetic susceptibility. Signals recorded using both z and x components of the RF drive contain both torque contributions–from the net moment along $x(\propto m_{\mathrm{x}}^{DC} H_{\mathrm{z}}^{RF})$ and from the RF magnetic susceptibility along $x(\propto \chi_{\mathrm{x}}^{RF} H_{\mathrm{x}}^{RF} H_{\mathrm{z}}^{DC})$ as derived in the Eq.(5.9), where χ is the magnetic susceptibility tensor of the permalloy island.

Figure 5.14 demonstrates the ability of the nanocavity optomechanical torque sensor to capture, in high-resolution measurements, the fine structure

in the hysteresis that is the fingerprint of intrinsic disorder unique to a given permalloy island, and cannot be predicted by the idealized micromagnetic simulations described above. The high energy density of vortex cores makes them susceptible to pinning at imperfections (surface roughness and grain boundaries) in the polycrystalline island. With diameters on the order of tens of nanometres, the cores finely probe the magnetic landscape as their positions change with applied field [210].

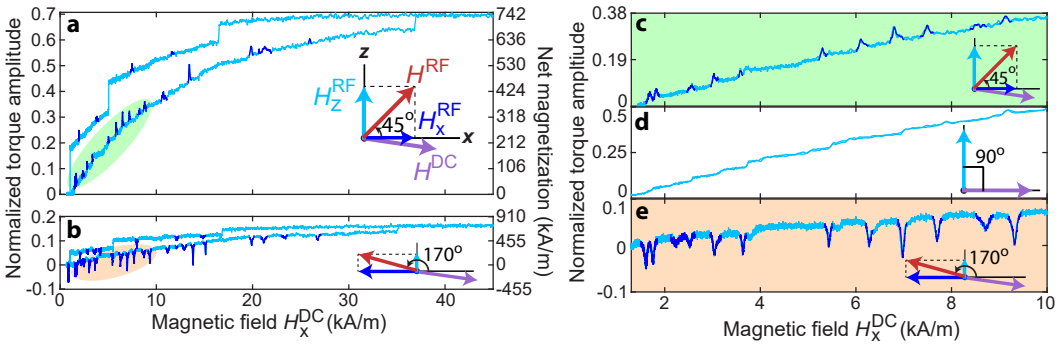

Figure 5.14: ***Enhanced room-temperature magnetic susceptibility at Barkhausen steps.*** ***a,b,*** *Hysteresis sweep with H^{RF} set to 45° (equal and same sign x and z components)* ***(a)*** *and 170° (opposite signed x and z components)* ***(b)****. A select number of upward and downward peaks are highlighted in blue to show the contribution to the torque from susceptibility.* ***c-e,*** *Low-field H_x^{DC} single forward and backward sweeps at three H^{RF} positions, 45°* ***(c)****, 90°* ***(d)*** *and 170°* ***(e)****. In all cases, the drive field $H^{RF} = 35 Am^{-1}$.*

Figure 5.14a,b shows the full hysteresis loops for two different RF field orientations, 45° (Fig. 5.14a) and 170° (Fig. 5.14b) anticlockwise from the horizontal. The torque values remain normalized to the 90° orientation. Corresponding close-ups of the low-field sections are shown in Figs. 5.14c,e. The peaks and dips newly found in the data are RF susceptibility signatures that arise when the energy barrier between neighbouring pinning sites is small enough that the in-plane RF field is able to drive the core synchronously back-and-forth. These measurements are new as of RF susceptibility due to the Barkhausen effect at the single pinning event level, though averaged events have been studied

previously [234].

Pinning and depinning events are captured as Barkhausen steps, with notable reductions in slope of the hysteresis curve seen when the cores are pinned. Figure 5.14 shows a rich spectrum of repeatable events whose character varies depending on the orientation of H^{RF}, as indicated in each of Figs. 5.14a-e. Repeatable events for H^{RF} perpendicular to the permalloy film (that is, along z) visible in section D of Fig. 5.13 are shown in close-up in Fig. 5.14d. If the applied field is kept below the first vortex-core annihilation field, curves like Fig. 5.14d show distinct steps without hysteresis when the field strength is ramped down.

5.5.3 Magnetic Susceptibility Peaks Analysis

5.5.3.1 Magnetic Susceptibility Peaks and Torque Terms

The magnetic torque formula including magnetic susceptibility terms was investigated analytically, and then estimate observed experimental susceptibility values. It was assumed that the net mechanical torque on the torsional resonator is equal to the net magnetic torque on the permalloy island and that the resulting mechanical amplitudes of motion were small enough to neglect all effects of physical rotation of the sample on its magnetism. With application of an RF field, the net magnetic moment and total applied field can be written as

$$\begin{aligned} \mathbf{m} &= \boldsymbol{m}^{\mathrm{DC}} + V_{\mathrm{Py}}\boldsymbol{\chi}\boldsymbol{H}^{\mathrm{RF}}, \\ \boldsymbol{H} &= \boldsymbol{H}^{\mathrm{DC}} + \boldsymbol{H}^{\mathrm{RF}}, \\ \chi &= \begin{pmatrix} \chi_{\mathrm{x}} & 0 & 0 \\ 0 & \chi_{\mathrm{y}} & 0 \\ 0 & 0 & \chi_{\mathrm{z}} \end{pmatrix} \end{aligned} \tag{5.7}$$

where $\boldsymbol{m}^{\mathrm{DC}}$ is the static response to $\boldsymbol{H}^{\mathrm{DC}}$, $\boldsymbol{\chi}$ is a magnetic susceptibility tensor, and V_{Py} is the volume of the permalloy island. The exerted torque at ω_{m} can be obtained by inserting the above equation into $\boldsymbol{\tau} = \mathbf{m} \times \mu_0 \boldsymbol{H}$, so that

$$\boldsymbol{\tau} = \boldsymbol{m}^{\mathrm{DC}} \times \mu_0 \boldsymbol{H}^{\mathrm{RF}} + V_{\mathrm{Py}} \boldsymbol{\chi} \boldsymbol{H}^{\mathrm{RF}} \times \mu_0 \boldsymbol{H}^{\mathrm{DC}}. \tag{5.8}$$

The torque in the y-direction can then be extracted:

$$\tau_{\mathrm{y}} \equiv \tau_{\mathrm{m_x}} + \tau_{\mathrm{m_z}} + \tau_{\chi_{\mathrm{x}}} = -\mu_0 m_{\mathrm{x}}^{\mathrm{DC}} H_{\mathrm{z}}^{\mathrm{RF}} + \mu_0 m_{\mathrm{z}}^{\mathrm{DC}} H_{\mathrm{x}}^{\mathrm{RF}} - \mu_0 V_{\mathrm{Py}} \chi_{\mathrm{x}} H_{\mathrm{z}}^{\mathrm{DC}} H_{\mathrm{x}}^{\mathrm{RF}}. \tag{5.9}$$

where $\tau_{\mathrm{m_x}}$ and $\tau_{\mathrm{m_z}}$ are DC-moment torques, and $\tau_{\chi_{\mathrm{x}}}$ is the torque generated by the RF moment. Note that $H_{\mathrm{y}}^{\mathrm{RF}}$ cannot contribute to this torque term.

When the sample is positioned on the coil axis, it is driven by a pure $H_{\mathrm{z}}^{\mathrm{RF}}$ and the torque on the sample is proportional only to $m_{\mathrm{x}}^{\mathrm{DC}}$ (χ_{z} is ignored due to the shape anisotropy inherent in the thin permalloy island). When the sample is offset from the coil axis, $H_{\mathrm{x}}^{\mathrm{RF}} \neq 0$ and the in-plane magnetic susceptibility χ_{x} can contribute to the net torque.

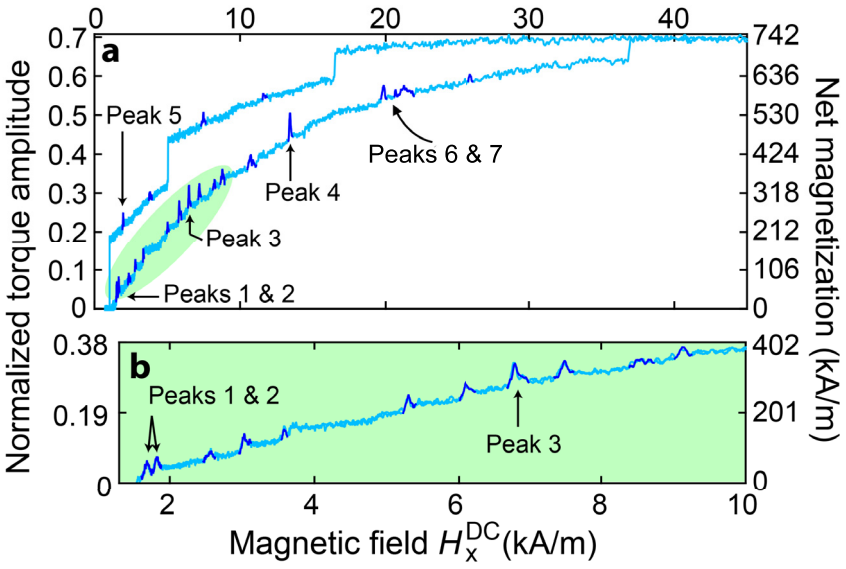

Figure 5.15: ***Peak labels.*** *The full magnetic hysteresis with peak numbers and lower branch zoom-in shown in* ***a*** *and* ***b*** *measured at non-zero out-of-plane drive amplitude.*

The on-axis torque term $\mu_0 m_x^{DC} H_z^{RF}$ is the regular net moment that produces the hysteresis curve shown in Fig. 5.13 . The additional torque exhibited at peaks and dips in Fig. 5.14, some of them labeled in Fig. 5.15, is describable by the term proportional to χ_x. A key feature is the sign change of only the magnetic susceptibility contribution when the measurements made with the sample to the left of coil center are compared with those made to the right (inverting the phase of H_x^{RF} relative to H_z^{RF}). Finally, m_z^{DC} is small on account of the shape anisotropy of the permalloy island, but should be resolvable in future experiments if back-to-back measurements can be performed at different relative phases of H_x^{RF} and H_z^{RF} while keeping all magnitudes constant.

5.5.3.2 Magnetic Hysteresis Curve Variation with RF Field Amplitude

The effect of the RF drive on the magnetic susceptibility was measured, the demonstration is shown in Fig. 5.16. It shows the hysteresis curves with peaks repeat themselves back and forth, at a specific RF drive (H^{RF}), when the H^{DC} is swept from low to high and high to low field range. The absence of any minor hysteresis at each step in Fig. 5.16 is the result of very rapid (in comparison with the measurement bandwidth) thermally activated hopping between neighbouring pinning centres [210, 211], such that the apparatus records a temporal average weighted by the relative dwell times in the two sites. Given the important role of thermally driven rapid hopping in eliminating the observed minor hysteresis at Barkhausen steps [210], the synchronization must be thermally assisted.

The peak height is proportional to the torque generated by the magnetic susceptibility term in Eq.(5.9), at each H^{RF}. In this case the device was at $\Delta x = 1.9$mm, where $|H_x^{RF}| = |H_z^{RF}|$, so that the torque response is considered for $|H_x^{RF}| = |H_z^{RF}|$. The behaviour of peaks, including peaks 1-4 labeled in Fig. 5.15, with RF drive is shown in Fig. 5.16 in this measurement window.

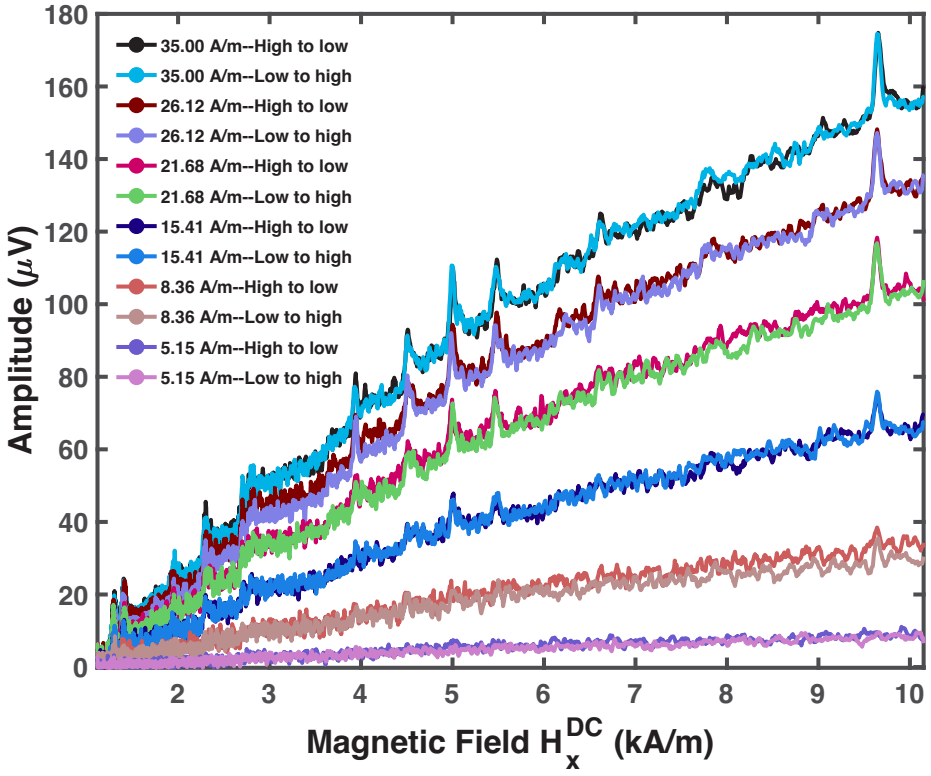

Figure 5.16: ***Hysteresis curve section with various applied RF drives*** (H^{RF})***.*** *The legend shows the corresponding calculated* H_z^{RF} *for each curve.*

The peaks 6 & 7 labelled in Fig. 5.15 were measured in a separate measurement window shown in Fig. 5.17. One can clearly observe a minor hysteresis present beside peak 7 in Fig. 5.17. This minor hysteresis loop opens up with the H^{RF}, as the peaks scale up with increasing H^{RF}. The minor hysteresis is the result of pinning of the vortex core at a pinning site where thermally activated hopping between neighbouring pinning centres is no longer valid within the measurement timeframe. The pinning barrier for this site is more than the thermal barrier for the vortex core. The main hysteresis part of the curve is still repeatable as can seen in Fig. 5.17 with high to low and low to high field sweeps overlapping each other.

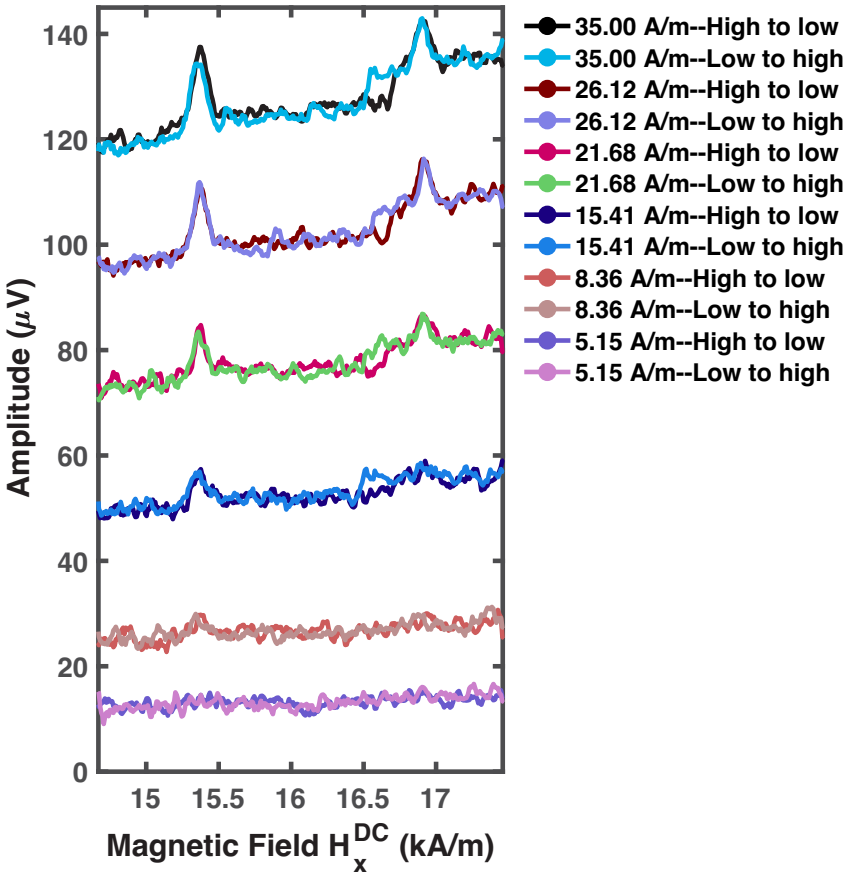

Figure 5.17: ***Peak 6 & 7 and minor hysteresis loop variation with RF drive (H^{RF}).*** *The legend outside the figure shows the corresponding calculated H_z^{RF} for each curve.*

The peak height can be calculated by subtracting the peak top from the hysteresis baseline curve value. After subtracting the baseline, what remains is the magnetic torque related to magnetic susceptibility peaks, according to the Eq.(5.9). The height for each labeled peak was calculated and then plotted in Fig. 5.18 for each RF drive level (H^{RF}). The plot clearly shows the linear response of peaks amplitude with H^{RF}. The data was then linearly fitted with $y = a + b(x)$, where the slope b represents the sensitivity of each peak with H^{RF}. The more sensitive a peak is with the H^{RF}, the more height it will get with increasing H^{RF} dependent on the pinning and dipping events at specific pinning sites. The intercept for peaks 4, 5 and 6 is negative showing that the

peak direction gets reversed. This means that the magnetic susceptibility can be positive or negative depending upon the relative RF fields.

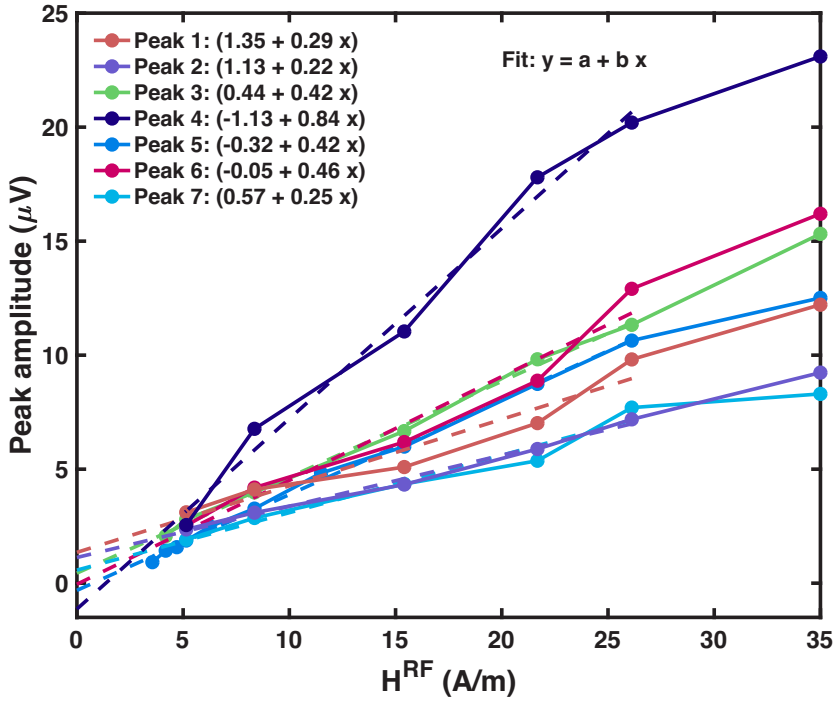

Figure 5.18: ***The experimental peak amplitude for different RF drives*** ***(H^{RF}).***

5.5.3.3 Magnetic Susceptibility Calculations for Peaks

The experimental RF susceptibility χ_{x} at each Barkhausen step is calculated based on the ratio of $\tau_{\chi_{\mathrm{x}}}/\tau_{\mathrm{m_x}}$ from Eq.(5.9), the torques generated by the RF and DC magnetization respectively,

$$\frac{\tau_{\chi_{\mathrm{x}}}}{\tau_{\mathrm{m_x}}} = \frac{\mu_0 V_{\mathrm{Py}} \chi_{\mathrm{x}} H_{\mathrm{z}}^{\mathrm{DC}} H_{\mathrm{x}}^{\mathrm{RF}}}{\mu_0 m_{\mathrm{x}}^{\mathrm{DC}} H_{\mathrm{z}}^{\mathrm{RF}}}. \tag{5.10}$$

that can be simplified to the following:

$$\chi_{\mathrm{x}} = \frac{m_{\mathrm{x}}^{\mathrm{DC}} H_{\mathrm{z}}^{\mathrm{RF}}}{V_{\mathrm{Py}} H_{\mathrm{z}}^{\mathrm{DC}} H_{\mathrm{x}}^{\mathrm{RF}}} \frac{\tau_{\chi_{\mathrm{x}}}}{\tau_{\mathrm{m_x}}}. \tag{5.11}$$

A numerical estimate of $\chi_{\rm peak}$ at each peak can be made by considering $|\tau_{\chi_{\rm x}}|$ as the size of the peak overshoot (or undershoot) normalized to $|\tau_{\rm m_x}|$, the torque from the magnetic moment at that setting of DC applied field. The numerical scale would be set by the saturation moment of the film ($V_{\rm Py}$ multiplied by the saturation magnetization $M_{\rm s} = 700{\rm kA/m}$). For $\Delta x = 1.9{\rm mm}$, where $|H_{\rm x}^{\rm RF}| = |H_{\rm z}^{\rm RF}|$, the peak magnetic susceptibility is expressed as

$$\chi_{\rm x}^{\rm peak} = \frac{m_{\rm x}^{\rm DC}}{V_{\rm Py} H_{\rm z}^{\rm DC}} \left| \frac{\tau_{\chi_{\rm x}}}{\tau_{\rm m_x}} \right|. \tag{5.12}$$

The definition of the net magnetization, $m_{\rm x}^{\rm DC}/V_{\rm Py} \equiv M_{\rm x}^{\rm DC}$ (which can be read off the graph) allows one to write:

$$\chi_{\rm x}^{\rm peak} = \frac{M_{\rm x}^{\rm DC}}{H_{\rm z}^{\rm DC}} \left| \frac{\tau_{\chi_{\rm x}}}{\tau_{\rm m_x}} \right|. \tag{5.13}$$

The magnetic susceptibility values estimated from measurements for five representative peaks are shown in Fig. 5.19a as a function of RF drive amplitude. Figure 5.19b shows sample calculations for the $\chi_{\rm x}^{\rm peak}$. Figure 5.19a shows that for a given peak, $\chi_{\rm x}^{\rm peak}$ is approximately constant (within measurement uncertainty) as a function of $H_{\rm x}^{\rm RF}$, as expected for a linear magnetic response. The measured values of $\chi_{\rm x}^{\rm peak}$ range between 40 - 400, depending on the peak. The maximum value of $\chi_{\rm x}^{\rm peak}$ is ~ 10 times larger than the quasi-static low field magnetic susceptibility in the absence of pinning (unattainable in practice). On the other hand, the enhancement is ~ 25 times larger than a typical magnetic susceptibility with the core pinned.

The enhanced sensitivity provided by these susceptibility peaks can be estimated as follows. For a given minimum detectable torque $\tau_{\rm min}$, the susceptometry can be performed on a volume of magnetic material $V_{\rm min} = \tau_{\rm min}/\mu_0 \chi_{\rm x} H_{\rm x}^{\rm RF} H_{\rm z}^{\rm DC}$. Similarly, this expression can be written in terms of a minimum detectable field $H_{\rm z,min}^{\rm DC} = \tau_{\rm min}/V_{\rm Py}\mu_0 \chi_{\rm x} H_{\rm x}^{\rm RF}$. Each of these expressions illustrates that operating near a point where $\chi_{\rm x}$ is enhanced owing to

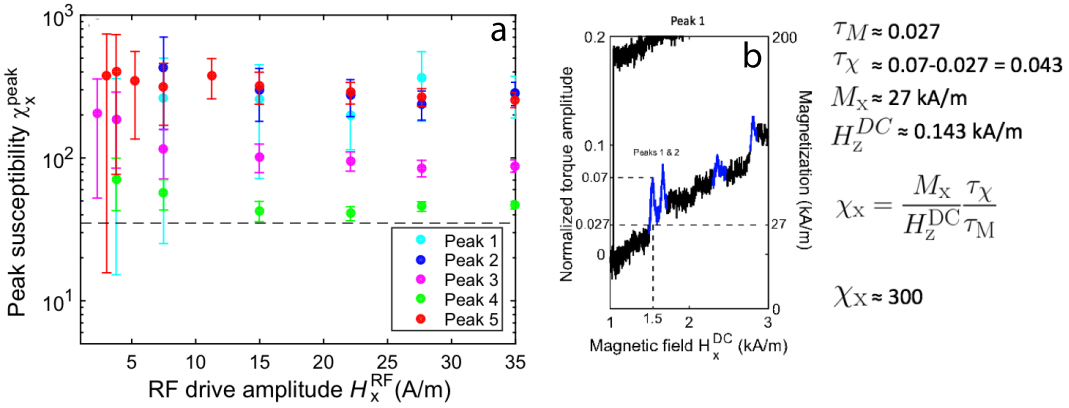

Figure 5.19: ***Estimated peak susceptibility*** *at select Barkhausen steps for* $|H_x^{RF}| = |H_z^{RF}| = 15A/m$*, for each peak identified in Fig. 5.15 as a function of RF drive.* ***a,*** *Susceptibility of each peak as a function of RF drive.The dashed lines shows the low-field quasi-static susceptibility that would be found in the lower branch in the absence of pinning (slope of linear fit to data in Fig. 5.15).* ***b,*** *Susceptibility calculation of peak 1 as sample calculations.*

microscopic properties of the material allows improved sensitivity for a given RF field. Note that owing to the mixing between RF and DC fields responsible for these peaks, the minimum detectable quantities presented above are parametrized by either the H_z^{DC} or H_x^{RF} externally controlled operating conditions.

The larger transitions between spin textures in the main loop are irreversible and therefore exhibit no accompanying RF susceptibility features. The effective susceptibility $\partial m/\partial H$ will be largest when the RF drive amplitude is just above the threshold required for a synchronous response, where the ratio of ∂m (set to a first approximation by the moment change at the Barkhausen jump) to ∂H is largest. Observed enhancements of up to 25 times over the susceptibilities when the core is pinned suggest RF susceptibility engineering in applications such as field-sensing magnetometry and detecting small volumes of magnetic material. Operating the device at a low temperature in future work is required to search for the threshold behaviour.

5.5.3.4 Effect of RF Field Direction on Peaks

Both the ratios of amplitudes and the relative signs of the net moment and magnetic susceptibility contributions in Fig. 5.14 are consistent with the changes of the RF field direction. Implementation of a scheme with an independent control of RF field components will enable quantitative separation of the magnetic susceptibility and magnetometry components through π phase shifts of individual RF drives without changing anything else, which provides further confirmation of the phenomena described above. A proof-of-principle demonstration of the ability to probe different components of the magnetic susceptibility through reconfiguration of the RF field direction is presented in this section, where the off-diagonal magnetic susceptibility of the pinning events is detected in this way.

To demonstrate the Barkhausen susceptibility features arising from the RF drive, a circuit board was designed and fabricated incorporating two separate planar transmission line circuits for generation of both in-plane and out-of-plane RF fields [15], shown in the inset of Fig. 5.20 and in Fig. 5.23. The rectangular outer loop provides H_{z}^{RF} while the central stripline applies the in-plane H_{y}^{RF} component. Each can be driven separately through 50 Ohm transmission lines using RF power amplifiers, and are designed for reduction of cross-talk between the fields generated by each loop.

Figure 5.20a shows the magnetic hysteresis for the case when only the central stripline is driven, applying an RF field that is dominantly in the y-direction. Although the magnetic susceptibility response is dominantly in the y-direction, an off-diagonal contribution to the susceptibility can result in an RF driven magnetic moment along x that produces a torque with H_{z}^{DC}, resulting in torsional deflection of the device.

Depending on the relative position of the pinning sites along x the torque generated through the susceptibility can be positive or negative. The reconfiguration of applied field geometries should allow for precise mapping of the

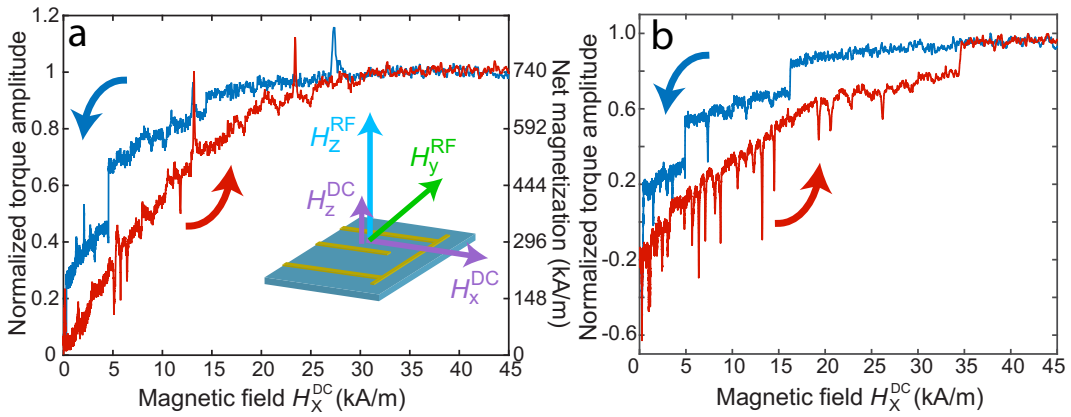

Figure 5.20: ***Magnetic hysteresis and susceptibility measurement using a planar transmission line. a,*** *The hysteresis loop was acquired while sweeping H_x^{DC} and applying the RF drive along y using the central stripline (inset). The colours of the trace represent the direction of sweep.* ***b,*** *The hysteresis loop acquired at a slightly different position (500 μm away from center) on the stripline.*

magnetic susceptibility landscape in mesoscopic magnetic structures. Figure 5.20b shows the peaks in the reverse direction, where the device was at a slightly different position on the stripline than in Fig. 5.20a. It is demonstrated that the peaks can be up-side or down-side depending upon the H^{RF} components and direction.

5.5.3.5 Effect of DC Magnetic Field Direction on Peaks

To confirm that the fine features seen in the data are Barkhausen steps, another in-plane bias field $H_y^{DC} = 300$ A/m perpendicular to H_x^{DC} was applied using a second one-inch permanent magnet positioned near the device, as shown in Fig. 5.7. Figure 5.21a show the occurrence of peak 4 at the specified H^{DC} when the second magnet is brought close to it at various distances. This additional field shifts the vortex core position in the x-direction.

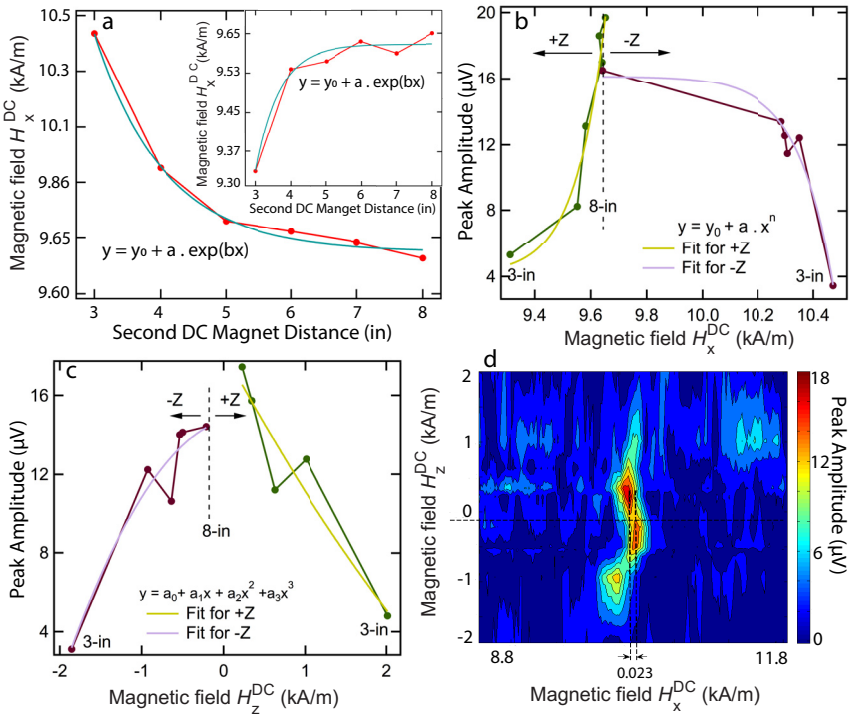

Figure 5.21: ***Peak 4 amplitude variation with varying*** H^{DC} *by adding another DC magnet at various distances and polarities.* ***a,*** H_x^{DC} *when the second magnet is in the* $-Z$ *direction. The* H_x^{DC} *is shown in the inset when the second magnet is in the* $+Z$ *direction.* ***b,*** *the peak amplitude with varying* H_x^{DC} ***c,*** *the peak amplitude with varying* H_z^{DC} ***d,*** *the peak amplitude on the map of* $H_{x,z}^{DC}$*. The horizontal dashed lines shows the* H_z^{DC} *without second magnet. The difference of 0.023 kA/m on the horizontal axis is due to the different* H_x^{DC} *by inverting the magnet direction from* $-Z$ *to* $+Z$*.*

The peak amplitude was then analyzed in Fig. 5.21b showing that the peak has maximum amplitude when the second magnet is at it's furthest distance (8 inches). Bringing the second magnet close to the device reduces the susceptibility peak amplitude. A similar amplitude response can be seen in Fig. 5.21c when the peak is analyzed with the H_z^{DC}. Figures 5.21b,c show that the peak amplitude can be altered and dependent on the H_x^{DC} and H_z^{DC}, which can be tuned by the pole direction and distance of the second magnet. The peak amplitude itself can be seen on the planar field of $H_{x,z}^{DC}$ in the colour map of Fig. 5.21d. Hence, the second magnet alters the H^{DC} components and thus alters the peak field position and amplitude.

It is expected that some different pinning sites will be encountered in the magnetizing curve versus H_x^{DC}, as found in Fig. 5.22b. Removal of the second magnet also led to a restoration of the peaks shown in Fig. 5.22a, demonstrating the robustness of these signals.

5.6 Torque-Mixing Magnetic Resonance Spectroscopy (TMRS)

One can study the transverse RF components of precessing magnetization by torque-mixing magnetic resonance spectroscopy (TMRS). TMRS allows the simultaneous recording of spin resonances and net magnetic moment of the magnetic material under observation. This simultaneous recording is possible because of the availability of ultrahigh frequency lock-in instruments (UHF, Zurich), RF transmission line actuators, and on-chip torque sensors. The multilayer circuit board of the transmission line allows one to apply RF fields, generated by a ultrahigh multifrequency lock-in amplifier through the RF power amplifier (ENI 510L 9.5W linear, 45dB, 1.7-500MHz). The resulting mechanical torque amplitude is optically read by the taper fiber in the nanocavity.

5.6.1 Control Measurements

To rule out possible optical effects such as thermo-optical shift of the cavity resonance influencing the signals, the same measurement was repeated at various laser powers. As shown in Fig. 5.22c, a reduction of input power by a factor of five did not significantly alter the Barkhausen fingerprint for a given magnetic configuration at the given frequency.

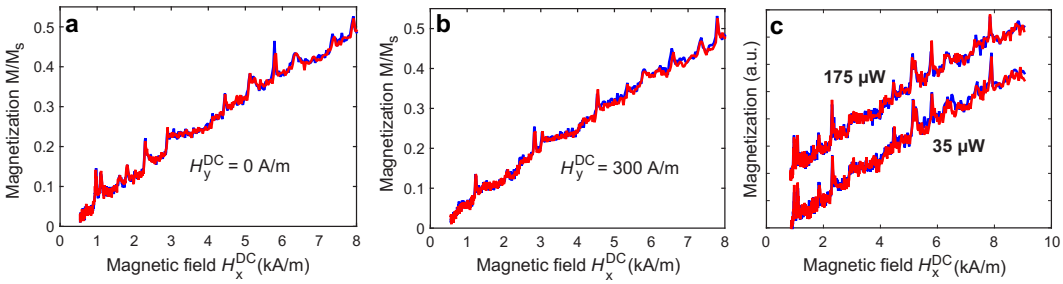

Figure 5.22: ***Characterization of low field sweeps.*** ***a****, Field sweeps with a drive field of* $H_z^{RF} = 35A/m$ *(averaged for a* $\sqrt{12}$ *noise reduction factor) in the low field regions of the curve reveal features produced by the Barkhausen effect. The upper blue and red traces are the in-phase signals of the decreasing and increasing field sweeps.* ***b****, Same as* ***a*** *except a bias field* $H_y^{DC} = 300\ A/m$ *is applied.* ***c****, Device response at different input laser power as* H_x^{DC} *is swept at low fields. The responses at 175* μW *and 35* μW *power were normalized and slightly offset for ease of comparison.*

However, the plastic (ABS) 3D printed stage for the chip didn't have a good heat sink, when device was operated under high frequency range ($\sim 500MHz$), for the torque-mixing resonance spectroscopy measurements. An example of the temperature measurements around the ABS stage, measured with an infrared (IR) thermometer, is shown in Fig. 5.23a. So, for the torque-mixing resonance spectroscopy measurements, an aluminum based stage was machined to provide a better heat sink as shown in Fig. 5.23b.

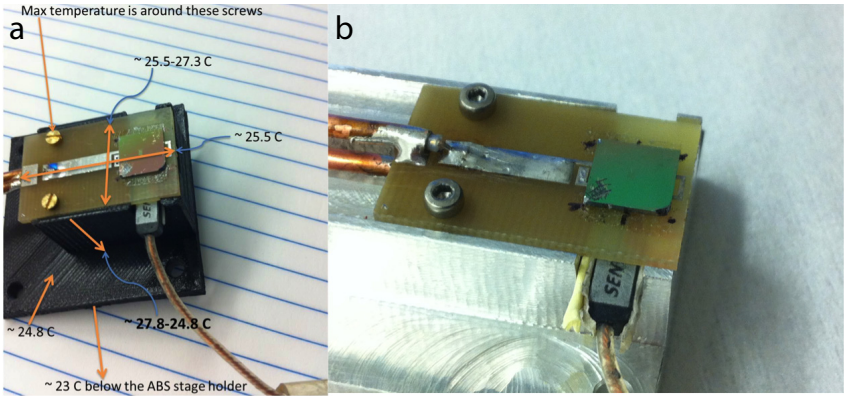

Figure 5.23: ***Transmission lines and stage.*** ***a,*** *the stage made from ABS plastic and its temperature map during the measurement.* ***b,*** *aluminum based stage to provide a better heat sink.*

5.6.2 Torque-Mixing Resonance Measurements

For torque-mixing fields were applied according to the field axes shown in Fig. 5.20. The applied RF fields were $\boldsymbol{H}_1^{\mathrm{RF}} = \boldsymbol{H}_{1\mathrm{x}}^{\mathrm{RF}} + \boldsymbol{H}_{1\mathrm{y}}^{\mathrm{RF}} = H_{1\mathrm{x}}^{\mathrm{RF}}\hat{x} + H_{1\mathrm{y}}^{\mathrm{RF}}\hat{y}$, where $|\boldsymbol{H}_1^{\mathrm{RF}}| = H_1 cos(2\pi f_1 t)$, and $\boldsymbol{H}_2^{\mathrm{RF}} = \boldsymbol{H}_{\mathrm{z}}^{\mathrm{RF}} = H_2 cos(2\pi f_2 t)\hat{z}$. The $\boldsymbol{H}^{\mathrm{DC}}$ had all three axis components with the primary component in $\hat{x}$ direction, and the secondary component in $\hat{z}$ direction. The net mixing torque by these fields can be calculated from the following equations:

$$\begin{aligned} \mathbf{m} &= \boldsymbol{m}^{\mathrm{DC}} + V_{\mathrm{Py}}\boldsymbol{\chi}\boldsymbol{H}_1^{\mathrm{RF}} + V_{\mathrm{Py}}\boldsymbol{\chi}\boldsymbol{H}_2^{\mathrm{RF}}, \\ \boldsymbol{H} &= \boldsymbol{H}^{\mathrm{DC}} + \boldsymbol{H}_1^{\mathrm{RF}} + \boldsymbol{H}_2^{\mathrm{RF}}, \\ \boldsymbol{\chi} &= \begin{pmatrix} \chi_{\mathrm{xx}} & \chi_{\mathrm{xy}} & \chi_{\mathrm{xz}} \\ \chi_{\mathrm{yx}} & \chi_{\mathrm{yy}} & \chi_{\mathrm{yz}} \\ \chi_{\mathrm{zx}} & \chi_{\mathrm{zy}} & \chi_{\mathrm{zz}} \end{pmatrix} \end{aligned} \tag{5.14}$$

where $\boldsymbol{m}^{\mathrm{DC}}$ is the static response to $\boldsymbol{H}^{\mathrm{DC}}$, $\boldsymbol{\chi}$ is the magnetic susceptibility tensor having its transverse components, and V_{Py} is the volume of the permalloy island. The exerted torque at mechanical frequency, f_{mech}, can be obtained by inserting the above equation into:

$$\begin{aligned} &\boldsymbol{\tau} = \mathbf{m} \times \mu_0 \boldsymbol{H}, \text{so that} \\ &\boldsymbol{\tau} = (\boldsymbol{m}^{\mathrm{DC}} + V_{\mathrm{Py}}\boldsymbol{\chi}\boldsymbol{H}_1^{\mathrm{RF}} + V_{\mathrm{Py}}\boldsymbol{\chi}\boldsymbol{H}_2^{\mathrm{RF}}) \times \mu_0(\boldsymbol{H}^{\mathrm{DC}} + \boldsymbol{H}_1^{\mathrm{RF}} + \boldsymbol{H}_2^{\mathrm{RF}}). \end{aligned} \tag{5.15}$$

then,

$$\begin{aligned} \boldsymbol{\tau} &= \boldsymbol{m}^{\mathrm{DC}} \times \mu_0 \boldsymbol{H}^{\mathrm{DC}} + \boldsymbol{m}^{\mathrm{DC}} \times \mu_0 \boldsymbol{H}_1^{\mathrm{RF}} + \boldsymbol{m}^{\mathrm{DC}} \times \mu_0 \boldsymbol{H}_2^{\mathrm{RF}} \\ &+ V_{\mathrm{Py}}\boldsymbol{\chi}_{f_1}\boldsymbol{H}_1^{\mathrm{RF}} \times \mu_0 \boldsymbol{H}^{\mathrm{DC}} + V_{\mathrm{Py}}\boldsymbol{\chi}_{f_1}\boldsymbol{H}_1^{\mathrm{RF}} \times \mu_0 \boldsymbol{H}_1^{\mathrm{RF}} + V_{\mathrm{Py}}\boldsymbol{\chi}_{f_1}\boldsymbol{H}_1^{\mathrm{RF}} \times \mu_0 \boldsymbol{H}_2^{\mathrm{RF}} \\ &+ V_{\mathrm{Py}}\boldsymbol{\chi}_{f_2}\boldsymbol{H}_2^{\mathrm{RF}} \times \mu_0 \boldsymbol{H}^{\mathrm{DC}} + V_{\mathrm{Py}}\boldsymbol{\chi}_{f_2}\boldsymbol{H}_2^{\mathrm{RF}} \times \mu_0 \boldsymbol{H}_1^{\mathrm{RF}} + V_{\mathrm{Py}}\boldsymbol{\chi}_{f_2}\boldsymbol{H}_2^{\mathrm{RF}} \times \mu_0 \boldsymbol{H}_2^{\mathrm{RF}}. \end{aligned} \tag{5.16}$$

Substituting $\boldsymbol{H}^{\mathrm{DC}} = H_{\mathrm{x}}^{\mathrm{DC}}\hat{x} + H_{\mathrm{z}}^{\mathrm{DC}}\hat{z}$, $\boldsymbol{H}_1^{\mathrm{RF}} = H_{1\mathrm{x}}^{\mathrm{RF}}\hat{x} + H_{1\mathrm{y}}^{\mathrm{RF}}\hat{y}$, and $\boldsymbol{H}_2^{\mathrm{RF}} = H_{2\mathrm{z}}^{\mathrm{RF}}\hat{z}$, the torque equation becomes,

$$\begin{aligned}
\boldsymbol{\tau} &= (m_{\mathrm{x}}^{\mathrm{DC}}\hat{x} + m_{\mathrm{z}}^{\mathrm{DC}}\hat{z}) \times \mu_0(H_{\mathrm{x}}^{\mathrm{DC}}\hat{x} + H_{\mathrm{z}}^{\mathrm{DC}}\hat{z}) \\
&+ (m_{\mathrm{x}}^{\mathrm{DC}}\hat{x} + m_{\mathrm{z}}^{\mathrm{DC}}\hat{z}) \times \mu_0(H_{1\mathrm{x}}^{\mathrm{RF}}\hat{x} + H_{1\mathrm{y}}^{\mathrm{RF}}\hat{y}) \\
&+ (m_{\mathrm{x}}^{\mathrm{DC}}\hat{x} + m_{\mathrm{z}}^{\mathrm{DC}}\hat{z}) \times \mu_0(H_{2\mathrm{z}}^{\mathrm{RF}}\hat{z}) \\
&+ V_{\mathrm{Py}}\boldsymbol{\chi}_{f_1}(H_{1\mathrm{x}}^{\mathrm{RF}}\hat{x} + H_{1\mathrm{y}}^{\mathrm{RF}}\hat{y}) \times \mu_0(H_{\mathrm{x}}^{\mathrm{DC}}\hat{x} + H_{\mathrm{z}}^{\mathrm{DC}}\hat{z}) \\
&+ V_{\mathrm{Py}}\boldsymbol{\chi}_{f_1}(H_{1\mathrm{x}}^{\mathrm{RF}}\hat{x} + H_{1\mathrm{y}}^{\mathrm{RF}}\hat{y}) \times \mu_0(H_{1\mathrm{x}}^{\mathrm{RF}}\hat{x} + H_{1\mathrm{y}}^{\mathrm{RF}}\hat{y}) \\
&+ V_{\mathrm{Py}}\boldsymbol{\chi}_{f_1}(H_{1\mathrm{x}}^{\mathrm{RF}}\hat{x} + H_{1\mathrm{y}}^{\mathrm{RF}}\hat{y}) \times \mu_0(H_{2\mathrm{z}}^{\mathrm{RF}}\hat{z}) \\
&+ V_{\mathrm{Py}}\boldsymbol{\chi}_{f_2}(H_{2\mathrm{z}}^{\mathrm{RF}}\hat{z}) \times \mu_0(H_{\mathrm{x}}^{\mathrm{DC}}\hat{x} + H_{\mathrm{z}}^{\mathrm{DC}}\hat{z}) \\
&+ V_{\mathrm{Py}}\boldsymbol{\chi}_{f_2}(H_{2\mathrm{z}}^{\mathrm{RF}}\hat{z}) \times \mu_0(H_{1\mathrm{x}}^{\mathrm{RF}}\hat{x} + H_{1\mathrm{y}}^{\mathrm{RF}}\hat{y}) \\
&+ V_{\mathrm{Py}}\boldsymbol{\chi}_{f_2}(H_{2\mathrm{z}}^{\mathrm{RF}}\hat{z}) \times \mu_0(H_{2\mathrm{z}}^{\mathrm{RF}}\hat{z})
\end{aligned} \tag{5.17}$$

$$\begin{aligned}
\tau_{\mathrm{y}} &= \mu_0 m_{\mathrm{x}}^{\mathrm{DC}} H_{\mathrm{z}}^{\mathrm{DC}} - \mu_0 m_{\mathrm{z}}^{\mathrm{DC}} H_{\mathrm{x}}^{\mathrm{DC}} - \mu_0 m_{\mathrm{z}}^{\mathrm{DC}} H_{1\mathrm{x}}^{\mathrm{RF}} \\
&+ \mu_0 m_{\mathrm{x}}^{\mathrm{DC}} H_{2\mathrm{z}}^{\mathrm{RF}} + \mu_0 V_{\mathrm{Py}}\boldsymbol{\chi}_{f_1} H_{\mathrm{z}}^{\mathrm{DC}} H_{1\mathrm{x}}^{\mathrm{RF}} + \mu_0 V_{\mathrm{Py}}\boldsymbol{\chi}_{f_1} H_{1\mathrm{x}}^{\mathrm{RF}} H_{2\mathrm{z}}^{\mathrm{RF}} \\
&- \mu_0 V_{\mathrm{Py}}\boldsymbol{\chi}_{f_2} H_{\mathrm{x}}^{\mathrm{DC}} H_{2\mathrm{z}}^{\mathrm{RF}} - \mu_0 V_{\mathrm{Py}}\boldsymbol{\chi}_{f_2} H_{1\mathrm{x}}^{\mathrm{RF}} H_{2\mathrm{z}}^{\mathrm{RF}}
\end{aligned} \tag{5.18}$$

Using the simple equations, $\boldsymbol{m} = \boldsymbol{M}V$, $\boldsymbol{M} = \boldsymbol{\chi}\boldsymbol{H}$, and $\boldsymbol{m} = V\boldsymbol{\chi}\boldsymbol{H}$, the above equation can be written as:

$$\begin{aligned}
\tau_{\mathrm{y}} &= \mu_0(V_{\mathrm{Py}}\chi_{\mathrm{x}} H_{\mathrm{x}}^{\mathrm{DC}}) H_{\mathrm{z}}^{\mathrm{DC}} - \mu_0(V_{\mathrm{Py}}\chi_{\mathrm{z}} H_{\mathrm{z}}^{\mathrm{DC}}) H_{\mathrm{x}}^{\mathrm{DC}} - \mu_0(V_{\mathrm{Py}}\chi_{\mathrm{z}} H_{\mathrm{z}}^{\mathrm{DC}}) H_{1\mathrm{x}}^{\mathrm{RF}} \\
&+ \mu_0(V_{\mathrm{Py}}\chi_{\mathrm{x}} H_{\mathrm{x}}^{\mathrm{DC}}) H_{2\mathrm{z}}^{\mathrm{RF}} + \mu_0 V_{\mathrm{Py}}\boldsymbol{\chi}_{f_1} H_{\mathrm{z}}^{\mathrm{DC}} H_{1\mathrm{x}}^{\mathrm{RF}} + \mu_0 V_{\mathrm{Py}}\boldsymbol{\chi}_{f_1} H_{1\mathrm{x}}^{\mathrm{RF}} H_{2\mathrm{z}}^{\mathrm{RF}} \\
&- \mu_0 V_{\mathrm{Py}}\boldsymbol{\chi}_{f_2} H_{\mathrm{x}}^{\mathrm{DC}} H_{2\mathrm{z}}^{\mathrm{RF}} - \mu_0 V_{\mathrm{Py}}\boldsymbol{\chi}_{f_2} H_{1\mathrm{x}}^{\mathrm{RF}} H_{2\mathrm{z}}^{\mathrm{RF}}
\end{aligned} \tag{5.19}$$

Rearranging the above equation,

$$\begin{aligned}
\tau_{\mathrm{y}} &= \mu_0 V_{\mathrm{Py}}(\chi_{\mathrm{x}} - \chi_{\mathrm{z}}) H_{\mathrm{x}}^{\mathrm{DC}} H_{\mathrm{z}}^{\mathrm{DC}} + \mu_0 V_{\mathrm{Py}}(\boldsymbol{\chi}_{f_1} - \chi_{\mathrm{z}}) H_{\mathrm{z}}^{\mathrm{DC}} H_{1\mathrm{x}}^{\mathrm{RF}} \\
&+ \mu_0 V_{\mathrm{Py}}(\chi_{\mathrm{x}} - \boldsymbol{\chi}_{f_2}) H_{\mathrm{x}}^{\mathrm{DC}} H_{2\mathrm{z}}^{\mathrm{RF}} + \mu_0 V_{\mathrm{Py}}(\boldsymbol{\chi}_{f_1} - \boldsymbol{\chi}_{f_2}) H_{1\mathrm{x}}^{\mathrm{RF}} H_{2\mathrm{z}}^{\mathrm{RF}}
\end{aligned} \tag{5.20}$$

The transverse susceptibility terms can be evaluated from the above equation. For the in-plane field $\boldsymbol{H}_1^{\mathrm{RF}} = H_1^{\mathrm{RF}} cos(2\pi f_1 t)$ and out of plane field $\boldsymbol{H}_2^{\mathrm{RF}} = H_2^{\mathrm{RF}} cos(2\pi f_2 t)$, the last torque term can be written as:

$$\begin{aligned}
\tau_{\mathrm{y}}^{\mathrm{RF}} &= \mu_0 V_{\mathrm{Py}} (\boldsymbol{\chi}_{f_1} - \boldsymbol{\chi}_{f_2}) H_1^{\mathrm{RF}} cos(2\pi f_1 t) H_2^{\mathrm{RF}} cos(2\pi f_2 t) \\
\tau_{\mathrm{y}}^{\mathrm{RF}} &= \mu_0 V_{\mathrm{Py}} (\boldsymbol{\chi}_{f_1} - \boldsymbol{\chi}_{f_2}) \frac{H_1^{\mathrm{RF}} H_2^{\mathrm{RF}}}{2} \left(cos(2\pi(f_1 - f_2)t) + cos(2\pi(f_1 + f_2)t) \right)
\end{aligned} \tag{5.21}$$

When the device is driven at f_{mech}, in-plane components of $(\boldsymbol{\chi}_{f_1} - \boldsymbol{\chi}_{f_2})$ contributing to the $\tau_{\mathrm{y}}^{\mathrm{RF}}$ would only be detected due to geometry of the device. For thin films, χ_{z} and other transverse components in the susceptibility tensor are ignored due to the shape anisotropy inherent in the thin films i.e., permalloy island in this device. So, only in-plane transverse susceptibility (χ_{xy}) components would be contributing to $\tau_{\mathrm{y}}^{\mathrm{RF}}$ such that:

$$\tau_{\mathrm{y}}^{\mathrm{RF}}|_{(f_{\mathrm{mech}})} = \xi \cdot \chi_{xy} \tag{5.22}$$

where ξ is constant proportional to magnetic element volume, H_1^{RF}, H_2^{RF}, and f_{mech}. The transverse moment is proportional to the transverse susceptibility. The RF torque term is proportional to the $(cos(2\pi(f_1 - f_2)t) + cos(2\pi(f_1 + f_2)t)$, where $f_{\mathrm{mech}} = f_1 - f_2$. The orthogonal RF fields $\boldsymbol{H}_1^{\mathrm{RF}}$ and $\boldsymbol{H}_2^{\mathrm{RF}}$ with frequencies f_1 and f_2, respectively, produces torque at $f1 - f2$ and $f1 + f2$. By applying the fields at f_1 and f_2, spectroscopic maps can be obtained having the information about dynamic modes of the vortex.

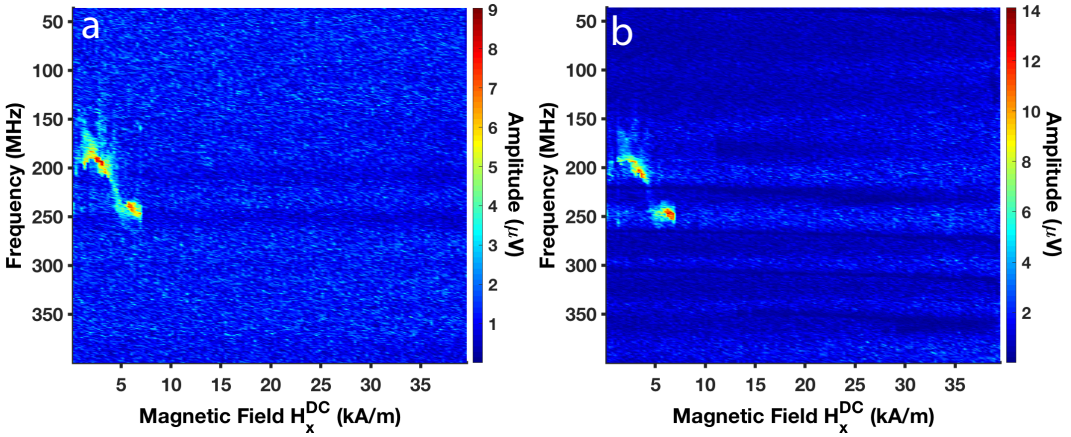

Figure 5.24: ***Torque-mixing resonance amplitude in full field range.*** ***a,*** *sweeping the field from high to low.* ***b,*** *sweeping the field from low to high. The frequency axes correspond to* f_1.

The net magnetic moment within the magnetic element in a quasi-static state is spatially nonuniform but has a well-defined spin texture. The permalloy island has a two vortex ground state at $H^{DC} = 0$ as shown in section D of Fig. 5.13. To observe the spin resonances of these vortex states, spectroscopic scans were performed in a well-defined field and frequency range. Firstly, the full field range (as in Fig. 5.13) was selected in a frequency range (25-400MHz) to find the region of interest, as shown in Fig. 5.24. The field strength increment was in 0.3759 kA/m steps during this measurement. Vortex spin resonances were found in the low field range because vortices annihilate at high fields.

The spectroscopic line scans (large field/frequency step increments) for the map of spin resonances is presented in Fig. 5.25 in the region of interest to find a rough pattern before doing the high resolution maps. The field step was 0.2321 kA/m during this measurement for high to low sweeping, and 0.2243 kA/m from low to high sweep. The data of Fig. 5.25a exhibit the vortex creation and its gyration to low field and relative high frequency. In the low to high field sweep, various modes occur whose amplitudes have an opposite trend in the frequency scale and tend to reduce in the high field region. The factors contributing to this mode behaviour are as follows: (1) at high fields

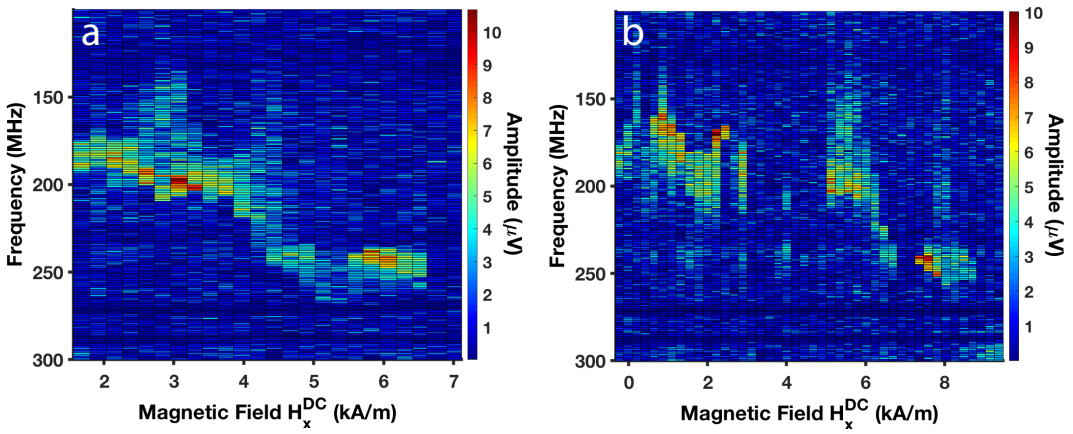

Figure 5.25: ***Torque-Mixing resonance amplitude line scans in the low-field range. a,*** *high to low field sweep.* ***b,*** *low to high field sweep.*

the spin texture tends to be more uniform, and as a result the RF contribution to the torque becomes less, (2) similarly due to high RF contribution at low fields the modes appear to be stronger in high to low field sweeps.

The regions of interest in the line scans were then acquired with high resolution scans to observe detailed features as depicted in Fig. 5.26. The torque-mixing resonance spectroscopy (TMRS) map of the vortex state of the permalloy island shows the gyrotropic frequency variations. The vortex nucleates near 6.764 kA/m and its first order gyration mode can be seen in Fig. 5.26a, while vortex annihilation and its first order gyration behaviour is shown in Fig. 5.26b. After the nucleation process, the core can be driven for gyration creating the resonance signals. The random gyration is dependent on the random polycrystalline nature of the permalloy element. The broad range gyration of the vortex core depicts the nature of the pinning sites. The quasi-uniform spin texture resonances ends at 6.764 kA/m and a new configuration of vortex nucleation appeared. The results were repeated multiple times to confirm its existence, and were averaged where required.

Figure 5.26b shows the zoom-in scan of the gyration feature when the field was swept from high to low. The apparent slightly different shape is because of

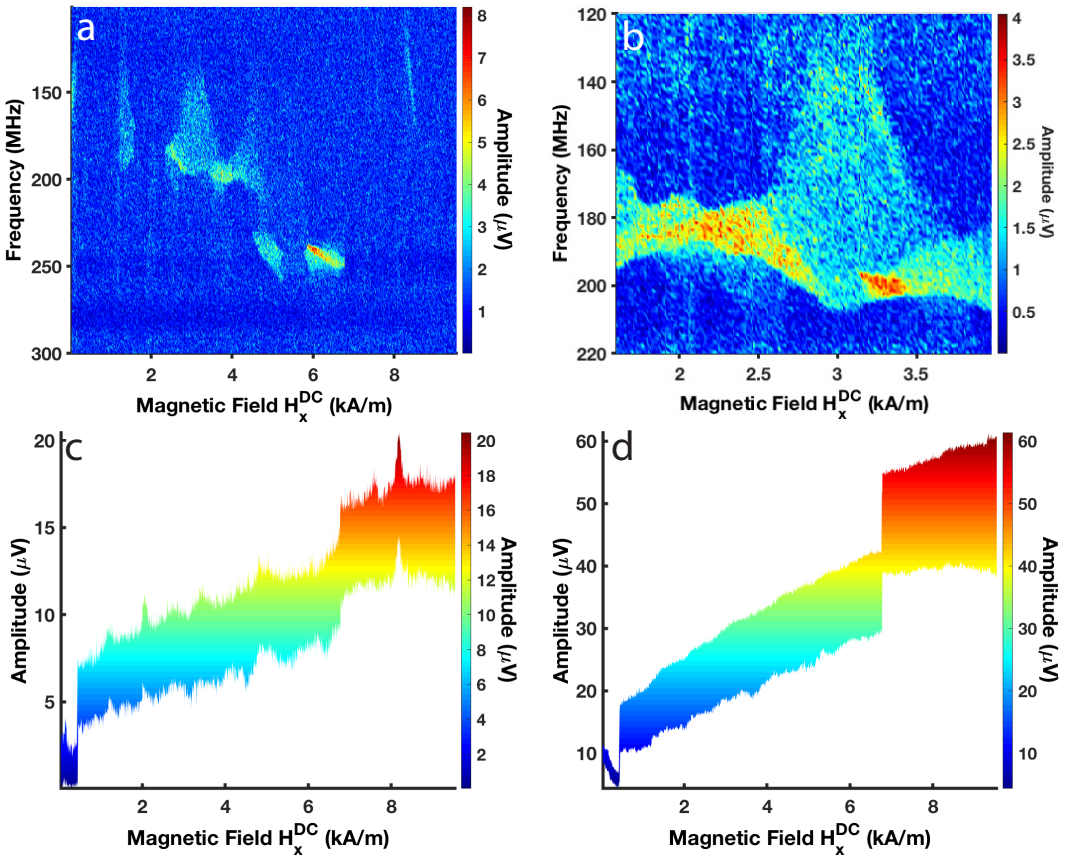

Figure 5.26: ***High resolution torque-mixing resonance amplitude for high to low field sweep.*** ***a,*** *high to low field sweep in low field range with 0.0111 kA/m steps.* ***b,*** *zoom-in scan in the specified field range with 0.0112 kA/m steps.* ***c,*** *simultaneous acquisition of direct-torque actuated by* H_y^{RF}. ***d,*** *simultaneous acquisition of direct-torque actuated by* H_z^{RF}.

the scaling and slightly different initial conditions of the scan. The most critical parameter is the heating by the high frequency sweeps that changed the cavity modes and hence changes the optical coupling that affects the signal. The vortex continues to gyrate in a particular frequency window (160-200MHz) while the field is stepping down.

These gyration modes from the mixing torque can be compared with the magnetization curve from the direct torque acquired simultaneously. Figure 5.26c shows the direct torque obtained when $\boldsymbol{H}_1^{\mathrm{RF}}$ is actuated having the susceptibility peaks described in the previous sections. The $\boldsymbol{H}_2^{\mathrm{RF}}$ actuation gives

the corresponding direct torque as shown in the Figure 5.26d. The broader width of the data is due to the overlap of all frequency sweeps. The TMRS resonance modes in Fig. 5.26a are independent of the susceptibility peaks in Fig. 5.26c. The independent actuation of resonance modes and susceptibility peaks is a key advantage of the TMRS technique.

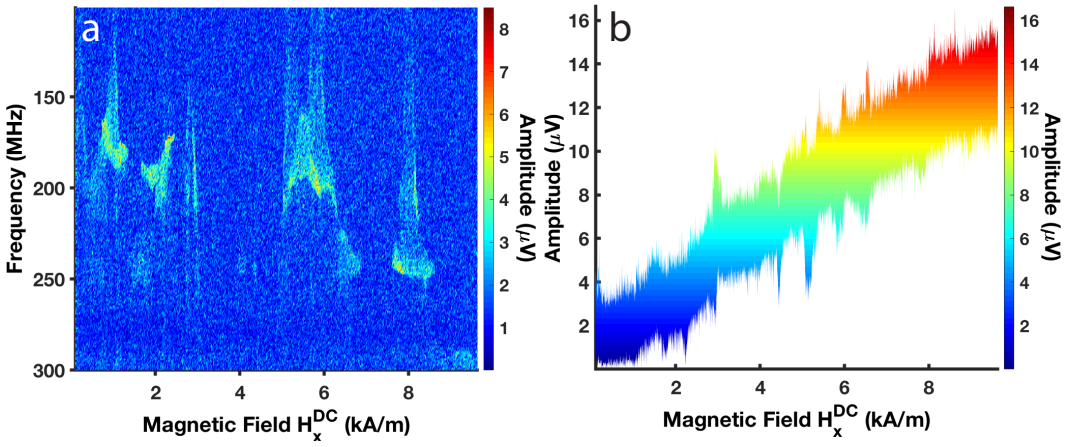

Figure 5.27: ***High resolution torque-mixing resonance amplitude for low to high field sweep. a,*** *low to high field sweep in the low field range with 0.0111 kA/m steps.* ***b,*** *simultaneous acquisition of direct-torque actuated by* H_y^{RF}.

The spectroscopic map from a low to high sweep in the low field range is shown in Fig. 5.27a. The resonance peaks appear with the vortex core gyration which annihilate completely at 8.595 kA/m. The corresponding direct torque actuated by $\boldsymbol{H}_1^{\mathrm{RF}}$ is shown in Fig. 5.27b.

5.7 Reproducibility and Throughput

The data presented above in this chapter were obtained from a single device that was observed to display the largest optomechanical magnetic transduction of those fabricated for this study. However, other devices were observed to display similar magnetic properties. The quality of the signal obtained from these devices was typically lower owing to poorer fibre coupling, lower Q_{o}, or larger

misalignment of the permalloy pad with the nanobeam pad. These limitations are primarily a result of fluctuations in the electron beam lithography dose during device fabrication.

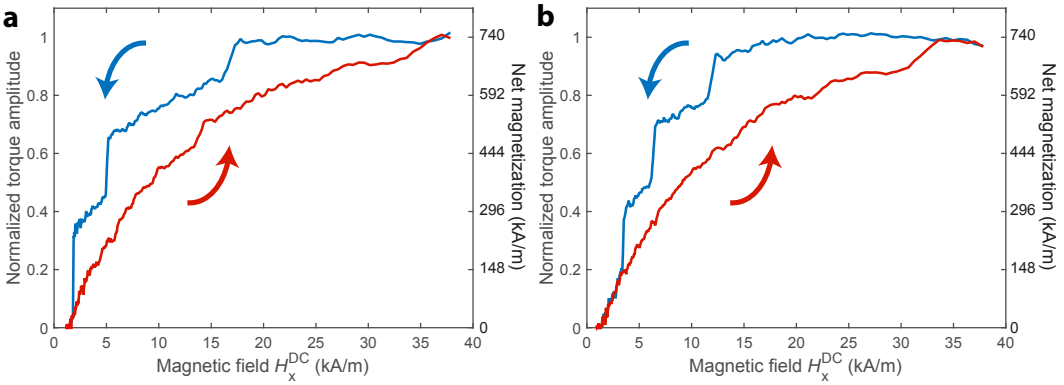

Figure 5.28: ***Magnetic hysteresis of neighbouring devices.*** *Magnetic hysteresis measurements for devices fabricated immediately to the left* ***a*** *and right* ***b*** *on the same chip as the devices studied throughout this chapter.*

Figure 5.28 shows low-resolution magnetic hysteresis measurements of the devices fabricated immediately to the left and right of the device studied throughout in this chapter. The magnetization of these devices displays qualitatively similar jumps and hysteresis related to vortex formation. Note that these measurements are affected by larger than optimal drift in device relative position, as well as irregular magnetic field step size. These technical issues were reduced during the measurements presented in previous sections.

5.8 Comparison with other technologies

Among torque magnetometers, the reported device has state-of-the-art sensitivity of 1.3×10^{-20} Nm, despite operating in ambient conditions where its mechanical resonances are significantly damped. Among optomechanical torque sensor devices not yet used for magnetometry, devices with better sensitivity have been demonstrated operating in vacuum and/or cryogenic conditions. For

example, a see-saw double-photonic-crystal nanobeam [206] reaches torque sensitivity of $9.6 \times 10^{-21}\mathrm{Nm}(\mathrm{Hz}^{1/2})^{-1}$ in 10^{-4} Torr vacuum, and optomechanical devices in mK conditions have been measured with record $10^{-24}\mathrm{Nm}(\mathrm{Hz}^{1/2})^{-1}$ sensitivity [40]. However, none of these devices have yet been used for magnetometry or to probe other systems. These devices can reach, if not surpass, those sensitivities in similar conditions, where Q_m is expected to increase by orders of magnitude owing to elimination of air damping in vacuum and reduction of internal damping in silicon at low temperature [228].

5.9 Conclusion

In conclusion, nanocavity optomechanical detection for torque magnetometry and RF susceptometry have been demonstrated experimentally. The devices presented here enabled a detailed study, under ambient conditions, of the magnetostatic response and thermally assisted driven vortex-core hopping dynamics in a mesoscopic permalloy element under an applied field. This torque magnetometry technique complements other device-based nanoscale magnetic probes. Compared to planar micro-Hall approaches [142], which have been used to probe single pinning sites but have not been used to measure RF susceptibility, nanocavity torque magnetometry offers a higher frequency operation. Although it has yet to offer the single-spin sensitivity of nitrogen-vacancy-centre based imaging [155, 159], it provides a comparatively fast acquisition of net magnetization, which allows measurement of magnetic hysteresis and susceptibility. Reconfiguration of the RF fields allows the probing of enhanced susceptibility components of single pinning events, and demonstrates that this magnetometry approach fulfils key requirements for an optomechanical lab-on-a-chip for nanomagnetism.

The nanocavity optomechanical device is ready to be integrated with nanoparticle assemblies, following the device optimization with permalloy as

a dry-run. The device has enough sensitivity to measure a countable number of nanoparticles in ambient conditions. This would be useful for studying the magnetism of live magnetotactic bacteria [235], spin frustration triangular magnetic lattice [236] (can be generated by magnetic nanoparticles), and single spin detection [43] in ambient conditions. The presented device here has excellent torque and magnetic moment sensitivities ,but relatively low magnetic field sensitivity. The sensitivity limit could be further improved by designed higher frequency resonators, and using better material for increased optomechanical coupling i.e., diamond [237, 61] and gallium phosphide [56]. New devices integrated with large magnetic volume were devised for ultra-high magnetic field sensing torque magnetometers, which are presented in Chapter 6.

Chapter 6

Nanomechanical Torque Magnetometry of a Thick YIG (Yittrium Iron Oxide) Disk

6.1 Motivation and Introduction

The development of modern technologies has made possible the emergence of nanoscale and power efficient devices. One key point for consideration is to utilize the devices and materials to also generate the operational energy by themselves [238]. This approach opens up the field of spintronics, among others, for the foundation of sustainable technologies. The excitation in electron spins in magnetic material results in spin waves that have a diverse dispersion relations depending on the material characteristics, applied fields and their orientations. Spin waves in magnetic materials usually occur in the microwave frequency range that can be tuned according to the required application [239]. Spin waves are normally excited by the ferromagnetic resonance (FMR) through the observation of ground state of magnetization at microwave frequencies. A standard FMR experiment demands that the sample has lateral dimensions in the sub-millimeter range (80 μm) [14].

In the top-down approach, the standard sample dimension needs to be scaled-down for the on-chip magnetic applications. This involves the reduction of the sample dimensions to nanometer range (i.e., thin films) for required applications, while taking care of high quality and low damping [240]. Nonetheless, the microwave properties of the spin waves changes with the sample dimensions. The bottom-up approach, on the other hand, require a compromise on sample dimensions for better spatial resolution in microwave frequency magnetic measurement of normal modes because of the inadequacy of spatial techniques. Thus, this approach requires larger sample dimensions for the highly spatially resolved spin dynamic modes [241]. Large magnetic moment (means large magnetic volume) is also required for the experiments which involve measurements of magnetomechanical ratio (Einstein-de Haas effect) [242]. An ultra-high sensitive field sensing magnetometer has been developed using the spin resonances of the magnetic element [243] with $5pT/\sqrt{Hz}$ sensitivity. The highest field sensitivity of 4μT was observed for torque magnetometer device in Chapter 5, thus provides motivation to look for torque magnetometers with ultra-high field sensitivity.

I aim to utilize a sample dimension range in between and top-down and bottom-up scales, for tuning the magnetic properties for simultaneously probing the above mentioned approaches i.e., (i) to control spin resonance frequencies for potential telecom and spintronic applications, (ii) to build miniature Einstein-de Haas experiment for reduced uncertainty in magnetomechanical ratio of the magnetic element, and (iii) to establish a platform for the ultra-high sensitive field sensing magnetometers. The approach here to design lab-on-chip devices for nanomagnetism with simultaneous acquisition of magnetization, susceptibility, and spin resonances for above experiments. I used yttrium iron garnet (YIG) milled down to a micrometer range, since all of the above experiments require large magnetic element volume.

The YIG ferrimagnet, having low-damping [244] and the narrowest

linewidth of the FMR, generally lower than 0.5 Gauss (39.79 kA/m) and with a magnon lifetime of a few hundred of nanoseconds and spatially observable at mesoscopic scales [239, 244], makes it the best material for microwave frequency and data transport applications. Being an insulator, YIG has no electrons in the conduction band, which reduces the dissipation resulting in low-damping and narrow linewidth. A magnonic field benefits the communication and information storage and processing using spin waves. The spin wave motion is widely used in logic devices such as spin-wave logic gates, data-buffering elements, magnon transistors and in electric control of magnetic materials [245]. YIG has profound linear, non-linear dynamics [246], high magneto-optical efficiency [247, 248], strong Faraday rotation [249] and low optical loss at communication wavelengths that makes it useful for various devices: oscillators [250, 251], generators [252], filters[251, 253], optical isolators [254], waveguides [255], power limiters [256], delay line [257], pulse separators, multi- channel receivers [239], compressive receivers [253], directional couplers [258] and circulators [259], signal-to-noise enhancers [260], parametric amplifiers [261] and convolvers [262], and other devices [239, 241, 244, 254, 263].

There have been complementary methods for measuring spins by performing magnetic resonance spectroscopy and microscopy. This includes electron spin resonance (ESR) [264], nuclear magnetic resonance (NMR) [265], magnetic resonance force microscopy (MRFM) [266], ferro-magnetic resonance force microscopy (FMRFM) [14], and torque-mixing magnetic resonance spectroscopy (TMRS) [15]. TMRS has the ability to measure the transverse RF components of precessing magnetization as well as DC torque components simultaneously. So far, TMRS is performed on small sample sizes but it can be scaled up to larger sample sizes without any limitations. I aim here to utilize a sample size in mesoscopic range and perform the TMRS for spin waves in the sample.

6.2 YIG Disk on the Silicon Membrane Nanomechanical Devices

A single crystal bismuth doped yttrium iron garnet (Bi:YIG) ferrimagnet was used in the experiment that has a complicated cubic crystal structure. Each unit cell has a dimension of 12.376Å containing 80 atoms [239, 263]. It has two octahedral and tetrahedral sub-lattices that are coupled antiferromagneticaly. The Bi:YIG films are grown by molecular beam epitaxy on top of a gallium gadolinium garnet (GGG) substrate with unit cell dimension of 12.383Å, having a close match with the unit cell of the Bi:YIG leading to the high quality of the grown film [239].

For the lateral dimensions of the sample in the sub-micron range, chemical etching is used that often may change the crystal properties, magnetizations and thus the spin dynamics of the YIG sample. In order to avoid chemical etching and reduced ion milling, mechanical polishing was used to get the film thickness of $7\mu m$. A disk of $17\mu m$ size was first cut with focused ion beam (FIB) from the polished film. The disk was oriented with the surface perpendicular to the $< 111 >$ axis. The details of sample preparation with mechanical polishing is summarized in Appendix E. The Ga+ ion damage to the YIG disks are presented in Appendix F, and related efforts for domain visualization are enclosed in Appendix G.

A current of 13 nA was used to mill the disk to the $7\mu m$ film thickness of the polished YIG. A metallic probe inside the FIB machine was used to pick, pluck, and place the fabricated disk on the $2\mu m$ thick silicon membrane. The YIG disk was welded to the silicon surface with carbon bonding by chemical vapor deposition in the FIB machine.

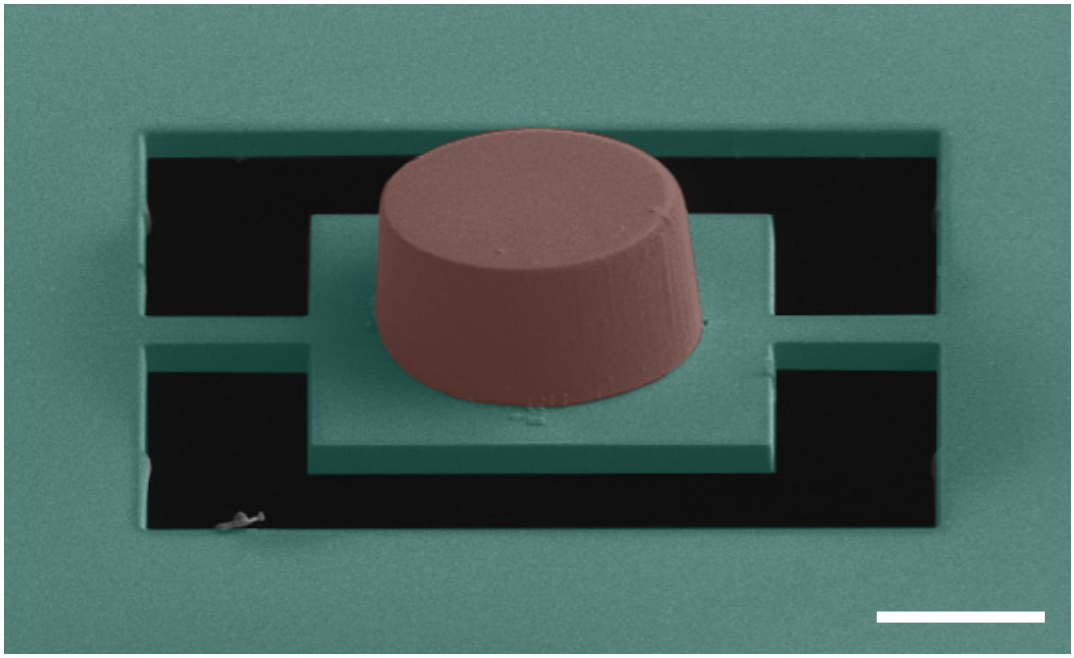

Figure 6.1: ***False colour SEM of the YIG disk on a fabricated nanomechanical device in the silicon membrane.*** *Green colour represents the nanomechanical device in the silicon membrane, and red colour shows the YIG disk. Scale bar is* $10\mu m$.

A nanomechanical device was then fabricated around the bonded YIG disk. A scanning electron microscope of the YIG disk on top of the fabricated nanomechanical device is shown in Fig. 6.1.

The frequency spectrum of the device was then obtained at the resonating paddle location and at the nearby membrane to rule out the membrane modes, as shown in Fig. 6.2. There were only two resonating frequencies detected for this device, one at 0.982 MHz and other at 1.426 MHz. The membrane mode appears at 1.285 MHz frequency in the blue (device) and grey (membrane) colour so it can be ruled out of the resonance modes of the device. The 0.982 MHz frequency mode only appears at the device and there is no membrane background at this frequency.

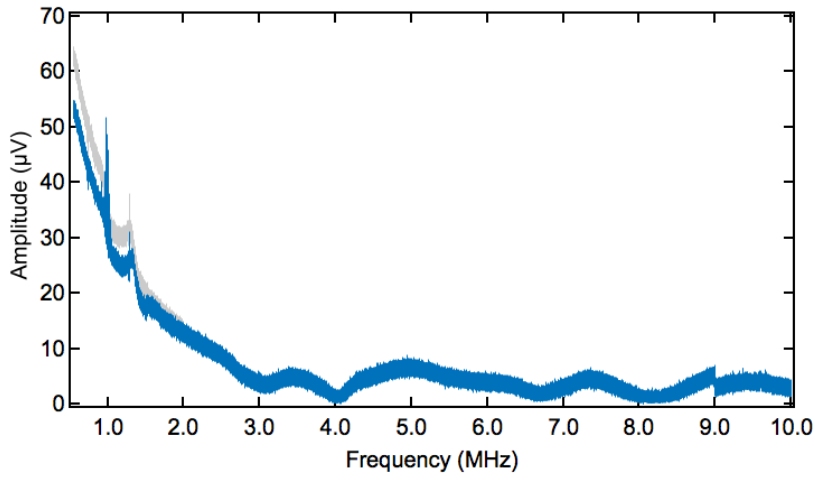

Figure 6.2: ***Spectral response of the device.*** *Grey colour represents the spectrum taken at the membrane near the device. Blue colour represents the spectral response of the device with the YIG disk.*

A nanomechanical device has two basic modes of resonance: a flexural mode and a torsional mode. For the aformentioned device, only one frequency (0.982MHz) was detected and the second resonance mode was not detectable with the described setup. The device was also scanned from 250 kHz to 1 MHz with high resolution to find the torsional mode but no torsional resonance peak appears except the background from RF drive. The device was measured at 0.982 MHz with the raster scans to find out the type of the resonance mode at this frequency. (Another device without a YIG disk was also tested to subtract the background modes as a control).

The raster scan measurements of the device at the 0.982MHz frequency were carried out as shown in Fig. 6.3. The tilted SEM image of the device with YIG disk is shown in Fig. 6.3a. The DC component of the raster scan is shown in Fig. 6.3b. The DC component of the reflected light determines the area and location of the scanned device. The AC component (R) of the torque amplitude is represented in Fig. 6.3c, which confirms the flexural mode of the device at 0.982MHz. The device breathes in and out of the plane in the flexural mode. The phase of the device in the AC torque component in Fig.

6.3d shows that the device resonates differently than the membrane around it and it endorses the flexural mode of the device.

These measurements are based on the laser interferrometric method explained in Chapter 2. The crescent inside the YIG disk area comes from the thickness variation of the disk, which is reflected as the signal contrast. The maximum DC reflectance and AC torque is at the position where the YIG disk has maximum thickness because of the mass load in the flexural mode.

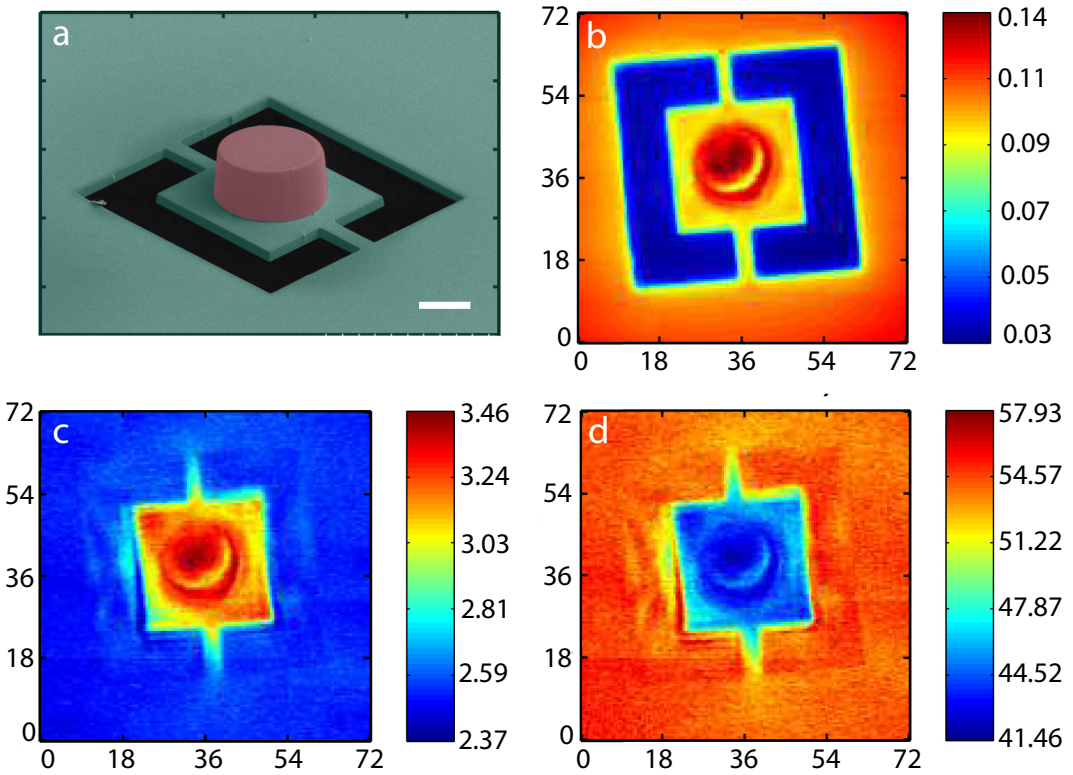

Figure 6.3: ***Raster scan of the YIG disk on a fabricated device in the silicon membrane at 0.982MHz.*** ***a,*** *Tilted false colour SEM of the YIG device. The scale bar is* $10\mu m$*.* ***b,*** *DC raster scan of the device.* ***c,*** *AC resonance scan of the device.* ***d,*** *phase of the resonance response. The x- and y-axis in* ***b,*** ***c,*** *and* ***d*** *are in microns. The colour bars show the amplitude in* μV *in* ***b*** *and* ***c,*** *and shows the phase in deg for* ***d****.*

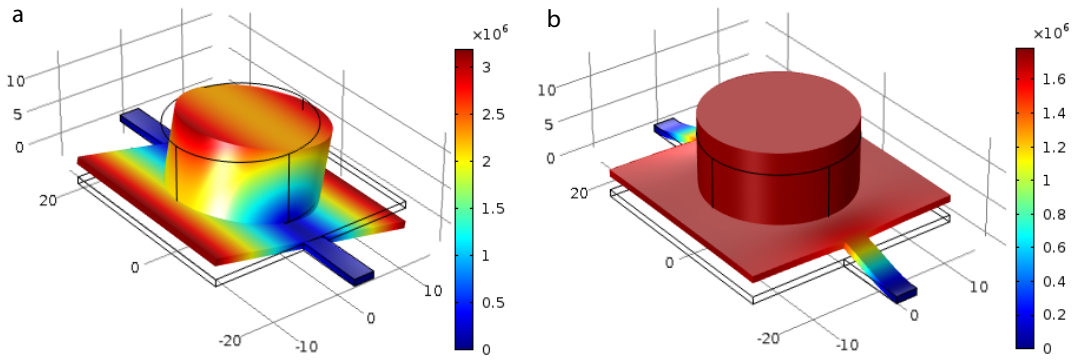

Figure 6.4: ***Comsol simulations of the YIG disk on the device. a,*** *torsional mode* ***b,*** *flexural mode.The colour bars are in arbitrary units.*

The AC signal fades out at the torsional rods and vanishes at the membrane. Figure 6.3c shows that the device has a little twist in the flexural mode since all the corners of the resonator paddle do not have the same amplitude. The frequency at 1.285 MHz is the membrane mode confirmed from the raster scan of the device and area around it. There is no other frequency found for the device and membrane other than these two frequencies, 0.982MHz and 1.285 MHZ, at 632 nm of the laser wavelength for the Fabry-Pérot cavity.

The Comsol simulations of the big YIG disk are shown in Fig. 6.4. The torsional mode occurs at 0.6378 MHz and the flexural mode occurs at 1.1467 MHz in the simulations, which are close to the experimentally determined frequencies 0.982 MHz and 1.285 MHZ. A primary magnetic hysteresis curve is presented in Fig. 6.5 and was obtained using the flexural mode of the device for the thick YIG disk. The maximum torque amplitude occurs near 40 kA/m instead at high field (80 kA/m). The shift of the maximum torque to lower values at higher applied field is caused by the misalignment of the laser beam, which is created due to the presence of magnetic parts in the setup. A three dimensional magnetic spin texture moves within the magnetic disk with the magnetic field sweeps. The magnetic spin texture finds the minimum energy to relax to at the low fields.

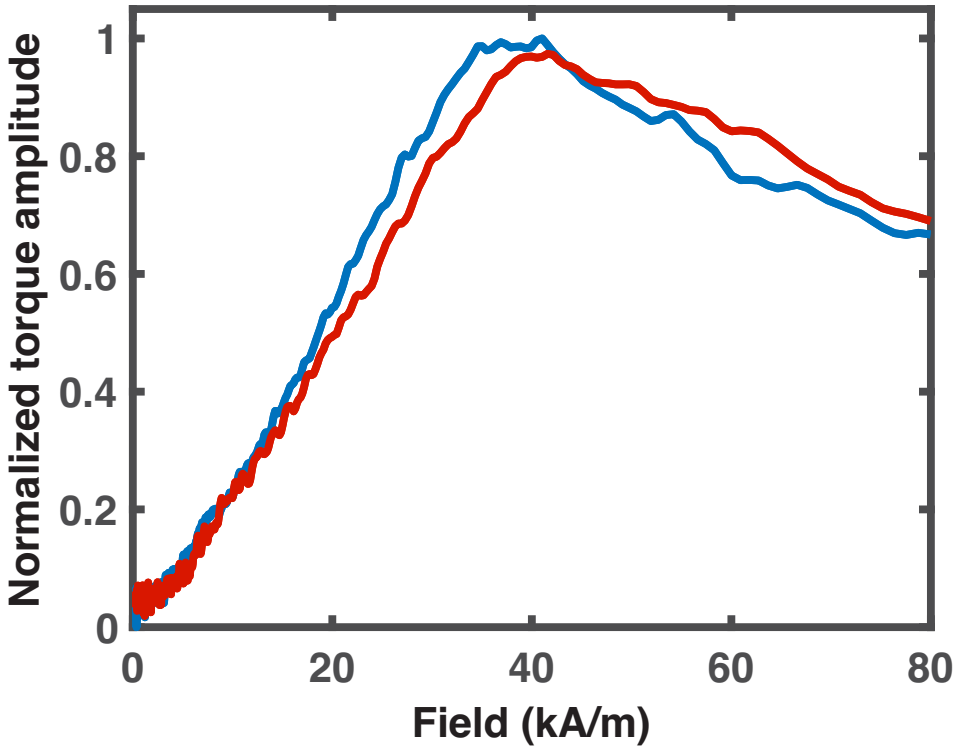

Figure 6.5: ***Magnetic hysteresis of the YIG disk on a fabricated device in the silicon membrane.*** *Blue colour traces the high to low field sweep while red colour shows the low to high field sweep.*

6.2.1 Optical Fiber Setup and Resonance Modes Detection via Optical Fiber

For the exploration of the torsional mode, an optical fiber laser setup was established at higher wavelengths (1546 nm instead of 632 nm) to increase the silicon transparency. The uniform background at the edges of the membrane could be due to the low interference visibility in Fig. 6.3b. The higher wavelength should resolve this issue. Figure 6.6 shows some of the fiber laser setup components. The setup operates at room temperature and ambient pressure conditions. The blue box was 3D printed from ABS plastic to avoid random air flow over the device. The optical microscope at the top was used to view the gap (less than a millimeter) between the sample and fiber laser.

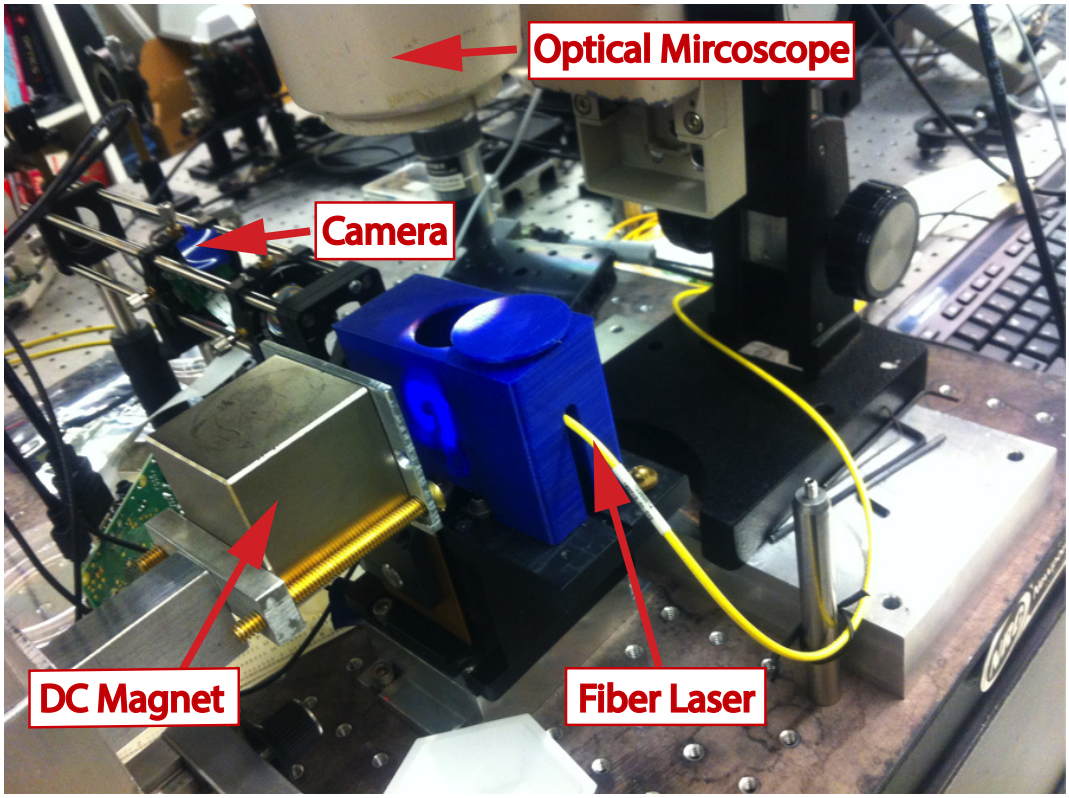

Figure 6.6: ***Optical fiber laser setup.***

A raspberry pi camera was used to view the devices from the rear and to align the laser in front of the silicon device. The Fabry-Pérot cavity isn't created in this case and the membrane was used without a silicon back-reflector. The DC magnet was mounted on the magnetic rail and was perpendicular to the AC coil and the optical microscope. The AC coil was attached to the back of the membrane chip. The camera, AC coil, chip, and fiber laser were aligned along one axis of the setup.

The resonance signal was obtained with a spectrum analyzer (HP 8594E, 9kHz-2.6GHz). The FFT applied in the spectrum analyzer on the overlapping sampling rate (data acquisition) gives us the real time peak that exists for the system under observation. The same peak at 0.982MHz was detected using the fiber laser setup, as shown in Fig. 6.7. A good peak is obtained for this flexural mode at 5mV of the applied RF field. A bandwidth of 10 dB and

span of 1MHz was used for the data obtained from the spectrum analyzer. It is concluded that the torsional mode might have a very small amplitude that is buried inside the noise floor and is beyond the sensitivity of the measuring setup and is due to the thick silicon membrane device.

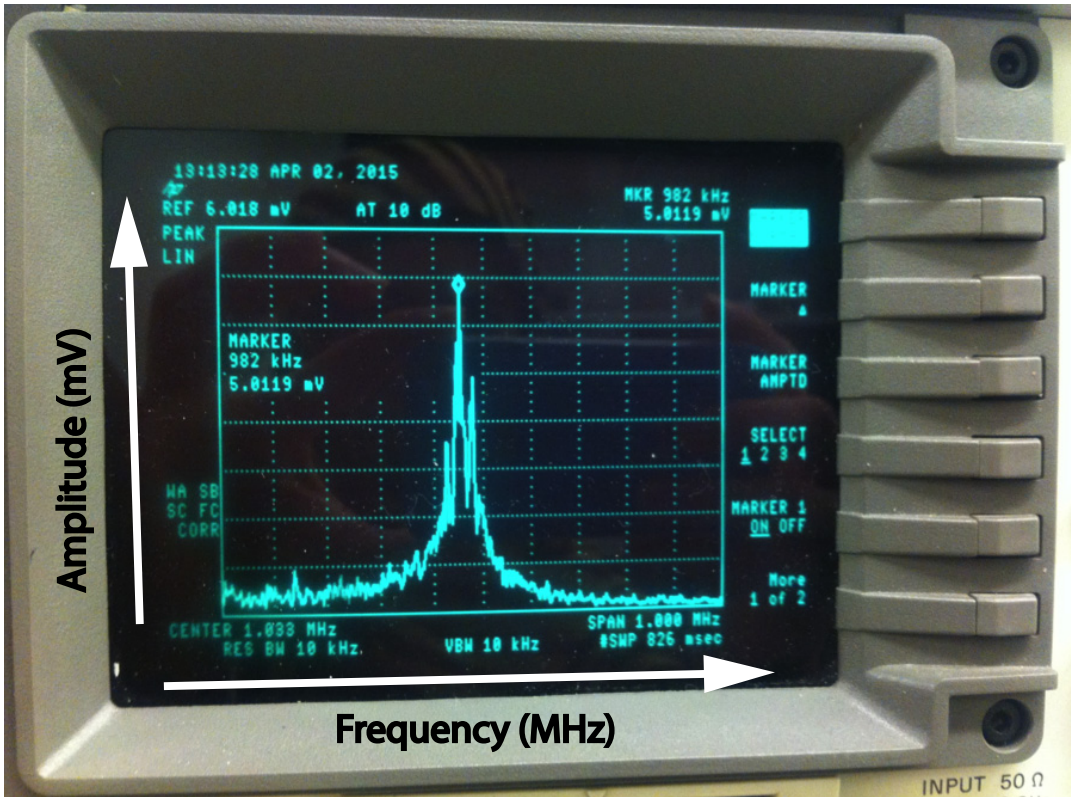

Figure 6.7: ***Resonance spectrum in optical fiber laser setup.***

6.3 YIG Disk on the SOI Nanomechanical Devices

New nanomechanical devices in the silicon-on-insulator (SOI) were made in order to observe good torsional mode torque amplitude and better signal to noise ratio. The device (paddle) size was reduced from $30\mu m$ to $6\mu m$. The YIG disk dimensions were reduced from $17\mu m$ to $2.8\mu m$ in diameter, and thickness from $7\mu m$ to $1.25\mu m$, since the silicon top layer was only 300 nm thick. Figure

6.8 shows scanning electron micrographs of the two types of nanomechanical devices with YIG disks. It was found that the device in Fig. 6.8a had a better amplitude signal than the device in Fig. 6.8b because of it's shape. The extra paddle around the square resonator in Fig. 6.8a provided good spots for laser focusing and increased the torque amplitude. These devices are used for torque magnetometry measurements by using the method described in Chapter 2.

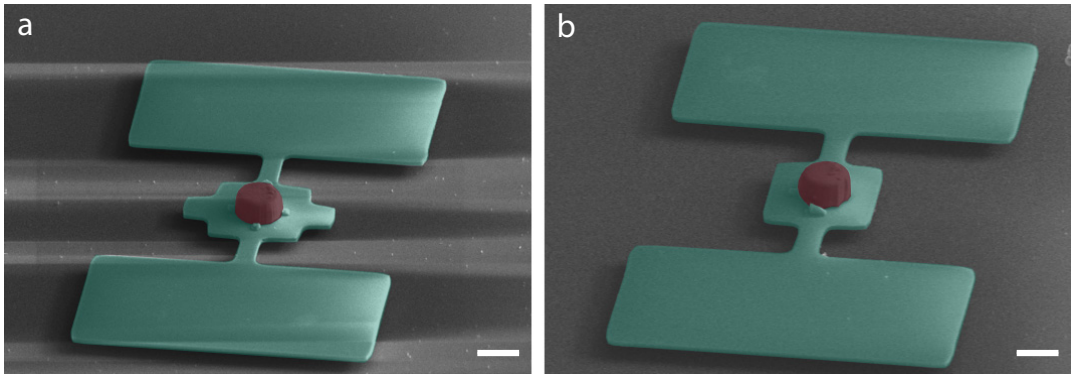

Figure 6.8: ***False colour SEM of the YIG disk on nanomechanical devices fabricated on a SOI chip. a,*** *device with ear-shaped resonating paddle.* ***b,*** *device with square shape resonating paddle. Green colour shows the devices while red colour shows the YIG disks. The scale bars are* $3\mu m$.

The spectral response of the device in Fig. 6.8a is shown in Fig. 6.9. Figure 6.9a shows the full range spectrum of the device which depicts the flexural mode at 1.326 MHz and torsional mode at 4.603 MHz. Fig. 6.9b shows the zoom-in spectrum of the resonance peak at torsional mode. The peak shows a perfect Lorentzian shape and the phase shift at the resonance peak gives us information about the difference of phase from the reference signal of the RF drive for the torsional mode at resonance.

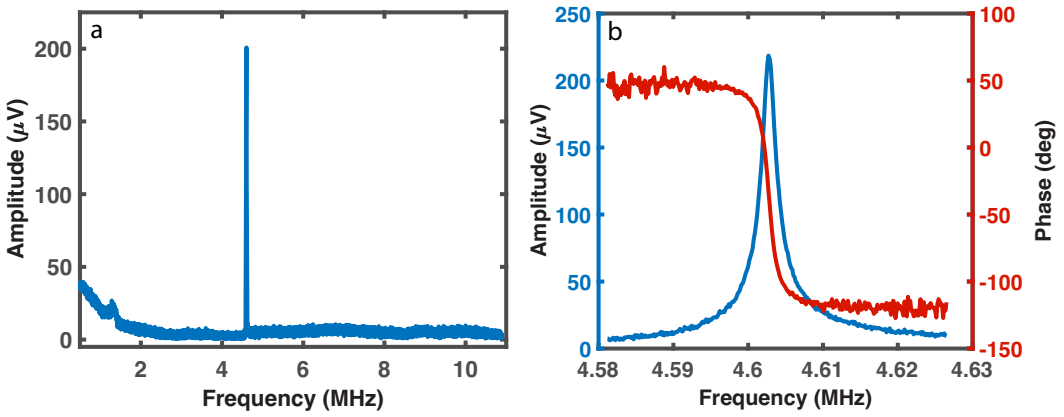

Figure 6.9: ***Spectral response of the device in Fig. 6.8a fabricated on a SOI chip.*** ***a,*** *resonance peak of the device with ear-shaped resonating paddle.* ***b,*** *zoom-in spectrum of the device. Blue colour represents the resonance peak and red colour shows the corresponding phase shift on resonance.*

To get the spectral response in Fig. 6.9, an AC dither coil was used to drive the device in the presence of DC bias field. The coil consists of three loops of insulated copper wire with a diameter of nearly 3mm to allow laser passage. The coil was driven at the resonance frequency of the device by a sinusoidal signal provided by the frequency generator and connected to the lock-in amplifier for reference. The setup was capable of spatial imaging by piezo-controlled (three axis movement) rastering with a 256×256 pixel resolution (at maximum). The diffraction limit of the optical objective lens for laser defined the optical resolution of the spatial image.

The device in Fig. 6.8a was raster scanned to find out the mode shape from the reflectance of the laser interferometric signal for the respective frequencies. Figure 6.10a represents the scanning electron micrograph of the same device and Fig. 6.10b shows the DC raster scan of the small central area of the device ($18\mu m \times 18\mu m$). The in-phase component of the AC torque amplitude is shown in Fig. 6.10c, which gives us the confirmation of the torsional mode at 4.603MHz, while the quadrature component of the AC torque amplitude is shown in Fig. 6.10d.

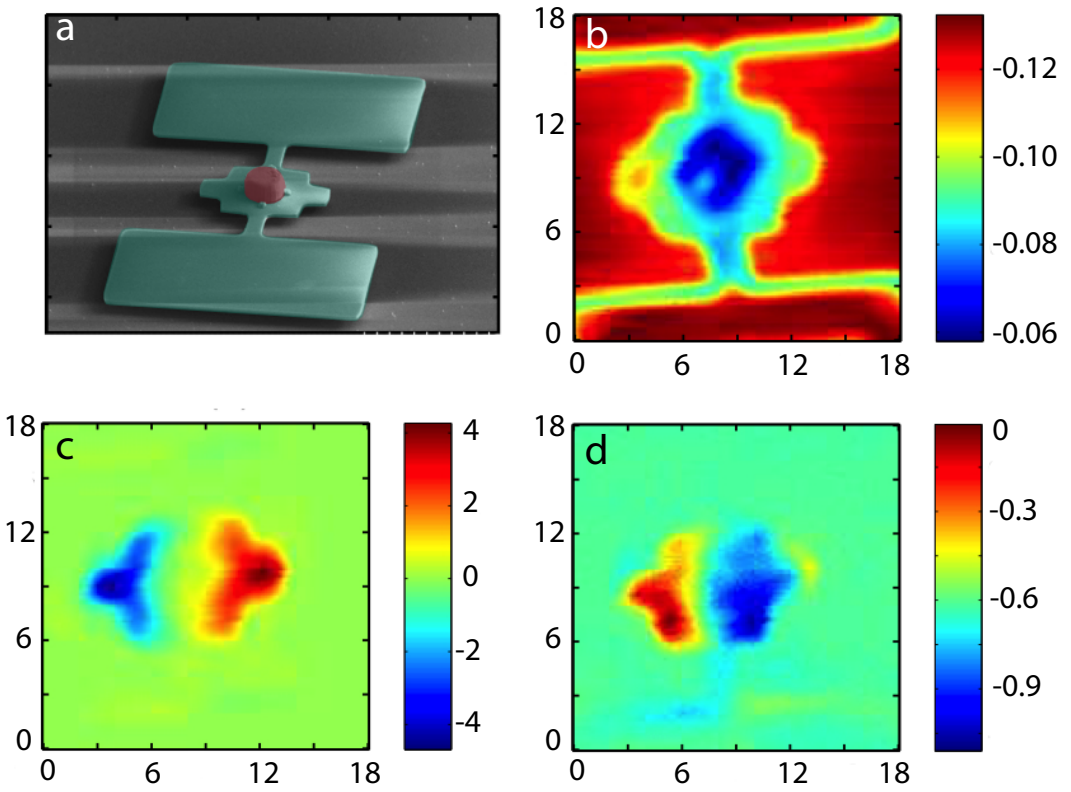

Figure 6.10: ***Raster scan of the YIG disk on the device in a SOI chip. a,*** *Tilted false colour SEM of the YIG device.* ***b,*** *DC raster scan of the device.* ***c,*** *x-component of the AC torque response of the device.* ***d,*** *y-component of the AC torque response of the device. The x- and y-axis in* ***b, d,*** *and* ***d*** *are in microns. The colour bars show the amplitude in μV.*

After the confirmation of the torsional mode of resonance, the magnetic measurements were taken. The magnetic hysteresis curve of the device under discussion is shown in Fig. 6.11. It shows both the magnetic hysteresis measured experimentally and obtained from simulation. A three dimensional spin texture is formed at point A in the hysteresis for the vortex nucleation that is created at B and relaxed to ground state at point C in the high to low field sweep. The three dimensional vortex starts to be annihilated at D and is completely annihilated at F after passing through the pinning site at E. The wider difference between the increasing and decreasing fields in the range $18 - 30$ kA/m for the experimental hysteresis compared to the simulated hys-

teresis curve is because of the different initial conditions. A uniform state of magnetization is assumed in the hysteresis simulation that can be a challenge experimentally for the thick YIG disk. The experimental hysteresis curve was repeated multiple times (giving similar results) and averaged. The spin texture of the labeled points in the experimental hysteresis curve are shown in Fig. 6.12.

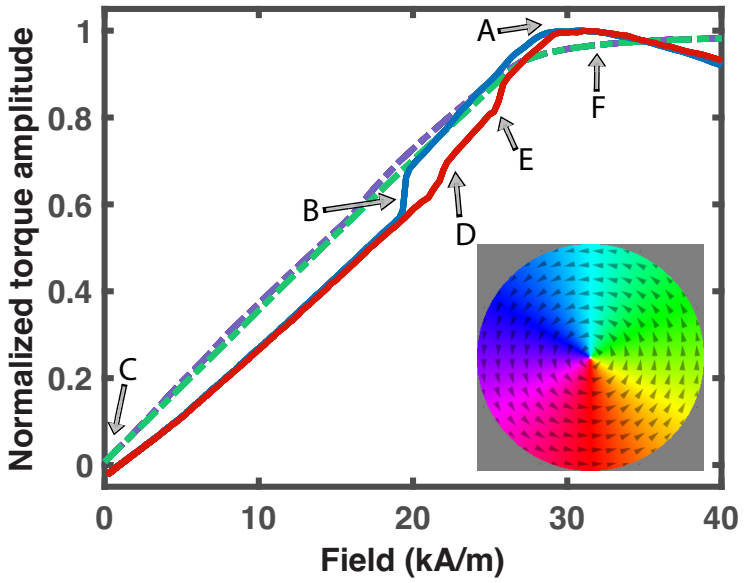

Figure 6.11: ***Magnetic hysteresis of the YIG disk.*** *Blue and red colours represent the high to low and low to high field sweeps of the experimental hysteresis curve respectively. Purple and green colours show the high to low and low to high field sweeps of the simulated hysteresis curve respectively. The inset is the colour scheme for magnetization orientation in simulations, for which the spin texture of the labeled points in experimental hysteresis curve are shown in the Fig. 6.12*

The circular disks of radii in the mircometer range or smaller produce the magnetic vortex configuration, with an out-of-plane component with a high energy density vortex core in the center of the disk, and an in-plane component with circular magnetization around the disk. If the thickness of the disk is smaller, the vortex stays in the two dimensional configuration around the perimeter of the disk, with the vortex core in the center of the disk. For disks, where the thickness becomes large and forms a cylindrical shape, the two dimen-

sional vortex transforms to the three dimensional vortex state having polarity and chirality. The polarity defines the in-plane and out-of-plane components of the vortex core, while the chirality defines the clockwise or counter-clockwise in-plane orientation.

The magnetic structure forms a three dimensional spin texture in the thick YIG disk. The transition at point B is from a three dimensional spin texture to a three dimension complex vortex state and becomes the seed for the spin texture in Fig. 6.12C, which represents the three dimensional vortex having two cores at opposite ends with opposite polarity and chirality. Figure 6.12D, E, and F represent the process of vortex annihilation.

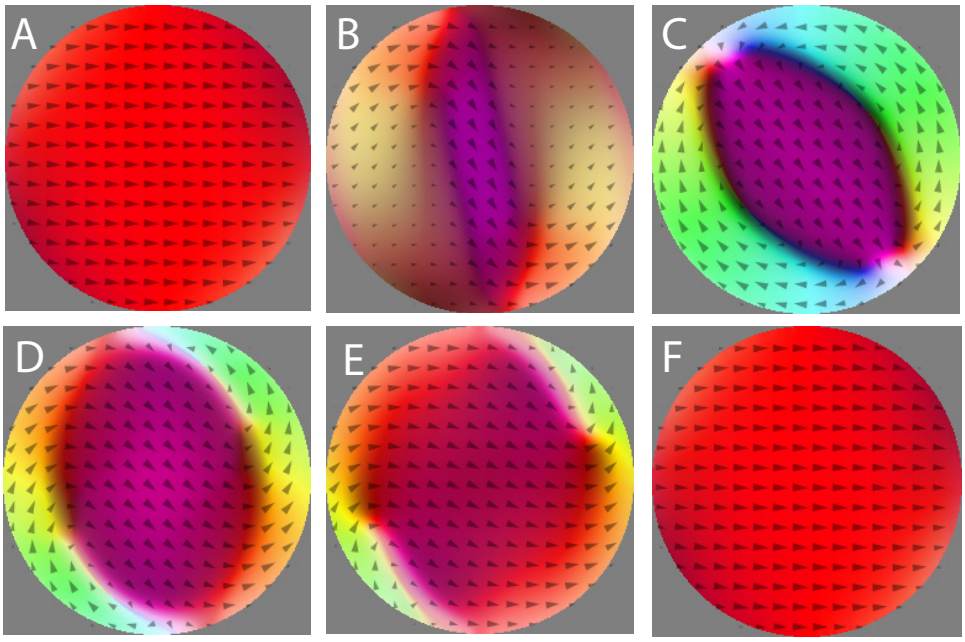

Figure 6.12: ***Spin texture of the magnetization from the micromagnetic simulations.*** ***A-F*** *are the images of spin texture at the points in experimental hysteresis curve labeled in the Fig. 6.11.*

The vortex core oscillates in a pattern when it is displaced from equilibrium with a field pulse. This forms the dynamic mode in gyration (gyrotropic mode) of the vortex. The gyrotropic mode is fundamental magnetic resonance modes where vortex core circulates around the equilibrium position. The vortex core

outsets in gyration when it is disturbed from its equilibrium position by applying an in-plane radio-frequency (RF) field pulse. Small RF drives result in linear gyrotropic modes while higher pulse amplitude (with respect to magnetic element dimensions) result into the nonlinear dynamics of vortex. The vortex core is a rigid column of out-of-plane magnetization in thin magnetic disks. In the fundamental gryrotropic mode (zero-order, uniform), core ends precess in-phase on top and bottom surfaces of the disk. Higher order gryotropic modes appear when the thickness of disk is increased, e.g., vortex core ends precess out-of-phase in one-node gryrotropic mode (first-order mode). The gyrotropic mode and its higher order modes occur in the hundreds of MHz and GHz frequency range, that depends on the dimensions of the disk. The pinning sites in disk shifts the gyrotropic frequency to higher range. These modes were acquired for YIG disk using the torque-mixing resonance spectroscopy (TMRS) when the DC bias field is perpendicular to the torsion rods. The fields axes scheme is described in [15] and also explained in Chapter 2 and in Chapter 5, and the results are described below.

The experimental TMRS taken from high to low field sweep, to obtain the field dispersion of resonances, looks very fluidic as shown in Fig. 6.13. The transition at 19.8 kA/m is that from the saturated state (quasi-uniform spin) to the complex vortex state, as seen in the hysteresis loop at point B of Fig. 6.11. Upon the transition to the 3D vortex texture (at 19.8 kA/m), the quasi-uniform spin resonances abruptly end and new 3D vortex resonances appear. The vortex creation was reproducibly observed as the frequency gets near to the first resonance mode.

The rich resonance spectrum for the confined magnetic structure of the YIG disk is present. The TMRS map of resonance modes of the complex vortex state in the single-crystalline YIG disk has fundamental gyrotropic, its higher order modes, and spin wave modes. There are more than two transitions (23, 22 and 19.8 kA/m) that occur in the mixing signal (Fig. 6.13) that also appear the net

moment in the hysteresis (Fig. 6.11) due to vortex nucleation and pinning. The spectrum shows the gyrotropic modes below 19.8 kA/m, and spin-wave modes above 19.8 kA/m. The fundamental gyrotropic mode (zero-order, uniform) and one-node gryrotropic mode (first-order mode) exist at 15 MHz and at 60 MHz and in 0-19.8 kA/m field range respectively, where the resonant frequency is almost constant. The resonance remains constant for these modes because the vortex core moves in the defect-free regions. The vortex core precess within the circular disk, in this case, under the potential profile of two dimensional harmonic oscillator defined by the in-plane magnetization stiffness [267, 268]. These fundamental gyrotropic modes appear at very low frequencies as compared to the anticipated values [269] in hundreds of MHz range. This thick YIG disk has lower gyrotropic frequency (15 MHz) because the disk dimensions are very large. The vacuum boundaries are far away for the disk which reduces the magnetic stiffness and hence reduces the gyrotropic mode frequency. The spin-wave modes (above 19.8 kA/m) move to higher frequencies at higher fields, useful for spin dynamics based resonance devices.

The vortex core becomes highly localized when it encounters a pinning site, which increases the magnetization stiffness resulting in higher frequency of the gyrotropic modes (higher order gyrotropic modes). These higher order gyrotropic modes exist for the current disk in 75-450 MHz frequency range and 0-19.8 kA/m field range (see Fig. 6.13). The gyration of vortex was driven to higher amplitudes in higher frequency area generating strong resonance signals in the unpinned areas of the disk. One of such strong resonance signal can be seen near 350 MHz and 11 kA/m. At the pinning sites, the reduced differential magnetic susceptibility is observed where the resonance signal drops out. The resonance modes can be controlled, by introducing the localized engineered defects [210] by focused ion beam milling, for potential applications, e.g., conversion of MHz signal to telecom wavelengths. The study of dynamic effects of vortex core pinning along the gyration path would be compelling to

observe. TMRS benefits for the study of broadband resonance spectrum in magnetic elements (includes thin and thick disks). Additionally, its ability to simultaneously acquire data for spin resonances (gyrotropic and spin-waves), susceptibility, and magnetization is of great use for lab-on-chip nanomagnetism. Einstein-de Haas experiment on these miniature devices is ongoing in the lab.

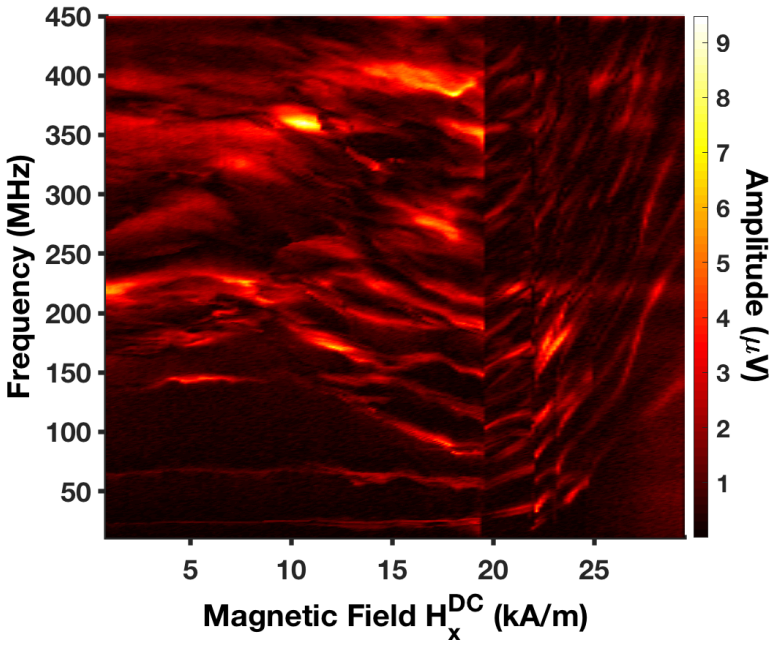

Figure 6.13: ***Torque-mixing resonance mode.*** *Spin texture of the AC torque-mixing resonance mode in the YIG disk from the experiment.*

The double paddle resonators were fabricated and two identical YIG disks were placed on the two paddles as shown in Fig. 6.14, for building ultra-high sensitive field sensing magnetometers. The idea is create an artificial pining site in one of the YIG disks while keeping the other as pristine disk. By driving the two disks simultaneously, the vortex will get pinned at the artificial pinning site in the modified disk and the effective susceptibility would reduce for this disk, while the susceptibility in the pristine disk would have the normal high value. The differential susceptibility two disk would result in ultra-high sensitivity for field. This experiment is also currently being performed in the lab.

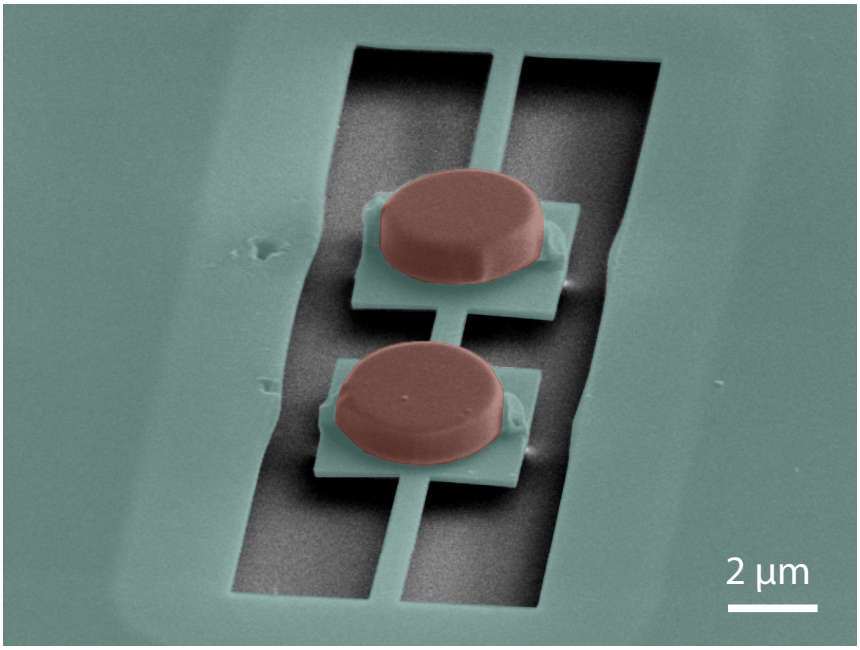

Figure 6.14: ***Ultra-high sensitive field sensing.*** *False colour SEM of two identical YIG disks on a fabricated nanomechanical Double paddle resonator in SOI. The YIG disks are* $0.85\mu m$ *in thickness and* $2.6\mu m$ *in diameter. Green colour represents the nanomechanical device, and red colour shows the YIG disks. (Image credit: J. Losby for device fabrication and M. Belov for YIG disk milling and transfer onto the device.)*

6.4 Conclusion

The YIG disk of larger size (2.8μm in diameter and 1.25μm thick) than previously reported [15] was used for the broadband spin resonance spectroscopy. TMRS for this sample was used from lower frequency (small induction) to the microwave frequency range (large induction signals). The spin resonances of the mesoscopic YIG disk were explored combined with the direct torque measurements, showing the transition of spin-wave modes to gyrotropic modes and its encounter with the local defects (pinning sites), advantageous for spin based resonance devices. Spin mode resonance frequencies could be further controlled by the engineering of pinning sites (defects). The measurements for a miniature Einstein-de Haas experiment and for the ultra-high sensitive field sensing mag-

netometers are currently in progress in the laboratory. The next step would be to integrate these large magnetic volumes on the nanophotonic optomechanical torque magnetometers developed in Chapter 5 for ultra-miniaturized lab-on-chip devices for nanomagnetism in ambient conditions.

Chapter 7

Conclusions & Future Recommendations

7.1 Conclusions

In this Thesis, nanomechanical torque magnetometery and highly-sensitive optomechanical torque magnetometery techniques were developed for the characterization of nanoscale magnetic elements. Early developments were focused on assembling the magnetic nanoparticles on the nanomechanical torque magnetometers. Later work concentrated on building new highly-sensitive optomechanical torque magnetometers and RF susceptometers for magnetic element characterization. The later work is the baseline for assembling a countable number of magnetic nanoparticles on the optomechanical torque devices.

In Chapter 3, nanomechanical torque magnetometry of the silicon nitride membrane-based devices was demonstrated. These devices were good enough to transduce a signal of ~ 350 stable single domain magnetic nanoparticles (55 nm in size), harvested from magnetotactic bacteria. This approach was capable of measuring the magnetic properties of small-scale stable single domain magnetic nanoparticles and larger assemblies of magnetic nanoparticles, but was not capable of measuring small size nanoparticles (9 nm). These devices had a

magnetic moment sensitivity of $7 \times 10^8 \mu_B$ under vacuum conditions.

The device sensitivity was further improved by extending the nanofabrication process to the nanomechanical torque sensors in silicon-on-insulator chip with greater sensitivity, as demonstrated in Chapter 4. Nanomechanical torque magnetometry was demonstrated on the geometrically patterned self-assembly of magnetic nanoparticles. The displacement, torque, and magnetic moment sensitivities were 7.5×10^{-14}m$(\text{Hz}^{1/2})^{-1}$, 7.0×10^{-20}Nm$(\text{Hz}^{1/2})-1$, and $5\times10^7 \mu_B$ for these devices under vacuum conditions.

The device sensitivities were further enhanced to ambient conditions, as presented in Chapter 5. New highly sensitive nanophotonic optomechanical torque magnetometers and RF magnetic susceptometers were developed and optimized using permalloy as a dry-run. The displacement, torque, and magnetic moment and magnetic field sensitivities were 1.0×10^{-11}m$(\text{Hz}^{1/2})^{-1}$, 1.3×10^{-20}Nm$(\text{Hz}^{1/2}) - 1$, and $2.4 \times 10^7 \mu_B$, and 4μT for these devices under ambient conditions. Excellent readout sensitivity of these devices allowed the quantitative characterization of three-dimensional magnetization and RF-driven responses of magnetic structures in ambient conditions. These optimized devices are ready to use for integrating magnetic nanoparticles on them.

To further enhance the magnetic field sensitivity, new routes were developed to utilize magnetic information of mesoscopic YIG disks, presented in Chapter 6. These thick YIG disks were fabricated to simultaneously probe the (i) spin resonances (low frequency to telecom wavelength) for potential applications, (ii) miniatured Einstein-de Haas experiment, and (iii) ultra-high sensitive field sensing magnetometers.

7.2 Future Recommendations

A prospective experiment would be to integrate the magnetic nanoparticles self-assembly to the highly sensitive nanophotonic optomechanical torque mag-

netometers. The design would allow one to achieve the magnetization of a single giant macro-spin of a superparamagnetic nanoparticle, or the single spin detection of any stable single-domain magnetic nanoparticle. The new magnetometers will be useful in the emerging field of spin-mechanics, which integrates the spins to the degrees of freedom in mechanics.

The optomechanical torsional resonators could be extended, in principle, to magnetic studies of individual nanoparticles through the deposition of more dilute suspensions, and through controlled deposition by the nanofabrication tools. Different kinds of nanoparticles can be incorporated, such as core-shell nanoparticles with a ferromagnetic-antiferromagnetic (FM-AFM) layered system. The exchange bias in the hysteresis, and Néel transition of FM-AFM systems can then be transduced in the optomechanical readout. The same technique could be applied to the magnetic thin films and the superconducting materials, once the experimental setup is updated to incorporate the low-temperature measurements. Many other magnetostatic properties can be explored, including the magnetic energy landscapes and the energy barriers.

The essence of spin-mechanics are the Einstein-de Haas or Barnett effects, where magnetic and mechanical armatures are coherently coupled. The best device candidate would have a cross-over of mechanical and magnetic resonance frequencies, where the later is mostly in the GHz range. So, there is a need to fabricate high frequency devices that can easily couple the magnetic resonance to the mechanical armature. Hence, the magnetization reversal could be mechanically assisted or vice-versa. Optomechanical devices in the MHz range were developed in Chapter 5, which could be improved to GHz range devices to observe magneto-mechanical coupling.

The magnetic vortex state of the YIG disk can be explored further. The acquisition of torque mixing spectra from low to high and high to low field sweeps would be of primary interest, to observe the vortex state, gyration mode, and higher order modes. The gyrotropic modes and higher order resonance modes

would then give us information about the pinning and dynamical behaviour of the disk. The whole setup could be extended to the higher frequency measurement mode in the giga Hertz (GHz) range. Some of the simplification in the RF electronics would involve the ultrahigh frequency lock-in amplifer (UHF) itself. Such devices have potential applications towards memory storage devices, spin transport devices and microwave and high frequency (GHz) devices.

The next big development would be nanophotonic circuits which are being produced using the nanofabrication tools and are replacing existing electronic circuits. Nanophotonic circuits have extensive applications in data computing companies. Possible areas of interest would be diamond nanophotonics, single spin detection with nitrogen vacancy (NV) centers. NV centers are solid state systems with consummate qubits that can be used in waveguides, nano-cavities for low optical and mechanical loss, and reaching the quantum state of the system. New ways could paved to incorporate nanomechanics and nanophotnics in diamond based resonators, for low optical and mechanical loss, and to build the bases of new diamond based torque magnetometers. It would provide a platform for hybrid optomechanical quantum devices.

Beside diamond, gallium phosphide (GaP) is another promising material that has large opto-mechanical coupling and could be very useful for new torque magnetometers for reduced losses. GaP has unique properties of absorption spectrum and is transparent in both visible and telecommunication wavelengths, highly useful for quantum optics applications. Torque magnetometers can be fabricated in GaP to utilize its quantum optical properties. The combination of torque magnetometry with quantum light applications will open up new avenues in the field of quantum optics and magnetometry.

Bibliography

[1] C. G. Martin, R. S. Jacques, and C. J.-B. Coignard. Premier mémoire sur l'électricité et le magnétisme. *Memoires De Lacademie Royale*, 570: 569–577, 1785.

[2] Henry Cavendish. Experiments to determine the density of the earth. *Phil. Trans. R. Soc. Lond.*, 88(1):469–526, 1798. ISSN 02610523. doi: 10.1098/rstl.1798.0022.

[3] S . J . Barnett. On magnetization by angular acceleration. *Science*, 30 (769):128–129, 1909.

[4] S. J. Barnett. Magnetization by rotation. *Physical Review*, 6(4):239–270, 1915. ISSN 0031899X. doi: 10.1103/PhysRev.6.239.

[5] O. W. Richardson. A mechanical effect accompanying magnetization. *Physical Review (Series I)*, 26(3):248–253, 1908. ISSN 0031899X. doi: 10.1103/PhysRevSeriesI.26.248.

[6] A Einstein and W. J. de Haas. Experimental proof of the existence of Ampère's molecular currents. *Koninklijke Akademie van Wetenschappen te Amsterdam, Proceedings*, 18:696–711, 1915. URL http://www.dwc.knaw.nl/DL/publications/PU00012546.pdf.

[7] S. Morita, F. J. Giessibl, E. Meyer, and R. Wiesendanger. *Noncontact Atomic Force Microscopy*. Springer, 2015. ISBN 9783319155876. doi: 10.1007/978-3-319-15588-3.

[8] F. A. Ferri, M. A. Pereira-Da-Silva, and E. Marega. Magnetic force microscopy: Basic principles and applications. In *Atomic Force Microscopy - Imaging, Measuring, and Manipulating Surfaces at the Atomic Scale*. InTech Publishing, 2012. ISBN 978-953-51-0414-8. doi: 10.5772/34833. URL http://www.intechopen.com/books/atomic-force-microscopy-imaging-measuring-and-manipulating-surfaces-at-the-a magnetic-force-microscopy-basic-principles-and-applications.

[9] J. A. Sidles, J. L. Garbini, K. J. Bruland, D. Rugar, O. Zger, S. Hoen, and C. S. Yannoni. Magnetic resonance force microscopy. *Reviews of Modern Physics*, 67(1):249–265, 1995. ISSN 00346861. doi: 10.1103/RevModPhys.67.249.

[10] S. A. Al'tshuler and B. M. Kozyev. *Electron paramagnetic resonance*. Academic Press, 2015. ISBN 9781482255041. doi: 10.1201/b18217-1. URL http://www.crcnetbase.com/doi/10.1201/b18217-1.

[11] K. Kamienska-Trela. *Nuclear magnetic resonance*. The Royal Society of Chemistry, 2011. ISBN 9781849732796. doi: 10.1039/9781849737678-00045. URL http://ebook.rsc.org/?DOI=10.1039/9781849737678-00045.

[12] A. Maddock. *Mossbauer spectroscopy principles and applications*. Horwood Publishing, 1997. doi: 10.1016/B978-1-898563-16-7.50002-8.

[13] H. A. Szymanski. *Raman spectroscopy*. Springer, 1970. ISBN 978-1-4684-3029-5. doi: 10.1007/978-1-4684-3027-1. URL http://link.springer.com/10.1007/978-1-4684-3027-1.

[14] V. Charbois, V. V. Naletov, J. Ben Youssef, and O. Klein. Mechanical detection of ferromagnetic resonance spectrum in a normally magnetized yttrium-iron-garnet disk. *Journal of Applied Physics*, 91(10):7337–7339, 2002. ISSN 00218979. doi: 10.1063/1.1456040.

[15] J. E. Losby, F. Fani Sani, D. T. Grandmont, Z. Diao, M. Belov, J. A. J. Burgess, S. R. Compton, W. K. Hiebert, D. Vick, K. Mohammad, E. Salimi, G. E. Bridges, D. J. Thomson, and M. R. Freeman. Torque-mixing magnetic resonance spectroscopy. *Science*, 350(6262):798–801, 2015.

[16] E. Ollier, L. Duraffourg, M. T. Delaye, H. Grange, S. Deneuville, J. Bernos, R. Dianoux, F. Marchi, D. Renaud, T. Baron, P. Andreucci, and P. Robert. NEMS devices for accelerometers compatible with thin SOI technology. In *Proceedings of the 2nd IEEE International Conference on Nano/Micro Engineered and Molecular Systems, IEEE NEMS 2007*, pages 180–185, 2007. ISBN 1424406102. doi: 10.1109/NEMS.2007.352257.

[17] L. Duraffourg and J. Arcamone. *Nanoelectromechanical Systems*. John Wiley \& Sons Inc., 2015. ISBN 0034-6748. doi: 10.1063/1.1927327. URL http://arxiv.org/pdf/cond-mat/0008187.pdf.

[18] S. Ben Sassi and F. Najar. Accurate reduced-order modeling of MEMS and NEMS microactuators under dynamic electrostatic loading and large strokes. *12th International Multi-Conference on Systems, Signals and Devices*, 2(1):1–5, 2015. doi: 10.1109/SSD.2015.7348248.

[19] A. Ziaei, M. Charles, M. Le Baillif, S. Xavier, A. Caillard, and C. S. Cojocaru. Capacitive and ohmic RF NEMS switches based on vertical carbon nanotubes. *International Journal of Microwave and Wireless Technologies*, 2(5):433–440, 2010. ISSN 17590787. doi: 10.1017/S1759078710000619.

[20] A. Zviagintsev, I. Brouk, I. Bloom, and Y. Nemirovsky. Self- heating effects in CMOS-SOI-NEMS transistors for uncooled passive IR sensors. In *2015 IEEE International Conference on Microwaves, Communications,*

Antennas and Electronic Systems, pages 1–5, 2015. ISBN 9781479974733. doi: 10.1109/COMCAS.2015.7360489.

[21] S. Gröblacher, S. Gigan, H. R. Böhm, A. Zeilinger, and M. Aspelmeyer. Radiation-pressure self-cooling of a micromirror in a cryogenic environment. *EPL*, 81:54003, 2008. ISSN 02955075. doi: 10.1209/0295-5075/81/54003.

[22] A. Tiwari and B. Raj. *Materials and failures in MEMS and NEMS*. John Wiley \& Sons Inc., 2015.

[23] R. J. Dolleman, D. Davidovikj, S. J. Cartamil-Bueno, H. S. J. Van Der Zant, and P. G. Steeneken. Graphene Squeeze-Film Pressure Sensors. *Nano Letters*, 16(1):568–571, 2016. ISSN 15306992. doi: 10.1021/acs.nanolett.5b04251.

[24] P. S. Waggoner and H. G. Craighead. Micro- and nanomechanical sensors for environmental, chemical, and biological detection. *Lab on a Chip*, 7:1238, 2007. ISSN 1473-0197. doi: 10.1039/b707401h. URL http://xlink.rsc.org/?DOI=b707401h.

[25] Michael Roukes. Nanoelectromechanical Systems : A New Opportunity For Microelectronics. In *Proceedings of ESSDERC*, page 23, 2009. ISBN 9781424443536. doi: 10.1109/ESSDERC.2009.5331370.

[26] J. Chaste, A. Eichler, J. Moser, G. Ceballos, R. Rurali, and A. Bachtold. A nanomechanical mass sensor with yoctogram resolution. *Nature Nanotechnology*, 7(5):301–304, 2012. ISSN 1748-3387. doi: 10.1038/nnano.2012.42. URL http://www.nature.com/doifinder/10.1038/nnano.2012.42.

[27] A. L. Buchachenko, F. I. Dalidchik, S. A. Kovalevskii, and B. R. Shub. Paramagnetic resonance and detection of a single electron spin.

Russian Chemical Reviews, 70(7):535, 2001. ISSN 0036-021X. doi: 10.1070/RC2001v070n07ABEH000652. URL http://stacks.iop.org/0036-021X/70/i=7/a=R01.

[28] C. L. Degen, M. Poggio, H. J. Mamin, and D. Rugar. Nuclear spin relaxation induced by a mechanical resonator. *Physical Review Letters*, 100: 137601, 2008. ISSN 00319007. doi: 10.1103/PhysRevLett.100.137601.

[29] Y. T. Yang, C. Callegari, X. L. Feng, K. L. Ekinci, and M. L. Roukes. Zeptogram-scale nanomechanical mass sensing. *Nano Letters*, 6(4):583–586, 2006. ISSN 15306984. doi: 10.1021/nl052134m.

[30] J. Lee, W. Shen, K. Payer, T. P. Burg, and S. R. Manalis. Toward attogram mass measurements in solution with suspended nanochannel resonators. *Nano letters*, 10:2537–2542, 2010. doi: 10.1021/nl101107u.

[31] A. Naik, O. Buu, M. D. LaHaye, A. D. Armour, A. A. Clerk, M. P. Blencowe, and K. C. Schwab. Cooling a nanomechanical resonator with quantum back-action. *Nature*, 443(7108):193–196, 2006. ISSN 14764687. doi: 10.1038/nature05027.

[32] G. Ranjit, M. Cunningham, K. Casey, and A. A. Geraci. Zeptonewton force sensing with nanospheres in an optical lattice. *Physical Review A*, 93(5):053801, 2016. ISSN 24699934. doi: 10.1103/PhysRevA.93.053801.

[33] M. Wu, N. L.-Y. Wu, T. Firdous, F. Fani Sani, J. E. Losby, M. R. Freeman, and P. E. Barclay. Nanocavity optomechanical torque magnetometry and radiofrequency susceptometry. *Nature Nanotechnology*, 12(2): 127–131, 2017. ISSN 1748-3387. doi: 10.1038/nnano.2016.226. URL http://dx.doi.org/10.1038/nnano.2016.226.

[34] Mo Li, H. X. Tang, and M. L. Roukes. Ultra-sensitive NEMS-based cantilevers for sensing, scanned probe and very high-frequency applica-

tions. *Nature Nanotechnology*, 2(2):114–120, 2007. ISSN 17483395. doi: 10.1038/nnano.2006.208.

[35] M. S O. Alink, A. B. J. Kokkeler, E. A. M. Klumperink, G. J. M. Smit, and B. Nauta. Spectrum sensing with high sensitivity and interferer robustness using cross-correlation energy detection. *IEEE Journal on Emerging and Selected Topics and Circuits and Systems*, 3(4):566–575, 2013.

[36] W. W. Johnson and M. Bocko. Approaching the quantum limit for force detection. *Phys. Rev. Lett*, 47(17):1184–1187, 1981.

[37] S. Schreppler, N. Spethmann, N. Brahms, T. Botter, M. Barrios, and D. M. Stamper-Kurn. Optically measuring force near the standard quantum limit. *Science*, 344(6191):1486–1489, 2014. ISSN 10959203. doi: 10.1126/science.1249850.

[38] P. L. Giscard, M. Bhattacharya, and P. Meystre. Quantum mechanical limits to inertial mass sensing by nanomechanical systems. *arXiv*, 2009. URL http://arxiv.org/abs/0905.1081.

[39] N. S. Kampel, R. W. Peterson, R. Fischer, P. L. Yu, K. Cicak, R. W. Simmonds, K. W. Lehnert, and C. A. Regal. Improving broadband displacement detection with quantum correlations. *Physical Review X*, 7(2): 021008, 2017. ISSN 21603308. doi: 10.1103/PhysRevX.7.021008.

[40] P. H. Kim, B. D. Hauer, C. Doolin, F. Souris, and J. P. Davis. Approaching the standard quantum limit of mechanical torque sensing. *Nature Communications*, 7:13165, 2016. ISSN 20411723. doi: 10.1038/ncomms13165. URL http://dx.doi.org/10.1038/ncomms13165.

[41] M. Bienert and P. Barberis-Blostein. Optomechanical laser cooling with

mechanical modulations. *Physical Review A*, 91(2):023818, 2015. ISSN 10941622. doi: 10.1103/PhysRevA.91.023818.

[42] L. T. Hall, P. Kehayias, D. A. Simpson, A. Jarmola, A. Stacey, D. Budker, and L. C.L. Hollenberg. Detection of nanoscale electron spin resonance spectra demonstrated using nitrogen-vacancy centre probes in diamond. *Nature Communications*, 7:10211, 2016. ISSN 20411723. doi: 10.1038/ncomms10211. URL http://dx.doi.org/10.1038/ncomms10211.

[43] D. Rugar, R. Budakian, H. J. Mamin, and B. W. Chui. Single spin detection by magnetic resonance force microscopy. *Nature*, 430(6997): 329–332, 2004. ISSN 0028-0836. doi: 10.1038/nature02658. URL http://www.nature.com/doifinder/10.1038/nature02658.

[44] A. A. Clerk and F. Marquardt. Basic theory of cavity optomechanics. In *Cavity Optomechanics, Quantum Science and Technology*, pages 1–357. Springer-Verlag Berlin Heidelberg, 2014. ISBN 9783642553127. doi: 10.1007/978-3-642-55312-7.

[45] M. Aspelmeyer, T. J. Kippenberg, and F. Marquardt. Cavity optomechanics. *Reviews of Modern Physics*, 86(4):1391–1452, 2014. ISSN 15390756. doi: 10.1103/RevModPhys.86.1391.

[46] J. Cripe, N. Aggarwal, R. Singh, R. Lanza, A. Libson, M. J. Yap, G. D. Cole, D. E. McClelland, N. Mavalvala, and T. Corbitt. Radiation-pressure-mediated control of an optomechanical cavity. *arXiv*, pages 1–7, 2017. ISSN 2469-9926. doi: 10.1103/PhysRevA.97.013827. URL http://arxiv.org/abs/1710.04700.

[47] O. Arcizet, P. F. Cohadon, T. Briant, M. Pinard, and A. Heidmann. Radiation-pressure cooling and optomechanical instability of a micromirror. *Nature*, 444:71–74, 2006. ISSN 14764687. doi: 10.1038/nature05244.

[48] A. Yilmaz, S. Schuster, P. Wolf, D. Schmidt, M. Eisele, C. Zimmermann, and S. Slama. Optomechanical damping of a nanomembrane inside an optical ring cavity. *New Journal of Physics*, 19(1):013038, 2017. ISSN 1367-2630. doi: 10.1088/1367-2630/aa55ee. URL http://stacks.iop.org/1367-2630/19/i=1/a=013038?key=crossref.4cc68182eea1af6787ca785cffc54f39.

[49] C. Metzger, M. Ludwig, C. Neuenhahn, A. Ortlieb, I. Favero, K. Karrai, and F. Marquardt. Self-Induced oscillations in an optomechanical system driven by bolometric backaction. *Physical Review Letters*, 101:133903, 2008. ISSN 00319007. doi: 10.1103/PhysRevLett.101.133903.

[50] T. J. Kippenberg and K. J. Vahala. Cavity opto-mechanics: back-action at the mesoscale. *Science*, 321(8):1172, 2008.

[51] M. Wu, A. C. Hryciw, C. Healey, D. P. Lake, H. Jayakumar, M. R. Freeman, J. P. Davis, and P. E. Barclay. Dissipative and dispersive optomechanics in a nanocavity torque sensor. *Phys. Rev. X*, 4:021052, 2014.

[52] I. Favero, S. Stapfner, D. Hunger, P. Paulitschke, H. Lorenz, E. M. Weig, and K. Karrai. Fluctuating nanomechanical system in a high finesse optical microcavity. *Opt. Express*, 17(15):12813, 2009.

[53] Z. Huang, K. Cui, Y. Li, X. Feng, F. Liu, W. Zhang, and Y. Huang. Strong optomechanical coupling in nanobeam cavities based on hetero optomechanical crystals. *Scientific Reports*, 5:15964, 2015. ISSN 20452322. doi: 10.1038/srep15964. URL http://dx.doi.org/10.1038/srep15964.

[54] J. Li, A. Xuereb, N. Malossi, and D. Vitali. Cavity mode frequencies and strong optomechanical coupling in two-membrane cavity optomechanics. *Journal of Optics (United Kingdom)*, 18(8):084001, 2016. ISSN 20408986. doi: 10.1088/2040-8978/18/8/084001.

[55] X. Jiang, M. Wang, M. C. Kuzyk, T. Oo, Gui-Lu Long, and H. Wang. Chip-based silica microspheres for cavity optomechanics. *Optics Express*, 23(21):27260, 2015. ISSN 1094-4087. doi: 10.1364/OE.23.027260. URL https://www.osapublishing.org/abstract.cfm?URI=oe-23-21-27260.

[56] M. Mitchell, A. C. Hryciw, and P. E. Barclay. Cavity optomechanics in gallium phosphide microdisks. *Applied Physics Letters*, 104(14):141104, 2014. ISSN 00036951. doi: 10.1063/1.4870999.

[57] L. Neuhaus, A. G. Kuhn, S. Zerkani, J. Teissier, D. Garc, T. Briant, and P. Cohadon. Fabry-Perot cavity optomechanics with ultra-high mechanical- Q -Factor quartz micropillars at cryogenic temperature. *IEEE*, 697(2010):243504, 2013.

[58] M. H. Bitarafan and R. G. DeCorby. On-chip high-finesse fabry-perot microcavities for optical sensing and quantum information. *Sensors*, 17 (8):1748, 2017. ISSN 14248220. doi: 10.3390/s17081748.

[59] W. H. P. Pernice, Mo Li, and Hong X. Tang. Optomechanical coupling in photonic crystal supported nanomechanical waveguides. *Optics Express*, 17(15):12424, 2009. ISSN 1094-4087. doi: 10.1364/OE.17.012424. URL https://www.osapublishing.org/oe/abstract.cfm?uri=oe-17-15-12424.

[60] K. Stannigel, P. Komar, S. J.M. Habraken, S. D. Bennett, M. D. Lukin, P. Zoller, and P. Rabl. Optomechanical quantum information processing with photons and phonons. *Physical Review Letters*, 109(1):013603, 2012. ISSN 00319007. doi: 10.1103/PhysRevLett.109.013603.

[61] B. Khanaliloo. *Optomechanical devices in single crystal diamond*. PhD thesis, University of Alberta, 2017.

[62] W. P. Bowen and G. J. Milburn. *Quantum optomechanics*. Taylor & Francis, 2016. ISBN 9781107003385. doi: 10.1063/PT.3.1640. URL http://link.aip.org/link/PHTOAD/v65/i7/p29/s1{&}Agg=doi.

[63] D. Blair, L. Ju, and Y. Ma. Optomechanics for gravitational wave detection from resonant bars to next generation laser interferometers. Technical report, Oxford University Press, 2017.

[64] U. Akram, W. Munro, K. Nemoto, and G. J. Milburn. Photon-phonon entanglement in coupled optomechanical arrays. *Physical Review A*, 86 (4):042306, 2012. ISSN 10502947. doi: 10.1103/PhysRevA.86.042306.

[65] H. Miao, H. Yang, R. X. Adhikari, and Y. Chen. Quantum limits of interferometer topologies for gravitational radiation detection. *Classical and Quantum Gravity*, 31(16):165010, 2014. ISSN 13616382. doi: 10.1088/0264-9381/31/16/165010.

[66] A. Belenchia, D. M.T. Benincasa, S. Liberati, F. Marin, F. Marino, and A. Ortolan. Testing quantum gravity induced nonlocality via optomechanical quantum oscillators. *Physical Review Letters*, 116(16):161303, 2016. ISSN 10797114. doi: 10.1103/PhysRevLett.116.161303.

[67] W. Yang, S. A. Gerke, K. Wei Ng, Y. Rao, C. Chase, and C. J. Chang-Hasnain. Laser optomechanics. *Scientific Reports*, 5:13700, 2015. ISSN 20452322. doi: 10.1038/srep13700. URL http://dx.doi.org/10.1038/srep13700.

[68] Y. Zheng, Q. Yu, K. Tao, and Z. Ouyang. All-optical tunable filters based on optomechanical effects in two-dimensional photonic crystal cavities. *Optics letters*, 38(21):4362–5, 2013. ISSN 1539-4794. doi: 10.1364/OL.38.004362. URL http://www.ncbi.nlm.nih.gov/pubmed/24177094.

[69] P. Rath. *Integrated optomechanics and single-photon detection in diamond photonic integrated circuits*. PhD thesis, Karlsruher Instituts für Technologie (KIT), 2016. URL http://arxiv.org/abs/1701.01770.

[70] S. Singamaneni, V. N. Bliznyuk, C. Binek, and E. Y. Tsymbal. Magnetic nanoparticles: recent advances in synthesis, self-assembly and applications. *Journal of Materials Chemistry*, 21(42):16819, 2011. ISSN 0959-9428. doi: 10.1039/c1jm11845e. URL http://xlink.rsc.org/?DOI=c1jm11845e.

[71] S. Bedanta, A. Barman, W. Kleemann, O. Petracic, and T. Seki. Synthesis, properties, and applications of single-domain magnetic nanoparticles. *Journal of Nanomaterials*, 2:130180, 2013.

[72] P. Kumbhakar, S. S. Ray, and A. L. Stepanov. Optical properties of nanoparticles and nanocomposites. *Journal of Nanomaterials*, 2014: 181365, 2014.

[73] A. P. Alivisatos. Semiconductor clusters, nanocrystals, and quantum dots. *Science*, 271:933–937, 1996.

[74] Y. A. Vlasov, X.-Z. Bo, J. C. Sturm, and D. J. Norris. On-chip natural assembly of silicon photonic bandgap crystals. *Nature*, 414:289, 2001.

[75] C. Burda, X. Chen, R. Narayanan, and M. A. El-sayed. Chemistry and properties of nanocrystals of different shapes. *Chemical Reviews*, 105: 1025, 2005. doi: 10.1021/cr030063a.

[76] Q. A. Pankhurst, J. Connolly, S. K. Jones, and J. Dobson. Applications of magnetic nanoparticles in biomedicine. *Journal of Physics D: Applied Physics*, 36(13):R167–R181, 2003. ISSN 0022-3727. doi: 10.1088/0022-3727/36/13/201. URL http://iopscience.iop.org/0022-3727/36/13/201.

[77] Paul Alivisatos. The use of nanocrystals in biological detection. *Nature Biotechnology*, 22(1):47–53, 2004. doi: 10.1038/nbt927.

[78] W. S. Seo, J. H. Lee, X. Sun, Y. Suzuki, D. Mann, Z. Liu, M. Terashima, P. C. Yang, M. V. Mcconnell, D. G. Nishimura, and H. Dai. FeCo/graphitic-shell nanocrystals as advanced magnetic-resonance-imaging and near-infrared agents. *Nature Materials*, 5(12): 971, 2006. doi: 10.1038/nmat1775.

[79] Y.-C. Li, H.-B. Xin, H.-X. Lei, L.-L. Liu, Y.-Z. Li, Y. Zhang, and B.-J. Li. Manipulation and detection of single nanoparticles and biomolecules by a photonic nanojet. *Light: Science and Applications*, 5:e16176, 2016. doi: 10.1038/lsa.2016.176.

[80] J. J. Dubowski and S. Tanev. *Photon-based nanoscience and nanobiotechnology*. Springer, 2005. ISBN 9781402055225.

[81] Z. Yujuan, H. Rao, Z. H. U. Xianfang, W. Lianzhou, and W. U. Chenxu. Synthesis, properties, and optical applications of noble metal nanoparticle-biomolecule conjugates. *Materials Science*, 57(2):238–246, 2012. doi: 10.1007/s11434-011-4747-x.

[82] J. Boken, P. Khurana, S. Thatai, D. Kumar, and S. Prasad. Plasmonic nanoparticles and their analytical applications : A review. *Applied Spectroscopy Reviews*, 52(9):774–820, 2017. ISSN 0570-4928. doi: 10.1080/05704928.2017.1312427. URL https://doi.org/10.1080/05704928.2017.1312427.

[83] Q.-H. Wei, K. Su, S. Durant, and X. Zhang. Plasmon resonance of finite one-dimensional Au nanoparticle chains. *Nano Letters*, 4(6):1067, 2004. doi: 10.1021/nl049604h.

[84] S. Karmakar, S. Kumar, R. Rinaldi, and G. Maruccio. Nano-electronics

and spintronics with nanoparticles. *Journal of Physics: Conference Series*, 292:012002, 2011. doi: 10.1088/1742-6596/292/1/012002.

[85] Z.-P. Lv, Z.-Z. Luan, H.-Y. Wang, S. Liu, C.-H. Li, D. Wu, J.-L. Zuo, and S. Sun. Tuning electron-conduction and spin transport in magnetic iron oxide nanoparticle assemblies via tetrathiafulvalene-fused ligands. *ACS Central Science*, 9(12):12205–12213, 2015. doi: 10.1021/acsnano.5b05444.

[86] M. S. Kamal, A. A. Adewunmi, A. S. Sultan, M. F. Al-hamad, and U. Mehmood. Recent advances in nanoparticles enhanced oil recovery : rheology, interfacial tension, oil recovery, and wettability alteration. *Journal of Nanomaterials*, 15:2473175, 2017.

[87] B. Kozissnik, A. C. Bohorquez, J. Dobson, C. Rinaldi, B. Kozissnik, A. C. Bohorquez, J. Dobson, and C. Rinaldi. Magnetic fluid hyperthermia : Advances , challenges , and opportunity. *International Journal of Hyperthermia*, 29(8):706, 2013. doi: 10.3109/02656736.2013.837200.

[88] C. Chappert, A. Fert, and F. N.V. Dau. The emergence of spin electronics in data storage. *Nature Materials*, 6:813–824, 2007.

[89] N. A. Frey, S. Peng, K. Cheng, and S. Sun. Magnetic nanoparticles : synthesis, functionalization, and applications in bioimaging and magnetic energy storage. *Chem. Soc. Rev.*, 38:2532–2542, 2009. doi: 10.1039/b815548h.

[90] S. Tanabe, S. Miwa, M. Mizuguchi, T. Shinjo, Y. Suzuki, and M. Shiraishi. Spin-dependent transport in nanocomposites of Alq 3 molecules and cobalt nanoparticles. *Applied Physics Letters*, 91:063123, 2007. doi: 10.1063/1.2769748.

[91] C. Sun, J. S. H. Lee, and M. Zhang. Magnetic nanoparticles in MR

imaging and drug delivery. *Advanced Drug Delivery Reviews*, 60(11): 1252–1265, 2008. ISSN 0169409X. doi: 10.1016/j.addr.2008.03.018.

[92] C. S. S. R. Kumar and F. Mohammad. Magnetic nanomaterials for hyperthermia-based therapy and controlled drug delivery. *Advanced Drug Delivery Reviews*, 63(9):789–808, 2011. ISSN 0169-409X. doi: 10.1016/j.addr.2011.03.008. URL http://dx.doi.org/10.1016/j.addr.2011.03.008.

[93] A. E. Deatsch and B. A. Evans. Heating efficiency in magnetic nanoparticle hyperthermia. *Journal of Magnetism and Magnetic Materials*, 354: 163–172, 2014. doi: 10.1016/j.jmmm.2013.11.006.

[94] D. J. Dunlop and Ozden Ozdemir. *Rock magnetism*. Cambridge University Press, 1997. ISBN 9780511612794.

[95] D. A. Bazylinski and S. Schübbe. Controlled biomineralization by and applications of magnetotactic bacteria. In *Advances in Applied Microbiology*, volume 62, pages 21–62. Elsevier Inc., 2007. ISBN 0123736692. doi: 10.1016/S0065-2164(07)62002-4.

[96] K. N. Trohidou. *Magnetic nanoparticle assemblies*. Taylor & Francis, 2009. ISBN 9789814411974. doi: 10.1201/b15657. URL http://arxiv.org/abs/0907.4417.

[97] L. Yan, S. Zhang, P. Chen, H. Liu, H. Yin, and H. Li. Magnetotactic bacteria, magnetosomes and their application. *Microbiological Research*, 167(9):507–519, 2012. ISSN 09445013. doi: 10.1016/j.micres.2012.04.002. URL http://dx.doi.org/10.1016/j.micres.2012.04.002.

[98] R. Blakemore. Magnetotactic bacteria. *Science*, 190(4212):377, 1975.

[99] J. Y. Cheng, F. Zhang, V. P. Chuang, A. M. Mayes, and C. A. Ross.

Self-assembled one-dimensional nanostructure arrays. *Nano Letters*, 6 (9):2099, 2006. doi: 10.1021/nl061563x.

[100] G. Chen, M. I. Bodnarchuk, M. V. Kovalenko, G. Springholz, W. Heiss, W. Jantsch, E. Platzgummer, H. Loeschner, and J. Schotter. Damascene process for controlled positioning of magnetic colloidal nanocrystals. *Adv. Mater.*, 22:1364–1368, 2010. doi: 10.1002/adma.200902884.

[101] A. P. Bartlett, A. K. Agarwal, and A. Yethiraj. Dynamic templating of colloidal patterns in three dimensions with nonuniform electric fields. *Langmuir*, 27(8):4313, 2011.

[102] S. Bedanta and W. Kleemann. Supermagnetism. *Journal of Physics D: Applied Physics*, 42:013001, 2009. doi: 10.1088/0022-3727/42/1/013001.

[103] Abhijit Biswas, Ilker S. Bayer, Alexandru S. Biris, Tao Wang, Enkeleda Dervishi, and Franz Faupel. Advances in top-down and bottom-up surface nanofabrication: Techniques, applications & future prospects. *Advances in Colloid and Interface Science*, 170(1-2):2–27, 2012. ISSN 00018686. doi: 10.1016/j.cis.2011.11.001. URL http://dx.doi.org/10.1016/j.cis.2011.11.001.

[104] V. Shklover and H. Hofmann. *Methods of self-assembling in fabrication of nanodevices*, volume 2. 2005. ISBN 1588830756. URL http://topaz.ethz.ch/function/SemiNano.pdf.

[105] D. Xia and S. R. J. Brueck. A facile approach to directed assembly of patterns of nanoparticles using interference lithography and spin coating. *Nano Letters*, 4(7):1295, 2004. doi: 10.1021/nl049355x.

[106] M. Grzelczak, J. Vermant, Eric M. Furst, and L. M. Liz-Marzan. Directed self-assembly of nanoparticles. *ACS Nano*, 4 (7):3591–3605, 2010. ISSN 1936-0851. doi: 10.1021/nn100869j.

URL http://pubs.acs.org/doi/pdf/10.1021/nn100869j{%}0Ahttp://pubs.acs.org/doi/abs/10.1021/nn100869j.

[107] Y. Min, M. Akbulut, K. Kristiansen, Y. Golan, and J. Israelachvili. The role of interparticle and external forces in naoparticle assembly. *Nature Materials*, 7:527–538, 2008. URL http://www.nature.com/nmat/journal/v7/n7/pdf/nmat2206.pdf.

[108] J. Kim, S E. Chung, S. E. Choi, H. Lee, J. Kim, and S. Kwon. Programming magnetic anisotropy in polymeric microactuators. *Nature Materials*, 10(10):747–752, 2011. ISSN 14764660. doi: 10.1038/nmat3090.

[109] E. Pauliac-Vaujour and P. Moriarty. Meniscus-mediated organization of colloidal nanoparticles. *Journal of Physical Chemistry C*, 111(44):16255–16260, 2007. ISSN 19327447. doi: 10.1021/jp074152t.

[110] Y. Cui, M. T. Bjork, J. A. Liddle, C. Sonnichsen, B. Boussert, and A. P. Alivisatos. Integration of colloidal nanocrystals into lithographically patterned devices. *Nano Letters*, 4(6):1093–1098, 2004. doi: 10.1021/nl049488i.

[111] J. Liao, X. Li, Y. Wang, C. Zhang, J. Sun, C. Duan, Q. Chen, and L. Peng. Patterned close-packed nanoparticle arrays with controllable dimensions and precise locations. *Small*, 8(7):991–996, 2012. ISSN 16136810. doi: 10.1002/smll.201102038.

[112] W. Cheng, N. Park, M. T. Walter, M. R. Hartman, and D. Luo. Nanopatterning self-assembled nanoparticle superlattices by moulding microdroplets. *Nature Nanotechnology*, 3(11):682–690, 2008. ISSN 17483395. doi: 10.1038/nnano.2008.279.

[113] Y. Yin, Y. Lu, B. Gates, and Y. Xia. Template-assisted self-assembly: A practical route to complex aggregates of monodispersed colloids with

well-defined sizes, shapes, and structures. *J. Am Chem. Soc.*, 123:8718–8729, 2001. doi: 10.1021/ja011048v.

[114] G. Zuccheri and B. Samorì. *DNA nanotechnology - methods and protocols*. Springer, 2011. ISBN 978-1-61779-141-3. doi: 10.1007/978-1-61779-142-0. URL http://link.springer.com/10.1007/978-1-61779-142-0.

[115] D. Chowdhury, R. Maoz, and J. Sagiv. Wetting driven self-assembly as a new approach to template-guided fabrication of metal nanopatterns. *Nano Letters*, 7(6):1770–1778, 2007. ISSN 15306984. doi: 10.1021/nl070842x.

[116] R. C. Bailey, K. J. Stevenson, and J. T. Hupp. Assembly of micropatterned colloidal gold thin films via microtransfer molding and electrophoretic deposition. *Adv. Mater.*, 12(24):1930–1934, 2000.

[117] S. Palacin, P. C. Hidber, J.-P. Bourgoin, C. Miramond, C. Fermon, and G. M. Whitesides. Patterning with magnetic materials at the micron scale. *Chem. Mater.*, 8:1316–1325, 1996. doi: 10.1021/cm950587u.

[118] E. Bellido, de R. Miguel, D. Ruiz-molina, A. Lostao, and D. Maspoch. Controlling the number of proteins with dip-pen nanolithography. *Adv. Mater.*, 22:352–355, 2010. doi: 10.1002/adma.200902372.

[119] M. Gleiche, L. F. Chi, and H. Fuchs. Nanoscopic channel lattices with controlled anisotropic wetting. *Nature*, 403:173, 2000.

[120] X. Liu, L. Fu, S. Hong, V. P. Dravid, and C. A. Mirkin. Arrays of magnetic nanoparticles patterned via "dip-pen" nanolithography. *Adv. Mater.*, 14(3):231–234, 2002.

[121] B. G. Prevo, Y. Hwang, and O. D. Velev. Convective assembly of antireflective silica coatings with controlled thickness and refractive index. *Chem. Mater.*, 17(2):3642–3651, 2005. doi: 10.1021/cm050416h.

[122] L. Malaquin, T. Kraus, H. Schmid, E. Delamarche, and H. Wolf. Controlled particle placement through convective and capillary assembly. *Langmuir*, 23:11513–11521, 2007. doi: 10.1021/la700852c.

[123] N. D. Denkov, O. D. Velev, P. A. Kralchevsky, I. B. Ivanov, H. Yoshimura, and K. Nagayamat. Mechanism of formation of two-dimensional crystals from latex particles on substrates. *Langmuir*, 8(17):3183–3190, 1992. doi: 10.1021/la00048a054.

[124] K. C. Elbert, D. Jishkariani, Y. Wu, J. D. Lee, B. Donnio, and C. B. Murray. Design, self-assembly, and switchable wettability in hydrophobic, hydrophilic, and janus dendritic ligand gold nanoparticle hybrid materials. *Chem. Mater.*, 29:8737–8746, 2017. doi: 10.1021/acs.chemmater.7b02928.

[125] H. Lee, S. You, P. V. Pikhitsa, J. Kim, S. Kwon, C. G. Woo, and M. Choi. Three-dimensional assembly of nanoparticles from charged aerosols. *Nano Letters*, 11(1):119–124, 2011. ISSN 15306984. doi: 10.1021/nl103787k.

[126] K. J. Si, D. Sikdar, Y. Chen, F. Eftekhari, Z. Xu, Y. Tang, W. Xiong, P. Guo, S. Zhang, Y. Lu, Q. Bao, W. Zhu, M. Premaratne, and W. Cheng. Giant plasmene nanosheets, nanoribbons, and origami. *ACS Nano*, 8(11):11086–11093, 2014. ISSN 1936086X. doi: 10.1021/nn504615a.

[127] S. Sun, C. B. Murray, D. Weller, L. Folks, and A. Moser. Monodisperse FePt nanoparticles and ferromagnetic FePt nanocrystal superlattices. *Science*, 287:1989–1992, 2000.

[128] K. Schwenke, L. Isa, and E. D. Gado. Assembly of nanoparticles at

liquid interfaces: crowding and ordering. *Langmuir*, 30:3069, 2014. doi: 10.1021/la404254n.

[129] X. M. Lin, H. M. Jaeger, C. M. Sorensen, and K. J. Klabunde. Formation of Long-Range-Ordered Nanocrystal Superlattices on Silicon Nitride Substrates. *The Journal of Physical Chemistry B*, 105(17):3353–3357, 2001. ISSN 1520-6106. doi: 10.1021/jp0102062. URL http://pubs.acs.org/doi/abs/10.1021/jp0102062.

[130] T. P. Bigioni, X. M. Lin, T. T. Nguyen, E. I. Corwin, T. A. Witten, and H. M. Jaeger. Kinetically driven self assembly of highly ordered nanoparticle monolayers. *Nature Materials*, 5(4):265–270, 2006. ISSN 14764660. doi: 10.1038/nmat1611.

[131] J. Ku, D. M. Aruguete, A. P. Alivisatos, and P. L. Geissler. Self-assembly of magnetic nanoparticles in evaporating solution. *Journal of the American Chemical Society*, 133(4):838–848, 2011. ISSN 00027863. doi: 10.1021/ja107138x.

[132] K. E. Mueggenburg, X. M. Lin, R. H. Goldsmith, and H. M. Jaeger. Elastic membranes of close-packed nanoparticle arrays. *Nature Materials*, 6(9):656–660, 2007. ISSN 14764660. doi: 10.1038/nmat1965.

[133] P. Kanjanaboos, X. M. Lin, J. E. Sader, S. M. Rupich, H. M. Jaeger, and J. R. Guest. Self-assembled nanoparticle drumhead resonators. *Nano Letters*, 13(5):2158–2162, 2013. ISSN 15306984. doi: 10.1021/nl401230z.

[134] P. Kanjanaboos, A. Joshi-Imre, X. M. Lin, and H. M. Jaeger. Strain patterning and direct measurement of Poisson's ratio in nanoparticle monolayer sheets. *Nano Letters*, 11(6):2567–2571, 2011. ISSN 15306984. doi: 10.1021/nl2014873.

[135] J. He, P. Kanjanaboos, N. L. Frazer, A. Weis, X. M. Lin, and H. M.

Jaeger. Fabrication and mechanical properties of large-scale freestanding nanoparticle membranes. *Small*, 6(13):1449–1456, 2010. ISSN 16136810. doi: 10.1002/smll.201000114.

[136] V. Salgueiriño-Maceira, M. A. Correa-Duarte, A. Hucht, and M. Farle. One-dimensional assemblies of silica-coated cobalt nanoparticles: Magnetic pearl necklaces. *Journal of Magnetism and Magnetic Materials*, 303(1):163–166, 2006. ISSN 03048853. doi: 10.1016/j.jmmm.2005.11.003. URL http://linkinghub.elsevier.com/retrieve/pii/S0304885305011194.

[137] C. F. Gauss. The intensity of the Earth's magnetic force reduced to absolute measurement. *Treatises of the Royal Scientific Society*, 8:3–44, 1832.

[138] A. Grosz, M. J. Haji-Sheikh, and S. C. Mukhopadhyay. *High sensitivity magnetometers*. Springer, 2017. ISBN 978-3-319-34068-5. doi: 10.1007/978-3-319-34070-8. URL http://link.springer.com/10.1007/978-3-319-34070-8.

[139] M. P. Blencowe. SQUIDs at the limit. *Nature Physics*, 4(October):753, 2008.

[140] D. Robbes. Highly sensitive magnetometers-a review. *Sensors and Actuators A*, 129:86–93, 2006. ISSN 09244247. doi: 10.1016/j.sna.2005.11.023.

[141] D. Vasyukov, Y. Anahory, L. Embon, D. Halbertal, J. Cuppens, L. Neeman, A. Finkler, Y. Segev, Y. Myasoedov, M. L. Rappaport, M. E. Huber, and E. Zeldov. A scanning superconducting quantum interference device with single electron spin sensitivity. *Nature Nanotechnology*, 8 (9):639–644, 2013. ISSN 1748-3387. doi: 10.1038/nnano.2013.169. URL http://www.nature.com/doifinder/10.1038/nnano.2013.169.

[142] M. Rahm, J. Biberger, V. Umansky, and D. Weiss. Vortex pinning at individual defects in magnetic nanodisks. *Journal of Applied Physics*, 93 (10 2):7429–7431, 2003. ISSN 00218979. doi: 10.1063/1.1558255.

[143] A. Banholzer, R. Narkowicz, C. Hassel, R. Meckenstock, S. Stienen, O. Posth, D. Suter, M. Farle, and J. Lindner. Visualization of spin dynamics in single nanosized magnetic elements. *Nanotechnology*, 22(29):295713, 2011. ISSN 0957-4484. doi: 10.1088/0957-4484/22/29/295713. URL http://stacks.iop.org/0957-4484/22/i=29/a=295713?key=crossref.08ba7b447debc978ff0eb2b4ac3a8232.

[144] S. Tamaru, K. Yakushiji, A. Fukushima, S. Yuasa, and H. Kubota. Ultrahigh sensitivity ferromagnetic resonance measurement based on microwave interferometer. *IEEE Magnetics Letters*, 5, 2014. ISSN 1949307X. doi: 10.1109/LMAG.2014.2365435.

[145] R. C. Richardson and E. N. Smith. *Experimental techniques in condensed matter physics at low temperatures*. Addison Wesley Pub. Co., 1988. ISBN 0201150026.

[146] C. L. Degen, M. Poggio, H. J. Mamin, C. T. Rettner, and D. Rugar. Nanoscale magnetic resonance imaging. *PNAS*, 106(5):1313–1317, 2009. ISSN 0027-8424, 1091-6490. doi: 10.1073/pnas.0812068106. URL http://www.ncbi.nlm.nih.gov/pubmed/19139397{%}5Cnhttp://www.pnas.org/content/106/5/1313.full.pdf.

[147] Y. Obukhov, D. V. Pelekhov, J. Kim, P. Banerjee, I. Martin, E. Nazaretski, R. Movshovich, S. An, T. J. Gramila, S. Batra, and P. C. Hammel. Local ferromagnetic resonance imaging with magnetic resonance force microscopy. *Physical Review Letters*, 100:197601, 2008. ISSN 00319007. doi: 10.1103/PhysRevLett.100.197601.

[148] H. J. Mamin, T. H. Oosterkamp, M. Poggio, C. L. Degen, C. T. Rettner, and D. Rugar. Isotope-selective detection and imaging of organic nanolayers. *Nano Letters*, 9(8):3020–3024, 2009. ISSN 15306984. doi: 10.1021/nl901466p.

[149] C. L. Degen. Scanning magnetic field microscope with a diamond single-spin sensor. *Applied Physics Letters*, 92(24), 2008. ISSN 00036951. doi: 10.1063/1.2943282.

[150] J. M. Taylor, P. Cappellaro, L. Childress, L. Jiang, D. Budker, P. R. Hemmer, A. Yacoby, R. Walsworth, and M. D. Lukin. High-sensitivity diamond magnetometer with nanoscale resolution. *Nature Physics*, 4(October):810–816, 2008. ISSN 1745-2473. doi: 10.1038/nphys1075. URL http://arxiv.org/abs/0805.1367{%}0Ahttp://dx.doi.org/10.1038/nphys1075.

[151] J. R. Maze, P. L. Stanwix, J. S. Hodges, S. Hong, J. M. Taylor, P. Cappellaro, L. Jiang, M. V. Gurudev Dutt, E. Togan, A. S. Zibrov, A. Yacoby, R. L. Walsworth, and M. D. Lukin. Nanoscale magnetic sensing with an individual electronic spin in diamond. *Nature*, 455(7213):644–647, 2008. ISSN 0028-0836. doi: 10.1038/nature07279. URL http://www.nature.com/doifinder/10.1038/nature07279.

[152] G. Balasubramanian, I. Y. Chan, R. Kolesov, M. Al-Hmoud, J. Tisler, C. Shin, C. Kim, A. Wojcik, P. R. Hemmer, A. Krueger, T. Hanke, A. Leitenstorfer, R. Bratschitsch, F. Jelezko, and J. Wrachtrup. Nanoscale imaging magnetometry with diamond spins under ambient conditions. *Nature*, 455(7213):648–651, 2008. ISSN 0028-0836. doi: 10.1038/nature07278. URL http://www.nature.com/doifinder/10.1038/nature07278.

[153] P. Maletinsky, S. Hong, M. S. Grinolds, B. Hausmann, M. D. Lukin,

R. L. Walsworth, M. Loncar, and A. Yacoby. A robust, scanning quantum system for nanoscale sensing and imaging. *Nature Nanotechnology*, 7(May):320–324, 2012. ISSN 1748-3387. doi: 10.1038/nnano.2012.50. URL http://arxiv.org/abs/1108.4437{%}0Ahttp://dx.doi.org/10.1038/nnano.2012.50.

[154] L. Rondin, J. P. Tetienne, S. Rohart, A. Thiaville, T. Hingant, P. Spinicelli, J. F. Roch, and V. Jacques. Stray-field imaging of magnetic vortices with a single diamond spin. *Nature Communications*, 4(May): 1–5, 2013. ISSN 2041-1723. doi: 10.1038/ncomms3279. URL http://www.nature.com/doifinder/10.1038/ncomms3279.

[155] J. P. Tetienne, T. Hingant, J.V. Kim, L. H. Diez, J. P. Adam, K. Garcia, J. F. Roch, S. Rohart, A. Thiaville, D. Ravelosona, and V. Jacques. Nanoscale imaging and control of domain-wall hopping with a nitrogen-vacancy center microscope. *Science*, 344(6190):1366–1369, 2014. ISSN 0036-8075. doi: 10.1126/science.1250113. URL http://www.sciencemag.org/cgi/doi/10.1126/science.1250113.

[156] T. Staudacher, F. Shi, S. Pezzagna, J. Meijer, J. Du, C. A. Meriles, F. Reinhard, and J. Wrachtrup. Nuclear Magnetic Resonance Spectroscopy on a (5-Nanometer)3 Sample Volume. *Science*, 339(6119): 561–563, 2013. ISSN 0036-8075. doi: 10.1126/science.1231675. URL http://www.sciencemag.org/cgi/doi/10.1126/science.1231675.

[157] M. S. Grinolds, S. Hong, P. Maletinsky, L. Luan, M. D. Lukin, R. L. Walsworth, and A. Yacoby. Nanoscale magnetic imaging of a single electron spin under ambient conditions. *Nature Physics*, 9(April):215–219, 2013. ISSN 1745-2473. doi: 10.1038/nphys2543. URL http://arxiv.org/abs/1209.0203{%}0Ahttp://dx.doi.org/10.1038/nphys2543.

[158] C. Müller, X. Kong, J.-M. Cai, K. Melentijević, A. Stacey, M. Markham,

D. Twitchen, J. Isoya, S. Pezzagna, J. Meijer, J. F. Du, M. B. Plenio, B. Naydenov, L. P. McGuinness, and F. Jelezko. Nuclear magnetic resonance spectroscopy with single spin sensitivity. *Nature Communications*, 5:4703, 2014. ISSN 2041-1723. doi: 10.1038/ncomms5703. URL http://www.nature.com/doifinder/10.1038/ncomms5703.

[159] D. Rugar, H. J. Mamin, M. H. Sherwood, M. Kim, C. T. Rettner, K. Ohno, and D. D. Awschalom. Proton magnetic resonance imaging using a nitrogenvacancy spin sensor. *Nat. Nano.*, 10(February):120–124, 2015.

[160] M. Pelliccione, A. Jenkins, P. Ovartchaiyapong, C. Reetz, E. Emmanouilidou, N. Ni, and A. C. B. Jayich. Scanned probe imaging of nanoscale magnetism at cryogenic temperatures with a single-spin quantum sensor. *Nature Nanotechnology*, 11(8):700–705, 2016. ISSN 1748-3387. doi: 10.1038/nnano.2016.68. URL http://www.nature.com/doifinder/10.1038/nnano.2016.68.

[161] J. P. Davis, D. Vick, D. C. Fortin, J. A J Burgess, W. K. Hiebert, and M. R. Freeman. Nanotorsional resonator torque magnetometry. *Applied Physics Letters*, 96(7):072513, 2010. ISSN 00036951. doi: 10.1063/1.3319502.

[162] J. E. Losby, Z. Diao, F. Fani Sani, D. T. Grandmont, M. Belov, J. A. J. Burgess, W. K. Hiebert, and M. R. Freeman. Nanomechanical AC susceptometry of an individual mesoscopic ferrimagnet. *Solid State Comm.*, 198:3–6, 2014.

[163] A. C. Hryciw and P. E. Barclay. Optical design of split-beam photonic crystal nanocavities. *Opt. Lett.*, 38:1612–1614, 2013.

[164] R. A. Barron, M. J. Tour, A. A. Busnaina, J. Y. Jung, S. Somu, Y. Kanj,

D. Potter, R. Daniel, and J. Ullo. Big things in small packages. *Oilfield Review*, 22(3):38–49, 2010. ISSN 09231730.

[165] U. Gysin, S. Rast, A. Aste, T. Speliotis, C. Werle, and E. Meyer. Magnetic properties of nanomagnetic and biomagnetic systems analyzed using cantilever magnetometry. *Nanotechnology*, 22(28): 285715, 2011. ISSN 0957-4484. doi: 10.1088/0957-4484/22/28/285715. URL http://stacks.iop.org/0957-4484/22/i=28/a=285715?key=crossref.2283010921461b8f5d3431efceb2d8ee.

[166] E. Alphandéry, Y. Ding, A. T. Ngo, Z. L. Wang, L. F. Wu, and M. P. Pileni. Assemblies of aligned magnetotactic bacteria and extracted magnetosomes: What is the main factor responsible for the magnetic anisotropy? *ACS Nano*, 3(6):1539–1547, 2009. ISSN 19360851. doi: 10.1021/nn900289n.

[167] R. E. Kopp and J. L. Kirschvink. The identification and biogeochemical interpretation of fossil magnetotactic bacteria. *Earth-Science Reviews*, 86:42–61, 2008. ISSN 00128252. doi: 10.1016/j.earscirev.2007.08.001.

[168] C. Binns, M. T. Qureshi, D. Peddis, S. H. Baker, P. B. Howes, A. Boatwright, S. A. Cavill, S. S. Dhesi, L. Lari, R. Kroger, and S. Langridge. Exchange bias in Fe@Cr coreshell nanoparticles. *Nano letters*, 13:3334, 2013. doi: 10.1021/nl401587t.

[169] P. S. Riehl, K. L. Scott, and R. S. Muller. Electrostatic charge and field sensors based on micromechanical resonators. *Journal of Microelectromechanical Systems*, 12(5):577–589, 2003. ISSN 1057-7157. doi: 10.1109/JMEMS.2003.818066.

[170] X. C. Zhang, E. B. Myers, J. E. Sader, and M. L. Roukes. Nanomechanical torsional resonators for frequency-shift infrared thermal sensing. *Nano Letters*, 13(4):1528–1534, 2013. ISSN 15306984. doi: 10.1021/nl304687p.

[171] I. Bargatin, E. B. Myers, J. S. Aldridge, C. Marcoux, P. Brianceau, L. Duraffourg, E. Colinet, S. Hentz, P. Andreucci, and M. L. Roukes. Large-scale integration of nanoelectromechanical systems for gas sensing applications. *Nano Letters*, 12(3):1269–1274, 2012. ISSN 15306984. doi: 10.1021/nl2037479.

[172] B. Ilic, Y. Yang, K. Aubin, R. Reichenbach, S. Krylov, and H. G. Craighead. Enumeration of DNA molecules bound to a nanomechanical oscillator. *Nano Letters*, 5(5):925–929, 2005. ISSN 15306984. doi: 10.1021/nl050456k.

[173] M. D. LaHaye, J. Suh, P. M. Echternach, K. C. Schwab, and M. L. Roukes. Nanomechanical measurements of a superconducting qubit. *Nature*, 459:960–964, 2009. ISSN 0028-0836. doi: 10.1038/nature08093. URL http://www.nature.com/doifinder/10.1038/nature08093.

[174] Amir H. Safavi-Naeini, Jasper Chan, Jeff T. Hill, Thiago P.Mayer Alegre, Alex Krause, and Oskar Painter. Observation of quantum motion of a nanomechanical resonator. *Physical Review Letters*, 108(3):033602, 2012. ISSN 00319007. doi: 10.1103/PhysRevLett.108.033602.

[175] S. J. Martin, M. A. Butler, J. J. Spates, W. K. Schubert, and M. A. Mitchell. Magnetically-excited flexural plate wave resonator. *IEEE Transactions on Ultrasonics, Ferroelectrics, and Frequency Control*, 45 (5):1381–1387, 1998. ISSN 08853010. doi: 10.1109/58.726465.

[176] R. Kazinczi, P. Turmezei, J. R. Mollinger, and A. Bossche. Design of low-cost resonant mode sensors. In *PROCEEDINGS OF SPIE*, page 4593, 2001.

[177] H. Lang, M. Hegner, and C. Gerber. Nanomechanical cantilever array sensors. In *Springer Handbook of Nanotechnology*, pages 443–459. Springer Berlin Heidelberg, 2007.

[178] P. L. Yu, T. P. Purdy, and C. A. Regal. Control of material damping in high-Q membrane microresonators. *Physical Review Letters*, 108(8): 083603, 2012. ISSN 00319007. doi: 10.1103/PhysRevLett.108.083603.

[179] B. M. Zwickl, W. E. Shanks, A. M. Jayich, C. Yang, A. C. B. Jayich, J. D. Thompson, and J. G. E. Harris. High quality mechanical and optical properties of commercial silicon nitride membranes. *Applied Physics Letters*, 92(10):103125, 2008. ISSN 00036951. doi: 10.1063/1.2884191.

[180] V. P. Adiga, B. Ilic, R. A. Barton, I. Wilson-Rae, H. G. Craighead, and J. M. Parpia. Modal dependence of dissipation in silicon nitride drum resonators. *Applied Physics Letters*, 99(25):253103, 2011. ISSN 00036951. doi: 10.1063/1.3671150.

[181] S. Schmid, K. D. Jensen, K. H. Nielsen, and A. Boisen. Damping mechanisms in high-Q micro and nanomechanical string resonators. *Physical Review B - Condensed Matter and Materials Physics*, 84(16):165307, 2011. ISSN 10980121. doi: 10.1103/PhysRevB.84.165307.

[182] A. R. Muxworthy and W. Williams. Critical superparamagnetic/single-domain grain sizes in interacting magnetite particles: implications for magnetosome crystals. *Journal of The Royal Society Interface*, 6 (41):1207–1212, 2009. ISSN 1742-5689. doi: 10.1098/rsif.2008.0462. URL http://rsif.royalsocietypublishing.org/cgi/doi/10.1098/rsif.2008.0462.

[183] S. H. Chung, A. Hoffmann, S. D. Bader, C. Liu, B. Kay, L. Makowski, and L. Chen. Biological sensors based on Brownian relaxation of magnetic nanoparticles. *Applied Physics Letters*, 85(14):2971–2973, 2004. ISSN 00036951. doi: 10.1063/1.1801687.

[184] An-Hui Lu, E. L. Salabas, and F. Schüth. Magnetic nanoparticles: synthesis, protection, functionalization, and application. *Angewandte*

Chemie (International ed. in English), 46(8):1222–44, jan 2007. ISSN 1433-7851. doi: 10.1002/anie.200602866. URL http://www.ncbi.nlm.nih.gov/pubmed/17278160.

[185] J. Xie, K. Chen, and X. Chen. Production , modification and bio-applications of magnetic nanoparticles gestated by magnetotactic bacteria. *Nano Res*, 2:261–278, 2009. doi: 10.1007/s12274-009-9025-8.

[186] D. A. Bazylinski and S. Schübbe. Controlled biomineralization by and applications of magnetotactic bacteria. *Advances in Applied Microbiology*, 62(07):21–62, 2007. ISSN 00652164. doi: 10.1016/S0065-2164(07)62002-4.

[187] Z. Diao, J. E. Losby, J. A. J. Burgess, V. T. K. Sauer, W. K. Hiebert, and M. R. Freeman. Stiction-free fabrication of lithographic nanostructures on resist-supported nanomechanical resonators. *Journal of Vacuum Science \& Technology B: Microelectronics and Nanometer Structures*, 31(5):051805, 2013. ISSN 21662746. doi: 10.1116/1.4821194.

[188] A. Sugawara, K. I. Fukunaga, M. R. Scheinfein, H. Kobayashi, H. Kitagawa, and A. Tonomura. Electron holography study of the temperature variation of the magnetic order parameter within circularly chained nickel nanoparticle rings. *Applied Physics Letters*, 91(26):262513, 2007. ISSN 00036951. doi: 10.1063/1.2827586.

[189] B.P. Pichon, C. Leuvey, D. Ihawakrim, P. Bernard, G. Schmerber, and S. Begin-Colin. Magnetic properties of mono- and multilayer assemblies of iron oxide nanoparticles promoted by SAMs. *Journal of Physical Chemistry C*, 118(7):3828–3837, 2014. ISSN 19327447. doi: 10.1021/jp412174k.

[190] M. Charilaou, J. Kind, I. García-Rubio, D. Schüler, and A. U. Gehring. Magnetic anisotropy of non-interacting collinear nanocrystal-chains. *Ap-*

plied Physics Letters, 104(11):112406, 2014. ISSN 00036951. doi: 10.1063/1.4869092.

[191] N. Kurti. *Selected works of Louis Neel*. Taylor & Francis, 1988. ISBN 2881243002. URL https://books.google.com/books?hl=en{&}lr={&}id=zudxaVjuLJgC{&}oi=fnd{&}pg=PR7{&}dq=Selected+Works+of+Louis+Neel{&}ots=J31d7hjxCs{&}sig=gKK9ZpzdpOF2uxO-vfidCCoDAK4.

[192] N. Louis. Theorie du tranage magnetique des substances massives dans le domaine de Rayleigh. *J. Phys. Radium*, 11(2):49–61, 1950.

[193] S. Bedanta, A. Barman, W. Kleemann, O. Petracic, and T. Seki. Magnetic nanoparticles: A subject for both fundamental research and applications. *Journal of Nanomaterials*, 2013:952540–22, 2013. ISSN 16874129. doi: 10.1155/2013/952540.

[194] Soshin Chikazumi. *Physics of magnetism*. John Wiley & Sons Inc., 1st editio edition, 1964. ISBN 978-0471155355.

[195] M. Coey. *Magnetism and magnetic materials*. Cambridge University Press, 2010. ISBN 9780511681929.

[196] L. Maldonado-Camargo, I. Torres-Díaz, A. Chiu-Lam, M. Hernández, and C. Rinaldi. Estimating the contribution of Brownian and Néel relaxation in a magnetic fluid through dynamic magnetic susceptibility measurements. *Journal of Magnetism and Magnetic Materials*, 412:223–233, 2016. ISSN 03048853. doi: 10.1016/j.jmmm.2016.03.087. URL http://dx.doi.org/10.1016/j.jmmm.2016.03.087.

[197] N. Tran and T. J. Webster. Magnetic nanoparticles: biomedical applications and challenges. *Journal of Materials Chemistry*, 20:8760, 2010.

ISSN 0959-9428. doi: 10.1039/c0jm00994f. URL http://xlink.rsc.org/?DOI=c0jm00994f.

[198] R.E. Rosensweig. Heating magnetic fluid with alternating magnetic field. *Journal of Magnetism and Magnetic Materials*, 252:370–374, 2002. ISSN 03048853. doi: 10.1016/S0304-8853(02)00706-0. URL http://www.sciencedirect.com/science/article/pii/S0304885302007060{%}5Cnhttp://linkinghub.elsevier.com/retrieve/pii/S0304885302007060{%}5Cnhttp://linkinghub.elsevier.com/retrieve/pii/S0304885302007060.

[199] Arun Prakash Upadhyay, Dilip Kumar Behara, Gyan Prakash Sharma, Raj Ganesh S. Pala, and Sri Sivakumar. Self-directed assembly of nanoparticles: A review on various approaches, 2015.

[200] W. C. Fon, K. C. Schwab, J. M. Worlock, and M. L. Roukes. Nanoscale, phonon-coupled calorimetry with sub-attojoule/Kelvin resolution. *Nano Letters*, 5(10):1968–1971, 2005. ISSN 15306984. doi: 10.1021/nl051345o.

[201] M. Li, W. H. P. Pernice, C. Xiong, T. Baehr-Jones, M. Hochberg, and H. X. Tang. Harnessing optical forces in integrated photonic circuits. *Nature*, 456:480–484, 2008.

[202] Y. Liu, H. Miao, V. Aksyuk, and K. Srinivasan. Wide cantilever stiffness range cavity optomechanical sensors for atomic force microscopy. *Opt. Express*, 20(16):18268–18280, 2012.

[203] G. Anetsberger, E. Gavartin, O. Arcizet, Q. P. Unterreithmeier, E. M. Weig, M. L. Gorodetsky, J. P. Kotthaus, and T. J. Kippenberg. Measuring nanomechanical motion with an imprecision below standard quantum limit. *Phys. Rev. A*, 82:61804, 2010.

[204] A. G. Krause, M. Winger, T. D. Blasius, W. Lin, and O. Painter. A

high-resolution microchip optomechanical accelerometer. *Nat. Photon.*, 6:768–772, 2012.

[205] P. H. Kim, C. Doolin, B. D. Hauer, A. J. R. MacDonald, M. R. Freeman, P. E. Barclay, and J. P. Davis. Nanoscale torsional optomechanics. *Applied Physics Letters*, 102(5):053102, 2013. ISSN 00036951. doi: 10.1063/1.4789442.

[206] H Li and M Li. Optomechanical photon shuttling between photonic cavities. *Nat. Nano.*, 9:913–919, 2014.

[207] J. Chan, T. P. M. Alegre, A. H. Safavi-Naeini, J.T. Hill, A. Krause, S. Groblacher, Aspelmeyer M., and O. Painter. Laser cooling of a nanomechanical oscillator into its quantum ground state. *Nature*, 478:89–92, 2011.

[208] X. Zhang, C. L. Zou, L. Jiang, and H. X. Tang. Cavity magnomechanics. *Sci. Adv.*, 2:1501286, 2016.

[209] A. C. Bleszynski-Jayich, W. E. Shanks, B. Peaudecerf, E. Ginossar, F. von Oppen, L. Glazman, and J. G. E. Harris. Persistent currents in normal metal rings. *Science*, 326:272 – 275, 2009. ISSN 0036-8075. doi: 10.1126/science.1178139. URL http://science.sciencemag.org/content/326/5950/272.

[210] J. A. J. Burgess, A. E. Fraser, F. F. Sani, D. Vick, B. D. Hauer, J. P. Davis, and M. R. Freeman. Quantitative magneto-mechanical detection and control of the Barkhausen effect. *Science*, 339(6123):1051–1054, 2013. ISSN 0036-8075. doi: 10.1126/science.1231390. URL http://www.sciencemag.org/cgi/doi/10.1126/science.1231390.

[211] R. L. Compton and P. A. Crowell. Dynamics of a pinned magnetic vortex. *Phys. Rev. Lett.*, 97:137202, 2006.

[212] J Moreland. Micromechanical instruments for ferromagnetic measurements. *J. Phys. D*, 36:R39–R51, 2003.

[213] J. E. Losby. *Nanomechanical torque magnetometry and AC susceptometry of mesoscopic magnetic structures*. PhD thesis, University of Alberta, 2014.

[214] T. Firdous, D. Vick, M. Belov, F. Fani Sani, A. Mcdermott, J. E. Losby, D. A. Bazylinski, T. Prozorov, D. K. Potter, and M. R. Freeman. Nanomechanical torque magnetometry of an individual aggregate of ˜350 nanoparticles. *Can. J. Phys*, 93(March):1252–1256, 2015. doi: dx.doi.org/10.1139/cjp-2014-0722.

[215] C. Ascoli, P. Baschieri, C. Frediani, L. Lenci, M. Martinelli, G. Alzetta, R. M. Celli, and L. Pardi. Micromechanical detection of magnetic resonance by angular momentum absorption. *Appl. Phys. Lett.*, 69 (December):3920–3922, 1996. ISSN 00036951. doi: 10.1063/1.117570.

[216] S. Forstner, E. Sheridan, J. Knittel, C. L. Humphreys, G. A. Brawley, H. Rubinsztein-Dunlop, and W. P. Bowen. Ultrasensitive optomechanical magnetometry. *Adv. Mater.*, 26:6348–6353, 2014.

[217] A. C. Hryciw, M. Wu, B. Khanaliloo, and P. E. Barclay. Tuning of nanocavity optomechanical coupling using a near-field fiber probe. *Optica*, 2(5):491–496, 2015. ISSN 2334-2536. doi: 10.1364/OPTICA.2.000491. URL http://www.osapublishing.org/optica/abstract.cfm?URI=optica-2-5-491.

[218] J. D. Jackson. *Classical electrodynamics*. John Wiley \& Sons Inc., 1998. ISBN 0 471 43131 1. doi: 10.1119/1.19136. URL http://link.aip.org/link/?AJPIAS/67/841/27)Z.

[219] C. P. Michael, M. Borselli, T. J. Johnson, C. Chrystal, and O. Painter. An

optical fiber-taper probe for wafer-scale microphotonic device characterization. *Optics Express*, 15(8):4745, 2007. ISSN 1094-4087. doi: 10.1364/OE.15.004745. URL https://www.osapublishing.org/oe/abstract.cfm?uri=oe-15-8-4745.

[220] B. D. Hauer, P. H. Kim, C. Doolin, A. J. R. MacDonald, H. Ramp, and J. P. Davis. On-chip cavity optomechanical coupling. *EPJ Techniques and Instrumentation*, 1(1):4, 2014. ISSN 2195-7045. doi: 10.1140/epjti4. URL http://epjtechniquesandinstrumentation.springeropen.com/articles/10.1140/epjti4.

[221] P. E. Barclay, K. Srinivasan, and O. Painter. Nonlinear response of silicon photonic crystal micresonators excited via an integrated waveguide and fiber taper. *Optics Express*, 13(3):801, 2005. ISSN 1094-4087. doi: 10.1364/OPEX.13.000801.

[222] B. D. Hauer, C. Doolin, K. S.D. Beach, and J. P. Davis. A general procedure for thermomechanical calibration of nano/micro-mechanical resonators. *Annals of Physics*, 339:181–207, 2013. ISSN 00034916. doi: 10.1016/j.aop.2013.08.003. URL http://dx.doi.org/10.1016/j.aop.2013.08.003.

[223] A. N. Cleland and M. L. Roukes. Noise processes in nanomechanical resonators. *Journal of Applied Physics*, 92(5):2758–2769, 2002. ISSN 00218979. doi: 10.1063/1.1499745.

[224] M. Eichenfield, J. Chan, R. M. Camacho, K. J. Vahala, and O. Painter. Optomechanical crystals. *Optics Express*, 17(22):20078–20098, 2009. ISSN 0028-0836. doi: 10.1038/nature08524. URL http://arxiv.org/abs/0906.1236{%}0Ahttp://dx.doi.org/10.1038/nature08524.

[225] J. Rigue, D. Chrischon, A. M. H. De Andrade, and M. Carara. A torque magnetometer for thin films applications. *Journal of Magnetism and*

Magnetic Materials, 324(8):1561–1564, 2012. ISSN 03048853. doi: 10.1016/j.jmmm.2011.12.002. URL http://dx.doi.org/10.1016/j.jmmm.2011.12.002.

[226] J. E. Losby, J. A. J. Burgess, C. M. B. Holt, J. N. Westwood, D. Mitlin, W. K. Hiebert, and M. R. Freeman. Nanomechanical torque magnetometry of permalloy cantilevers. *J. Appl. Phys.*, 108:123910, 2010.

[227] P. H. Kim, B. D. Hauer, C. Doolin, F. Souris, and J. P. Davis. Approaching the standard quantum limit of mechanical torque sensing. Technical report, University of Alberta, 2016. URL arxiv:1607.00069v1.

[228] A.H. Safavi-Naeini, S. Groblacher, Hill J. T., J. Chan, M. Aspelmeyer, and O. Painter. Squeezed light from a silicon micromechanical resonator. *Nature*, 500:185–189, 2013.

[229] J. Losby, J. A. J. Burgess, Z. Diao, D. C. Fortin, W. K. Hiebert, and M. R. Freeman. Thermo-mechanical sensitivity calibration of nanotorsional magnetometers. *Journal of Applied Physics*, 111(7):07D305, 2012. ISSN 00218979. doi: 10.1063/1.3676231.

[230] S. Forstner, S. Prams, J. Knittel, E. D. Van Ooijen, J. D. Swaim, G. I. Harris, A. Szorkovszky, W. P. Bowen, and H. Rubinsztein-Dunlop. Cavity optomechanical magnetometer. *Physical Review Letters*, 108(12):1–5, 2012. ISSN 00319007. doi: 10.1103/PhysRevLett.108.120801.

[231] J. W. van Honschoten, W. W. Koelmans, S. M. Konings, L. Abelmann, and M. Elwenspoek. Nanotesla torque magnetometry using a microcantilever. In *Proceedings of Eurosensors XXII, the European Conference on Solid-State Transducers*, 2008.

[232] X. Yin, Q. Jiao, L. Yuan, and S. H. Liou. MEMS torsion oscillator

magnetic field sensor. *IEEE Transactions on Magnetics*, 49(7):3890–3892, 2013. ISSN 00189464. doi: 10.1109/TMAG.2013.2252153.

[233] R .P. Cowburn, D. K. Koltsov, A. O. Adeyeye, M. E. Welland, and D. M. Tricker. Single-domain circular nanomagnets. *Phys. Rev. Lett*, 82:1042–1045, 1999.

[234] N. Abu-Libdeh and D. Venus. Dynamics of domain growth driven by dipolar interactions in a perpendicularly magnetized ultrathin film. *Phys. Rev. B*, 81:195416, 2010.

[235] D. Le. Sage, K. Arai, D. R. Glenn, S. J. Devience, L. M. Pham, D. Lukin, A. Yacoby, A. Komeili, and R. L. Walsworth. Optical magnetic imaging of living cells. *Nature*, 496(7446):486–489, 2013. doi: 10.1038/nature12072. Optical.

[236] F. Ye, R. S. Fishman, Y. Ren, H. J. Kang, Y. Qiu, and T. Kimura. Magnetic interactions in the geometrically frustrated triangular lattice antiferromagnet CuFeO2. *Phys. Rev. Lett*, 157201:157201, 2007. doi: 10.1103/PhysRevLett.99.157201.

[237] B. Khanaliloo, H. Jayakumar, A. C. Hryciw, D. P. Lake, H. Kaviani, and P. E. Barclay. Single crystal diamond nanobeam waveguide optomechanics. *Phys. Rev. X*, 5:041051, 2015. ISSN 2160-3308. doi: 10.1103/PhysRevX.5.041051. URL http://arxiv.org/abs/1502.01788{%}0Ahttp://dx.doi.org/10.1103/PhysRevX.5.041051.

[238] G. Siegel, M. C. Prestgard, S. Teng, and A. Tiwari. Robust longitudinal spin-seebeck effect in Bi-YIG thin films. *Scientific Reports*, 4:4429, 2014. ISSN 20452322. doi: 10.1038/srep04429.

[239] A. A. Serga, A. V. Chumak, and B. Hillebrands. YIG magnonics. *Journal*

of Physics D: Applied Physics, 43(26):264002, 2010. ISSN 00223727. doi: 10.1088/0022-3727/43/26/264002.

[240] P. Pirro, T. Brflcher, A. V. Chumak, B. Leven, and B. Hillebrands. Spin wave propagation in a microstructured YIG/Pt bilayer waveguide. Technical report. URL http://www.physik.uni-kl.de/fileadmin/hillebrands/Jahresberichte/Annual{_}report{_}2013/AR2013-Chapter4-8.pdf.

[241] E. R. J. Edwards, M. Buchmeier, V. E. Demidov, and S. O. Demokritov. Magnetostatic spin-wave modes of an in-plane magnetized garnet-film disk. *Journal of Applied Physics*, 113(10):103901, 2013. ISSN 00218979. doi: 10.1063/1.4794318.

[242] T. M. Wallis, J. Moreland, and P. Kabos. Einstein de Haas effect in a NiFe film deposited on a microcantilever. *Appl. Phys. Lett.*, 89:122502, 2006. doi: 10.1063/1.2355445.

[243] C. Hovde, B. Patton, E. Corsini, J. Higbie, and D. Budker. Sensitive optical atomic magnetometer based on nonlinear magneto-optical rotation. *Proceedings of SPIE - The International Society for Optical Engineering*, page 7693, 2010. doi: 10.1117/12.850302.

[244] S. Klingler, A. Chumak, T. Mewes, B. Khodadadi, C. Mewes, C. Dubs, O. Surzhenko, B. Hillebrands, and A. Conca. Measurements of the exchange stiffness of YIG films using broadband ferromagnetic resonance techniques. *Journal of Physics D: Applied Physics*, 48(1):15001, 2015. ISSN 13616463. doi: 10.1088/0022-3727/48/1/015001. URL http://dx.doi.org/10.1088/0022-3727/48/1/015001.

[245] Mahdi Jamali, Jae Hyun Kwon, Soo Man Seo, Kyung Jin Lee, and Hyunsoo Yang. Spin wave nonreciprocity for logic device applications. *Scientific Reports*, 3:3160, 2013. ISSN 20452322. doi: 10.1038/srep03160.

[246] V. E. Demidov, S. O. Demokritov, K. Rott, P. Krzysteczko, and G. Reiss. Linear and nonlinear spin-wave dynamics in macro- and microscopic magnetic confined structures. *Journal of Physics D: Applied Physics*, 41(16): 164012, 2008. ISSN 00223727. doi: 10.1088/0022-3727/41/16/164012.

[247] M. C. Onbasli, L. Beran, M. Zahradník, M. Kucera, R. Antoš, J. Mistrík, G. F. Dionne, M. Veis, and C. A. Ross. Optical and magneto-optical behavior of cerium yttrium iron garnet thin films at wavelengths of 200-1770 nm. *Scientific Reports*, 6:1–10, 2016. ISSN 20452322. doi: 10.1038/srep23640. URL http://dx.doi.org/10.1038/srep23640.

[248] T. Goto, M. C. Onbalò, and C. A. Ross. Magneto-optical properties of cerium substituted yttrium iron garnet films with reduced thermal budget for monolithic photonic integrated circuits. *Optics Express*, 20(27):28507, 2012. ISSN 1094-4087. doi: 10.1364/OE.20.028507. URL https://www.osapublishing.org/oe/abstract.cfm?uri=oe-20-27-28507.

[249] M. Gomi, K. Satoh, and M. Abe. Giant faraday rotation of ce-substituted yig films epitaxially grown by rf sputtering. *Japanese Journal of Applied Physics*, 27(8):L1536, 1988. ISSN 13474065. doi: 10.1143/JJAP.27.L1536.

[250] Micro Lambda Wireless Incorporation. YIG tuned oscillators. Technical Report 510, 2016.

[251] A. B. Ustinov, A. V. Drozdovskii, A. A. Nikitin, and B. A. Kalinikos. Spin-wave band-pass filters based on yttrium iron garnet films for tunable microwave photonic oscillators. *Journal of Physics: Conference Series*, 661(1):012058, 2015. ISSN 17426596. doi: 10.1088/1742-6596/661/1/012058.

[252] N. I. Mezin, A. A. Glushchenko, and Yu. E. Kuzovlev. Chaos generators based on yttrium-iron garnet films for communication systems with a

chaotic synchronous response. *Technical Physics Letters*, 38(10):876–879, 2012. ISSN 1063-7850. doi: 10.1134/S1063785012100082. URL http://link.springer.com/10.1134/S1063785012100082.

[253] Teledyne Microwave Solutions. YIG filter products. Technical report.

[254] S. Y. Sung, X. Qi, and B. J. H. Stadler. Fabrication of garnet waveguides and polarizers for integrated optical isolators. *Conference on Lasers and Electro-Optics, 2007, CLEO 2007*, pages 5–6, 2007. ISSN 19492081. doi: 10.1109/CLEO.2007.4452833.

[255] M. Collet, O. Gladii, M. Evelt, V. Bessonov, L. Soumah, P. Bortolotti, S. O. Demokritov, Y. Henry, V. Cros, M. Bailleul, V. E. Demidov, and A. Anane. Spin-wave propagation in ultra-thin YIG based waveguides. *Applied Physics Letters*, 110(9):092408, 2017. ISSN 00036951. doi: 10.1063/1.4976708.

[256] R. C. Cumming and D. W. Howell. YIG filters as envelope limiters. In *IEEE Transactions on Microwave Theory and Techniques*, page 616, 1965.

[257] F. G. Eggers and W. Strauss. A uhf delay line using single-crystal yttrium iron garnet. *Journal of Applied Physics*, 34(4):1180, 1963. ISSN 00218979. doi: 10.1063/1.1729423.

[258] J. Arnaud. Adjustable magnetostatic surface-wave multistrip directional coupler. *Electronics Letters*, 16(5):195, 1980.

[259] J. Warit, T. Veda, and M. Tsutsumi. Microwave circulator using yttrium iron garnet. In *Microwave Conference*, page 1212, 2000.

[260] H. Asao, M. Miyazaki, H. Oh-Hashi, and O. Ishida. A magnetostatic wave radiation impedence of symmetric slot line in signal-to-noise enhancer. *Electronics and Communications in Japan*, 79(6):53, 1996.

[261] J. G. Doidge. *Parametric devices using magnetic thin film and thin disks of yttrium iron garnet*. PhD thesis, 1963.

[262] J. P. Parekh, H. S. Tuan, and K. W. Chang. Magnetostatic wave convolvers. *Circuits Systems Signal Process*, 4(1-2):253, 1985. URL https://www.google.com/patents/US4341998.

[263] L. Bi, J. Hu, L. Kimerling, and C. A. Ross. Fabrication and characterization of As2S3/Y3Fe5O12 and Y3Fe5O12/SOI strip-loaded waveguides for integrated optical isolator applications. *Integrated Optics: Devices, Materials, and Technologies, SPIE.*, page 760406, 2010. doi: 10.1117/12.841832. URL http://proceedings.spiedigitallibrary.org/proceeding.aspx?doi=10.1117/12.841832.

[264] L Shtirberg, M Shklyar, and A Blank. ESR spectroscopy employing YIG-Tuned Oscillator in conjunction with low-quality factor resonators. In *22nd International Crimean Conference Microwave and Telecommunication Technology*, pages 124–125, 2012. ISBN 9789663353760. URL http://www.scopus.com/inward/record.url?eid=2-s2.0-84869824976{&}partnerID=40{&}md5=c71ffba0368ff541ac326370a40afb99.

[265] R. L. Streever and G. A. Uriano. Nuclear resonance study of gallium-substituted yttrium iron garnet. *Physical Review*, 139(1A):A305, 1965.

[266] Z. Zhang and P. C. Hammel. Magnetic resonance force microscopy with a ferromagnetic tip mounted on the force detector. *Solid State Nuclear Magnetic Resonance*, 11(1-2):65–72, 1998. ISSN 09262040. doi: 10.1016/S0926-2040(97)00097-0.

[267] S. Yakata, T. Tanaka, K. Kiseki, K. Matsuyama, and T. Kimura. Wide range tuning of resonant frequency for a vortex core in a regular triangle

magnet. *Scientific Reports*, 3:1–5, 2013. ISSN 20452322. doi: 10.1038/srep03567.

[268] P. H. Kim, F. Fani. Sani, M. R. Freeman, and J. P. Davis. Broadband optomechanical transduction of nanomagnetic spin modes. *Appl. Phys. Lett.*, 113:083104, 2018. ISSN 00036951. doi: 10.1063/1.5039640. URL http://arxiv.org/abs/1805.04186.

[269] V. Novosad, F. Y. Fradin, P. E. Roy, K. S. Buchanan, K. Yu. Guslienko, and S. D. Bader. Magnetic vortex resonance in patterned ferromagnetic dots. *Phys. Rev. B.*, 72:024455, 2005. doi: 10.1103/PhysRevB.72.024455.

[270] N. Hodgson and H. Weber. *Optical resonators*. Springer-Verlag London. ISBN 9781447135975.

[271] A. Prohl. *Computational micromagnetism*. Springer Fachmedien Wiesbaden, 2001. ISBN 9783519003588.

[272] M. Scheinfein. LLG micromagnetics simulator. URL (llgmi-cro@mindspring.com).

[273] M. J. Donahue and D. G. Porter. Oommf user's guide, version 1.0. interagency report nistir 6376, national institute of standards and technology, gaithersburg. Technical report, 1999.

[274] W. Scholz, J. Fidler, T. Schrefl, D. Suess, R. Dittrich, H. Forster, and V. Tsiantos. Scalable parallel micromagnetic solvers for magnetic nanostructures. *Computational Materials Science*, 28(2):366–383, 2003. ISSN 09270256. doi: 10.1016/S0927-0256(03)00119-8.

[275] A. Vansteenkiste, J. Leliaert, M. Dvornik, F. Garcia-Sanchez, and B. Van Waeyenberge. The design and verification of Mumax3 - code examples. *AIP Advances*, 4(10):107133, 2014. ISSN 21583226. doi: 10.1063/1.4899186. URL http://arxiv.org/abs/1406.7635.

[276] Thomas Fischbacher, Matteo Franchin, Giuliano Bordignon, and Hans Fangohr. A systematic approach to multiphysics extensions of finite-element-based micromagnetic simulations: Nmag. *IEEE Transactions on Magnetics*, 43(6):2896–2898, 2007. ISSN 00189464. doi: 10.1109/TMAG.2007.893843.

[277] G. S. Abo, Y. K. Hong, J. Park, J. Lee, W. Lee, and B. C. Choi. Definition of magnetic exchange length. *IEEE Transactions on Magnetics*, 49(8): 4937, 2013. ISSN 00189464. doi: 10.1109/TMAG.2013.2258028.

[278] S. Whitelam and R. L. Jack. The statistical mechanics of dynamic pathways to self-assembly. *Annual Review of Physical Chemistry*, 66(1):143–163, 2015. ISSN 0066-426X. doi: 10.1146/annurev-physchem-040214-121215. URL http://www.annualreviews.org/doi/10.1146/annurev-physchem-040214-121215.

[279] S. Ilday, G. Makey, G.B. Akguc, Ö. Yavuz, O. Tokel, I. Pavlov, O. Gülseren, and F. Ö. Ilday. Rich complex behaviour of self-assembled nanoparticles far from equilibrium. *Nature Communications*, 8:14942, 2017. ISSN 2041-1723. doi: 10.1038/ncomms14942. URL http://www.nature.com/doifinder/10.1038/ncomms14942.

[280] Z. M. Sherman and J. W. Swan. Dynamic, directed self-assembly of nanoparticles via toggled interactions. *ACS Nano*, 10(5):5260–5271, 2016. ISSN 1936086X. doi: 10.1021/acsnano.6b01050.

[281] Jonathan R. Davis and Athanassios Z. Panagiotopoulos. Monte Carlo simulations of amphiphilic nanoparticle self-assembly. *Journal of Chemical Physics*, 129:194706, 2008. ISSN 00219606. doi: 10.1063/1.3009183.

[282] Xi. Zhao, Y. Leng, and P. T. Cummings. Self-assembly of 1,4-benzenedithiolate/tetrahydrofuran on a gold surface: A Monte Carlo

simulation study. *Langmuir*, 22(9):4116–4124, 2006. ISSN 07437463. doi: 10.1021/la0532252.

[283] B. B. Bokhonov, M. R. Sharafutdinov, D. R. Whitcomb, and L. P. Burleva. In situ self-assembly of silver nanoparticles. *Journal of Physical Chemistry C*, 118(22):11980–11989, 2014. ISSN 19327455. doi: 10.1021/jp501508a.

[284] Li-Tang Yan and Xu-Ming Xie. Computational modeling and simulation of nanoparticle self-assembly in polymeric systems: Structures, properties and external field effects. *Progress in Polymer Science*, 38(2):369–405, 2013. ISSN 00796700. doi: 10.1016/j.progpolymsci.2012.05.001. URL http://linkinghub.elsevier.com/retrieve/pii/S0079670012000408.

[285] M. Thomas and R. Schwartz. Quantitative computational models of molecular self-assembly in systems biology. *Physical Biology*, 14:035003, 2017.

[286] W. Xie, G. Xu, and X. Feng. Self-assembly of lipids and nanoparticles in aqueous solution: Self-consistent field simulations. *Theoretical & Applied Mechanics Letters*, 2(1):14004, 2012. ISSN 20950349. doi: 10.1063/2.1201404. URL http://dx.doi.org/10.1063/2.1201404.

[287] E. M. Schwen, I. Mazilu, and D. A. Mazilu. A two-state stochastic model for nanoparticle self-assembly: Theory, computer simulations and applications. *European Journal of Physics*, 36(2):0–13, 2015. ISSN 13616404. doi: 10.1088/0143-0807/36/2/025003.

[288] I. Mazilu, E. M. Schwen, W. E. Banks, B. K. Pope, and D. A. Mazilu. A stochastic model of nanoparticle self-assembly on Cayley trees. *Journal of Physics: Conference Series*, 574:012086, 2015. ISSN 1742-6588. doi: 10.1088/1742-6596/574/

1/012086. URL http://stacks.iop.org/1742-6596/574/i=1/a=012086?key=crossref.a4934c817f9874272bfcf79fc97185c9.

[289] X. Xue, K. Liu, and E. P. Furlani. Theoretical study of the self-assembly and optical properties of 1D chains of magnetic-plasmonic nanoparticles. *Journal of Physical Chemistry C*, 121(17):9489–9496, 2017. ISSN 19327455. doi: 10.1021/acs.jpcc.7b00824.

[290] P. Victor, G. Venkat, A. Z. Panagiotopoulos, H. Liu, and S. K. Kumar. Modeling the anisotropic self-assembly of spherical polymer-grafted nanoparticles. *The Journal of Chemical Physics*, 131:221102, 2009. doi: https://doi.org/10.1063/1.3267729View.

[291] K. Mertens, V. Putkaradze, D. Xia, and S. R. J. Brueck. Theory and experiment for one-dimensional directed self-assembly of nanoparticles. *Journal of Applied Physics*, 98(3):034309, 2005. ISSN 00218979. doi: 10.1063/1.1999029.

[292] S. Pankavich, Z. Shreif, Y. Miao, and P. Ortoleva. Self-assembly of nanocomponents into composite structures: Derivation and simulation of Langevin equations. *Journal of Chemical Physics*, 130(19):1, 2009. ISSN 00219606. doi: 10.1063/1.3134683.

[293] Ki-bum Kim. Nanofabrication process using electron beam lithography. Technical report, 2009.

[294] J. A. Bau. *Transition metal oxide materials for electrocatalytic and photocatalytic water*. PhD thesis, 2015.

[295] A. Peigneux, C. Valverde-Tercedor, R. López-Moreno, T. Pérez-González, M. A. Fernández-Vivas, and C. Jiménez-López. Learning from magnetotactic bacteria: A review on the synthesis of biomimetic nanoparticles

mediated by magnetosome-associated proteins. *Journal of Structural Biology*, 196(2):75–84, 2016. ISSN 10958657. doi: 10.1016/j.jsb.2016.06.026.

[296] D. Faivre and Di. Schuler. Magnetotactic bacteria and magnetosomes. *Chemical Reviews*, 108(9):4875–4898, 2008.

[297] E. Alphandery. Applications of magnetosomes synthesized by magnetotactic bacteria in medicine. *Frontiers in Bioengineering and Biotechnology*, 2(March):1–6, 2014. ISSN 2296-4185. doi: 10.3389/fbioe.2014.00005. URL http://journal.frontiersin.org/article/10.3389/fbioe.2014.00005/abstract.

[298] R. Uebe and D. Schüler. Magnetosome biogenesis in magnetotactic bacteria. *Nature Reviews Microbiology*, 14(10):621–637, 2016. ISSN 17401534. doi: 10.1038/nrmicro.2016.99. URL http://dx.doi.org/10.1038/nrmicro.2016.99.

[299] J. Li and Y. Pan. Environmental factors affect magnetite magnetosome synthesis in magnetospirillum magneticum AMB-1: implications for biologically controlled mineralization. *Geomicrobiology Journal*, 29(4):362–373, 2012. ISSN 01490451. doi: 10.1080/01490451.2011.565401.

[300] A. Mohtasebzadeh, L. Ye, and T. Crawford. Magnetic nanoparticle arrays self-assembled on perpendicular magnetic recording media. *International Journal of Molecular Sciences*, 16(8):19769–19779, 2015. ISSN 1422-0067. doi: 10.3390/ijms160819769. URL http://www.mdpi.com/1422-0067/16/8/19769/.

[301] R. M. Choueiri, E. Galati, H. Thérien-Aubin, A. Klinkova, E. M. Larin, A. Querejeta-Fernández, L. Han, H. L. Xin, O. Gang, E. B. Zhulina, M. Rubinstein, and E. Kumacheva. Surface patterning of nanoparticles with polymer patches. *Nature*, 538(7623):79–83, 2016. ISSN

14764687. doi: 10.1038/nature19089. URL http://dx.doi.org/10.1038/nature19089.

[302] A. Aqeel, I. J. Vera-Marun, B. J. van Wees, and T. T. M. Palstra. Surface sensitivity of the spin Seebeck effect. *Journal of Applied Physics*, 116(15): 1–5, 2014. ISSN 10897550. doi: 10.1063/1.4897933.

[303] V. A. Barinov, V. A. Tsurin, V. S. Gaviko, A. Ye Yermakov, Ye I. Teytel, N. I. Shegoleva, F. Leccabue, B. E. Watts, R. Panizzieri, G. Bocelli, and S. Díaz Castañón. Effects of mechanical grinding on magneto-structural properties of BaFe12O19powders. *Journal of Magnetism and Magnetic Materials*, 139(1-2):143–150, 1995. ISSN 03048853. doi: 10.1016/0304-8853(95)90039-X.

[304] J. W. Nielsen, D. A. Lepore, J. Zneimer, and G. B. Townsend. Effect of mechanical, thermal, and chemical treatment of the ferrimagnetic resonance linewidth on lithium ferrite crystals. *Journal of Applied Physics*, 33(3):1379–1380, 1962. ISSN 00218979. doi: 10.1063/1.1728741.

[305] Stephan Leitenmeier, Andreas Heinrich, Jorg K N Lindner, and Bernd Stritzker. Growth of epitaxial bismuth and gallium substituted lutetium iron garnet films by pulsed laser deposition. *Journal of Applied Physics*, 99(8):08M704, 2006. ISSN 00218979. doi: 10.1063/1.2170057.

[306] M. Baluktsian, K. Keskinbora, U. T. Sanli, and G. Schütz. Micromachining of Si3N4 by Ga+ -ion implantation and dry etching. *Microscopy and Microanalysis*, 22(S3):170–171, 2016. ISSN 1431-9276. doi: 10.1017/S1431927616001707. URL http://www.journals.cambridge.org/abstract{_}S1431927616001707.

[307] D. Qian, C. Ma, K. L. More, Y. S. Meng, and M. Chi. Advanced analytical electron microscopy for lithium-ion batteries. *NPG Asia Materials*, 7

(6):e193, 2015. ISSN 18844057. doi: 10.1038/am.2015.50. URL http://dx.doi.org/10.1038/am.2015.50.

[308] K. Pagowska, R. Ratajczak, A. Stonert, A. Turos, L. Nowicki, N. Sathish, P. Jóźwik, and A. Muecklich. RBS/channeling and TEM study of damage buildup in ion bombarded GaN. *Acta Physica Polonica A*, 120(1):153–155, 2011. ISSN 05874246.

[309] C. R. Elliott, T. Ambridge, and R. Heckingbottom. Ion implantation damage in GaAs: A TEM study of the variation with ion species and stoichiometry. *Solid State Electronics*, 21(6):859–863, 1978. ISSN 00381101. doi: 10.1016/0038-1101(78)90310-6.

[310] V. A. Skuratov, J. O'Connell, A. S. Sohatsky, and J. Neethling. TEM study of damage recovery in SiC by swift Xe ion irradiation. *Nuclear Instruments and Methods in Physics Research, Section B: Beam Interactions with Materials and Atoms*, 327(1):89–92, 2014. ISSN 0168583X. doi: 10.1016/j.nimb.2013.10.082. URL http://dx.doi.org/10.1016/j.nimb.2013.10.082.

[311] R. Miranda and J. M. Rojo. Influence of ion radiation damage on surface reactivity. *Vacuum*, 34(12):1069, 1984.

[312] N. I. Kato. Reducing focused ion beam damage to transmission electron microscopy samples. *Journal of Electron Microscopy*, 53(5):451–458, 2004. ISSN 00220744. doi: 10.1093/jmicro/dfh080.

[313] G. Hlawacek, V. Veligura, R. van Gastel, and B. Peolsema. Helium ion microscopy. *Surface Science Techniques*, pages 461–497, 2013. ISSN 2166-2746. doi: 10.1007/978-3-642-34243-1_16. URL http://www.springer.com/physics/condensed+matter+physics/book/978-3-642-34242-4.

[314] Z. Liao, T. Zhang, M. Gall, A. Dianat, R. Rosenkranz, R. Jordan, G. Cuniberti, and E. Zschech. Lateral damage in graphene carved by high energy focused gallium ion beams. *Applied Physics Letters*, 107(1):013108, 2015. ISSN 00036951. doi: 10.1063/1.4926647.

[315] P. Roediger, H. D. Wanzenboeck, S. Waid, G. Hochleitner, and E. Bertagnolli. Focused-ion-beam-inflicted surface amorphization and gallium implantation-new insights and removal by focused-electron-beam-induced etching. *Nanotechnology*, 22(23):235302, 2011. ISSN 09574484. doi: 10.1088/0957-4484/22/23/235302.

[316] S. Rubanov and P. R. Munroe. Damage in III V compounds during focused Ion beam milling. *Microscopy Microanalysis*, 11:446–455, 2005.

[317] T. Yamamoto, J. Yanagisawa, K. Gamo, S. Takaoka, and K. Murase. Estimation of damage induced by focused Ga ion beam irradiation. *Japanese Journal of Applied Physics*, 32(12 S):6268–6273, 1993. ISSN 13474065. doi: 10.1143/JJAP.32.6268.

[318] K. A. Unocic, M. J. Mills, and G. S. Daehn. Effect of gallium focused ion beam milling on preparation of aluminium thin foils. *Journal of Microscopy*, 240(3):227–238, 2010. ISSN 00222720. doi: 10.1111/j.1365-2818.2010.03401.x.

[319] J. M. Costantini, J. M. Desvignes, A. Perez, and F. Studer. Local order and magnetic behavior of amorphous and nanocrystalline yttrium iron garnet produced by swift heavy ion irradiations. *Journal of Applied Physics*, 87(4):1899–1907, 2000. ISSN 00218979. doi: 10.1063/1.372110.

[320] J. M. Costantini, F. Brisard, and J. L. Flament. Electronic transport in disordered ion-bombarded yttrium iron garnet. *Philosophical Magazine Part B*, 65(4):873–880, 1992. ISSN 1364-2812. doi:

10.1080/13642819208204929. URL http://www.tandfonline.com/doi/abs/10.1080/13642819208204929.

[321] J .M. Costantini, F. Rrisard, J. L. Flament, A. Meftah, M. Toulemonde, and M. Hage-Ali. High energy heavy ion irradiation. *Nuclear Instruments and Methods in Physics Reseach B*, 65:568, 1992.

[322] M. Levy, R. M. Osgood, A. Kumar, and H. Bakhru. Epitaxial liftoff of thin oxide layers: Yttrium iron garnets onto GaAs. *Applied Physics Letters*, 71(18):2617–2619, 1997. ISSN 00036951. doi: 10.1063/1.120192.

[323] J. M. Costantini, S. Miro, F. Beuneu, and M. Toulemonde. Swift heavy ion-beam induced amorphization and recrystallization of yttrium iron garnet. *Journal of Physics Condensed Matter*, 27(49):496001, 2015. ISSN 1361648X. doi: 10.1088/0953-8984/27/49/496001.

[324] J.-M. Costantini, S. Miro, G. Lelong, M. Guillaumet, and M. Toulemonde. Damage induced in garnets by heavy ion irradiations: a study by optical spectroscopies. *Philosophical Magazine*, 6435(January):1–17, 2017. ISSN 14786443. doi: 10.1080/14786435.2017.1403659. URL https://doi.org/10.1080/14786435.2017.1403659.

[325] A. Meftah, H. Benhacine, A. Benyagoub, J. J. Grob, M. Izerrouken, S. Kadid, N. Khalfaoui, J. P. Stoquert, M. Toulemonde, and C. Trautmann. Data consistencies of swift heavy ion induced damage creation in yttrium iron garnet analyzed by different techniques. *Nuclear Instruments and Methods in Physics Research, Section B: Beam Interactions with Materials and Atoms*, 366:155–160, 2016. ISSN 0168583X. doi: 10.1016/j.nimb.2015.10.030. URL http://dx.doi.org/10.1016/j.nimb.2015.10.030.

[326] J. M. Costantini, F. Brisard, L. Autissier, M. Caput, and F. Ravel.

Study of the amorphization of ion-irradiated yttrium iron garnet by high-resolution diffraction techniques. *J. Phys. D: Appl. Phys.*, 26:A57, 1993.

[327] H. A. Algra and J. M. Robertson. The influence of ion-implantation on the spin waves in (La,Ga):YIG films. *Journal of Magnetism and Magnetic Materials*, 15(18):1107–1108, 1980.

[328] E. Jensen. Types of imaging, part 1: Electron microscopy. *Anatomical Record*, 295(5):716, 2012. ISSN 1932-8494. doi: 10.1002/ar.22465. URL http://www.ncbi.nlm.nih.gov/pubmed/22495891.

[329] J. A. Hinks. A review of transmission electron microscopes with in situ ion irradiation. *Nuclear Instruments and Methods in Physics Research, Section B: Beam Interactions with Materials and Atoms*, 267(23-24):3652–3662, 2009. ISSN 0168583X. doi: 10.1016/j.nimb.2009.09.014. URL http://dx.doi.org/10.1016/j.nimb.2009.09.014.

[330] David Williams and C Carter. *Transmission electron microscopy*, volume 2. 2009. ISBN 9780387765006.

[331] Y. Liao. *Practical electron microscopy and database*. 2017. ISBN 3082342418. doi: 10.1002/ejoc.201200111.

[332] M. Vijayalakshmi, S. Saroja, and R. Mythili. Convergent beam electron diffraction A novel technique for materials characterisation at submicroscopic levels. *Sadhana*, 28(August):763–782, 2003. ISSN 0256-2499. doi: 10.1007/BF02706458.

[333] Z. Han, M. Vehkamäki, M. Mattinen, E. Salmi, K. Mizohata, M. Leskelä, and M. Ritala. Selective etching of focused gallium ion beam implanted regions from silicon as a nanofabrication method. *Nanotechnology*, 26(26):265304, 2015. ISSN 0957-4484. doi: 10.1088/0957-4484/

26/26/265304. URL http://stacks.iop.org/0957-4484/26/i=26/a=265304?key=crossref.9eae4b23b711aba253bb4e1372554c0e.

[334] S. J. Zinkle and L. L. Snead. Implatated ion on the amorphization of ceramics. In *8th International Conference on Radiation Effects in Insulators*, page 11, 1995.

[335] E. Salvati, L.R. Brandt, C. Papadaki, H. Zhang, S.M. Mousavi, D. Wermeille, and A.M. Korsunsky. Nanoscale structural damage due to focused ion beam milling of silicon with Ga ions. *Materials Letters*, 213: 346–349, 2018. ISSN 18734979. doi: 10.1016/j.matlet.2017.11.043. URL https://doi.org/10.1016/j.matlet.2017.11.043.

[336] A. Peltonen, H. Q. Nguyen, J. T. Muhonen, and J. P. Pekola. Milling a silicon nitride membrane by focused ion beam. *Journal of Vacuum Science & Technology B*, 062201(November):062201, 2016. ISSN 21662754. doi: 10.1116/1.4963895. URL http://dx.doi.org/10.1116/1.4963895.

[337] M. R. Wilson, P. B. Kosel, Y. D. Shen, and B. M. Welch. Rapid thermal annealing of implanted layers in silicon nitride encapsulated gallium arsenide. *J. Electrochem. Soc.: Solid-State Science and Technology*, 134 (10):2560–2565, 1987.

[338] F. Fransen, R. V. Berghe, R. Vlaeminck, M. Hinoul, J. Remmerie, and H. E. Maes. Electron and ion beam irradiation effects in AES analysis of silicon nitride and oxynitride thin films. *Surface and Interface Analysis*, 7(2):79, 1985. ISSN 02534177.

[339] W. J. Arora, H. I. Smith, and G. Barbastathis. Membrane folding by ion implantation induced stress to fabricate three-dimensional nanostructures. *Microelectronic Engineering*, 84(5-8):1454–1458, 2007. ISSN 01679317. doi: 10.1016/j.mee.2007.01.182.

[340] Y. R. Kim, P. Chen, M. J. Aziz, D. Branton, and J. J. Vlassak. Focused ion beam induced deflections of freestanding thin films. *Journal of Applied Physics*, 100(10):104322, 2006. ISSN 00218979. doi: 10.1063/1.2363900.

[341] H. Hopster and H. P. Oepen. *Magnetic microscopy of nanostructures*. 2005. ISBN 3540401865.

[342] W. X. Xia, Y. S. Chun, S. Aizawa, K. Yanagisawa, Kannan M. Krishnan, D. Shindo, and A. Tonomura. Investigation of magnetic structure and magnetization process of yttrium iron garnet film by Lorentz microscopy and electron holography. *Journal of Applied Physics*, 108(12):123919, 2010. ISSN 00218979. doi: 10.1063/1.3524273.

[343] M. Schneider, H. Hoffmann, and J. Zweck. Lorentz microscopy of circular ferromagnetic permalloy nanodisks. *Applied Physics Letters*, 77(18):2909, 2000. ISSN 00036951. doi: 10.1063/1.1320465. URL http://scitation.aip.org/content/aip/journal/apl/77/18/10.1063/1.1320465.

[344] J. W. Lau, J. K. Bording, M. Beleggia, and Y. Zhu. Energy barrier to magnetic vortex nucleation. *Applied Physics Letters*, 88(1):012508, 2006. ISSN 00036951. doi: 10.1063/1.2150272.

[345] S. A. Nepijko and G. Schönhense. Quantitative Lorentz transmission electron microscopy of structured thin permalloy films. *Applied Physics A: Materials Science and Processing*, 96(3):671–677, 2009. ISSN 09478396. doi: 10.1007/s00339-009-5131-4.

[346] Kazuya Takayanagi, Shigeo Mori, and Yoshihiko Togawa. Magnetic ripple in permalloy narrow wires investigated by Lorentz microscopy. In *IEEE Region 10 Annual International Conference, Proceedings/TENCON*, pages 1875–1877, 2010. ISBN 9781424468904. doi: 10.1109/TENCON.2010.5686384.

[347] X. Wang, I. Purnama, M. C. Sekhar, and W S. Lew. Highly Stable Vortex State in Sub-100 nm Nanomagnets. *Appl. Phys. Expr.*, 5:053001, 2012. ISSN 1882-0778. doi: 10.1143/APEX.5.053001.

[348] T. Uhlig and J. Zweck. Direct observation of switching processes in Permalloy rings with Lorentz microscopy. *Physical Review Letters*, 93(4): 047203–1, 2004. ISSN 00319007. doi: 10.1103/PhysRevLett.93.047203.

[349] T. Dias, E. Menéndez, H. Liu, C. Van Haesendonck, A. Vantomme, K. Temst, J. E. Schmidt, R. Giulian, and J. Geshev. Rotatable anisotropy driven training effects in exchange biased Co/CoO films. *Journal of Applied Physics*, 115(24), 2014. ISSN 10897550. doi: 10.1063/1.4885157.

[350] D. Eom. Direct Imaging of an order-to-disorder transition in an exchange-coupled CoO/Co bilayer. *Journal of the Korean Physical Society*, 67(10): 1792–1797, 2015. ISSN 0374-4884. doi: 10.3938/jkps.67.1792. URL http://link.springer.com/10.3938/jkps.67.1792.

[351] T. Ambrose and C. L. Chien. Dependence of exchange coupling on antiferromagnetic layer thickness in NiFe / CoO bilayers. *Journal of Applied Physics*, 83(11):6822–6824, 1998. doi: 10.1063/1.367863.

[352] D .L. Roy, R. Morel, A. Brenac, S. Pouget, and L. Notin. Perpendicular magnetization in CoO (111) layers induced by exchange interaction with ferromagnetic Co and Ni60Cu40 nanoclusters. *J. Appl. Phys.*, 111(May): 083901, 2012. doi: 10.1063/1.3702445.

[353] Anne D. Lamirand, Márcio M. Soares, Aline Y. Ramos, Hélio C N Tolentino, Maurizio De Santis, Julio C. Cezar, Abner De Siervo, and Matthieu Jamet. Robust perpendicular exchange coupling in an ultrathin CoO/PtFe double layer: Strain and spin orientation. *Physical Review B - Condensed Matter and Materials Physics*, 88(14):1040401(R), 2013. ISSN 10980121. doi: 10.1103/PhysRevB.88.140401.

[354] J. B. Yi and J. Ding. Exchange coupling in CoO-Co bilayer. *Journal of Magnetism and Magnetic Materials*, 303:e160–e164, 2006. ISSN 03048853. doi: 10.1016/j.jmmm.2006.01.118.

[355] D. Kumar, S. Singh, and A. Gupta. Effect of interface roughness on exchange coupling in polycrystalline Co/CoO bilayer structure: An in-situ investigation. *Journal of Applied Physics*, 120(8):085307, 2016. ISSN 10897550. doi: 10.1063/1.4961521.

[356] F. Zhang, Z. Y. Liu, F. S. Wen, L. Li, P. W. Wang, X. C. Li, and X. B. Ming. Exchange biasing and interlayer coupling in Co/Pt/Co/CoO multilayers with perpendicular anisotropy. *Thin Solid Films*, 623:102–109, 2017. ISSN 00406090. doi: 10.1016/j.tsf.2016.12.052.

[357] P. K. Manna, E. Skoropata, Y. W. Ting, K. W. Lin, J. W. Freeland, and J. Van Lierop. Interface mixing and its impact on exchange coupling in exchange biased systems. *Journal of Physics Condensed Matter*, 28(48): 486004, 2016. ISSN 1361648X. doi: 10.1088/0953-8984/28/48/486004.

[358] R. L. Stamps, R. E. Camley, and R. J. Hicken. Spin wave frequency shifts in exchange coupled ferromagnet/antiferromagnet structures: Application to Co/CoO. *Journal of Applied Physics*, 81(1997):4485–4487, 1997. ISSN 0021-8979. doi: 10.1063/1.364986.

[359] R. Stamps, R. Camley, and R. Hicken. Influence of exchange-coupled anisotropies on spin-wave frequencies in magnetic layered systems: Application to Co/CoO. *Physical Review B*, 54(6):4159–4164, 1996. ISSN 0163-1829. doi: 10.1103/PhysRevB.54.4159.

[360] D. L. Cortie, C. Shueh, P. Chen, J. Gao, F. Klose, J. V. Lierop, and K. L. Ã. Probing exchange bias effects in CoO/Co bilayers with pillar-like CoO structures. *Japanese Journal of Applied Physics*, 51:11PG01, 2012. ISSN 00214922. doi: 10.1143/JJAP.51.11PG01.

Appendix A

Optical Cavities

An optical cavity or optical resonator consists of mirrors that reflect light waves to generate standing wave resonances. Various shapes of optical cavity mirrors exist for different applications (lasers, interferometers, nanophotonic resonators, oscillators, delay lines, filters, spectrometers, spectrum analyzers, and in gravitational wave detection). For example, regular curved mirrors for laser cavity, rings for whispering gallery modes, and two reflecting surfaces of a transparent plate for etalon, and highly reflecting two parallel mirrors are used for a Fabry-Pérot cavity. The geometry of the optical cavity is optimized for stable output. A gain medium is generally used inside the optical cavity for laser applications. The optical cavity modes (or eigenmodes) depend on the mirror shape, geometry and curvature (plane-parallel, concentric (spherical), confocal, hemispherical, concave-convex).

A.1 Fabry-Pérot Cavity

A Fabry-Pérot cavity, having two reflecting parallel mirrors, can be used as an interferometer. The entering and circulating light in the cavity undergoes interference and produces an interference pattern with light maxima (constructive interference with light beams in phase) and minima (destructive interference

with light beams out of phase). These light intensity distributions after each round trip in the optical cavity are of interest for practical use. Generally, light reflects multiple times in the cavity with least dissipation resulting in a very high optical quality factor, high finesse, and narrow linewidth. When the light beams are in destructive interference, the light energy cannot be stored inside the cavity, and is dissipated around the cavity.

To achieve steady state condition in the cavity , the amplitude and phase of light both should be reproducible after a round trip. That is achieved by the interference resonance condition of the cavity: the cavity length should be the integral of half of the light wavelength. If the mirrors have L_0 spacing (geometrical path length between mirrors) and a medium having a refractive index n inside the mirrors, then the wavelength λ_q in a vacuum for integral mode q in a steady state field distribution would be [270]:

$$\lambda_q = \frac{2L}{q} \tag{A.1}$$

where $L = L_0 n$ is the optical path length between mirrors. The resulting resonance frequencies after interference would have a periodic sequence as below:

$$\Delta\nu = \frac{c_0}{\lambda_q} - \frac{c_0}{\lambda_{q-1}} = \frac{c_0}{2L} \tag{A.2}$$

where c_0 is the speed of light in vacuum. The intensity minima is not zero if the mirror reflectivity is not 100%, which broadens the resonance peaks (Eq. A.2). The optical quality factor (Q_o)of the cavity is defined as the ratio of resonance frequency f_r to the bandwidth Δf:

$$Q_o = \frac{f_r}{\Delta f} \tag{A.3}$$

This is equivalent to the ratio of energy stored in the cavity to the energy

dissipated per cycle due to damping:

$$Q_o = 2\pi \frac{\text{energy stored}}{\text{energy dissipated per cycle}} = 2\pi f_r \frac{\text{energy stored}}{\text{power loss}} \tag{A.4}$$

The average lifetime of a photon circulating in the cavity can be estimated from the optical quality factor (Q_o) of the cavity. The exponential time constant (τ), attenuation rate (α), damping ratio (ζ) and the optical quality factor (Q_o) are related to each other such that:

$$Q_o = \pi \tau f_r = \frac{\pi f_r}{\alpha} = \frac{1}{2\zeta} \tag{A.5}$$

A.2 Nanophotonic Cavity

The nanophotonic cavity is explained in Section 2.3.1 of Chapter 2. Photonic crystals are the building blocks of nanophotonic cavities. The periodic holes change the refractive index and work on the principle of total internal reflection and Bragg reflection. The periodic structure can be modified to produce low losses and highest quality factor. The standing waves inside the cavity produces modes of high intensity patterns for the light field. The nanophotonic cavity results in ultra-high Q_o (hundreds of thousands) when the cavity dimensions are much larger than the light wavelength. However, cavities of the order of the wavelength of light are difficult to make because of the radiation losses (radiation losses and cavity size are inversely proportional).

Appendix B

Micromagnetic Simulation Methods

Micromagnetism involves the behaviour of magnetization patterns at the scales where discrete atomic structure is fused into the continuum with distinguishable details. Integration and differentiation methods are used instead of summation and differences for the problem solving. The magnetization orientation is obtained from the continuous function over the medium, and equilibrium magnetization is obtained by magnetization direction variation for total energy minimization. The energy minimization is performed by solving the differential equations. The results of these differential equations are known as micromagnetic solutions in terms of magnetization patterns of the material [194].

The Landau-Lifshitz-Gilbert equation is based on the magnetization behaviour inside the magnetic material in the presence of external magnetic field, and expresses the magnetization precession in the magnetic material. The internal and external magnetic field interactions of the material produce magnetic torques, which rotates the magnetization. Landau and Lifshitz initially formulated the following equation (LL equation) [271]:

$$\frac{d\mathbf{M}}{dt} = -\gamma \mathbf{M} \times \mathbf{H}_{\text{eff}} - \lambda \mathbf{M} \times (\mathbf{M} \times \mathbf{H}_{\text{eff}}) \tag{B.1}$$

where γ is the electron gyromagnetic ratio and λ can be written as:

$$\lambda = \alpha \frac{\gamma}{M_s} \tag{B.2}$$

where α is the damping factor and H_{eff} includes the external magnetic field and the internal magnetic field due to the magnetization.

The magnetization derivative term was included by Gilbert in 1955 in the Landau-Lifshitz (LL) equation such that the equation became as the Landau-Lifshitz-Gilbert (LLG) equation:

$$\frac{d\mathbf{M}}{dt} = -\gamma \left(\mathbf{M} \times \mathbf{H}_{\text{eff}} - \eta \mathbf{M} \times \frac{d\mathbf{M}}{dt} \right) \tag{B.3}$$

where η is the damping parameter, which is dependent on the material characteristics. The solution to LLG equation for a particular geometry of magnetic material gives the time dependent magnetization of the material [195, 271]. A number of numerical solvers and simulators use the LLG equation for numerical solutions of magnetizations.

Micromagnetic simulations are based on the Landau-Lifshitz and Gilbert (LLG) equation. Based on the LLG equation, there are many software applications for simulations, like the LLG micromagnetic simulator [272], OOMMF [273], Magpar [274], mumax [275], and nmag [276], some of which are CPU and GPU based programs. The GPU based software is much faster than the CPU based software. The speed and usage of simulation in the GPU is based on the capacity of the available memory (RAM). I have used mumax and nmag as the platforms for the simulations. Mumax is GPU based program (in the Go programming language) with a speed of the order of 100 times the CPU-based simulations and is best for low memory use for large simulations since it uses 16 million finite difference (FD) cells in a 2GB of GPU RAM (nVIDIA GeForce GTX TITAN, in our case). Nmag is a CPU based finite element (FE) micromagnetic simulation package in the Python programming language.

The LLG equation is solved repeatedly on the spatially resolved discrete geometry and then integrated to give the final results from the geometry. The geometry can be spatially resolved by either FD or FE methods depending upon the shape of the geometry. The finite difference creates the discrete cubiods (cells) and thus is preferred for cubic geometry. The finite element generates tetrahedral meshes of the geometry, and thus is useful for spheres and curvatures. FD uses less memory than FE meshes. However, FD faces the staircase effect that causes the pinning of magnetization in simulations. In the following section, the simulation general parameters along with special cases are presented. The simulation parameter details for nanoparticles, permalloy and YIG are also described.

B.1 Simulation Introduction

After the geometry discretization process, the important step for simulation is to choose the number of cells and cell size. In mumax, any combination of number of cells and cell size can be chosen, but the total number of cells should be a multiple of 2^n. The staircase effect has been reduced by the smoothing function in mumax. After the geometry and cell size selection, the next parameter to describe is the saturation magnetization, M_s. The saturation magnetization parameter is chosen at the temperature required for the physical problem to be solved, because it is temperature dependent.

The exchange constant, A_{ex}, is the next parameter to be defined in the simulations, which is described as the density of exchange magnetic energy. The exchange length is different from the exchange constant (from the exchange integral). The exchange length can be defined as follows for soft materials [277]:

$$l_{\mathrm{ex1}} = \sqrt{\frac{2A_{ex}}{\mu_0 M_{\mathrm{s}}^2}} \tag{B.4}$$

and the following equation for hard materials (with K_1 as the anisotropy con-

stant):

$$l_{\text{ex2}} = \sqrt{\frac{A_{ex}}{K_1}} \tag{B.5}$$

After calculating the exchange length from both equations, the smaller value should be used for simulation purposes. The cell size should be smaller than the exchange length of the material.

Magnetic anisotropy is another important parameter in the simulation, after defining M_s, A_{ex}, and l_{ex}. Magnetic anisotropy can be extrinsic (shape) or intrinsic (crystalline). The shape anisotropy is inherited in the geometry of the simulation, while the crystalline anisotropy is expressed by the anisotropy constants. The crystalline anisotropy can be either uniaxial or cubic depending on the crystal structure. The shape anisotropy is utilized in the demagnetization factor calculations. The Gilbert damping constant, α, is also set to a value in the simulation. The other parameter is the temperature. The default temperature in mumax simulations is 0 K. A thermal seed is required to provide a thermal field. Finally, a magnetic field of pre-determined step-size is applied to simulate hysteresis.

B.2 Nanoparticle Simulations

For magnetic nanoparticles described in Chapter 3, the micromagnetic simulations were performed in mumax, with cell size $3nm \times 3nm \times 3nm$, $M_s = 480$ kA/m and $A_{ex} = 13.3$ pJ/m. The Gilbert damping constant, α, was 1 to simulate at fast rate. The simulations were performed with and without anisotropy for the described assembly of nanoparticles in Chapter 3. The effect of temperature, for nanoparticles, in simulations is shown in Fig. B.1. At higher temperature, the hysteresis curve gets smoother and matches with the experimental results. Thus, increasing the temperature shows a tendency towards a smoother transition of magnetization.

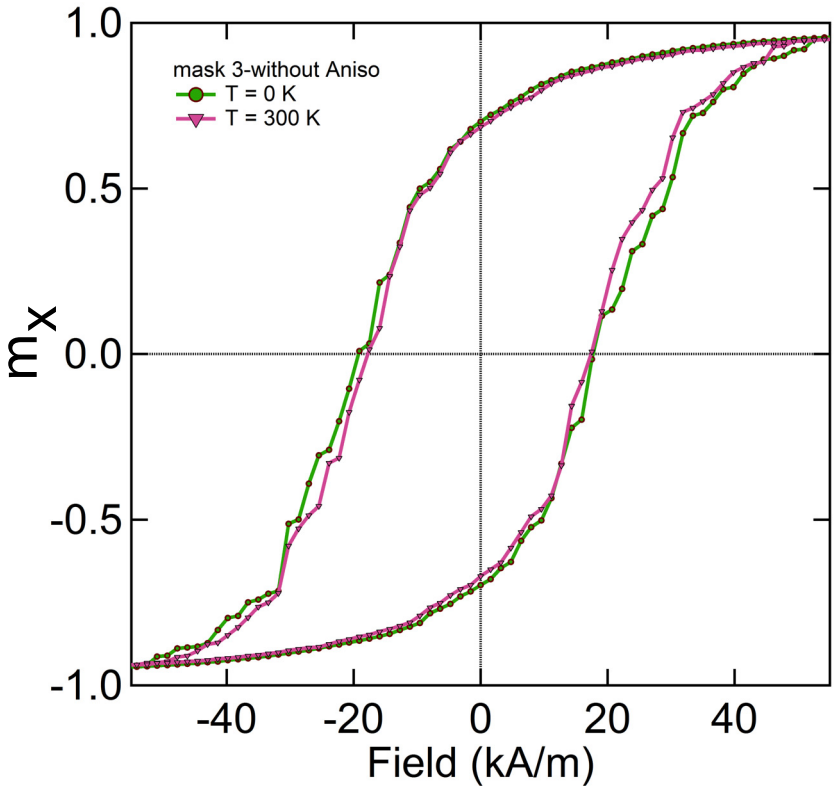

Figure B.1: ***Micromagnetic simulations of magnetic nanoparticles in mumax.*** *The effect of temperature on the magnetic hysteresis in masked magnetite nanoparticles. The blue curve is at 0K and green curve is simulated at 300K. The anisotropy was neglected in these simulations.*

The micromagnetic simulations of nanoparticles used in Chapter 4 were performed in the nmag program. The tetrahedral meshes were generated in a GMSH mesh generating software (.msh format) and then the mesh was exported to the "nmesh.h5" format as input for nmag. The obtained data was processed in python to plot the hysteresis. An example of the generated mesh of nanoparticles for nmag is displayed in Fig. B.2. These meshes for nanoparticles are created in the FE domain and are not memory efficient. Simulations for a large number of nanoparticles would take huge memory, thus many CPUs connected in parallel would be required to simulate a large number of nanoparticles in nmag.

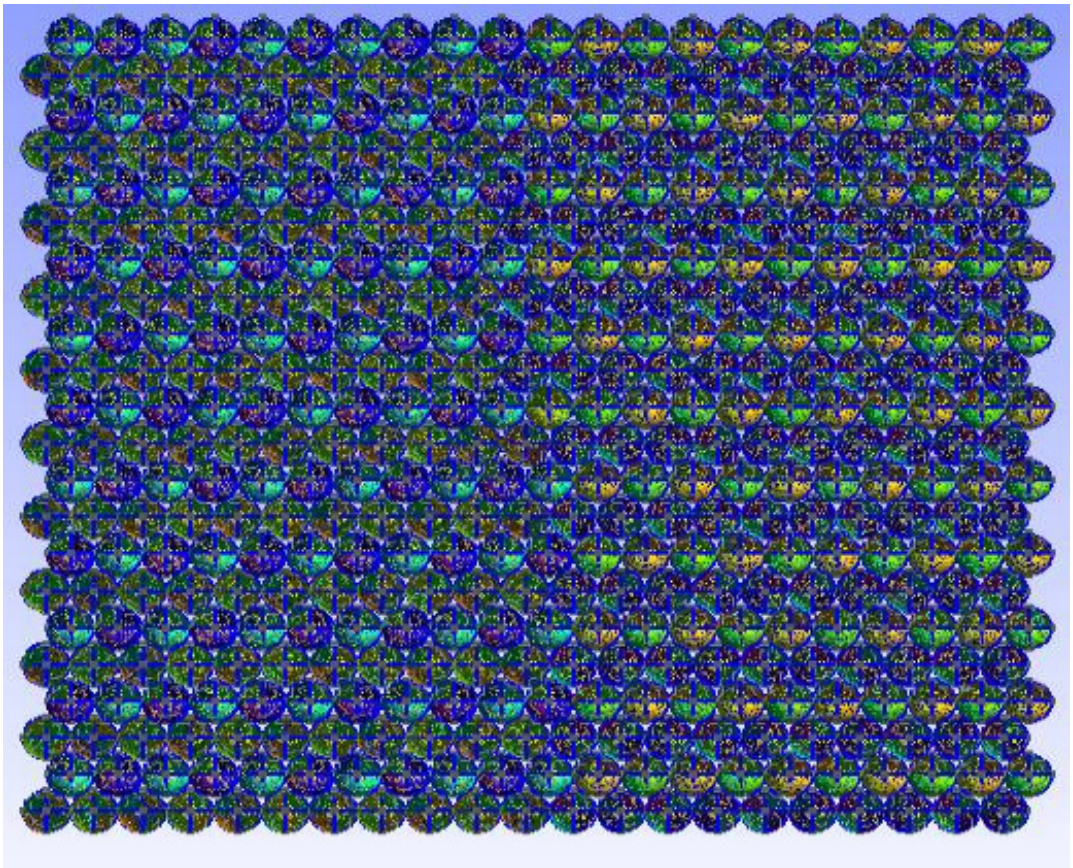

Figure B.2: ***Tetrahedral mesh of magnetic nanoparticles in GMSH for nmag simulations.*** *The geometry file (*.geo) was created in python and then GMSH software was used for the FE mesh generation. This example is for* 21×22 *nanoparticles in a layer.*

B.3 Magnetic Anisotropy of ∼350 Magnetic Nanoparticles

The collective orientation of ∼350 magnetic nanoparticles may affect the hysteresis due to the magnetic anisotropy. If the nanoparticles have net orientation at a particular angle with respect to x-axis, then the magnetic hysteresis would have reduced saturation due to partial magnetic torque signal in y-direction. Also if the nanoparticles are randomly oriented, then magnetic hysteresis would be similar whether the bias field is applied from positive or negative axis. The

assembly of nanoparticles in Fig. 3.6 was used in order to find out the collective orientation of nanoparticles. The angle for major and minor axes, with respect to the x-axis, of each nanoparticle in Fig. 3.6a are calculated using angle tool in the GIMP software. The minor axis are aligned on the paddle at the statistical value of 76.4° from the x-axis, while the major axis can be described at 166.4° or can be calculated as −13.6° near to the x-axis. The micromagnetic simulations for the magnetic hysteresis are performed with external bias field at these calculated axis, as shown in Fig. B.3. The hysteresis loop for −13.6° is similar to the 0° loop, because the field is nearly aligned with the major axis of the nanoparticles. The hysteresis obtained at 166.4° loop is reflected on the vertical axis as compared to −13.6° because the field is applied in the opposite direction to the anisotropy major axis (−13.6°).

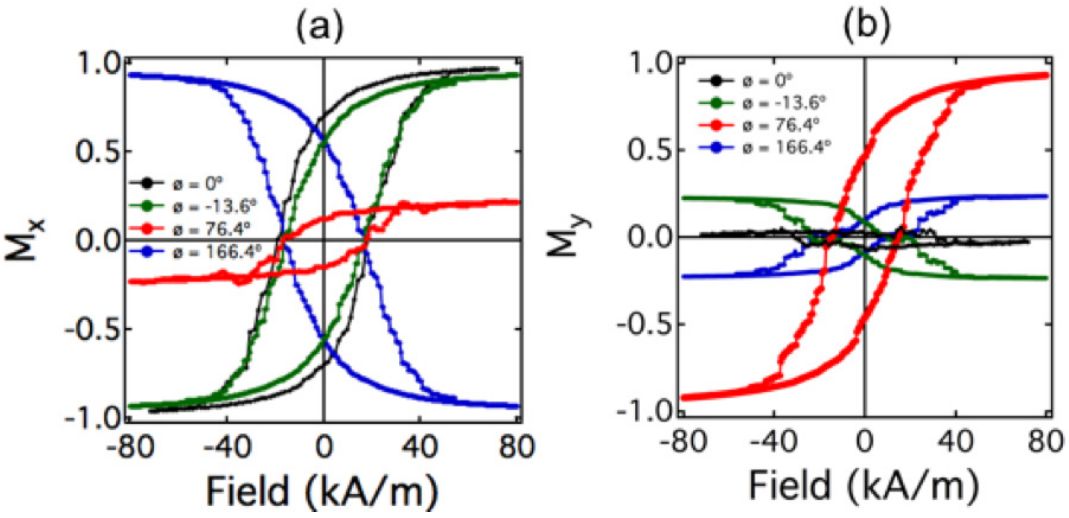

Figure B.3: ***Micromagnetic simulation of magnetic hysteresis by varying the applied DC bias magnetic field angles.*** ***(a)*** *M_x is the normalized x-component of magnetization,* ***(b)*** *M_y is the normalized y-component of magnetization*

The magnetization in the hysteresis loop has x-component as shown by M_x in Fig. B.3a, and y-component as M_y, as shown in Fig. B.3b. The reduced M_x at 76.4° is because of minor axis of the nanoparticles and less bias field component in the x-axis. This can be described as energy barrier due to the collective shape anisotropy. This work is very useful for the gryo-remanent

magnetization (GRM) experiment where external bias field is applied along the major axis of the magnetic element.

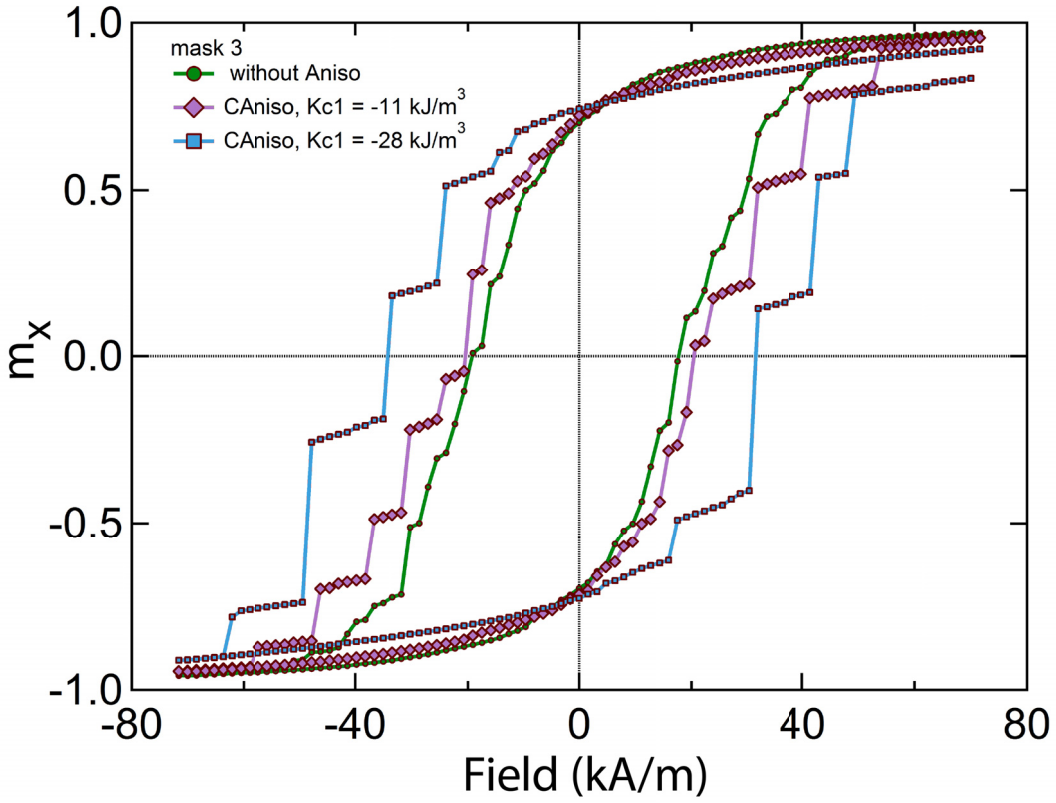

Figure B.4: ***The effect of anisotropy in the hysteresis loops of magnetite nanoparticles.*** *The legend shows the various uniaxial anisotropy constant values used for simulations.*

To encounter the intrinsic anisotropy in the simulation, anisotropy constant values are used for the magnetite nanoparticles. A comparison is shown in Fig. B.4 for the simulations with and without anisotropy values. The hysteresis from experiment in Fig. 3.6b matches with the hysteresis in simulation without anisotropy in Fig. B.4. The reason could be the cartesian staircase in the simulations causing the pinning for the moment.

B.4 YIG Simulations

For a YIG specimen, the simulations were performed with cell size $10nm \times 10nm \times 10nm$, $M_s = 140$ kA/m and $A_{ex} = 2.0$ pJ/m. The cubic anisotropy constants are $K_{c1} = -610$ J/m^3 and $K_{c2} = -26$ J/m^3 with anisotropy axis $c_1 = (-0.4085, 0.7075, 0.5774), c_2 = (-0.8165, 0.7075, 0.5774)$, and $c_3 = c_1 \times c_2$. The negative anisotropy constant values makes these axis as the hard axis and the easy axis is perpendicular to these axis. The Gilbert damping constant was again chosen as 1 for faster simulations. The cell size is large but still below the exchange length value of 12 nm.

B.5 Permalloy Simulations

For the permalloy sample, the simulations were performed with a cell size of $5nm \times 5nm \times 5nm$, $M_s = 780$ kA/m and $A_{ex} = 13.0$ pJ/m. The crystalline anisotropy is not included in the simulations for permalloy because of its small values. However, the M_s and A_{ex} values were varied, since the experimental saturation magnetization was found to be 770 kA/m as described in Chapter 5. From the simulations, the net magnetization of the structure at an applied field of 45 kA/m was found to be $M = 0.965M_s$ for permalloy in Chapter 5. The Gilbert damping constant was set to $\alpha = 1$ to minimize the simulation time required for the quasistatic hysteresis. The calculated exchange length is 5.72 nm, so the cell size is less than that.

The variation of these values are represented in Fig. B.5. By changing the parameters, the obtained hysteresis could be quite different, so that the parameters should be chosen wisely and close to the experimental values. Figure B.5 shows the 3D and 2D simulation with different parameters of thin film of permalloy. The selection of cell as 3D or 2D makes a huge difference to the simulation. The 3D results are a better match with the experimental data.

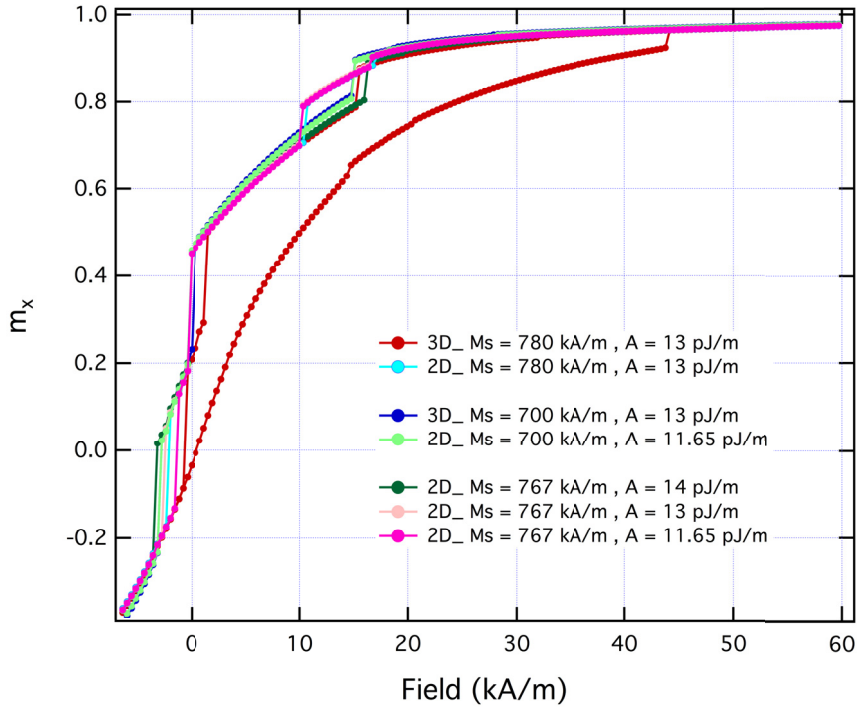

Figure B.5: ***Micromagnetic simulation of permalloy in mumax.*** *Changing the parameters effects the hysteresis curve.*

Appendix C

Devices Fabrication

The nanomechanical devices were fabricated in a silicon nitride membrane and in the silicon-on-insulator (SOI) chips, along with the optomechanical devices. In the following sections, the general procedures followed for the device fabrications are presented. Some special cases are also described for better explanation of the related experimental problems.

C.1 Fabrication of Nanomechanical Devices in Silicon Nitride Membranes

The design of nanomechanical triple paddle devices was created in raith software and then implemented in the FIB machine (Ziess NVision 40). A good device fabricated in the silicon nitride membrane is shown in Chapter 3, however, if the ion beam conditions are not chosen wisely for the material to be fabricated, strange shapes of the device can come to existence after the ion beam exposure. One example of a deformed device, with a paddle curling up, is shown in Fig. C.1. Figure C.1 shows the bending of the membrane itself around the device edges, which could cause a change in the resonance frequency; the quality of the device degrades accordingly. The maximum distorsion can

be seen in the torsional rod that has been curled into a spring like structure. The ion beam dose was 80 pA and the accelerating voltage was 30 kV with a stage tilt of 54° for the fabricated device in Fig. C.1. The stage was tilted such that the ion beam was perpendicular to the device surface. A Ziess NVision FIB machine can simultaneously acquire the SEM images during the milling process; the SEM column was at an angle of 36° from the device surface.

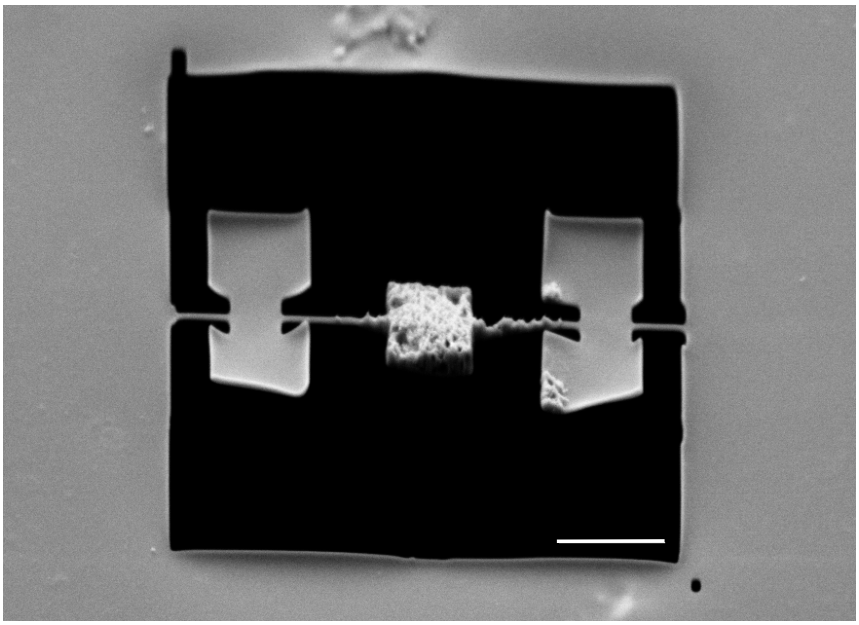

Figure C.1: ***Curling of device.*** *Triple paddle device fabricated in the silicon nitride membrane. The scale bar is 2 μm.*

C.2 Fabrication of Nanomechanical Devices in SOI Chips

The fabrication process was started on the silicon-on-insulator (SOI) chips (5×5 mm in lateral size). The chips were diced from a 6 inch diameter wafer with a top silicon layer of 300 nm, 220 nm or 145 nm, the buried oxide layer thickness of 1μm and the silicon handle layer of about 700μm. The process recipe has structured steps, some of which are represented in Fig. C.2. The details of

each of these steps is described below. The steps in Fig. C.2a-d are named as the first cycle, and Fig. C.2e-h are named as the second cycle. The first cycle is used for device fabrication and the second cycle is used for magnetic element deposition.

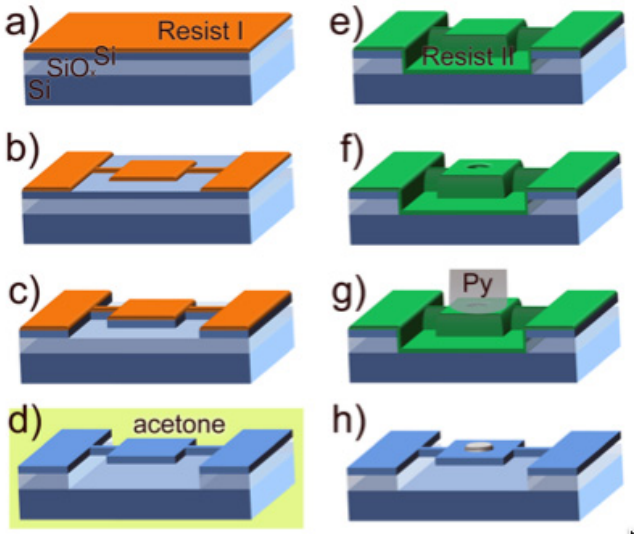

Figure C.2: ***Device fabrication step for SOI chips.*** *Reprinted with permission from [187]*

The fabrication process includes the following steps in the first cycle:

1. Raith design
2. Piranha cleaning
3. Resist spin coating: Fig. C.2a
4. Electron beam lithography (EBL): Fig. C.2b
5. Cold development
6. Plasma etching (ICPRIE): Fig. C.2c
7. Resist lift-off
8. Oxide etching (BOE): Fig. C.2d
9. Critical point drying (CPD)

Raith design: The raith design was created for both resist types (positive (ZEP) and negative(HSQ)). The HSQ (Hydrogen silsesquioxane, XR-1541 from Dow Corning, MI, USA) and ZEP (11% methyl styrene and chloromethyl acrylate copolymer (solid) and 89% anisole (solvent), molecular weight of 57,000, ZEP520A from ZEON Corp., Tokyo, Japan) were used at the NanoFab, University of Alberta.

Piranha cleaning: The first step is the standard cleaning procedure with a combination of sulfuric acid (H_2SO_4) and hydrogen peroxide (H_2O_2), which removes the organic compounds on the substrates. Standard operating procedures were followed for piranha cleaning. The sulfuric acid and hydrogen peroxide were mixed in a ratio of 3:1. The chips were placed vertically in the honeycomb teflon tray and covered with a teflon cover. The assembly was then immersed in the piranha solution for 20 minutes in glass containers. The chips were then rinsed with water five times and then air blowed for drying.

Resist spin coating: The resist was spin coated for a thickness of 150 nm. The chips were dried at 180°C on a hotplate (Laurell hotplate) for 5 minutes and then cooled down on paper towels for 5 minutes. The resist was allowed to be at room temperature from the fridge temperature for proper spinning. The chip was placed on top of the spin coater (Laurell spinner) and a few drops of resist were dropped on top of the chip so that whole chip was covered with resist. The spinner was then ramped up to 100 rpm for 5 s, and then was spun at 4000 rpm for 40 s. After spin coating the desired number of chips, the chips were baked at 180°C for 10 minutes (150°C for 5 minutes for HSQ), and then were allowed to cool on clean paper towels with aluminum foil cover in order to avoid radiation exposure to the resist before EBL. The chips were transferred to the gel box to carry them to the EBL room. The whole procedure was performed with clean metal tweezers. The negative (6% HSQ) was diluted in a MIBK solution in a ratio of 1:2 (2.5 ml of HSQ: 5 ml of MIBK), the positive resist (ZEP) can be diluted in anisole (1:1) to get a standard spinning curve

because it evaporates over time.

Electron beam lithography (EBL): EBL (Raith 150-Two machine) transfers the design pattern for the first cycle of raith software on the positive or negative resist used. The chips were loaded on the sample stage of the EBL and the vacuum was turned on. The sample stage was aligned in the machine. After the stage alignment, a standard manual procedure was used for the electron beam focusing and pattern writing. A pre-dose test was carried out for proper dose values. An area dose of $80 - 125\text{pC/cm}^2$ for ZEP ($200 - 400\mu\text{C/cm}^2$ for HSQ) was used in various resists, since the calibration curve for each resist will change over time. The sample was unloaded after the design writing with an electron beam on the resist. For a positive resist, the electron beam exposes the areas of the device, and for a negative resist, the electron beam exposes the inverted areas of the device. An electron voltage of 30kV for ZEP, 10kV for HSQ and aperture of 10μm diameter was used in the EBL. An average beam current was 37 pA for ZEP and 22 pA for HSQ.

Cold development: The ZEP resist was developed in a cold environment for better spatial resolution and sharp edges. A 15 ml of ZED-N50 and 15 ml of IPA were cooled at $-15°$C on a Stir-Kool SK-12D cold plate. Silicone oil was used to provide optimal contact of the beaker with the cold plate for heat transfer, and a small magnetic stirrer (60 rpm) was used in each glass beaker for temperature homogeneity. A standard procedure was followed to setup the cold plate. The chips were immersed in the ZED-N50 solution for 20 s, then in IPA for 20 s, and then air dried with nitrogen purge afterwards. The HSQ was developed in 25% tetramethylammonium hydroxide (TMAH) for 60 s.

Plasma etching (ICPRIE): Reactive ion etching (RIE) was used for etching the silicon layer under the exposed resist. The inductively coupled plasma RIE (ICPRIE) was used in the Oxford Instruments PlasmaLab System. The chamber was conditioned with a dummy silicon wafer for 10 minutes, with standard conditions (16 sccm of SF_6,12 sccm of C_4F_8, RF power of 25 W and

a ICP power of 3,500 W). The chips were then loaded into the chamber with silicone oil at the bottom. The chips were exposed to the plasma etching for 35 s (30 s for 145 nm, and 40 s for 300 nm). The chips were cleaned from the bottom side with IPA to remove the oil, after the completion of the etching process.

Resist lift-off: The resist lift-off was carried out in heated NMP (N-Methyl-2-Pyrrolidone) at 70°C for 30 minutes. The chips were placed in IPA for 2 minutes and then air dried. The resist lift-off can also be performed in acetone for 24 hours.

Oxide etching - BOE: The silicon oxide layer is the buffer layer, where undercut was created to release the devices. The oxide layer etching is also called buffered oxide etching (BOE). A concentrated solution in a 10:1 ratio of hydrofluoric acid (HF) and ammonium bifluoride was used in teflon containers (because it will eat the glass containers). HF etches at 55 nm/min. The chips were placed in the HF solution for 32 minutes (paddle size was 3 μm = 3000 nm, so 1500/55 = 27 min etch, I added 5 more mins), and then placed in deionized water for 5 minutes. The chips were then transferred to an IPA solution from water. A standard procedure was followed for cleaning the wet deck after HF use with $CaCl_2$. The etching time varies with the device dimension; for a bigger paddle it takes a longer time to etch.

Critical point drying (CPD): The chips were then transferred to the critical point dryer for drying to avoid stiction. The whole transfer procedure was performed in the IPA solution medium so that the chips remain in a liquid environment until the drying in a critical point dryer. The temperature in the critical point dryer reaches up to 0°C and chips remain in it for 1 hr in a CO_2 environment. The released and dried devices from the critical point dryer were saved for further use. The drying procedure in pentane was also performed for some of the chips seperatly.

The second fabrication cycle includes the following steps:

9. Released devices
10. Resist spin coating: Fig. C.2e
11. Electron beam lithography (EBL): Fig. C.2f
12. Resist development
13. Magnetic element deposition: Fig. C.2g
14. Resist lift-off: Fig. C.2h
15. Critical point drying (CPD)

Resist spin coating for second cycle: A second layer of resist poly methyl methacrylate (PMMA) was used for coating in the spinner. A bilayer resist was created with PMMA A2 495k and PMMA A8 950k using the same recipe as described in step 3. The chips were first placed in the acetone to provide a liquid environment to the released devices. The first resist was dropped on top of acetone on the chip (allow 10 s for resist to take place of acetone) when placed in the spin coater. The resist was then spun and baked at the described temperature. The resist is supposed to flow in the undercut below the device. After baking of first resist layer, the second resist layer was spin coated and then baked at a given temperature (180°C for 10 minutes, and cool for 5 min).

Electron beam lithography for second cycle: EBL for electron beam exposure was done at 10kV electron voltage and at the area dose (200 $\mu C/cm^2$). A triple point alignment in EBL was carried out before the exposure for each write-field area. The steps in sequence are: load in EBL, adjust (10 kV and 10 aperture), do alignment on the diamond cut and measure current, adjust XY and UV coordinates (absolute), go to first alignment mark (AM), do the write-field (WF) alignment, go to the AM of the WF, center to AM, go to 3-point alignment, adjust UVW to local, adjust P1 (10μm, 10μm) three times, flag place in center, position to next AM, read position using dropper and click check, adjust three times, adjust P1 (10μm, 10μm), P1 (90μm, 10μm), and P1 (10μm, 90μm), add design in position list, adjust position (50μm, 50μm), scan

layer 63 (AM only), do it three times, set optimum dose, scan for layer 0, reset UV for each WF.

Resist development for second cycle: The PMMA resist was developed in a solution of MIBK:IPA (1:3) for 60 s and then in IPA for 20 s. The chips were washed with deionized water and air dried later.

Magnetic element deposition: The magnetic element deposition was done at this stage. The magnetic nanoparticles or permalloy were deposited in our case. The magnetic nanoparticles were deposited as described in Chapter 4 and in Appendix D. The permalloy was deposited using a collimated electron beam evaporator (EFM 3, Omicron Vakuumphysik GMBH) in an ultra-high vacuum chamber (10^{-10} Torr).

Resist lift-off: The resist lift-off was performed in heated NMP at 70°C for 30 minutes in the case of permalloy. The chips were placed in IPA for 2 minutes and then air dried. For magnetic nanoparticles, the chips were placed in acetone for 24 hours.

Critical point drying: To dry the chips at the final step, chips were placed in the IPA and transferred to the critical point dryer. The chips were examined under the SEM for final pattern and were then ready to use for magnetometry measurements.

C.3 Fabrication of Optomechanical Devices in SOI Chips

The same procedure was followed for optomechanical device fabrication as for the nanomechanical device fabrication explained above. The difference is in the design, which contains the split beam nanocavities.

Appendix D

Magnetic Nanoparticles Self-Assembly Experiments

I performed experiments for the self-assembly of nanoparticles on the silicon surface and on the silicon-on-insulator nanomechanical devices. There are several ways for the self-assembly of nanoparticles via a bottom-up approach such as direct, indirect, free and assisted self-assembly. I followed the approach of self-assembly using the hydrophobic liquid interface, as described in Chapter 4.

All bottom-up approaches for nanoparticle self-assembly have similar principles, which are based on the dynamics of the thermodynamics and forces involved in the equation of motion and kinetics. The general equations of motion involve the fluid dynamics models like Navier-Stokes equations combined with the heat equations for incorporating thermodynamics.

Various theoretical models have been created for the molecular description of the process of interest such as the Toy model [278, 279], toggle interaction model [280] and monte-carlo simulations [281, 282]. These models can be defined on the basis of statistical mechanics. Self-assembly has been well studied, theoretically and experimentally, on the colloidal scale. However, the study of time resolved evolution of equilibrium in such systems is still under progress.

In-situ microscopy and x-ray diffraction of the assembled structures has enabled an understanding of molecular and atomic scale processes and time resolved information of self-assembly in some cases [283].

Pattern formation in such systems is usually recognized as 'self-organization'. A typical experiment of self-assembly is comprised of components such as molecules, proteins, DNA, nanoparticles or colloids suspended in a solvent, which are poured into a container or onto a surface (the target) and then letting it rest. When poured onto a surface, the nanoparticle solution undergoes Brownian motion, at an initial stage, constrained by the chemistry of the target surface, surface chemistry of the nanoparticles, and surface tension of the droplet or the volume poured. The process has been explained in a number of ways including the physical characteristics of the system, statistical mechanical models [278], computational models [281, 284, 285, 286], dynamics pathways [279, 287, 288] and their theoretical descriptions [289, 290, 291, 292].

The process of self-assembly in our experiments started with the ferrofluid (an iron oxide, Fe_3O_4 magnetite nanoparticle suspension from Sigma-Aldrich). After successful deposition on the silicon nitride and silicon surfaces, the nanoparticles were deposited on the nanomechanical devices. At later stages, custom-made anisotropic nanoparticles were also deposited and propitiously self-assembled. Free and assisted self-assembly from the ferrofluid was also achieved afterwards.

In the following sections, the general results of the procedures for self-assembly are presented, with representative micrographs. Some cases are presented for a better explanation of the related experimental investigations. The Appendix concludes with a general procedure of preliminaries used in this work to demonstrate how to self-assemble the nanoparticles on nanomechanical devices and on the silicon surface.

D.1 Self-Assembly Preliminaries

In self-assembly, fluid dynamics are involved that can describe the simple to complex nanostructure formation of multiple nanoparticles. The basic parameters to consider are concentration of nanoparticles, cleanliness of the surface where the nanoparticles are to be deposited (target surface), volume of droplet, air quality in the environment, suspension quality of ferrofluid, and homogeneity of the nanoparticles. Other important factors are surface chemistry of nanoparticles and silicon surface, surface tension and hydrophobicity of components involved, and environment temperature and pressure conditions for evaporation oversight. For accurate results, the experiment must be performed in a controlled environment, in which the contamination is reduced and the process can be analyzed quantitatively. A combination of the above mentioned parameters have been used.

The dynamics formed a coffee stain at initial stages when the ferrofluid (nanoparticle suspension) was dropped on top of the silicon surface. An additional hydrophobic drop of deionized water was used as an interfacial layer to reduce the coffee-stain mechanism. This extra water droplet was in between the target silicon surface and the nanoparticle solution. A drop of ferrofluid was poured on top of the water drop with a micro-pipette (0.1 μL). The surface tension of the water droplet beneath the nanoparticle solution drives the self-organization of the nanoparticles. As the slow evaporation of water occurs, the layer of self-assembled nanoparticles on top of the hydrophobic water surface settles and lays down on the silicon surface. The final bonding forces between nanoparticles and the silicon surface are strong enough to hold them during nanofabrication processes.

The process implicating the self-assembly of nanoparticles on the nanomechanical devices requires the use of various chemicals in the nanofabrication, such as poly methyl methacrylate (PMMA), acetone, pentane, hydrogen

silsesquioxane (HSQ), and $\alpha-$methylstyrene (ZEP). In order that the intended nanoparticles (Fe_3O_4, 20 nm in size, in toluene solvent, from Sigma-Aldrich) are first tested and deposited in combination with these chemicals on the silicon surface, the following subsections will describe the results of the interaction of these nanoparticles with the above mentioned chemicals.

D.1.1 Patterning Nanoparticles using PMMA

To investigate the patterning behaviour of nanoparticles using PMMA, a raith design was created for the experiment, to be used in electron beam lithography (EBL). Various shapes including rectangles, squares, and circles were created in the initial raith design. The raith design was used in the EBL for patterning the shapes on the resist. The deposition of nanoparticles after the EBL exposure was performed at later stages of nanofabrication.

The process started with cleaning the silicon-on-insulator (SOI) chips (5×5 mm in lateral size) by the piranha process in nanofabrication. The SOI chips have a top silicon layer of 300 nm or 145 nm, the buried oxide layer thickness is 1μm and the silicon handle layer is about 700μm.The chips were then washed with deionized water and blow dried with a nitrogen air flow. The clean chips were then spin coated with PMMA, in a double layer structure.

Firstly, the poly-methyl methacrylate (PMMA 950k A8 from Microchem Corp., MA, USA) was spin coated on the clean chips using a Laurell spinner with an initial speed of 500rpm for 5 seconds ramped up to 4000rpm for 40 seconds. The coated chip was baked on the hot plate (Laurell hot plate) at 180°C for 10 minutes and cooled down for 10 minutes. A second layer of the poly-methyl methacrylate (PMMA 495k A2 from Microchem Corp., MA, USA) was spin coated on top of the PMMA-950k layer using the same speeds of the spin coater. The second PMMA layer was baked following the same steps as for the first layer. The double layer spin coating of PMMA is usually undertaken to avoid the extra backscattering of electrons from the EBL exposure.

The coated chip with PMMA was then carried to the EBL for electron beam exposure with a selection of 10 kV electron voltage for an optimum exposure and for reduced effect of charging. The resist was first exposed on the alignment marks in the raith design for the beam alignment. A dose test was carried out separately to choose the appropriate area dose (200 $\mu C/cm^2$). The electron beam exposed various shapes and sizes of circles, rectangles and squares. The exposed resist was developed in isopropyl alcohol (IPA) for 80 s and development was stopped by cleaning the chips with deionized water for 90 s.

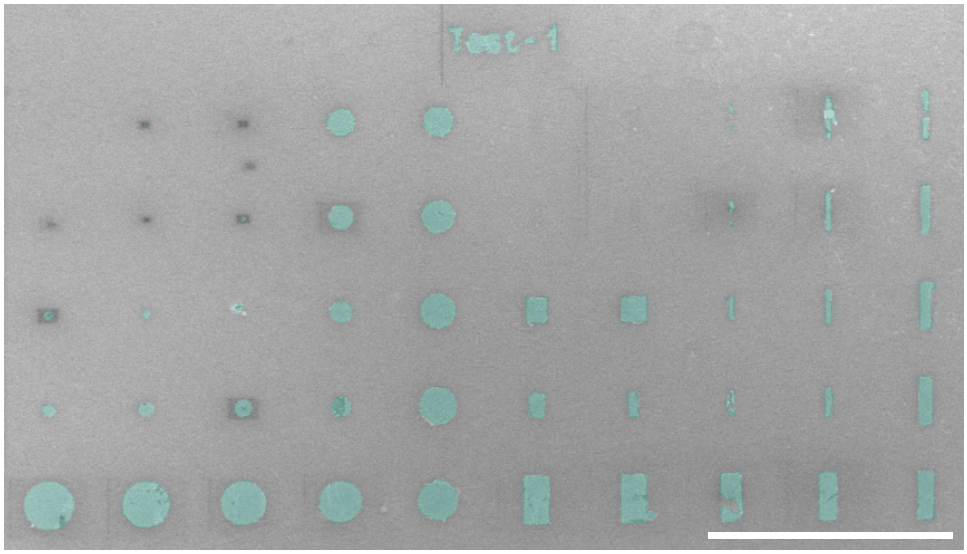

Figure D.1: ***Nanoparticles self assembly using PMMA.*** *False colour SEM image of patterned circles and rectangles of magnetic nanoparticles. The scale bar is 50μm.*

The nanoparticle solution was deposited on top of the developed resist using the water droplet during the deposition process explained above and in Chapter 4. As the water evaporates and the solution dries out, the nanoparticles get into the holes created by the EBL exposure in the resist. The nanoparticles lay down on the bare silicon surface inside the shaped holes. The rest of the area of the chip is still covered by the resist. The resist lift-off was carried out, to remove it completely, in the acetone instead of with heated NMP (N-Methyl-

2-Pyrrolidone) at 70°C. The idea was to reduce the exposure of nanoparticles to various chemicals, if possible, and to avoid high temperature because it can vary the magnetic properties of nanoparticles.

Figure D.1 shows an SEM image of the circles and rectangles of the deposited nanoparticles. The deposition size is varied between 20 μm to 100 nm in diameter for the circles and 20 μm to 100 nm in length for the rectangles. The figure shows the array of well-defined and precisely aligned various shapes of magnetic nanoparticles. The nanoparticles also followed the pattern of the text "Test-1" as the title of the trial experiment.

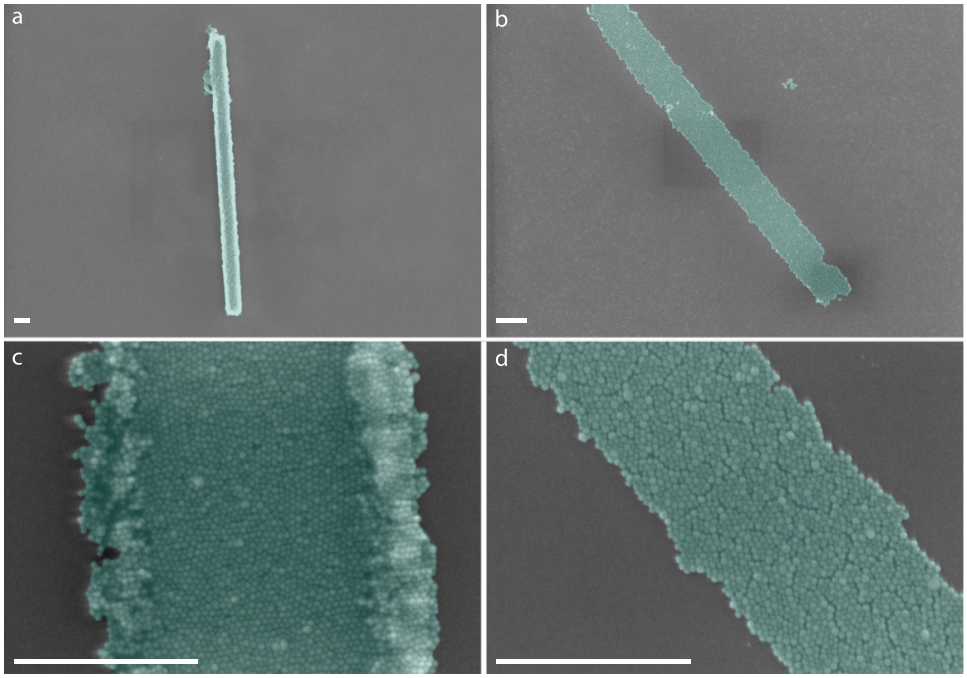

Figure D.2: ***Clearing the borderline of nanoparticles assembly. a-d,*** *False colour SEM images of patterned rectangles of magnetic nanoparticles.* ***c,*** *is the zoomed image of an area in* ***a****.* ***d,*** *is the zoomed image of an area in* ***b****. All scale bars are 500 nm.*

A cluttered borderline was formed when a double layer of PMMA was spun onto the chip as shown in Fig. D.2 a and c. The over-exposure of the resist caused the nanoparticles to congregate at the edges of the assembly. The problem was resolved by removing one layer of the PMMA, that is only using a

single layer of the PMMA. The clear edges and boundaries of the nanoparticle assembly can be seen in Fig. D.2 b and d. Several dry-runs were performed to achieve the desired results using PMMA-950k A8, PMMA-495 A8 and PMMA-495 A2 (depending upon the molecular weight and the viscosity). The process of this shape formation was much easier than the stencil mask process, and resulted in high resolution, high contrast and sharp edges and corners [293].

An example of patterned circles of nanoparticles using PMMA is shown in Fig. D.3. It is demonstrated that patterns can be easily fabricated down to 100 nm in diameter as shown in Fig. D.3a and a clean circular pattern of bigger size is shown in Fig. D.3b.

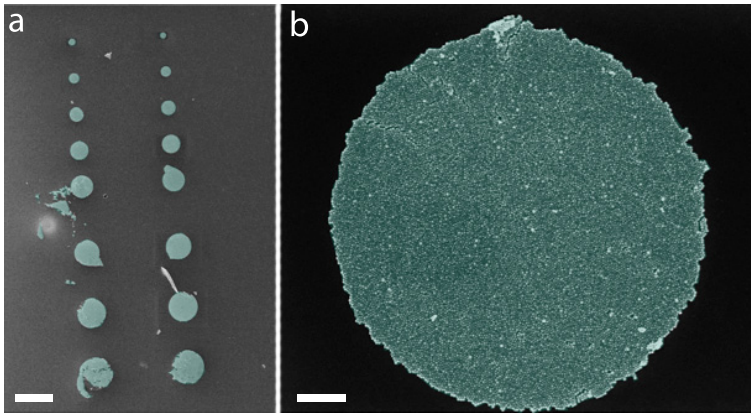

Figure D.3: ***Nanoparticle circles.*** ***a-b,*** *False colour SEM images of patterned circles of magnetic nanoparticles. The scale bar in* ***a,*** *is 20µm and in* ***b,*** *is 200 nm.*

D.1.2 Patterning Nanoparticles using Pentane

Pentane is a part of the nanofabrication procedure, in place of critical point drying, for the nanomechanical devices, so testing the nanoparticles self assembly with pentane is self-evident. Pentane is also used for drying the nanomechanical devices because of its fast evaporation rate. The pentane droplet was established on top of the silicon surface and then the nanoparticle solution was dropped on top of the pentane droplet. The chip with droplet was enclosed the gel-box to reduce the evaporation rate of toluene and pentane, which are highly

volatile. A nice self-assembly was obtained using this procedure as shown in Fig. D.4. Certain deformations and clustering of nanoparticles was observed because of the high evaporation rate compared to water. The evaporation could be controlled using deionized water in combination with pentane and toluene. These deformations were not observed with acetone as shown in Chapter 4.

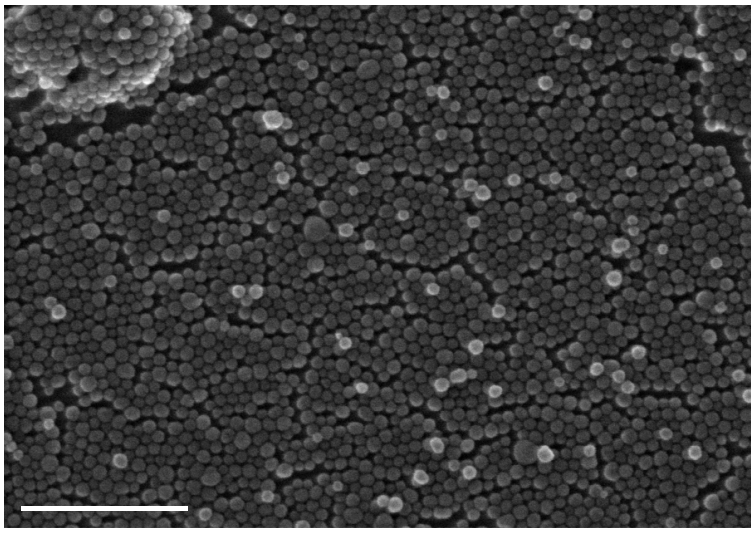

Figure D.4: ***Nanoparticles assembly with pentane.*** *SEM image of patterned layer of magnetic nanoparticles. The scale bar is 200 nm.*

D.1.3 Patterning Nanoparticles using HSQ

After testing nanoparticles with acetone (Sigma-Aldrigh), pentane (Caledon Laboratories) and PMMA on the silicon surface of SOI chips, the nanoparticles were also tested with HSQ (XR-1541 from Dow Corning, MI, USA) and ZEP (ZEP520A from ZEON Corp., Tokyo, Japan) separately on the silicon surface. Here I describe self-assembly of nanoparticles on the nanomechanical devices made using an HSQ resist, which is considered as a negative resist with excellent e-beam resolution ($\sim$10 nm) and admirable line-edge roughness. These characteristics have made HSQ in the top ranked resists for EBL, however, the shorter shelf life is one of its drawbacks. After the expiry date, the dose rate changes drastically and makes it over sensitive along with precipitation of

particles inside it.

The nanoparticles with high concentration (in a ratio of 1:100 of 5mg/ml of nanoparticle in toluene) were deposited on top of the fabricated devices. The fabrication of nanomechanical devices using HSQ is described in Appendix C. The nanoparticle deposition was carried out using the process illustrated in Chapter 4. Figure D.5a shows a set of devices suspended above the support silicon layer (base). Figures D.5b and c are magnified views of the device itself and the deposition of nanoparticles. The nanoparticles cover the device because of the high concentration (see Fig. D.5b). Figure D.5c shows the zoomed-in image of a resonating paddle, where layers of nanoparticles can be seen more prominently. The multi-layers of self-assembled nanoparticles or a 3D assembly of nanoparticles can be achieved and controlled by changing the concentration of nanoparticles.

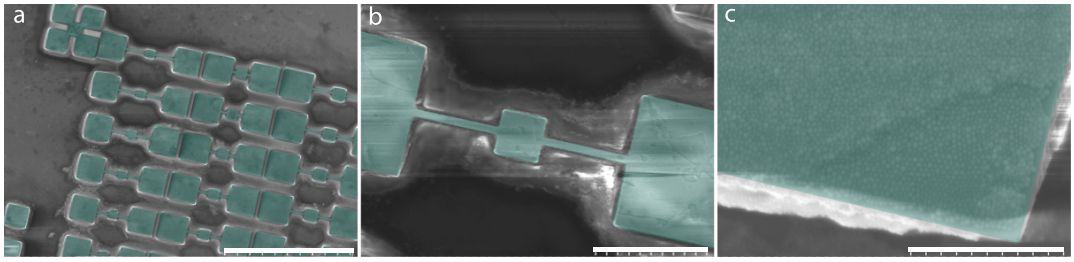

Figure D.5: ***Nanoparticle assembly on devices with HSQ resist.*** *False colour SEM image of patterned devices with HSQ and magnetic nanoparticles.* ***a,*** *colour shows set of devices. The scale bar is 30 µm.* ***b,*** *colour shows a device covered with nanoparticles. The scale bar is 5 µm.* ***c,*** *colour shows a resonating paddle covered with nanoparticles. The scale bar is 500 nm.*

D.1.4 Patterning Nanoparticles using ZEP

The nanoparticles in optimum concentration (in a ratio of 1:50 of 5mg/ml of nanoparticle in toluene) were deposited on top of the devices (fabricated with ZEP resist). The fabrication of nanomechanical devices using ZEP is described in Appendix C. The results presented here are without the PMMA layer just to show the deposition on ZEP made devices. The ZEP and PMMA can be used

after the expiry date because they show less sensitivity for the exposure change and dose changes. The known viscosity of these chemicals can be achieved by adding the solvent to get the desired thickness of the resist on top of the chip in the spin coater. The nanoparticle deposition was carried out using the process illustrated in Chapter 4.

Figure D.6a shows the set of devices engraved in the SOI matrix. One of the devices is magnified in Fig. D.6b showing the device itself and the suspended nanoparticles on the whole device. The zoomed image of a torsional rod is shown in Fig. D.6c for the same device presented in Fig. D.6b. The nanoparticle film on top of the device sags as it move away from the torsional rod to the edges of the device, and acts as the support for the drumhead like membrane of nanoparticles. The covered and broken drumhead were observed for the devices shown in Fig. D.6a.

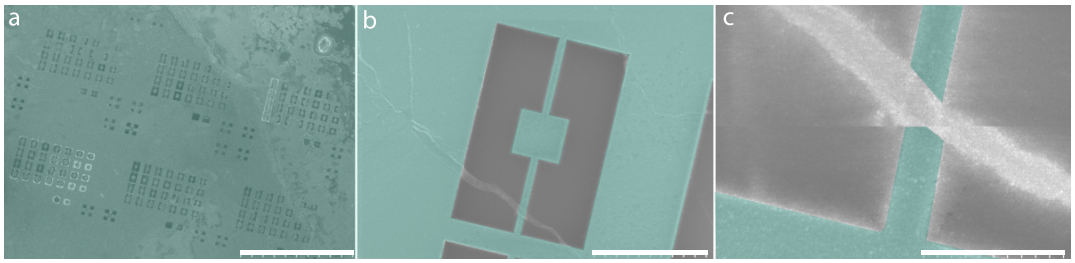

Figure D.6: ***Nanoparticle assembly on devices with ZEP resist.*** *False colour SEM image of patterned devices with ZEP and magnetic nanoparticles.* ***a,*** *set of devices. The scale bar is 100 μm.* ***b,*** *colour shows a device covered with nanoparticles. The scale bar is 5 μm.* ***c,*** *colour shows a resonating torsional rod covered with nanoparticles. The scale bar is 1 μm.*

D.2 Other Methods for Nanoparticle Assembly

As an illustration, the goal here was to get the desired self-assembled stable structures of nanoparticles. It is important to study the magnetic anisotropy

of nanoparticles along with the self-assembly itself. The magnetic anisotropy can be intrinsic (crystalline anisotropy) or extrinsic (shape anisotropy of the nanoparticles and the shape anisotropy of the assembly). The nanoparticles in the above section are spherical and have shape anisotropy from the geometrical assembly. However, it is also important to study the shape anisotropy of other anisotropic nanoparticles. The commercially available nanoparticles are either isotropic and/or smaller in size (superparamagnetic nanoparticles) so alternative nanoparticles were explored (stable single domain ferromagnetic nanoparticles, or anisotropic nanoparticles).

Various approaches were followed to obtain alternative nanoparticles and to get a nice assembly from anisotropic and single domain nanoparticles. Sections below discuss the results from nanoparticles with shape anisotropy and anisotropy from the assembly.

D.2.1 Shape Anisotropic Nanoparticles

Anisotropic nanoparticles (iron-nickel oxide nanoparticles) were synthesized by a thermal decomposition process. Various shapes, including stars and cubes, of iron-nickel oxide nanoparticles were achieved by modifying the synthetic conditions. These single-crystal [Ni,Fe]O nanoparticles were highly stable under ambient conditions and stable thermally at high temperatures [294].

These nanoparticles were then deposited on the silicon nitride membrane. The nanomechanical devices were then fabricated using the process described in Chapter 3. Figure D.7a shows the self-assembly of [Ni,Fe]O star shaped nanoparticles, 6 nm in size, and Fig. D.7b represents the cube shaped nanoparticles, 9 nm in size. The size of these anisotropic nanoparticles is in the superparamagnetic range.

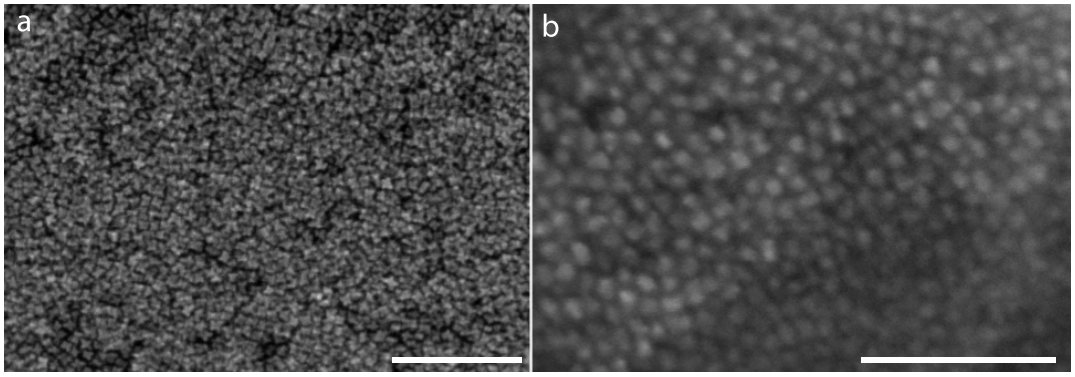

Figure D.7: ***Anisotropic nanoparticles. a,*** *star and* ***b,*** *cube nanoparticle assemblies. Both scale bars are 100 nm.*

D.2.2 Nanoparticles from Bacteria

However, the above mentioned nanoparticles (star and cube shaped) are smaller in size, and for some practical applications single domain nanoparticles of larger size are required. Magnetic nanoparticles of larger size (stable single domain) are present in magnetotactic bacteria. A lot of work has been done on magnetotactic bacteria and on getting the magnetic nanoparticles from the bacteria [97, 295, 296, 297, 298].

Magnetospirillum magnetotacticum ATCC 31632 bacteria were used as a base culture. The bacteria cells were first cultured and then lysed using the recipe described in reference [299]. The main chemicals used in the procedure are: Wolfe's Vitamin Solution, Wolfe's Mineral Solution; R7017 Sigma (1g), Resazurin sodium salt, powder, BioReagent, suitable for cell culture; A5960 Sigma (25g), L-Ascorbic acid, BioXtra; T400 Aldrich (25g), DL-Tartaric acid, ReagentPlus; 138622 Aldrich (25g), D-(-)-Quinic acid; S9512 Sigma (100g), Succinic acid BioReagent, suitable for cell culture, suitable for insect cell culture; 157740 Sigma-Aldrich (5g), Iron(III) chloride, reagent grade; R7017-5G resazurin sodium salt, bioreagent; A4403-100MG, L-ascorbic acid, T400-25G, DL-tartaric acid, reagent plus(R); S9512-100G, succinic acid; 138622-25G D-(-)-quinic acid; 157740-5G, iron(III) chloride, reagent grade; 60216-25G, potas-

sium phosphate monobasic; S5022-1KG, sodium nitrate, plant cell culture tested; S5636-250G, sodium acetate, anhydrous cell culture; and A1296-100G, agar.

Figure D.8 shows the SEM image of magnetic nanoparticles arranged in a chain form inside the lysed matrix. Another procedure is required to separate the magnetic inclusions from the matrix.

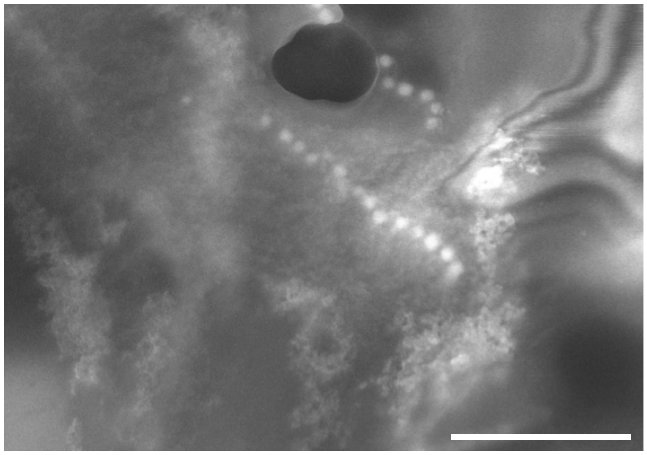

Figure D.8: ***Bacterial Nanoparticles lysed in matrix.*** *The scale bar is 500 nm.*

D.2.3 Nanoparticles Embedded in Polymer on Recording Media

The variety between naturally occurring nanoparticles and laboratory synthesized nanoparticles comprise various synthesis conditions. Besides the above mentioned efforts, self-assembly was also achieved by using nanoparticles from magnetic recording media. The nanoparticles are hard to use in liquid form on devices so assembling them on the devices is necessary. The reading and writing bits of the media head act as the magnetic field for the nanoparticles. This mechanism serves as the assisted self-assembly of nanoparticles. The recording can be longitudinal or perpendicular recording. This work has been done in collaboration with Thomas Crawford and Rahman (personal communication).

The nanoparticle solution was prepared in a ratio of 1:200:2 of nanoparticles (FerroTech: Fe_3O_4, 30 nm), deionized water and Polybutylene succinate (PBS). The solution was vortexed for 10 s for homogeneity. The prepared solution, in 100 μL, was dropped on top of the clean recording media for 10 minutes. The solution gets dry on top of the recording media during the process. The coated nanoparticles over the recording media can be transferred onto the polymer. The nanoparticle coated recording media were then spin coated with Disccoat (a water based peelable polymer) for 15 s at 1700 rpm, and dried for 15 minutes. The nanoparticles were then transferred from recording media to polymer using a circular shaped tape reinforcement. The concentration of nanoparticles, strength and bits of recording media, and spin coating recipe determines the pattern of nanoparticles [300, 301]. Figure D.9 shows an examples of such an assembly known as a nanoparticle polymer diffraction grating. The spectrograph in Fig. D.9b shows the magnified image of the assembly of nanoparticles presented in Figure D.9a.

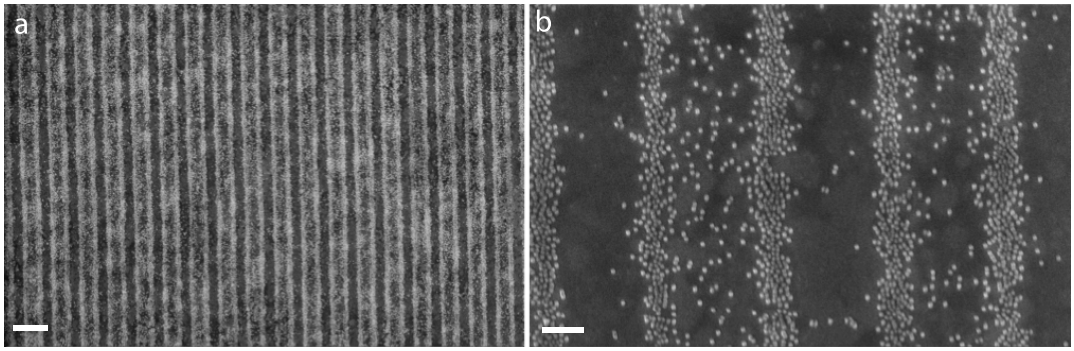

Figure D.9: ***Nanoparticle assembly in columns in polymer with magnetic tape.*** *Image credit: Thomas Crawford and Rahman.*

The peeled nanoparticle assembly was placed on an empty silicon nitride window, to fabricate the nanomechanical resonator in the polymer in the Ziess NVision 40 FIB machine. The heating of polymer caused problems like charging, swelling, melting and bending of polymer in the ion beam exposed areas. Various ion beam doses were tried to minimize the heating. The FIB exposure

in a cold environment was planned as the next step for the device fabrication.

Appendix E

Thin Sectioning of YIG

In Chapter 6, I performed the thin sectioning of yttrium iron garnet (YIG) to make disks in the micron range. This Appendix discusses the preliminary sample preparation for the YIG disks used in Chapter 6, for the samples used in Appendix F for the study of ion damage on YIG, and for the Lorentz microscopy of YIG disks in Appendix G.

E.1 Introduction

The sample preparation of YIG disks involves various methods, including chemical etching, mechanical grinding, mechanical polishing, single crystal formation, powder formation, and fabrication with a focused ion beam (FIB), depending upon the application. Each one of these methods has its own effects on the crystalline and magnetic properties of YIG. It has been well reported that chemical etching, mechanical grinding and FIB alters the magnetic characteristics to some extent. The mechanical treatment of a YIG single crystal surface is strongly influenced by the spin Seebeck effect because of the surface strains [302]. A rapid decrease in the magnetization is observed after the short mechanical treatment due to the paramagnetic phase formation in barrium ferrite [303]. Ferromagnetic line width was optimized by optimizing the mechanical

process timings in lithium ferrite spheres [304]. The mechanical grinding and polishing and thinning by Argon ion sputtering was used for lutetium bismuth iron garnet (LBIG) samples and many others [305]. The important point is the extent of damage for each of these factors. The depth of damage reduces, in order, from FIB, mechanical grinding, mechanical polishing, to chemical etching, from the mesoscopic range to nanometer range, respectively.

The YIG disk prepared purely by FIB, from bulk, encompasses hundreds of nanometers of dead-layer of material around it. This is because of the high dose of the ion beam from all sides of the YIG disk, for cutting the disk. In order to reduce the over exposure of the ion beam and minimize the ion damage, mechanical polishing may be incorporated into the procedure. This approach was developed for making a precise sample with reduced damage. The chemicals etching was avoided in order to bypass various chemical used for etching and cleaning processes. Another drawback for chemical etching is the lack of control of the shape of the etch.

Cleaning the sample is another crucial step in milling the nano-structures and structures in the mesoscopic range by FIB. It can also be performed in the FIB but it is a costly, inefficient, and risky (for the beam) procedure. The contamination can scatter the FIB ion beam during the charging and milling process, which reduces the beam quality and may introduce additional damage. Hence, it is difficult to clean the sample purely with a FIB ion beam.

The sample preparation, thus, started with mechanical polishing followed by mechanical grinding. At the later stages cutting and plucking in the FIB was performed to extract the disk from the lamella. The mechanical grinding and mechanical polishing are described in the following sections of this Appendix, while the ion damage by the FIB is detailed in Appendix F. The mechanical cutting was also achieved by dicing along an axis in the dicing machine. The following sections describe the details of grinding, polishing, cutting, and dicing of the YIG material.

E.2 Thin sections of YIG by Mechanical Polishing

In this study, I used the YIG/GGG/YIG layers wafer (3-inch diameter, from ShinEtsu). The YIG layers are in the $< 111 >$ orientation in the out of plane direction. The thicknesses of the YIG/GGG/YIG layers are 110/500/110 microns respectively. The wafer was diced in the $1cm \times 1cm$ and $5mm \times 5mm$ chips. The chips layers cross-sectional view is illustrated by an optical image shown in Fig. E.1. The chip was held in the saw-tweezer for the optical image. The YIG layers are opaque and the GGG layer is transparent in this thickness range. The $5mm \times 5mm$ chips were used further for the mechanical grinding.

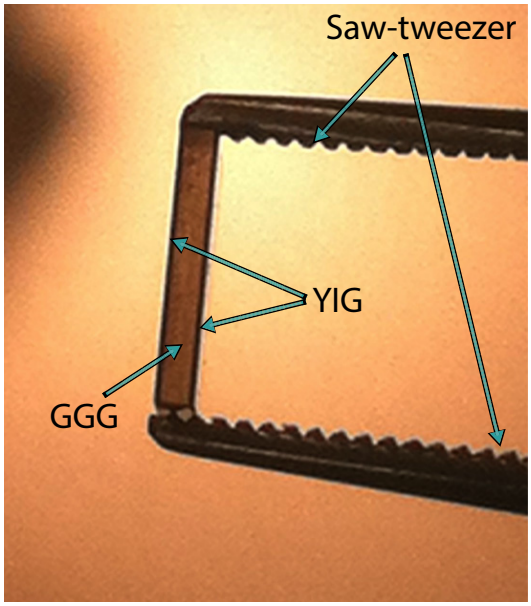

Figure E.1: ***YIG and GGG sandwich.*** *Optical image of the cross-section of* $5mm \times 5mm$ *chips.*

E.2.1 Mechanical Grinding of YIG

The sample for mechanical grinding was prepared by mounting the $5mm \times 5mm$ chip on top of the special quartz crystal with a crystal-bond (Crystalbond 821-

1 by Ted Pella Ted). The crystal-bond was heated at 120°C inside the fume hood on top of a uniform hotplate (200°C at the hotplate), for melting flow to fix the chip in it. The chip was then embedded in the crystal-bond on top of the quartz crystal, to compensate the flattening of the crystal-bond first in the grinding machine before top YIG layer, and to set the angles for grinding. After the melting of the crystal-bond, the YIG chip was gently pressed into the crystal-bond. An additional crystal-bond was added to fully cover the chip to fully protect the surface during the grinding and polishing processes. The chip was placed in the center and the surface tension of the melted crystal-bond helped to position the chip. The chip was held in place during the cooling process, controlled by a set of tweezers. The whole setup was cleaned with IPA and acetone and air dried before the sample mounting.

The quartz crystal and the crystal-bond can be seen in Fig. E.2. The mounted unit (quartz crystal in the small aluminum polishing block inset) was fixed in a polishing block holder (tripod polisher Southbay technology, model 590 TEM), having legs (with pads) and micrometer screw gauges at the ends to maintain the angles during the grinding, and was ground all together for parallel and flat grinding. The holder was calibrated (without quartz crystal) with all three pads laid on a flat surface and by adjusting the micrometer screw gauges. After calibration, the quartz crystal was installed and the two pads were aligned horizontally and a third pad is constrained to grant the quartz crystal (with the chip) to hold its weight. The position and angle of the chip was adjusted by changing the micrometer screw gauges, which changed the pad heights. No vertical force by hand was applied, however, it was held firmly horizontally over the moving wheel with gratings.

The sample was inspected frequently under the optical microscope for quick observations. The whole process of grinding and polishing was performed under water flow to absorb extra heat and to remove and clean the polished material. Extra measures were used to avoid contamination in the sample. The

contamination may come from water, abrasion material, grating material, and the polishing machine.

The quartz crystal, the crystal-bond and GGG layer are all transparent so that the transparency of the YIG can easily seen as the thickness diminishes. Figure E.2a shows all the components together; a pristine YIG/GGG/YIG chip was brought near with a tweezer, to compare with the mechanically ground YIG/GGG/YIG chip for which the top YIG and GGG layers are milled away and only the bottom YIG layer is present. Figure E.2b shows the tilted optical image of the same YIG layer as in Fig. E.2a to show the opaqueness of the YIG film at 100 microns.

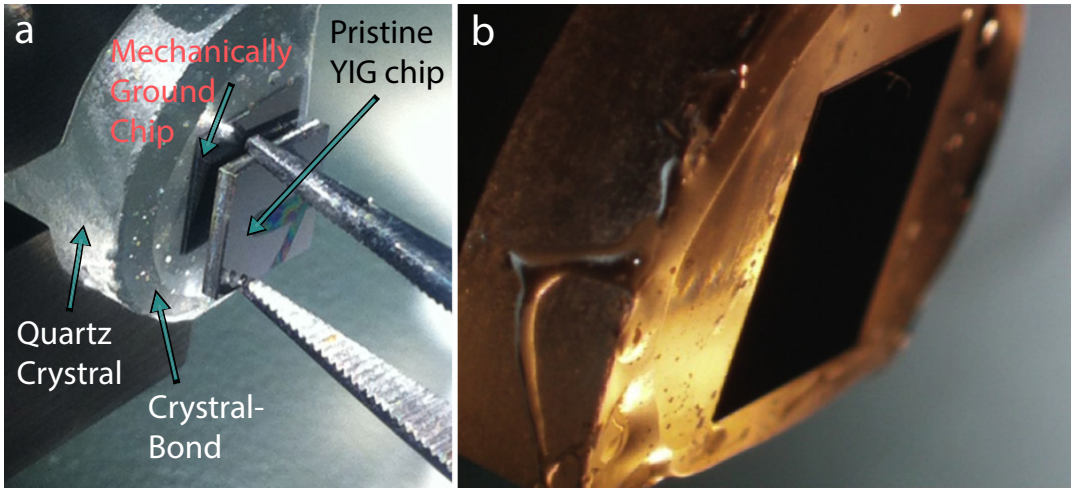

Figure E.2: ***Mechanical grinding.*** *Grinding of the YIG sandwich until the bottom layer of the YIG is left.* ***a,*** *comparison of ground chip bonded on top of quartz crystal, with pristine chip.* ***b,*** *tilted optical image of the bottom YIG layer for transparency. The chip dimensions are* $4.8mm \times 5.1mm$.

The grinding machines used were from SouthBay (Southbay technology model 650 low speed diamond wheel saw and Southbay Technology Model 900 grinder/ polisher) with various grinding discs optimized for coarse and fine grinding. The premium diamond lapping films (plain back, 8 inches in size, Allied High Tech) were used in steps, ranging from 60 microns to 0.1 micron particle size (60-1200 grit according to the USA grading system). It features

flatness, plain backs, long-lasting, excellent uniformity, and can be used in wet or dry conditions. The particle size of SiC (silicon carbide) discs was reduced gradually as the thickness of the YIG/GGG/YIG chip minimizes in accordance. The chip was grinded with these abrasive grinding discs at an initial speed of 30 rpm for several hours. The speed was then reduced with decreasing grit size, and the elapses time was enhanced to slow down the grinding rate for uniformity and better control.

E.2.2 Mechanical Polishing of YIG

As the thickness of the YIG film reduces, it enters into the transparent regime, as shown in Fig. E.3. When the transparency shown in Fig. E.3a was achieved, the mounted chip setup was then transferred from the grinding machine to the polishing machine (Southbay technology model 910 lapping and polishing machine). The chip polishing was initially obtained with a diamond polisher. The silica particles (suspension, colloidal silica by Allied High Tech part number 180-2000) were used in a sequence of 0.05 μm and 0.02 μm at 5 rpm for several hours, respectively.

The chip was then polished with colloidal silica OPS (oxide polishing suspension, 40 nm particle size, Buehler, Lake Bluff, IL, U.S.A.), to remove surface damage due to diamond particles. The colloidal silica particles serve both the mechanical and chemical polishing for the chip. A wedge shaped polishing was performed at this stage, when the transparency of Fig. E.3a was achieved, to get a range of thickness of the final YIG lamella. The reason lies in the lack of information available for the correspondence between the visible transparency and the thickness of the YIG film. A final wedge shaped YIG film was obtained as shown in Fig. E.3b.

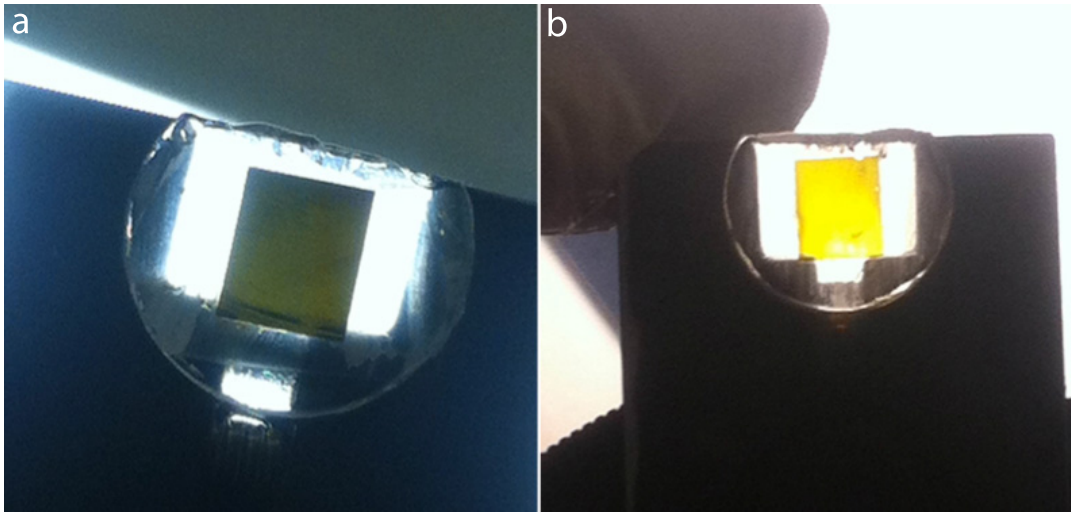

Figure E.3: ***Mechanical polishing.*** ***a,*** *onset of transparency of the YIG film with dark brown to green colour.* ***b,*** *Polishing of YIG film until yellow transparency to obtain required thickness. The chip dimensions are* $4.8mm \times 5.1mm$.

The yellow YIG film was then released in acetone, to remove the crystal-bond, for 48 hours. The film was suspended on top of the carbon grid inside the acetone in order to save its shape. The thickness of the wedge film was measured in the range from 1μm to 8μm in the SEM. The grinding, polishing and cleaning of the samples were done in the same way for several chips for process optimization.

The YIG wedge film was then safely mounted on an SEM stub for the disk fabrication in the FIB (Zeiss NVision 40). YIG disks of various sizes were fabricated by using the raith design in the FIB. Figure E.4 is a representation of such disks. The YIG disks prepared by this method have minimum ion damage because only the curved side of the disks are exposed to ions. The top and bottom sides are flat; the top side is mechanically polished by silica nanoparticles, and the bottom side is already chemically flat, since the film is grown by molecular beam epitaxy.

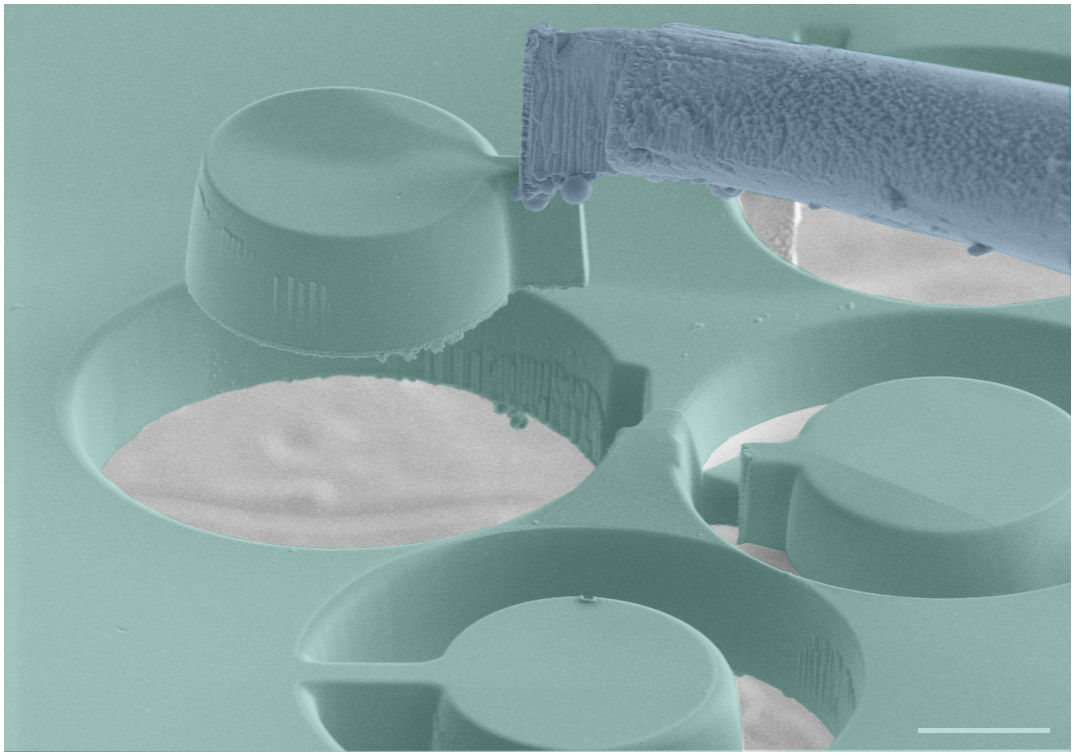

Figure E.4: ***FIB fabricated YIG disks.*** *False colour SEM image of the fabrication of the YIG disks from the polished film in the FIB. The green colour shows the YIG disks and lamella and the blue colour is the handle of the metallic probe for plucking. The scale bar is 10 μm. (Image credit: M. Belov for YIG disks fabrication in FIB.)*

E.3 Thin sections of YIG by Dicing Machine

The procedure mentioned in the above section is beneficial but it is time consuming. Another approach was followed for the thin slicing of YIG chips using a dicing machine (Disco DAD 3240 Dicing Saw) instead of the mechanical grinding. This approach is very useful for the transmission electron microscope (TEM) sample preparation. The idea is explained in Fig. E.5. In this study, a thin slice of sectioned sample on top of the TEM grid bonded with the special TEM bond in the vertical direction was fabricated. The section was then taken to the TEM to prepare the ultra-thin lamella.

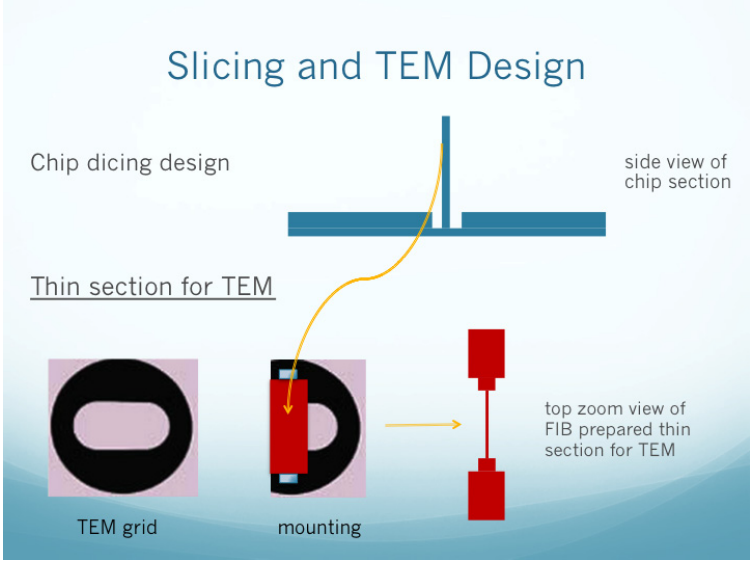

Figure E.5: ***Idea to make the thin sections for TEM.*** *The red colour is the top view of the blue coloured thin slice of the diced sample. Ultra thin sections were prepared in the TEM as shown in the red colour.*

E.3.1 Dicing of Silicon

A computer program and recipe were created in the dicing machine for dicing in a desired pattern. The dicing machine was equipped with auto alignment, programable designs, and high throughput. Different types of designs were created and diced as shown in Fig. E.6 and in Fig. E.7. The silicon wafer was diced to test the dicing recipes in place of the YIG at first. The $5mm \times 5mm$ silicon chip was mounted on blue sticky tape in a 8-inch frame, serving as a holder for the chip in the dicing machine. After cross-hair alignment, the created design program was run under water flow. The same procedure has been examined under surfactant flow but the results from water flow gave better results and clean chips.

Fig. E.6 shows SEM images of diced silicon chips and thin slices with the dicing blade (Dicso-Z09-SD2000-Y1-90). Figure E.6a and b shows the staircase designs and Fig. E.6c shows a top view of a thin section diced with this blade. The spindle speed was 18000 rpm and the feed rate was 2 mm/s for this

cutting. The chipping to the top was observed due to the higher speed rate. The standard procedure from the Disco company was followed to install and remove the blade.

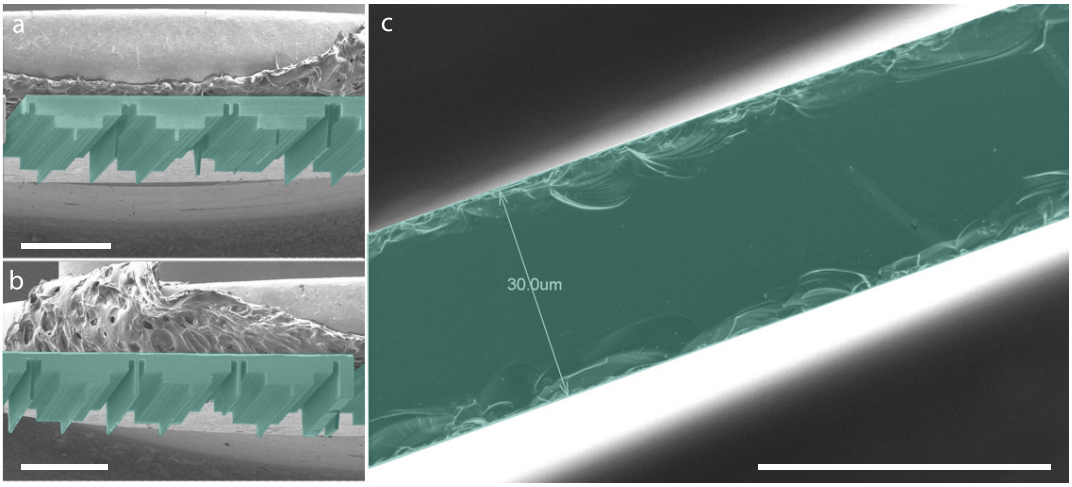

Figure E.6: ***Dicing silicon with SD2000 blade.*** *False colour SEM images of the silicon chips.* ***a-b*** *stair-case silicon dicing.* ***c,*** *magnified image of one thin-section. The width of the thin-section is 30 μm. The scale bar in* ***a,*** *and* ***b,*** *is 1 mm, and 40 μm in* ***c.***

Fig. E.7 shows SEM images of diced silicon chips and thin slices with the dicing blade (Disco-SD4000-Y1-60). Figure E.7a and c show the stair-case designs and thin diced sections of the chip. The blade from reduced diamond grit size (from 90 to 60) helped a bit in reducing the chipping. The spindle speed was 11000 rpm and the feed rate was 0.3 mm/s for this cutting. The blade cooler nozzle was set to zero, and shower nozzle was 0.5 L/min. All blades were dressed on a PB08-F40 pre-cut dressing board. The chipping to the top was still observed due to the higher speed rate. The depth of shallow cuts is 0.18 mm and deep cuts are 0.48 mm. Figure E.7b is the magnified image of Fig. E.7a, and Fig. E.7d is the magnified image of one of the slices in Fig. E.7c. A thin slice of 9 μm was obtained using this blade at the mentioned speed on the silicon chip, which is an acceptable width for TEM sample preparation. There were a slight number of slices that broke during the cutting process due

to high speeds.

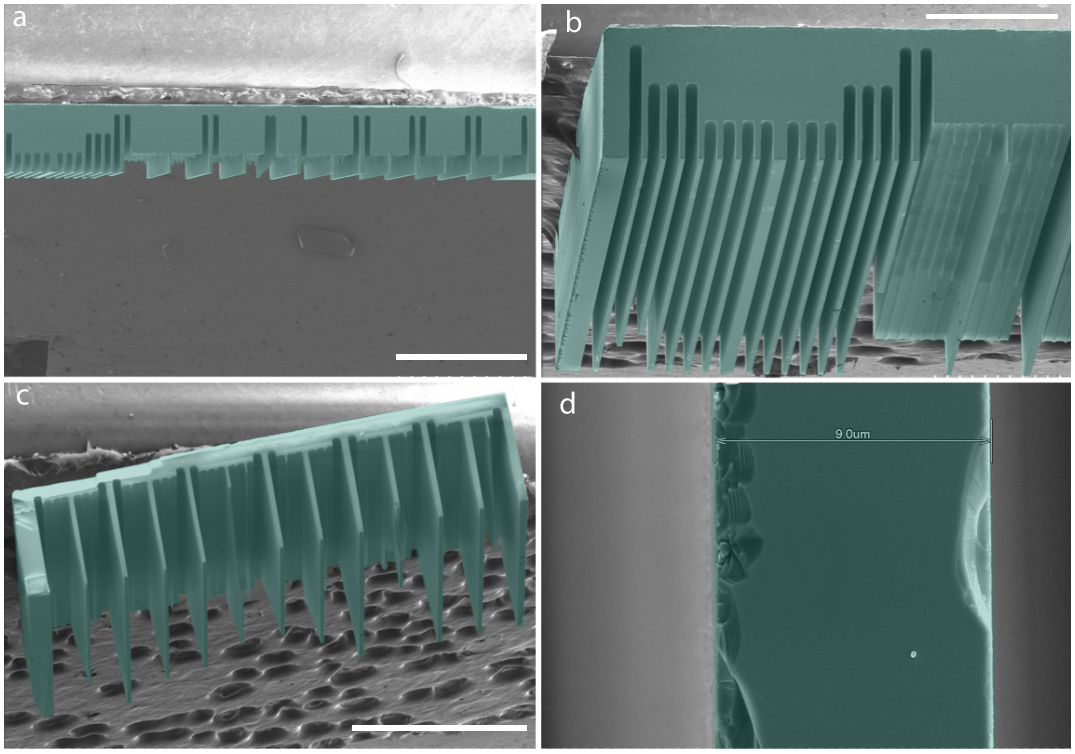

Figure E.7: ***Dicing silicon with a SD4000 blade.*** *False colour SEM image of the silicon chips.* ***a-c*** *stair-case and thin slices of silicon dicing.* ***d,*** *magnified image of one thin-section. The width of the thin-section is 9 μm. The scale bar is 1 mm in* ***a*** *and* ***c,*** *500 μm in* ***b,*** *and is 5 μm in* ***d.***

E.3.2 Dicing of YIG

Finally, the dicing was performed for YIG chips of the same size (as for silicon, $5mm \times 5mm$). The chips were also tested with another finer blade (Disco-SD4800, less grit size) along with the blade (Disco-SD4000-Y1-60) for reduced chipping. The spindle speed of 5000 rpm was used for finer results. Figure E.8a shows the dicing of the YIG/GGG/YIG sandwich. Figure E.8b shows a magnified image of one of the thin slices in Fig. E.8a. The width of the thin slice was found to be 5.5μm, which is a good width obtained from dicing saw machine, and is very advantageous for TEM sample preparation.

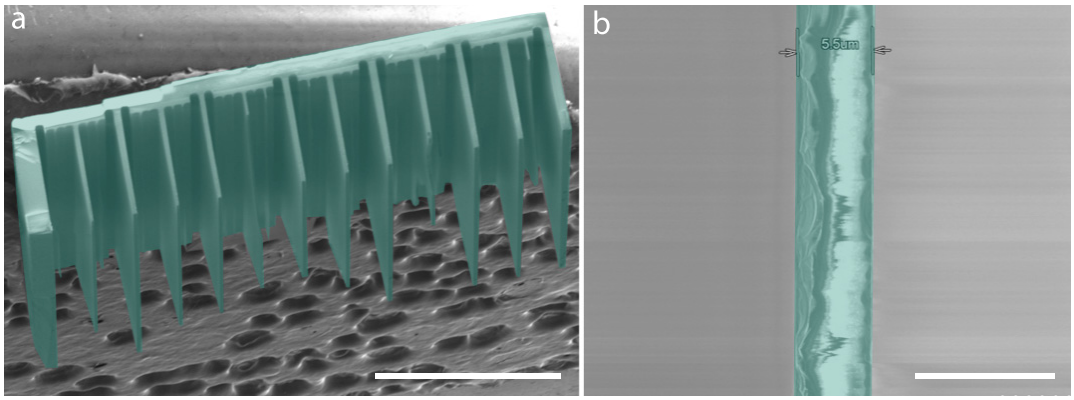

Figure E.8: ***Dicing YIG with a SD4000 blade.*** *False colour SEM image of the silicon chips.* ***a,*** *thin slices of YIG slab.* ***b,*** *magnified image of one thin-section. The width of the thin-section is 5.5 µm. The scale bar is 1 mm in* ***a,*** *and 10 µm in* ***b****.*

E.4 Thin Slices of YIG for FIB and TEM

The thin slices obtained from mechanical grinding and thin-sectioning were then transferred to the FIB for TEM sample preparation. Figure E.9 shows the sample prepared for TEM in the FIB machine. The details of TEM sample preparation are described in Appendix F and G .

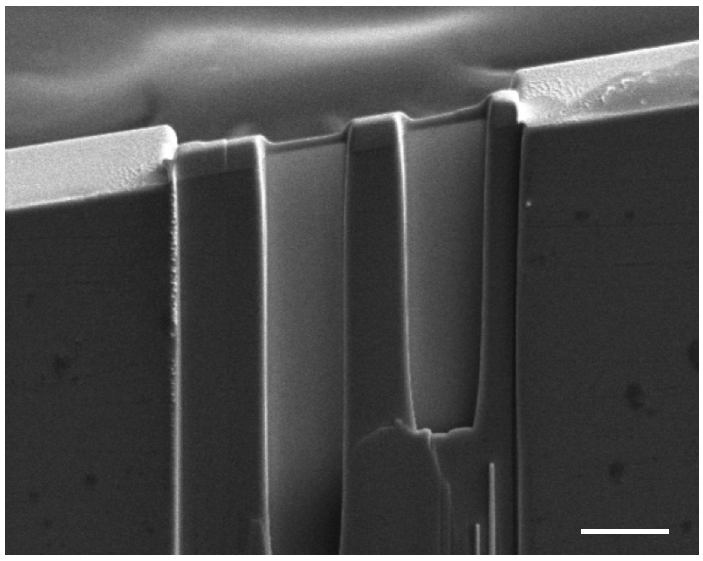

Figure E.9: ***Ultra-thin sections for TEM.*** *Sample prepared in the FIB by a high energy ion beam. The scale bar is 5 µm.*

Appendix F

Ga+ Ion Damage on YIG and Silicon Nitride by Focused Ion Beam (FIB)

F.1 Introduction

Focused Ion Beam (FIB) is a powerful, versatile, and well-established method for nanofabrication using ion beam lithography without masks and resists. It can precisely machine 3D structures on mesoscopic and nanometer scales. With FIB, it is possible to extract the specimens in a desired pattern and from very specific locations. Ion implantation occurs during the ion beam exposure and causes the amorphization of crystal structure depending on the degree of implantation. The amorphization or the damage caused from the ion beam can be useful or disadvantageous depending on the goal of the study [306]. For example, ion implantation is used to improve many electronic devices, and batteries [307], and on the other hand, it may damage the crystalline, mechanical and magnetic properties. The milling of samples for the transmission electron microscope (TEM) is a well known application of FIB among other utilizations. The low-kV FIB conditions are very useful for such sample preparation in order

to minimize ion damage and to make high quality specimens. Gallium ions are most commonly used in the FIB ion beams, among others like helium ions, argon ions etc. The milling and sputtering rates depend on the material properties and beam charging (current, dwell time, and spot size) on the material surface.

Many systematic studies about ion damage (Ga+, Ar+, Au+, He+, Si+, Cu+, etc) to various materials (metals, semiconductors, magnetic materials, biological specimens and others) have been reported in the literature, and well studied with various techniques and methods (depending on the properties under observation) [308, 309, 310, 311, 312, 313, 314, 315, 316, 317, 318]. The stoichiometric effects can be observed after annealing the ion implantation [309]. The damage recovery is possible in some cases depending upon the amorphization and annealing procedures [310]. The ion irradiation can increase the chemical reactivity of the surface because of induced defects, adsorption, and catalysis [311]. FIB has also been used for etching (using molecular chlorine) as maskless and resistless removal of silicon and can also be used to remove FIB-induced crystal damage and ion implantation [306, 315].

The ion damage in YIG has been reported with various ion irradiation and implantation methods. Thin epitaxially grown YIG films irradiated with swift heavy ions showed change in the crystalline, electronic, and magnetic phases [319, 320]. Coexistence of crystalline and disordered phases have also been reported [319, 321]. Large etch selectivity is observed when YIG was implanted with ions [322]. Ion induced thermal instability and phonon mode behaviour were studied with Raman spectroscopy for a YIG [323, 324]. Structural damage and swelling as a result of ion damage has been studied via scanning force microscopy [325], and TEM [326]. The spin wave resonance study of YIG sample after ion implantation has been executed to obtain resonance spectra [327].

A TEM uses an electron gun, electric and magnetic lenses, and apertures

to control the electron beam. Detectors at various locations inside the TEM receive the electron signals and produce the TEM images and diffraction patterns of the desired output. The electron beam transmits through the ultra-thin sample and a combination of objectives, apertures and detectors produce the desired results. Information regarding the structure, morphology and composition can be extracted using TEM [328]. In-situ irradiation in TEM gives the time resolved evolution of the damage and other time-domain information [329].

The sample preparation in the FIB inherently involves damaging the sample and thus degrading the sample to an extent. The ion damage artifacts related to the TEM sample preparation method are well understood [318]. This Appendix discusses the ion beam induced damage and artifacts in YIG and silicon nitride. The Ga+ ion damage is studied using TEM imaging and diffraction techniques.

F.2 Ga+ Ion Damage in YIG

A clean mechanically polished YIG sample, details of which are described in Appendix E, was used for the gallium ion (Ga+) implantation. A raith (Elphy Quantum) design was created with alignment marks for the ion damage as shown in Fig. F.1b. It consists of 8 reference parallel lines (made up of dots) with 156.16×10^7 ion beam dose (4684.8×10^7 keV) and 7 lines of variable doses, which are expressed in Table. F.1. The dot radius in the design is 5 nm and dot separation is 5 nm, such that the dots are overlapping and create a line. The lines are separated by 300nm. The beam diameter is 13 nm determined by the 10 pA probe with nominal 50 % energy. For cutting and etching, ratio of areas ($(\pi(13)^2)/(\pi(5)^2) = 5.3$) should be greater than 1. An SEM image of the exposed area with raith design in Fig. F.1b is shown in Fig. F.1a. An ion beam of 30 keV was used with a 10 pA current for the minimum dose line, in the FIB machine (Ziess NVision 40). The dot dwell time was 0.5 ms, and there

Table F.1: Dose and energy of each line

line #	Dose factor	Dose (ions/line)	Energy (keV)
0	2^7	156.16×10^7	4684.8×10^7
1	2^6	78.08×10^7	2342.4×10^7
2	2^5	39.04×10^7	1171.2×10^7
3	2^4	19.52×10^7	585.6×10^7
4	2^3	9.76×10^7	292.8×10^7
5	2^2	4.88×10^7	146.4×10^7
6	2^1	2.44×10^7	73.2×10^7
7	2^0	1.22×10^7	36.6×10^7

were 400 dots in the 2μm line. No FIB imaging was done on the sample in order to avoid any Ga+ ion exposure during the imaging. The exposures were performed in a horizontal fashion. The dose was calculated by the following equation:

$$\text{dose} = \text{current} \times \text{dwell time} \times \text{number of exposures} \times \frac{ions}{1.602 \times 10^{-19}} \quad \text{(F.1)}$$

and the energy was calculated as:

$$energy = dose \times \text{base energy} \quad \text{(F.2)}$$

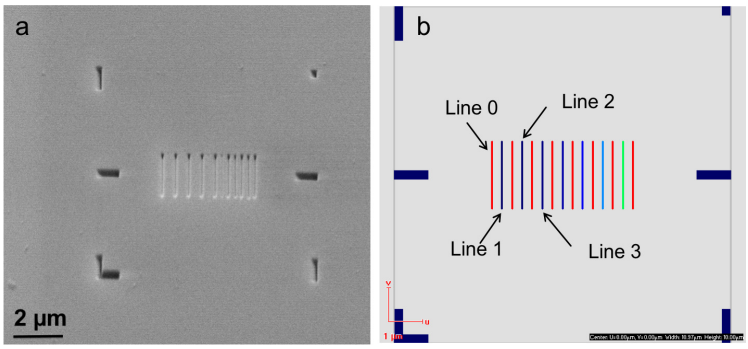

Figure F.1: ***Design for ion beam exposure.*** ***a,*** *SEM image of the ion beam exposed area in the YIG.* ***b,*** *Raith software design for the exposure. Red colour shows the reference line, and blue-to-green colour shows the lines with variable beam dose.*

F.2.1 Sample Preparation for TEM

Transmission electron microscope results are based on the electron-specimen interactions that gives us information up to the atomic level. The electron beam transmits through the ultra-thin specimen, for which it is called as "transmission" electron microscopy. The transmission requires an ultra-thin specimen, usually less than 100 nm. The sample thickness is chosen based on the expected information from the TEM results and on the material itself.

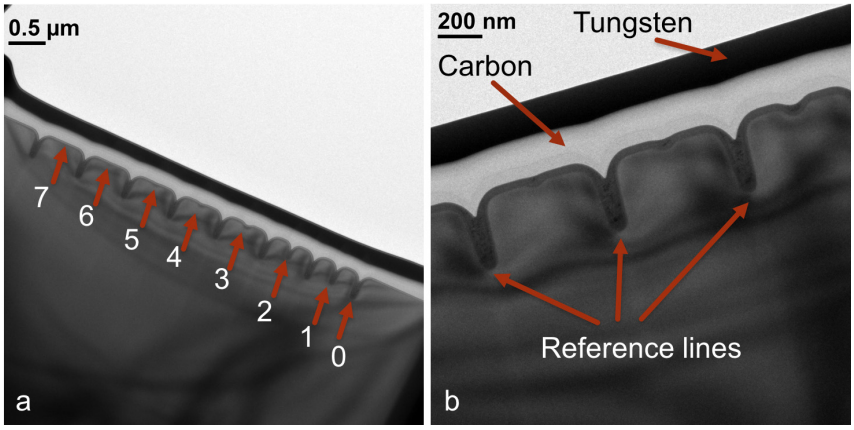

Figure F.2: ***Bright field cross sectional TEM micrographs of all damaged lines in the YIG. a,*** *Full view of the damaged lines with Ga ions. The lines are indicated with arrows and numbers.* ***b,*** *magnified image of lines 5, 6 and 7 in between the reference lines. Carbon and tungsten are deposited as sacrificial layers for specimen preparation.*

Ultra-thin cross sections for the YIG samples were prepared using FIB (Zeiss NVision 40 Cross Beam Microscope), details are discussed in Appendix G . An illustration of the cross sections is shown in Fig. F.2. Figure F.2a shows full view of all the exposed lines, and Fig. F.2b shows the area for lines 5, 6, and 7 between reference lines. Carbon and tungsten are deposited, after the ion beam exposure, to protect the YIG during the TEM specimen preparation. An initial 50 nm of carbon was deposited in the sputter coater (Gatan 682 with Gatan 681-20000 film thickness monitor) and 150 nm in the gas assisted sputtering (GIS; gas injection system). Initial milling for TEM sample preparation was

done with Ga+ ion (at 30 keV), the energy was reduced (5 keV) as the specimen reduces in thickness. Final polishing was executed at 1 keV and at 0.3 keV, in an Hitachi NB5000. The specimen was then taken to the TEM (Hitachi H-9500 (300kV accelerating voltage), and JEOL 2200FS (200kV accelerating voltage)) for imaging and diffraction patterns.

F.2.2 Bright Field (BF) Images

Bright field (BF) images are created, in the TEM bright field mode, when only the transmitted beam is allowed to pass through an aperture. All the scattered light is blocked by an objective aperture in the back focal plane of the objective lens. The sample images are parallel to the direct electron beam, and only a small number of electrons are used for imaging in this mode, thus it produces low contrast images that have bright backgrounds [330].

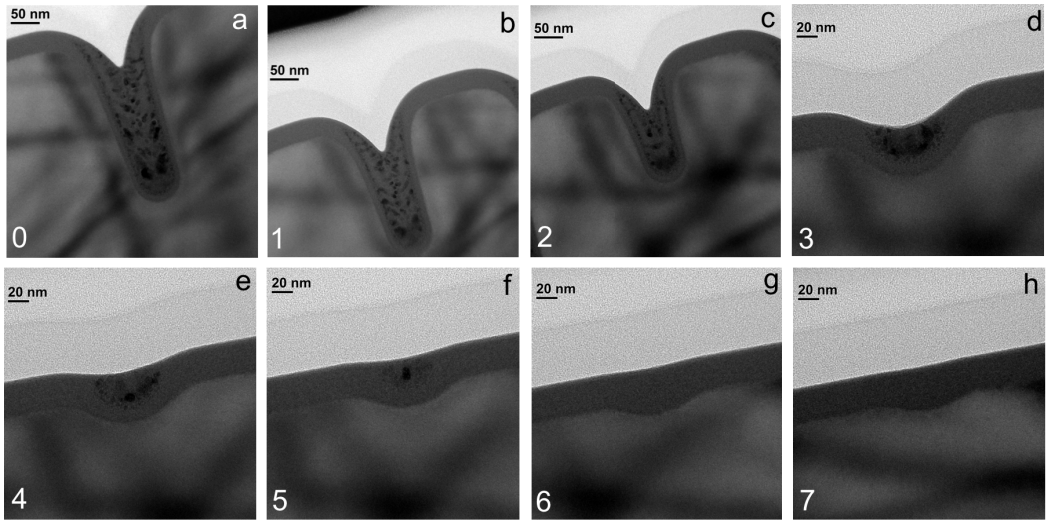

Figure F.3: ***Magnified bright field cross sectional TEM micrographs of damaged lines in YIG. a-h,*** *BF images for lines 0-7 respectively, as labelled.*

Figure F.3 shows the BF images for all the exposed lines. The damaged area widths and depths are calculated from these BF images and are represented in Fig. F.12. The difference in carbon deposition can also be seen in Fig.

F.3b-h. An initial 50 nm thick layer of carbon was deposited in the sputter coater and and then another 150 nm was deposited in the FIB by GIS (gas injection system) method, before tungsten deposition at a later stage. This gave a contrast in carbon deposition that is clearly observable. The depth of lines gradually decreases and becomes only a surface phenomenon as the ion beam exposure dose reduces (see Fig. F.3a-h).

F.2.3 STEM

Bright field images can also be created in the scanning TEM (STEM) mode, which is capable of producing BF and dark field (DF) images as well. BF, DF, high angle annular dark field (HAADF), and convergent beam electron diffraction (CBED) can be performed in the STEM mode. HAADF imaging assembles the incoherently scattered electrons at high angles. It gives high contrast (Z contrast) images depending upon the specimen properties and thickness.

For the DF images, an opaque aperture is used under the condenser lens. The scattered light is gathered in the dark background and thus it produces high contrast images. The electron beam is focused to a narrow spot that is raster scanned on the sample. The scattered electron intensity is gathered from each position and plotted at the end versus position of the sample. STEM results in a much better contrast and spatial resolution than ordinary SEM images, such that structural details are easily observable [328, 331].

DF usually gives information on the crystallinity and defects in the specimen. Figure F.4a and b shows BF and DF images in the STEM mode of TEM. One can clearly observe the crystal, polycrystal and amorphous phases in the damaged areas of each line. Small crystal phases are present in the damaged line in conjunction with the amorphized phase. The dark spots in BF and bright spots in the DF images show the crystalline phase in Figure F.4a and b, respectively. The DF images also show the heat radiated to the YIG crystalline phase from the bottom of the line that may damage the crystal and magnetic

properties of the YIG.

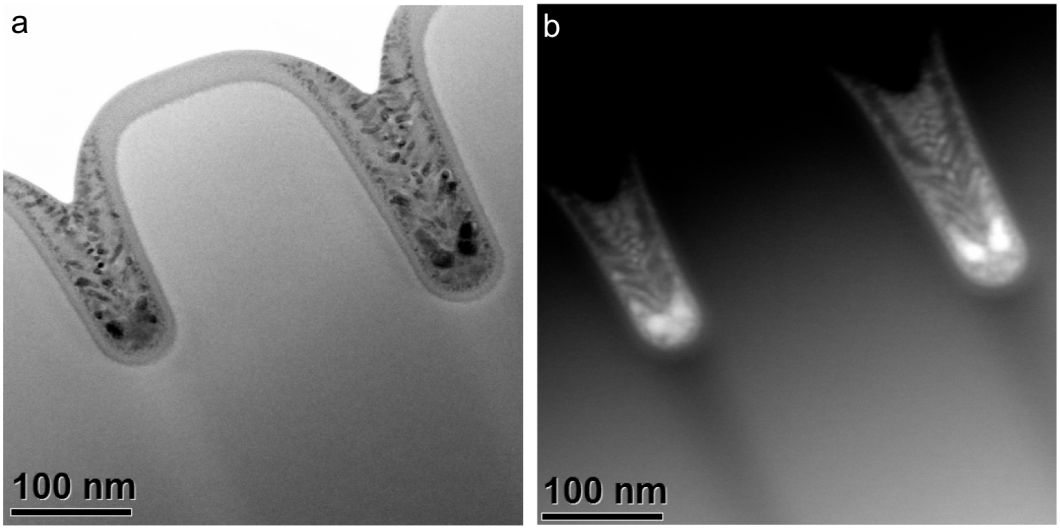

Figure F.4: ***STEM images of damaged lines 0 and 1 in the YIG. a,*** *BF TEM micrograph of lines 0 and 1.* ***b,*** *DF TEM micrograph of lines 0 and 1.*

F.2.4 High Resolution TEM (HRTEM)

High-resolution TEM (HRTEM) is the phase contrast obtained in the conventional TEM (CTEM) mode [331]. The phase contrast information is obtained from the interference pattern of the transmitted and scattered beams (diffraction) at the atomic scale. Crystal structure and atomic arrangement information can be obtained from the HRTEM. It usually requires ultra-thin samples tens of nanometer thickness, and gives real-space images of the atomic configuration [328]. Figure F.5a-h shows HRTEM micrographs of the interface of damaged areas and crystalline phase of the YIG sample for each exposed line, respectively, as labelled. The damaged areas are amorphized and the unexposed areas are still in the crystalline phase.

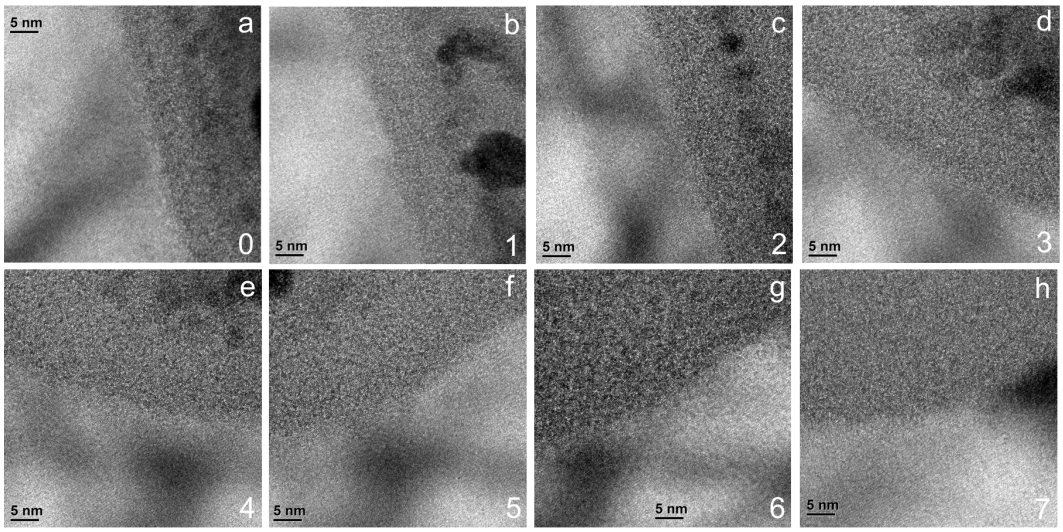

Figure F.5: ***HRTEM images of damaged areas in the YIG. a-h,*** *the HRTEM of each line labelled from 0 to 7 respectively.*

F.2.5 Nanobeam Beam Diffraction (NBD)

Nanobeam electron diffraction (NBD) is a technique, in the conventional TEM (CTEM) mode, to measure strain in the crystalline specimen. NBD is a simple method in comparison to HAADF and CBED. In NBD, a parallel electron beam is used over the area of interest in the sample and then the diffraction patterns are recorded and analyzed for each location. The location and brightness of bright spots in the diffraction pattern gives one information about crystallinity and deformations. Figure F.6b-e shows the NBD patterns obtained at the labelled locations in Fig. F.6a of line number 8. Locations 1 and 2 are in the crystalline YIG and locations 3, 4, and 5 are in the damaged areas of the line. The locations 2 and 3 are just across the interface of the damaged and crystalline phase areas of the YIG. The crystalline phase is amorphized as one moves from location 1 to location 4. One can also observe the enhanced strains and heat transformation from location 1 to location 3 by the reduction in brightness of the diffraction spots. At location 4, the crystalline phase is

completely destroyed and the YIG becomes amorphous. A BF image was obtained at location 5 to see the contrast.

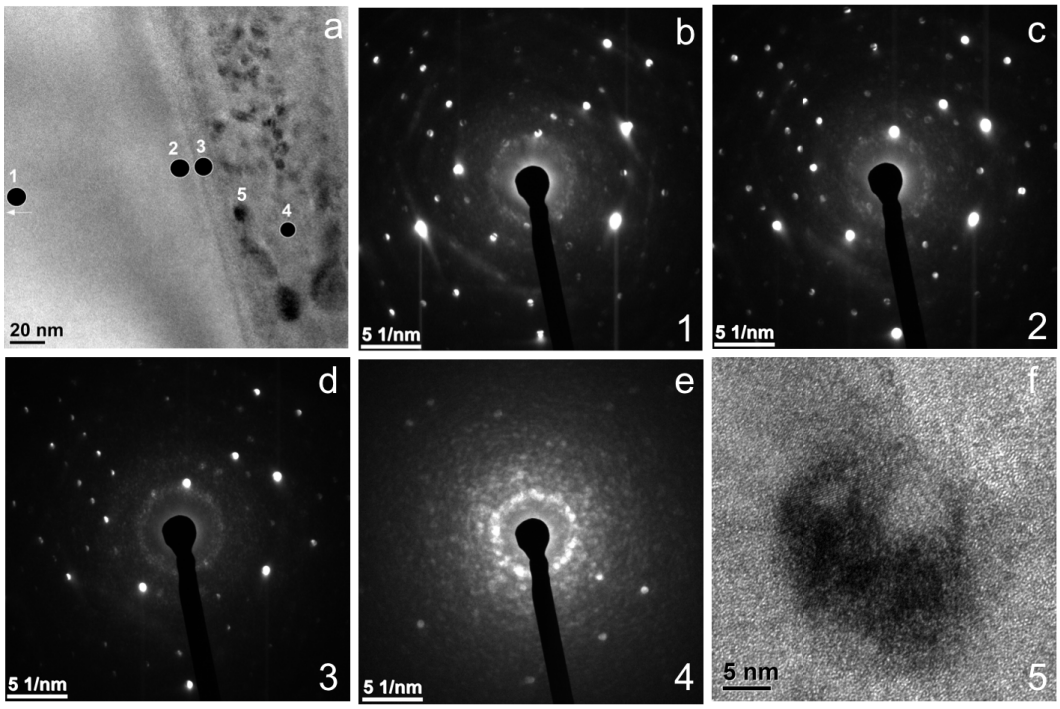

Figure F.6: ***NBD patterns of defined areas in the YIG. a,*** *locations labelled for the NBD pattern for line 8.* ***b-e,*** *NBD pattern of locations 1-4 in order.* ***f,*** *BF image at location 5.*

NBD patterns were also obtained in between exposed lines to observe the damage at those locations. Figure F.7 shows the locations and diffraction patterns at those locations. Location 5 is in the YIG thin film, location 6 is the top damaged YIG layer, and location 7 is in the carbon deposition layer. The locations in Fig. F.7a are magnified in Fig. F.7b. Figure F.7c shows the crystalline phase of the YIG film because of the ion implantation. The top damaged YIG is in the polycrystalline form as shown in Fig. F.7d, while the carbon deposition is in the amorphous phase as shown in Fig. F.7e.

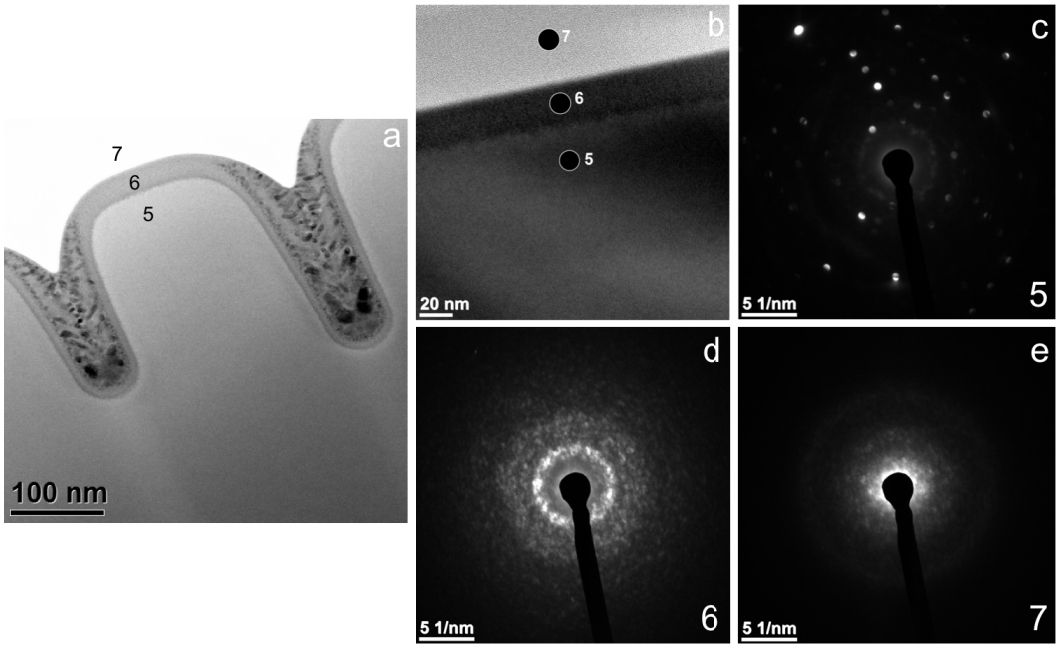

Figure F.7: ***NBD patterns of defined areas in the YIG. a-b,*** *locations labelled for the NBD pattern.* ***c-e,*** *NBD pattern of locations 5-7 in order.*

F.2.6 Convergent Beam Electron Diffraction (CBED)

Convergent beam electron diffraction (CBED) is a diffraction method that can be used in both the conventional TEM (CTEM) and STEM mode. It is based on the convergence of the electron beams to a small probe on the sample instead of parallel beams. The size of diffraction disks is dependent on the convergence angle on the electron beams. CBED gives information in the reciprocal space of the lattice under observation and contributes to the localized crystallographic analysis. It provides information about the lattice parameters, and crystal symmetry [330, 332]. The lattice parameters are obtained by calculating the radius of each ring and taking the inverse of radius for conversion into real space.

Figures F.8b-h show the CBED patterns of the locations labelled in Fig. F.8a. Location 5 is in the crystalline YIG film, location 4 is at the verge of

the damaged line but still in the crystal YIG area, location 1 is exactly at the boundary of the damaged line, and the locations 2, 3, 6, and 7 are inside the damaged area on line 0. Figure F.8b shows the CBED pattern of location 1, which is completely the amorphous phase. The locations 4 and 5 are in the crystal phase and crystallinity has reduced a bit at location 4, as shown in Fig. F.8f and e respectively. A mixture of crystal and amorphous phases exist at locations 2, 3, 6 and 7, as shown in Fig. F.8c, d, g and h respectively. It is concluded that the crystalline phases are present inside the damaged line. Ion-beam recrystallization of the tracks is also possible after the exposure and settling down procedure [323]

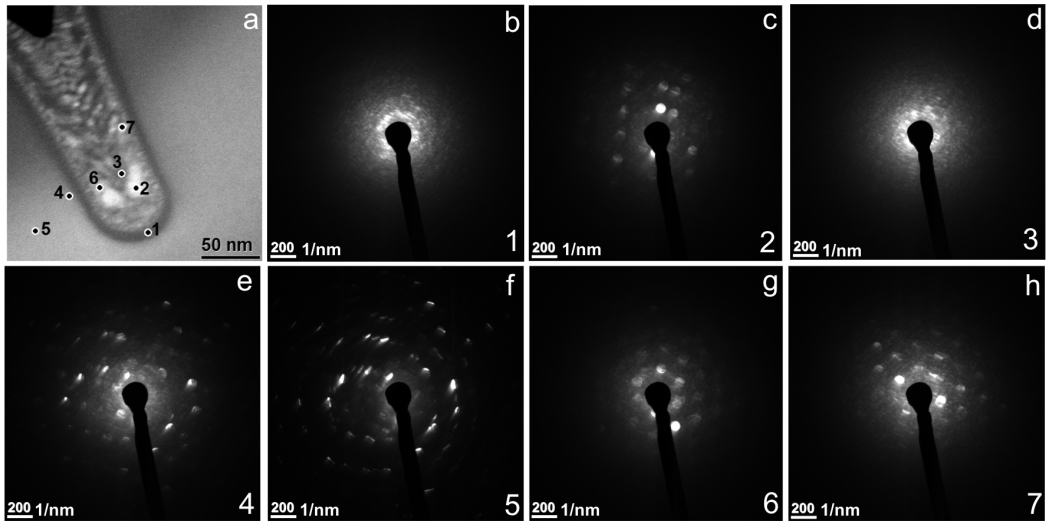

Figure F.8: ***CBED patterns of defined areas in the YIG. a,*** *locations labelled for the CBED pattern.* ***b-h,*** *CBED pattern of locations 1-7 in order.*

F.2.7 Elemental Mapping (EDS) and Energy-Filtered TEM (EFTEM)

Energy-dispersive X-ray spectroscopy (EDS) is a technique that can give information about the composition of the specimen. The characteristic X-ray emissions by the electron beam bombardment on the specimen characterize

the elemental composition of the specimen. EDS can provide the X-ray spectrum and the elemental maps of the area under observation. However, it may contain a continuous background from the copper holder, copper and gold grids and other TEM machine components.

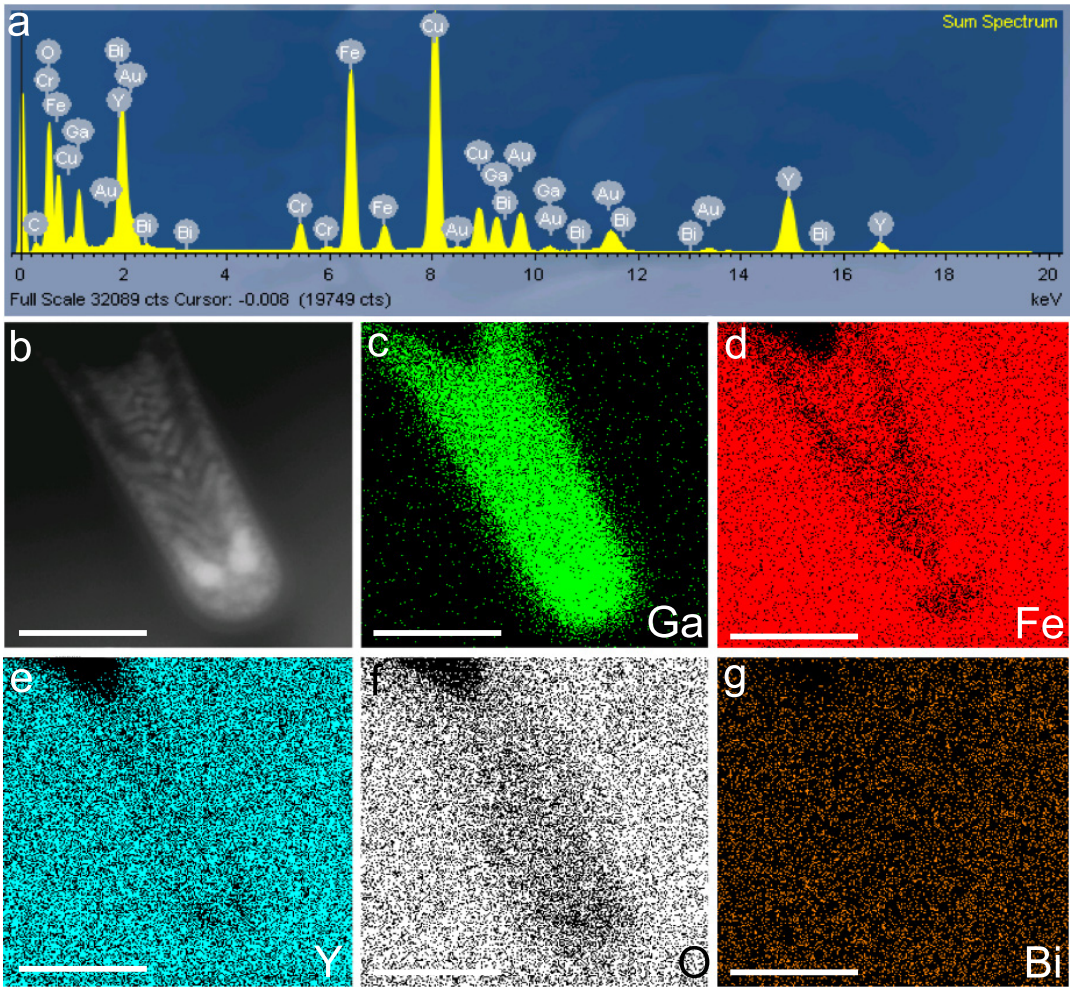

Figure F.9: ***EDS of line 0 in the YIG. a,*** *EDS X-ray spectrum.* ***b,*** *DF image of the area of interest of line 0.* ***c-g,*** *elemental maps for Ga, Fe, Y, O, and Bi respectively. All scale bars are 100 nm.*

Additionally, the EDS can be compared to the energy-filtered TEM (EFTEM), which also provide the compositional information. In EFTEM, electrons of a particular energy are allowed to pass from the slit to form images. The energy selection corresponds to the elements present in the specimens. The

specific energy selection grants the improved contrast and diffraction patterns. The inelastic scattered electrons are removed during the process. The EFTEM images gave similar results as the EDS, thus are omitted in this Appendix.

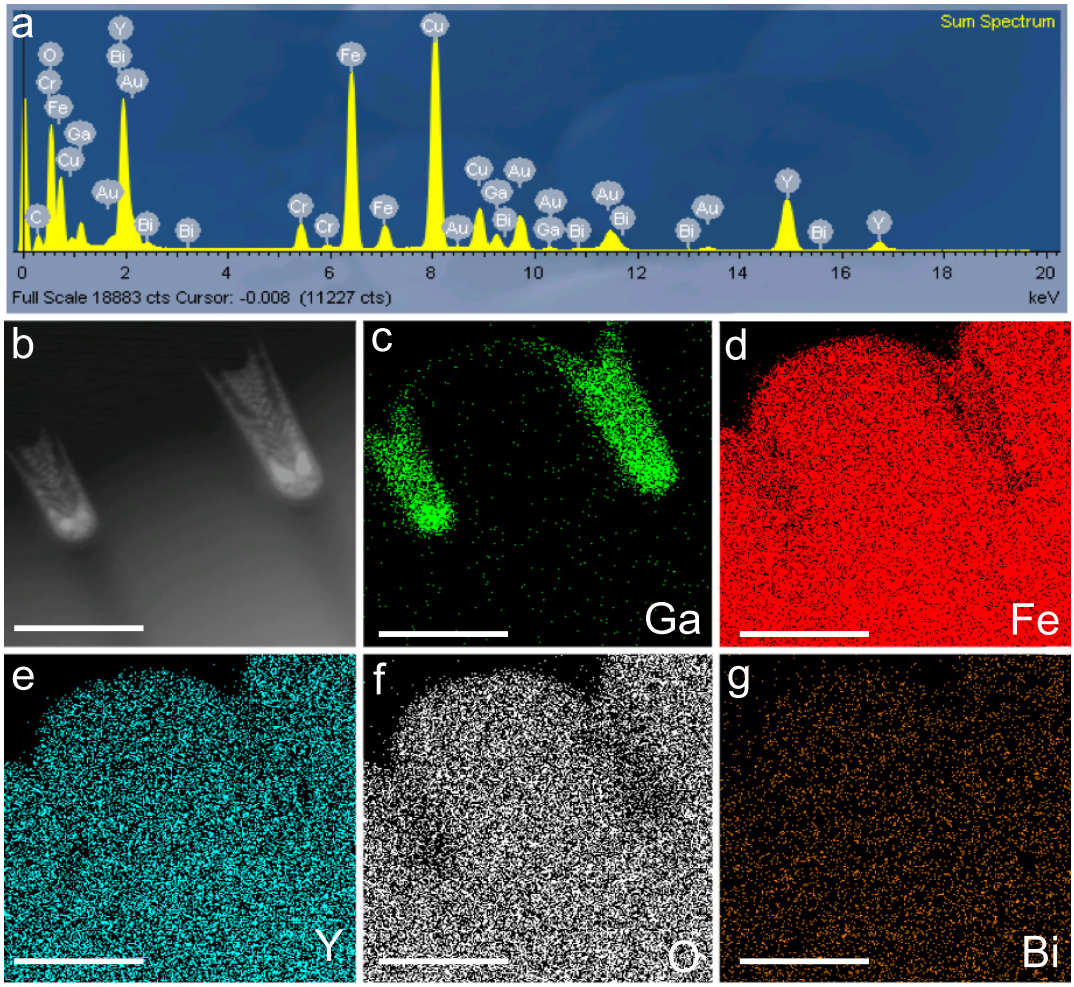

Figure F.10: ***EDS of line 0 and line 1 in the YIG. a,*** *EDS X-ray spectrum.* ***b,*** *DF image of the area of interest of line 0.* ***c-g,*** *elemental maps for Ga, Fe, Y, O, and Bi respectively. All scale bars are 100 nm.*

Figure F.9 shows the EDS spectrum and images for elemental mapping. Figure F.9a shows the X-ray spectrum of selected elements. It is observed that the main elements are Y, Bi, Fe, O, Cr, Au, C, and Cu. One can differentiate the elements from the specimen and from the background by acquiring the elemental maps in the image from of the area of interest.

Figure F.9b shows the line 0 for which elemental maps are acquired for this spectrum. Figures F.9c-g show that the elements Ga, Fe, Y, O and Bi are present in the specimen, hence the elements Cr, Au, C, and Cu are coming from the background in the spectrum. Figure F.9c shows that the Ga+ are implanted in the damaged area while Fe, Y, O and Bi are the YIG characteristic elements, less likely to be present in the damaged area. The same behaviour is observed for the EDS analysis when the area of interest is increased from line 0 to line 0 and line 1 together as shown in Figure F.10.

F.2.8 HRTEM and Selected Area Electron Diffraction (SAED)

Selected-area electron diffraction (SAED) is another basic technique in TEM along with HRTEM. For SAED, an aperture of selective size and selective image plane is used to choose area of interest for the diffraction pattern. SAED is used for crystal structure identification, lattice parameters and miller indices (hkl) plane determination. The pattern identified by SAED is in the reciprocal lattice space like NBD and CBED. The basic principle is the same as in X-ray powder diffraction, which is also used for material characterization. SAED is performed on relatively large samples in TEM, however CBED requires small volumes of samples for diffraction pattern generation.

SAED results in diffusive rings for amorphous samples, small spots reinforcing the rings for polycrystalline samples, and bright spot for crystalline samples. For a crystal structure the hkl miller indices can be calculated from the bright spots locations and the radius of rings. Thence, the lattice parameters can be calculated from the miller indices.

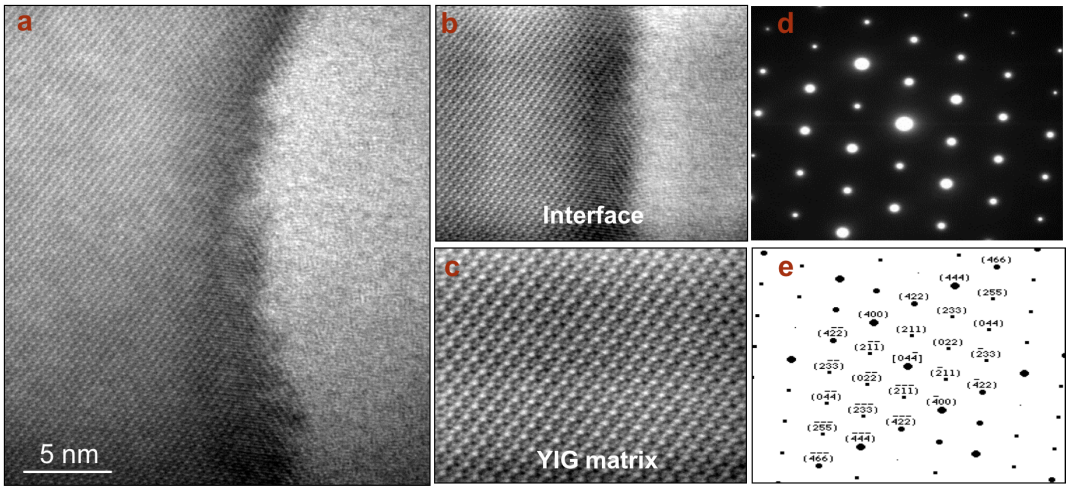

Figure F.11: ***HRTEM and SAED images in the YIG. a,*** *HRTEM at the interface of line 0* ***b,*** *magnified area of the interface.* ***c,*** *magnified area of the YIG matrix.* ***d,*** *SAED pattern for the YIG matrix,* ***e,*** *calculated miller indices for the SAED pattern.*

Figure F.11 shows the HRTEM and SAED of the YIG matrix and damage interface. Figure F.11a is the HRTEM of the interface of the damaged area across the crystalline YIG of line 0. Figure F.11b shows a magnified image of Fig. F.11a, and the YIG crystalline matrix can be clearly seen in Fig. F.11c. Figure F.11d represents the SAED of the YIG matrix, which is in pure crystal form. The hkl miller indices are determined and are shown in Fig. F.11e.

F.2.9 Damage Depth Calculations

At the end, the damage depth and width were calculated for each line for the YIG sample, as shown in Fig. F.12. The parameters for depths and width are labelled in Fig. F.12a and the analysis is shown in Fig. F.12b. The depth L_0 is constant (32 nm) for all lines meaning that the surface damage occurred during the ion beam raster procedure when GIS carbon was deposited on top of the sputter coater carbon (50 nm). The 50 nm carbon from the sputter coater was not enough to shield the Ga+ ions to the YIG surface. There is a significant drop in depths L_1, L_2, and L_3 at line 3, which shows the criticality of the dose

to the YIG sample. After line 3 up to line 7, the change in the line damage depth is small in comparison to line 1. The damaged area (dead layer) around the milled YIG disk would be more than 100 nm, calculated from W_1.

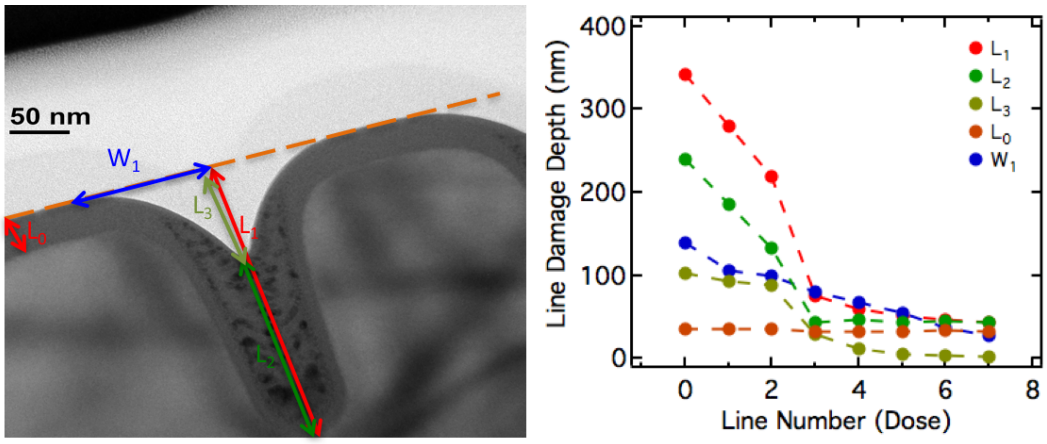

Figure F.12: ***Damage depth variations with Ga dose in the YIG.***

F.3 Ga+ Ion Damage in Silicon Nitride

Silicon nitride is used extensively in the silicon industry and beyond for its characteristics. It can be used as a mask and serve as a sacrificial layer for silicon in many cases [306, 333]. Amorphization and damage in Si_3N_4 was observed by high energy ion irradiation in the literature [334, 335]. The change in stress and mechanical properties of Si_3N_4 has been well studied [336]. The damage can be reduced by rapid thermal annealing [337]. A comparison of ion and electron bombardment has been studied by the annealing and diffusion process [338]. The ion irradiation effects on the Si_3N_4 cantilever creates folding and stresses, depending upon the cantilever dimensions and ion dose [339]. The deflections and stresses in a free standing silicon nitride membrane occur due to ion beam exposure [340].

The investigate of the ion beam caused damage to silicon nitride were studies used in Chapter 3. The purpose is bilateral; serving as a reference mark

in comparison to the damage that occurred in the YIG, and to determine the damage induced stresses in the Si_3N_4 membrane used for the experiments in Chapter 3. The ion beam exposure parameters, designs and other sample preparation techniques are the same as those used for the YIG sample preparation.

F.3.1 Bright Field (BF) Images

The BF images for Si_3N_4 are represented in Fig. F.13. Figure F.13a shows the BF image of all exposed lines, while Fig. F.13b-h show the BF images for each line respectively. It can be observed that there is a significant change in the line damage depths from line 3 to line 4. Thus, the dose for line 3 is critical for silicon nitride damage depth. The silicon nitride is 100 nm thick on top of the silicon base.

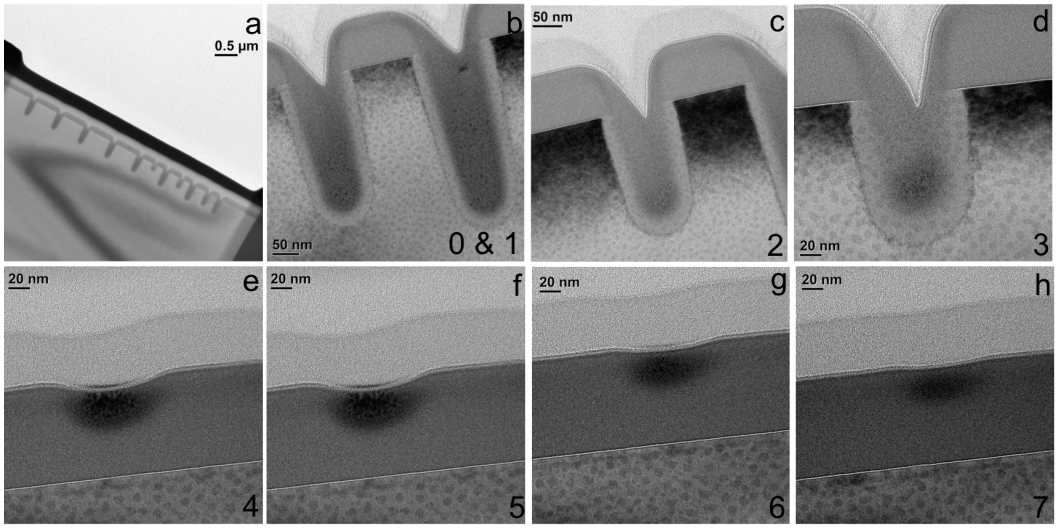

Figure F.13: ***Magnified bright field cross sectional TEM micrographs of damaged lines in*** Si_3N_4***. a-h,*** *BF images for lines 0-7 respectively, as labelled.*

F.3.2 STEM

The STEM BF and DF images for Si_3N_4 are shown in Fig. F.14a and b respectively. Figure F.14 indicates the damage and crystal structure changes in the damaged areas. The damage in Si_3N_4 is different from that in the YIG: in YIG, there is clear mixture of crystalline and amorphous phases inside the line, but the Si_3N_4 is in the polycrystalline phase and becomes amorphous completely in the damaged area.

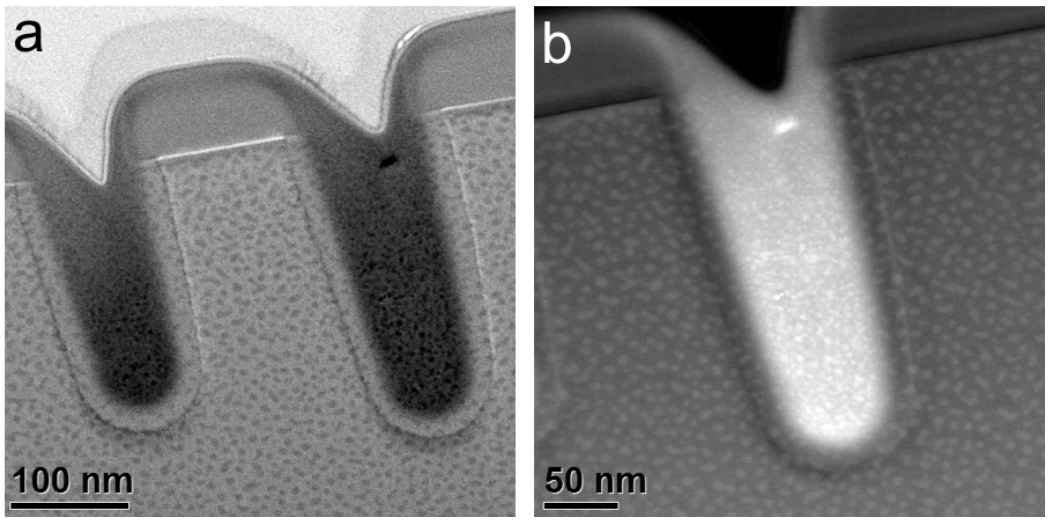

Figure F.14: ***STEM images of damaged lines in*** Si_3N_4***. a,*** *BF TEM micrograph of line 0 and 1.* ***b,*** *DF TEM micrograph of line 0.*

F.3.3 High Resolution TEM (HRTEM)

The High Resolution TEM (HRTEM) images of damaged lines for Si_3N_4 are shown in Fig. F.15. The damaged areas can be seen clearly in Fig. F.15a-h for lines 0-7 respectively. The crystalline and damaged areas can be clearly observed.

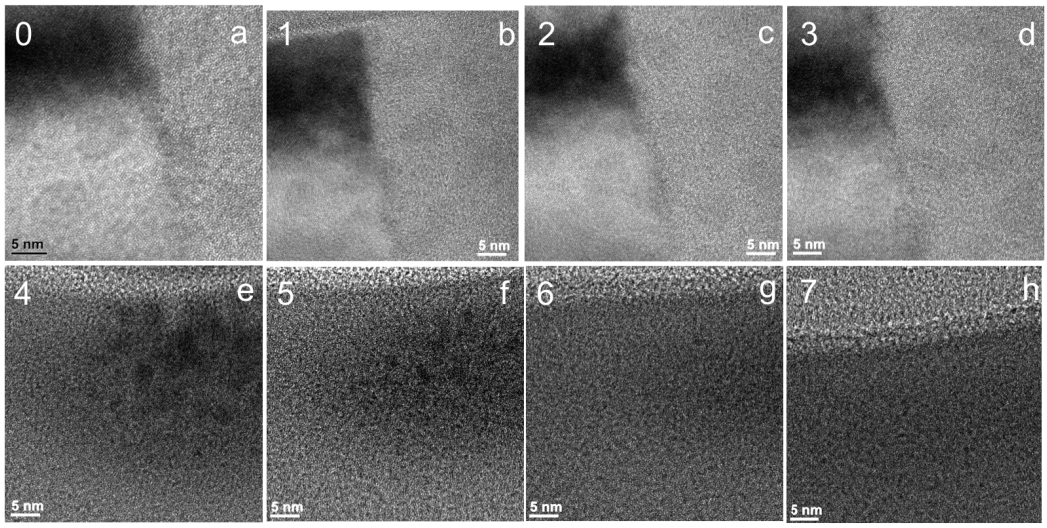

Figure F.15: ***HRTEM images of damaged areas in*** Si_3N_4***. a-h,*** *the HRTEM of each line labelled from 0 to 7 respectively.*

F.3.4 Convergent Beam Electron Diffraction (CBED)

The CBED patterns of Si_3N_4 at pre-defined locations is shown in Fig. F.16. The locations for line 0 are labelled in Fig. F.16a. Figures F.16b and d show the CBED for locations 1 and 2, and show the polycrytallinity of the Si_3N_4 sample. At locations 3, 4 and 5, the sample converts to an amorphous phase completely as shown by the diffusive ring in CBED in Fig. F.16d-f.

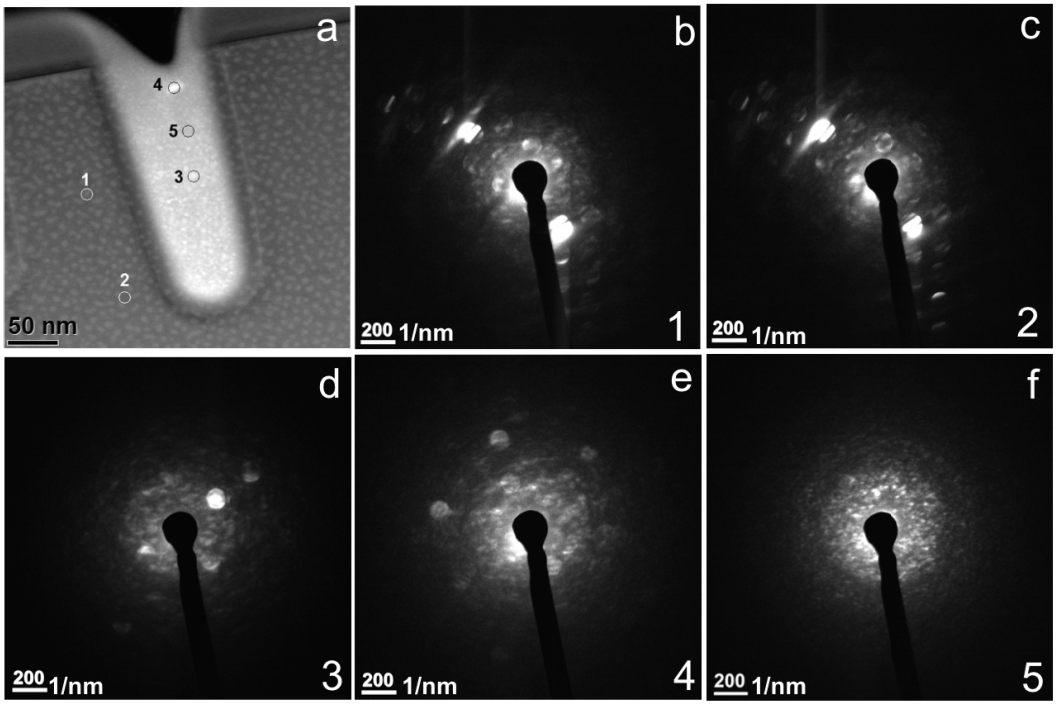

Figure F.16: ***CBED patterns of defined areas in*** Si_3N_4***. a,*** *locations labelled for the CBED pattern.* ***b-f,*** *CBED pattern of locations 1-5 in order.*

F.3.5 Elemental Mapping (EDS)

The elemental analysis for the Si_3N_4 was performed and is represented in Fig. F.17. Figure F.17a shows the EDS spectrum, having main elements Si, Ga, Cu, Au, and Cr. The elements Cu, Au, and Cr are from the background, Si is the material characteristic element, and Ga comes from the implanted ions. Figure F.17b shows the STEM DF image of the line 0, while Fig. F.17c shows the Ga ion map and Fig. F.17d shows the Si elemental map.

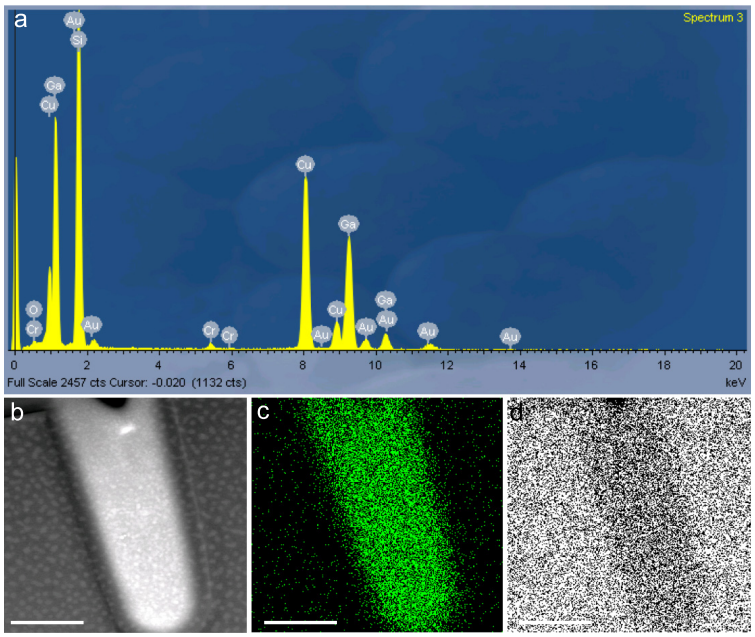

Figure F.17: ***EDS of line 0 in*** Si_3N_4***. a,*** *EDS X-ray spectrum.* ***b,*** *DF image of the area of interest of line 0.* ***c-d,*** *elemental maps for Ga, and Si respectively. All scale bars are 100 nm.*

The damage depth profile in Si_3N_4 is plotted in Fig. F.18. It can be clearly observed that there is a threshold dose of Ga+ ions for milling (i.e. line 4) and for the surface rastering the Si_3N_4 surface. In comparison with YIG, the milling occurs at a lower dose in Si_3N_4, and there is more depth profile and redeposition in Si_3N_4.

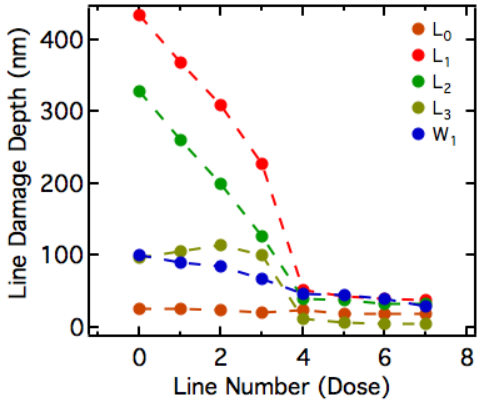

Figure F.18: ***Damage depth variations with Ga dose in*** Si_3N_4***.***

Appendix G

Preparation of YIG for Lorentz Microscopy

G.1 Introduction

Lorentz microscopy is one of the frequently used techniques to study magnetic properties. It is used to study the intrinsic and extrinsic magnetic properties of the material under observation. There are many advantages of Lorentz microscopy, which include high spatial resolution, direct observation of magnetic domains and access to the material characteristics (structural, compositional and electronic) of the same area of the sample in the nanometer range. Magnetic information like the domain shape, nature of domain walls and pinning and other micromagnetic information can be extracted. The experiments can be performed in the image mode or in the time-resolved observations. Details of Lorentz microscopy are available in reference [341].

Lorentz microscopy has been performed on YIG films to obtain micromagnetic information. Stray fields gave information about the domains, domain walls and their motion, that were dependent on the sample shape and dimensions [342]. However, Lorentz microscopy on YIG disks instead of YIG films is of interest for this Appendix, since YIG disks of variable sizes have been

studied in Chapter 6. It is worth making direct observations of domains in the YIG disks. This Appendix discusses the sample preparation of YIG disks for Lorentz microscopy. The sections below explain the sample preparation of the YIG and test runs of Lorentz microscopy on the permalloy samples.

G.2 Sample Preparation of YIG for Lorentz Microscopy

One limitation of Lorentz microscopy is the thickness of the specimen, that should be under 200 nm. The thickness of the specimen is more likely to be dependent on the atomic number of the material. Samples for Lorentz microscopy are usually prepared from the bulk sample by chemical etching or by FIB. In our case, a mechanically polished sample, as discussed in Appendix E, was taken initially for the ion-beam milling for TEM sample preparation. The sample preparation was performed in the FIB (Zeiss NVision 40 Cross Beam Microscope) machine.

Initial milling was started at 30 keV with Ga+ ions on the 5μm thin section of YIG, as shown in Fig. G.1a. When the wall thickness reduced to 2.8μm, a thick layer of carbon and platinum was deposited on the top for protection and to serve as a sacrificial layer, as shown in Fig. G.1b. The wall thickness was reduced for final thinning at 5 keV, as represented in Fig. G.1c. The final polishing in a two thin section shape was performed, after the wall thickness had reached 700 nm, at 1 keV and 0.5 keV beam energy, as shown in Fig. G.1d. A final thinkness of 100 nm was obtained for the two thin sections, which can be seen as a light colour in the SEM of Fig. G.1d.

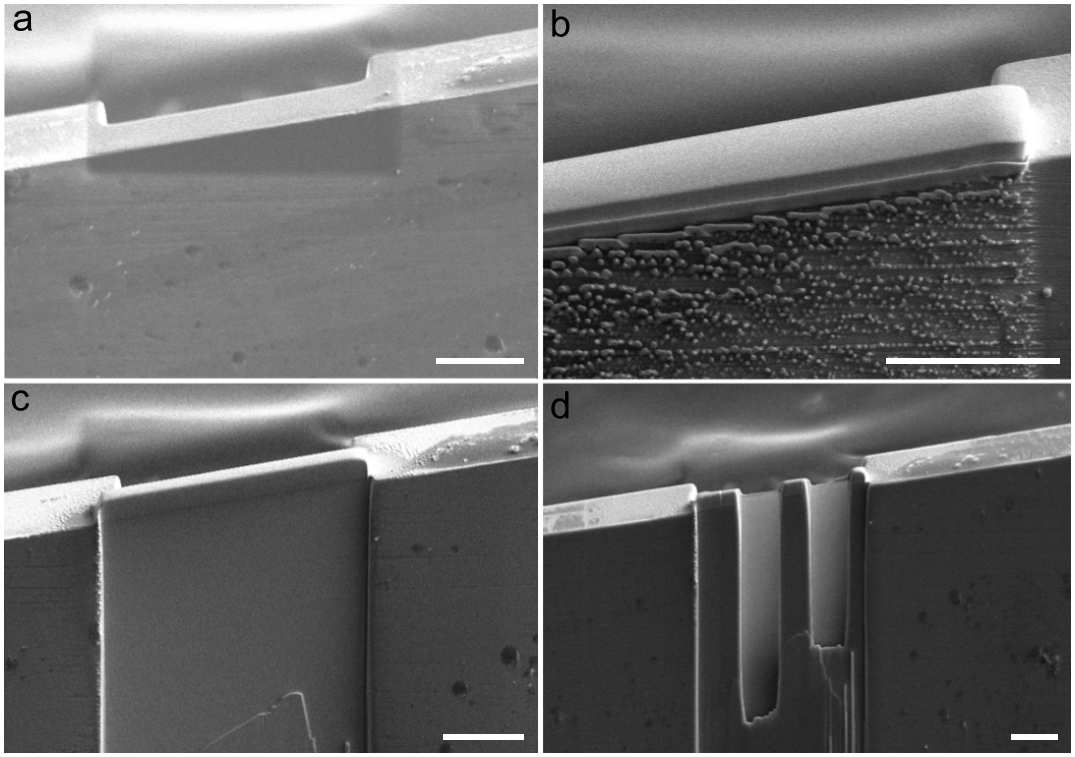

Figure G.1: ***TEM sample preparation of the YIG for Lorentz microscopy.*** ***a,*** *initial thinning at 30 keV.* ***b,*** *carbon and platinum deposition on top.* ***c,*** *further thinning at 5 keV.* ***d,*** *final polishing at 1 keV. All scale bars are 5μm.*

A family of YIG disks of various sizes (3μm, 1μm, 500 nm, and 200 nm in diameter) were created in the raith design and then fabricated in the thin sections of Fig. G.1d. Figure G.2 shows the four patterns of YIG disk families fabricated in the thin sections and in the bulk YIG.

The YIG family of disks were then plucked from the thin sections with a metallic probe inside the FIB machine (Hitachi NB5000) and then placed on top of the carbon grid as shown in Fig. G.3a. Figure G.3b shows the magnified image of the YIG disks on the carbon grid. A final step had to be performed to remove the handle of the YIG disks and to make them independent for the Lorentz microscopy. After that, the sample was ready for Lorentz microscopy.

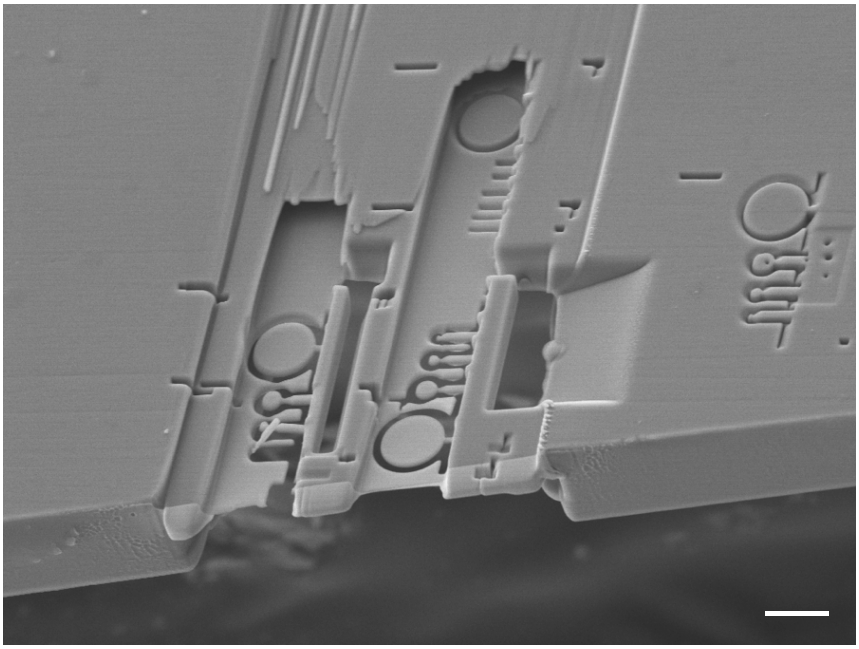

Figure G.2: ***Family of YIG disks.*** *YIG disks fabricated in the thin sections. Scale bar is 3μm.*

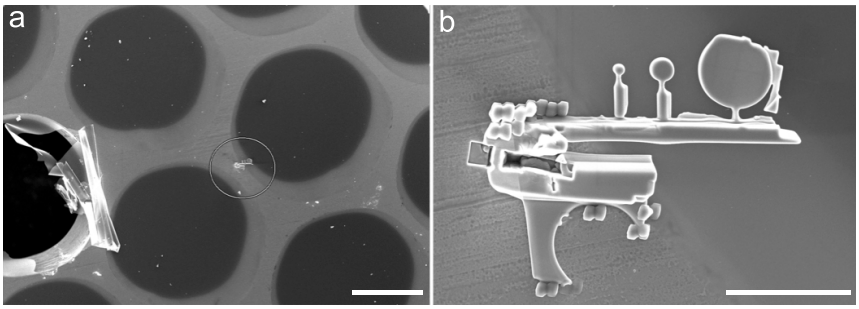

Figure G.3: ***YIG sample loading on carbon grid. a,*** *the YIG family is encircled.* ***b,*** *the YIG family is placed and welded onto the carbon grid. All scale bars are 5μm.*

G.3 Lorentz Microscopy of Permalloy

In Lorentz imaging, the electron beam faces a deflection when it passes through the magnetic specimen. This deflection can be detected by various modes in Lorentz microscopy, one of which is the Fresnel mode. The Lorentz images are taken out of focus (under-focus and over-focus) conditions in this mode, for

which the magnetic domains have characteristic brightness (dark or bright). The spatial resolution is, however, compromised because of the out of focus conditions in this mode [341].

Lorentz microscopy of permalloy (Py) in the Fresnel mode has been performed as a preliminary run, as shown in Fig. G.4. Figure G.4a shows the Lorentz image in the under-focus condition, Fig. G.4b in the in-focus, and Fig. G.4c in the over-focus conditions. Figures G.4a and c show the vortex state of the permalloy disks (1.8 μm in diameter). The obtained results are similar to the vortex state discussed in the literature, in circular form [343]. Permalloy has been well studied in different shapes like square [344], rectangule [345], nanowires [346], and rings [347], [348], with Lorentz microscopy. Py was used, as a test material for dry-runs, for Lorentz microscopy before trying for the YIG sample.

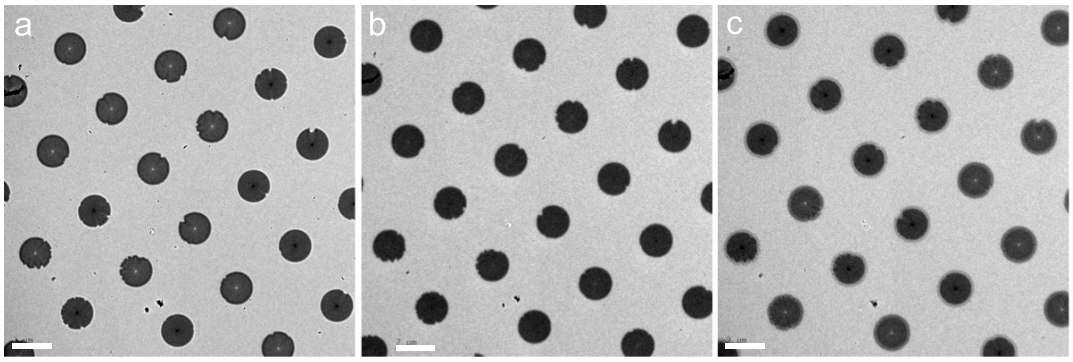

Figure G.4: ***Lorentz microscopy of permalloy.*** ***a,*** *under-focus condition* ***b,*** *in-focus condition* ***c,*** *over-focus condition. All scale bars are 2μm.*

Appendix H

Exchange Coupling in Co-CoO layers

The exchange coupling between ferromagnetic (FM) and antiferromagnetic (AFM) layers give rise to the exchange bias as a result of the proximity effect. It originates from the uncompenstated spins at the FM/AFM interface [349]. Exchange bias (EB) was discovered about six decades ago (1951) in cobalt oxide (CoO/Co) particles and is still a topic of research today. EB has been explored in core/shell particles, and thin film layers. EB has been studied using methods like magnetization hysteresis [349], X-ray diffraction, scanning tunneling microscopy [350]. In magnetization hysteresis, the hysteresis loop shifts along the field axis, with an increase in the coercive field. To observe EB, the sample is usually cooled down to below the blocking temperature of the system under observation. The anisotropy of AFM, and the Néel temperature and blocking temperature are the important parameters in observing EB. The dependence of EB on the AFM layer [351] and the pinning of FM spins at the interface has been well studied. Devices with EB are used in magneto-electronic applications, hard disk drives (HDD), magnetic tunneling junctions (MTJ), spin-valves, and in spintronics [350, 351, 352, 353].

CoO has a Néel temperature (291K) [354] that makes it a perfect material

to be used in FM/AFM layers for observing the EB phenomenon. Various effects including thickness, surface roughness, particle/domain size, crystallinity, antiferromagnetic order, and the phases of CoO in the FM/CoO layers have been studied [354, 355]. The thickness dependence of EB on CoO in NiFe/CoO layers has been observed [351]. Multilayers of FM and AFM are also good areas of interest and have been well studied [356, 357].

The layered structure of Co/CoO is of great interest because of strong FM/AFM coupling and due to the effective anisotropies, mostly the uniaxial anisotropy due to the EB. The spin wave resonances of Co/CoO layers were also studied. The frequency shift in the spin waves by the effective interfacial anisotropies has been demonstrated in Co/CoO [358, 359]. EB in Co/CoO was also studied with varying CoO thickness [360]. An order-to-disorder transition with temperature was observed in Co/CoO, and the metallic state changes [350]. A frequency dependent EB, the training effect, was also observed in the Co/CoO system [349]. An increase in EB and coercivity in Co/CoO was investigated because of the spin glass behaviour and increased crystallinity [354]. In-situ measurements of the dependence of EB on the interface roughness has been studied [355].

The study of EB and exchange coupling through the magnetization hysteresis in Co/CoO was aimed in here. The nanomechanical devices were fabricated using the same procedure as described in Appendix C. The Co and CoO were deposited on the devices via chemical vapour deposition. A representative set of devices is shown in Fig. H.1. The devices show the magnetic element in the center of the devices in black colour. The torsional mode resonance frequency for one of these devices was found to be 1.665MHz and the flexural mode was 2.517MHz. The device paddles were off-center from the torsional rod to produce high signal to noise ratio. However, the signal could not be confirmed due bad sample quality. It was decided to make a new set of devices with better sample quality.

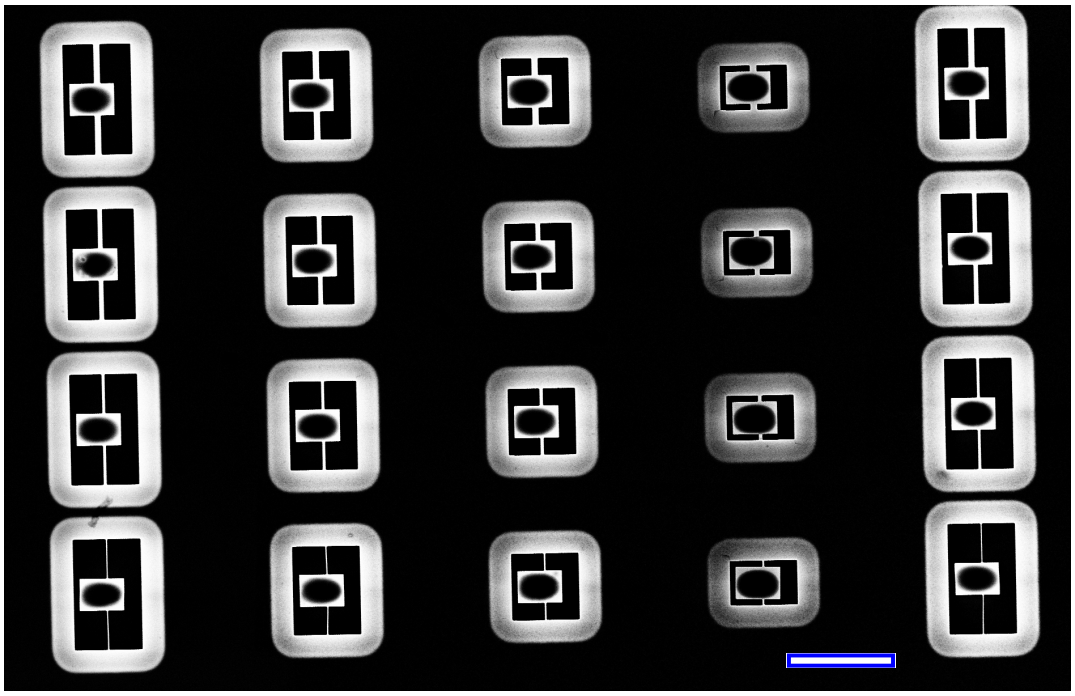

Figure H.1: ***SEM image of the Co/CoO layer devices.***